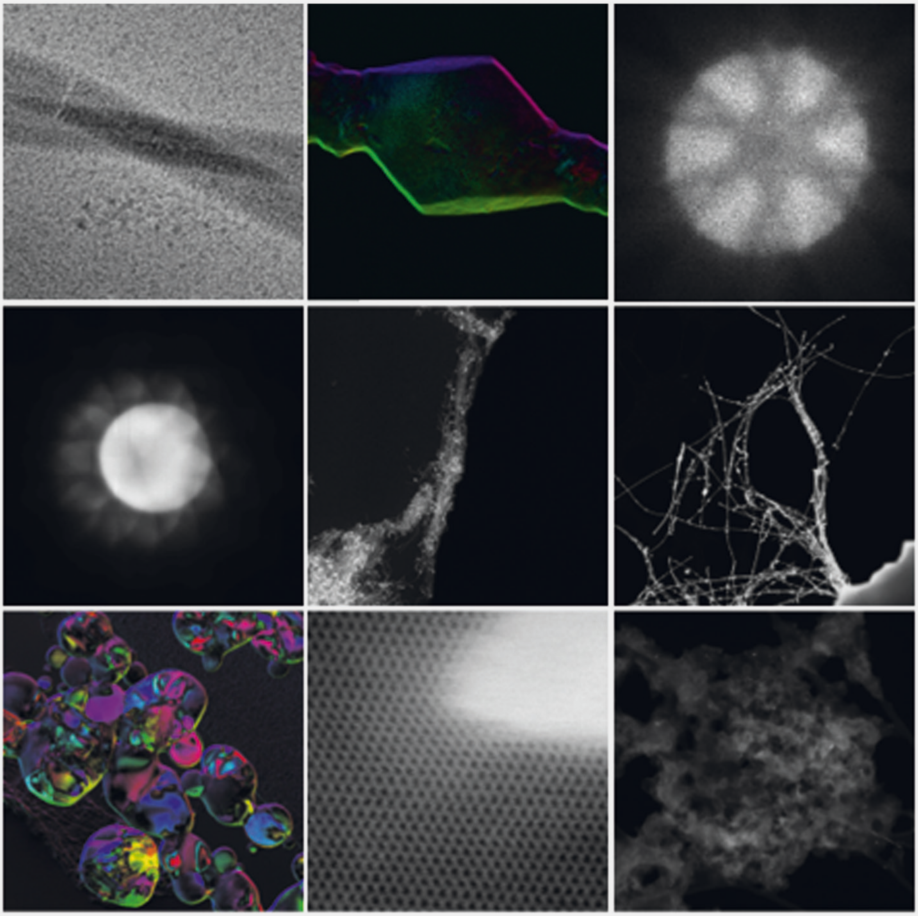

Quantitative atomic-level investigation of solid materials through multidimensional electron diffraction measurements

Hoelen Laurence Lalandec-Robert

Schlüsseltechnologien / Key Technologies
Band / Volume 277
ISBN 978-3-95806-735-6

Mitglied der Helmholtz-Gemeinschaft

JÜLICH
Forschungszentrum

Schriften des Forschungszentrums Jülich
Reihe Schlüsseltechnologien / Key Technologies Band / Volume 277

Forschungszentrum Jülich GmbH
Ernst Ruska-Centrum für Mikroskopie und Spektroskopie mit Elektronen (ER-C)
Physik Nanoskaliger Systeme (ER-C-1 / PGI-5)

Quantitative atomic-level investigation of solid materials through multidimensional electron diffraction measurements

Hoelen Laurence Lalandec-Robert

Schriften des Forschungszentrums Jülich
Reihe Schlüsseltechnologien / Key Technologies Band / Volume 277

ISSN 1866-1807 ISBN 978-3-95806-735-6

Bibliografische Information der Deutschen Nationalbibliothek.
Die Deutsche Nationalbibliothek verzeichnet diese Publikation in der
Deutschen Nationalbibliografie; detaillierte Bibliografische Daten
sind im Internet über http://dnb.d-nb.de abrufbar.

Herausgeber und Vertrieb: Forschungszentrum Jülich GmbH
Zentralbibliothek, Verlag
52425 Jülich
Tel.: +49 2461 61-5368
Fax: +49 2461 61-6103
zb-publikation@fz-juelich.de
www.fz-juelich.de/zb

Umschlaggestaltung: Grafische Medien, Forschungszentrum Jülich GmbH

Druck: Grafische Medien, Forschungszentrum Jülich GmbH

Schriften des Forschungszentrums Jülich
Reihe Schlüsseltechnologien / Key Technologies, Band / Volume 277

D 82 (Diss. RWTH Aachen University, 2023)

ISSN 1866-1807
ISBN 978-3-95806-735-6

Vollständig frei verfügbar über das Publikationsportal des Forschungszentrums Jülich (JuSER)
unter www.fz-juelich.de/zb/openaccess.

Contents

Abstract

The recording of a detailed diffraction pattern, as a function of scan position, was enabled in scanning transmission electron microscopy (STEM), thus giving rise to momentum-resolved STEM (MR-STEM). Whereas this technique provides a new framework for atomically-resolved quantitative analysis based on low-angle scattering, it also offers an opportunity to investigate single contributions to the intensity distribution in reciprocal space.

A first example of those contributions is inelastic scattering, whose understanding is critical for the determination of both structure and chemical composition in materials. Here, the influence of plasmon excitation on the diffracted intensity was investigated for Pt and Al. For this purpose, a new experimental approach was established, consisting in the combination of energy-filtering and momentum-resolution, thus permitting the formation of diffraction patterns with a restriction to specific losses of energy. As part of this study, it was found that, due to inelastic scattering, a diffuse intensity component arises at angles below 40-50 mrad, which leads to a mismatch between experimental results and conventional simulations. In order to solve this and enable the quantitative calculation of low-angle scattering, new simulation approaches were tested to account for energy-loss, employing transition potentials embedded in a multislice algorithm. In a second time, a simplified approach was also demonstrated for the inclusion of multiple plasmon scattering.

Another critical aspect of electron diffraction, as accessed in a MR-STEM experiment, is the role of imaging conditions. Specifically, it was found that, among STEM signals extracted from the diffraction patterns, disagreements of several nanometres exist in terms of the foci necessary to reach optima of image contrast. In order to further characterize the focus-dependences, a new experimental set-up was introduced, consisting in performing the measurement in a focal series. It was applied on an α-In$_2$Se$_3$ specimen. The experiments were then supplemented by extensive simulations. An important consequence of the focus mismatch is the inability to obtain all the extractable information with a constant image quality and precision. This therefore demonstrates a non-universality of the technique for the extraction of different specimen parameters from a single recording. In the other hand, it was also shown that the precise locations of contrast optima along the focus axis display a dependence to the positions of surfaces, thus permitting their detection. The experimental requirements for such a measurement were further explored through simulations.

Kurzfassung

Die Aufzeichnung eines detaillierten Beugungsmusters in Abhängigkeit von der Scanposition wurde in der Rastertransmissionselektronenmikroskopie (STEM) ermöglicht, wodurch die impulsaufgelöste STEM (MR-STEM) entstanden ist. Während diese Technik einen neuen Rahmen für die atomar aufgelöste quantitative Analyse auf der Grundlage der Niederwinkelstreuung schafft, bietet sie auch die Möglichkeit, einzelne Beiträge zur Intensitätsverteilung im reziproken Raum zu untersuchen.

Ein erstes Beispiel für diese Beiträge ist die inelastische Streuung, deren Verständnis für die Bestimmung der Struktur und der chemischen Zusammensetzung von Materialien entscheidend ist. Hier wurde der Einfluss der Plasmonenanregung auf die Beugungsintensität für Pt und Al untersucht. Zu diesem Zweck wurde ein neuer experimenteller Ansatz entwickelt, der in der Kombination von Energiefilterung und Impulsauflösung besteht und somit die Bildung von Beugungsmustern mit einer Beschränkung auf bestimmte Energieverluste ermöglicht. Im Rahmen dieser Studie wurde festgestellt, dass aufgrund inelastischer Streuung bei Winkeln unter 40-50 mrad eine diffuse Intensitätskomponente auftritt, die zu einer Diskrepanz zwischen experimentellen Ergebnissen und herkömmlichen Simulationen führt. Um dieses Problem zu lösen und eine quantitative Berechnung der Streuung bei niedrigen Winkeln zu ermöglichen, wurden neue Simulationsansätze zur Berücksichtigung von Energieverlusten getestet, bei denen Übergangspotentiale in einem Multislice-Algorithmus verwendet wurden. In einem zweiten Schritt wurde auch ein vereinfachter Ansatz für die Einbeziehung der Mehrfach-Plasmonenstreuung demonstriert.

Ein weiterer kritischer Aspekt der Elektronenbeugung, der in einem MR-STEM-Experiment untersucht wurde, ist die Rolle der Abbildungsbedingungen. Insbesondere wurde festgestellt, dass bei den aus den Beugungsmustern extrahierten STEM-Signalen Unstimmigkeiten von mehreren Nanometern hinsichtlich der zur Erreichung eines optimalen Bildkontrasts erforderlichen Brennpunkte bestehen. Um die Fokusabhängigkeit weiter zu charakterisieren, wurde ein neuer Versuchsaufbau eingeführt, der darin besteht, die Messung in einer Fokusreihe durchzuführen. Sie wurde an einer α-In_2Se_3-Probe durchgeführt. Die Experimente wurden dann durch umfangreiche Simulationen ergänzt. Eine wichtige Folge der Fokusfehlanpassung ist die Unfähigkeit, alle extrahierbaren Informationen mit einer konstanten Bildqualität und Präzision zu erhalten. Dies zeigt, dass die Technik nicht universell für die Extraktion verschiedener Probenparameter aus einer einzigen Aufnahme geeignet ist. Andererseits konnte auch gezeigt werden, dass die genaue Lage der Kontrastoptima entlang der Fokusachse eine Abhängigkeit von den Positionen der Oberflächen aufweist und somit deren Erkennung ermöglicht. Die experimentellen Voraussetzungen für eine solche Messung wurden durch Simulationen weiter erforscht.

Acknowledgements

I would like to first express my gratitude and appreciation toward my doctoral supervisor and thesis reporter Prof. Dr. Knut Müller-Caspary, who provided me with his extensive knowledge and experience and whose guidance and critical assessments allowed me to improve massively. It was thanks to him that I could both conclude on this work and initiate my academic career.

I am also very grateful toward my other two reporters, Prof. Dr. Rafal Dunin-Borkowski and Prof. Dr. Joachim Mayer, both directors at the Ernst Ruska-Centre for Microscopy and Spectroscopy with Electrons, where my doctoral work was carried out. I sincerely thank them for their enthusiasm, interest and support.

Furthermore, I would like to thank collaborators, on whom some important parts of my research depended. First, for their involvement in the work on inelastic electron scattering, I thank Prof. Dr. Kerstin Volz and Dr. Andreas Beyer, from Philips-Universität Marburg, and Prof. Dr. Andreas Rosenauer and Dr. Florian Krause, from Universität Bremen. For their support in the work on focal series, I also thank Em. Prof. Dr. Dirk Van Dyck, Prof. Dr. Sandra Van Aert and Dr. Ivan Lobato, from the University of Antwerp, and Prof. Dr. Qing Chen, from Peking University.

Finally, for their help, interesting discussions, and time, I would like to express my appreciation for my former colleagues Peng-Han Lu, Dr. Janghyun Jo, Dr. Paul Paciok, Ansgar Meise, Dr. Andras Kovacs, Dr. Florian Winkler, Dr. Teresa Wessels, Achim Strauch, Mauricio Cattaneo, Hubert Dulisch, Simon Arnoldi, Alexander Clausen and Dr. Dieter Weber.

List of publications

Influence of plasmon excitations on atomic-resolution quantitative 4D scanning transmission electron microscopy ; A. Beyer, F. F. Krause, **H. L. Robert**, S. Firoozabadi, T. Grieb, P. Kükelhan, D. Heimes, M. Schowalter, K. Müller-Caspary, A. Rosenauer, K. Volz ; Scientific Reports 10 (2020), 17890

Dynamical diffraction of high-energy electrons investigated by focal series momentum-resolved scanning transmission electron microscopy at atomic resolution ; **H. L. Robert**, I. Lobato, F. Lyu, Q. Chen, S. Van Aert, D. Van Dyck, K. Müller-Caspary ; Ultramicroscopy 233 (2021), 113425

Contribution of multiple plasmon scattering in low-angle electron diffraction investigated by energy-filtered atomically resolved 4D-STEM ; **H. L. Robert**, B. Diederichs, K. Müller-Caspary ; Applied Physics Letters 121 (2022), 213502

Shape sensitivity in first moment STEM and application of a continuous object model in conditions of dynamical electron diffraction ; H. Dulisch, **H. L. Robert**, P. Lu, F. Kirner, J. Jo, E. Sturm, R. E. Dunin-Borkowski, K. Müller-Caspary ; in preparation

Contributions to conferences

Momentum-resolved STEM as a tool to explore angle-dependent electron scattering ; **H. L. Robert**, K. Müller-Caspary ; PICO conference, 06.05-10.05 2019, Vaals (The Netherlands), poster presentation

Momentum-resolved STEM as a tool to study angle-dependent electron scattering in nanostructures ; **H. L. Robert**, A. Rosenauer, N. Ravishankar, D. Van Dyck, K. Müller-Caspary ; Microscopy conference (MC), 01.09-05.09 2019, Berlin (Germany), talk (15 minutes including questions)

Momentum-resolved, energy-filtered and focal series STEM for the investigation of angle-dependent electron scattering ; **H. L. Robert**, S. S. Firoozabadi, P. Kükelhan, A. Beyer, K. Volz, F. F. Krause, T. Grieb, M. Schowalter, A. Rosenauer, N. Ravishankar, D. Van Dyck, K. Müller-Caspary ; Asia-Pacific Microscopy Conference (APMC), 03.02-07.02 2020, Hyderabad (India), talk (10 minutes including questions)

Momentum-resolved STEM combined with focal series and energy-filtering for the investigation of angle-dependent electron scattering ; **H. L. Robert**, F. Winkler, S. S. Firoozabadi, P. Kükelhan, A. Beyer, K. Volz, F. F. Krause, T. Grieb, M. Schowalter, A. Rosenauer, N. Ravishankar, D. Van Dyck, and K. Müller-Caspary ; European Microscopy Conference (EMC) young scientists meeting, 24.11-26.11 2020, online, talk (15 minutes including questions)

Effect of probe defocus in momentum-resolved STEM experiments ; **H. L. Robert**, F. Winkler, I. Lobato, S. Van Aert, D. Van Dick, F. J. Lyu, Q. Chen, K. Müller-Caspary ; PICO conference, 02.05-06.05 2021, online, poster presentation

Impact of defocus in high-resolution momentum-resolved STEM ; **H. L. Robert**, F. Winkler, I. Lobato, S. Van Aert, F. J. Lyu, Q. Chen, K. Müller-Caspary ; Microscopy conference (MC), 22.08-26.08 2021, online, **invited talk (30 minutes including questions)**

Influence of inelastic scattering on high-resolution momentum-resolved STEM of bulk platinum ; **H. L. Robert**, F. F. Krause, A. Beyer, T. Grieb, S. S. Firoozabadi, P. Kükelhan, M. Schowalter, A. Rosenauer, K. Volz, K. Müller-Caspary ; Microscopy conference (MC), 22.08-26.08 2021, online, poster presentation (second contribution)

Investigation of the impact of multiple plasmon-loss on low-angle electron diffraction by energy-filtered 4D-STEM ; **H. L. Robert**, K. Müller-Caspary ; Microscopy conference (MC), 26.02-02.03 2023, Darmstadt, poster presentation

Abbreviations

TEM: transmission electron microscopy

CTEM: conventional TEM

STEM: scanning TEM

OP: object plane

IP: image plane

FP: focal plane

BFP: backfocal plane

OL: objective lens

CBED: convergent beam electron diffraction

PACBED: position-averaged CBED

PSF: point-spread function

MTF: modulation transfer function

FSR: focal series reconstruction

MR-STEM: momentum-resolved STEM

4D-STEM: four-dimensional STEM (alternative term for MR-STEM)

EF-MR-STEM: energy-filtered MR-STEM

FS-MR-STEM: focal series MR-STEM

C-STEM: conventional STEM

AR-STEM: angle-resolved STEM

DPC: differential phase contrast

DED: direct electron detector

BF: bright field

DF: dark field

ADF: annular dark field

HAADF: high-angle ADF

LAADF: low-angle ADF

CoM: center of mass

ZL: zero-loss

ZLP: zero-loss peak

PL: plasmon-loss

EEL: electron energy-loss

EELS: electron energy-loss spectroscopy

POA: phase object approximation

WPOA: weak phase object approximation

TDS: thermal diffuse scattering

FEG: field-emission gun

CFEG: cold field-emission gun

PTC: partial temporal coherence

PSC: partial spatial coherence

Naming conventions

Physical constants

$h = 6.62607004.10^{-34}\, m^2.kg.s^{-1}$: Planck constant

$c = 2.99792458.10^8\, m.s^{-1}$: Velocity of light in vacuum

$m = 9.10956.10^{-31}\, kg$: Rest mass of an electron

$e = 1.60217662.10^{-19}\, C$: Elementary charge

$\epsilon_0 = 8.85418781762039.10^{-12}\, A^2.s^4.kg^{-1}.m^{-3}$: Dielectric permittivity of vacuum

$k_B = 1.380649.10^{-23}\, m^2.kg.s^{-2}.K^{-1}$: Boltzmann constant

$C_R = \frac{4\pi mek_B{}^2}{h^3}$: Richardson constant

Imaging parameters

U: Acceleration voltage of an electron beam

α: Semi-convergence angle

δr_{Abbe}: Abbe criterion

$\delta r_{Rayleigh} = 1.22\delta r_{Abbe}$: Rayleigh criterion

$\delta z_{res.}$: Depth of focus

I_0: Incident electron intensity

v: Electron velocity

λ: Electron wavelength

γ: Lorentz factor

A: Numerical aperture

q_A: Radius of the numerical aperture in reciprocal space, determined by α and λ

σ: Interaction parameter

E: Energy of the electron wave function

f: Focus of the objective lens

Δf: Focus spread characterizing the partial temporal coherence of the experiment

C_c: Chromatic aberration of the objective lens

ΔE: Energy spread of the electron source

Δr: Effective source size characterizing the partial spatial coherence of the experiment

χ: Aberration function of the objective lens

$C_{a;b}$: Aberration modulus for the aberration of order a and b

$\beta_{a;b}$: Rotation angle for the aberration of order a and b

Physical variables

t: Specimen thickness

Ψ: Wave function of equivalent electrons

Φ: Component of Ψ with a slow variation against the depth z

V: Specimen potential

μ: Projected specimen potential

δE: Energy-loss

f_{e^-}: Electron scattering factor of a single atom

f_X: X-ray scattering factor of a single atom

Z: Atomic number of a given atom

Λ: Inelastic mean free path in a given material

Further functions and operators

$\widehat{\Delta}$: Laplacian operator

$\widehat{\vec{\nabla}}$: Nabla operator

P: Fresnel operator for near-field propagation

T: Transfer function

$\widehat{M_V}$: Multislice operator representing the interaction with the potential V

Introduction

Material design at the nanometric scale

Among the many scientific achievements of the last few decades, findings on the properties of solid matter, at the near-atomic scale, have been among the most impactful ones, owing to their potential for the development of advanced new technologies. At the heart of this field comes the understanding that macroscopic properties of materials are determined first and foremost by their atomic arrangement, and that deviations from a pristine crystal structure can affect the function of the devices made from them in a decisive manner [1]. Examples of this include defects such as interstitial atoms [2, 3], dopants [4, 5, 6] and vacancies [7, 8], as well as grain boundaries which, as they lead to misorientations of the crystal lattice and the appearance of interfaces, may also give rise to interesting phenomena [9, 10, 11]. Moreover, in the case of nanomaterials, meaning solid-state objects with sizes of the order of a few nanometers, the extreme reduction in one or two spatial dimensions and increased surface-to-volume ratio may result in physical behaviors significantly different from those found in their bulk counterparts [12, 13, 14].

In this context, it has become an important task, in the fields of condensed matter physics and materials science, to build solid-state devices at the nanometric level [15, 16], as a way to provide answers to the rising needs in higher computation power and lower energy consumption [17]. This can notably be done with subtractive [18, 19, 20, 21, 22], as well as additive [23, 24, 25, 26], methods. As part of the few most impactful developments in this field, one can count the discovery of giant magnetoresistance [27, 28], which consists of a large change in electrical resistance in stacked layers of magnetic and nonmagnetic materials due to the application of an external magnetic field. This phenomenon was exploited to design a new generation of magnetic field sensors, which was in turn used as part of the development and improvement of important technologies, including hard disk drives, microelectromechanical systems (MEMS) [29] and magnetoresistive random-access memories (MRAM) [30]. Another major discovery is the solid-state emission of light, in particular as it permitted the design of light-emitting diodes (LED) and lasers [31] which are at the heart of a wide range of technologies. Going toward applications in the production of energy, photovoltaic cells [32, 33] also represent a critical subject for materials science. More recent developments include, for instance, Van der Waals heterostructures [34], ferroelectric tunnel junctions [35] and graphene-based devices [36].

With the gradual improvement of quantum mechanical calculation methods, the properties of solid-state devices and materials are routinely predicted theoretically, directly from their atomic structure [37, 38, 39]. Those predictions then require validation by advanced characterization techniques, aiming at measuring both the macroscopic and microscopic properties [40, 41, 42]. Methodologies thus have to be developed that can provide such information at the atomic scale. An outstanding basis for this is transmission electron microscopy (TEM).

High-resolution scanning transmission electron microscopy

With the development of the transmission electron microscope [43], and partly thanks to advanced capacities in the correction of its aberrations [44, 45, 46, 47, 48, 49], the direct observation of atomic structures is nowadays a reality. The principle of the TEM technique is the illumination of a thin layer of matter by a beam of electrons, accelerated to more than half the speed of light. As those electrons are quantum particles, they are described by use of a wave function, whose wavelength is inversely proportional to the momentum through de Broglie's relation [50]. The resulting values of wavelength are found below 4 pm, which enables the formation of a micrograph providing a resolution sufficient to directly observe crystalline patterns. In addition to the potential for materials characterization this framework offers, it also constitutes a sophisticated source of information for experimental scattering science. Indeed, due to the wave characteristics of the probing electrons, crystalline lattices can be observed to induce Bragg scattering [51], which, because of the high strength of the Coulomb interaction with the nuclei, is dynamical in nature. By this, it is meant that new scattering events occur as a function of the depth traveled by the electrons within the specimen, concurrently to near-field propagation, thus leading to complex but very characteristic diffraction patterns. Such patterns, as well as the resulting images, require advanced simulation capacities for their interpretation. This, by itself, represents a challenge in the field, due to the multiple contributions to account for, such as inelastic scattering [52], lattice vibrations [53, 54] or the degree of incoherence in the incident beam [55].

The two main operation modes of the instrument are conventional TEM (CTEM), for which a plane wave illumination is employed, analogously to an optical microscope, and scanning TEM (STEM) [56, 57]. The operational principle of STEM consists of the employment of a convergent illumination to form an atomically small electron probe at the level of the specimen plane. This probe then propagates through matter and, upon exiting it, propagates to a detector in the far field. A diffraction pattern is thus formed resulting from the interaction with a correspondingly small volume of the observed specimen. Scanning the probe in a two-dimensional raster then permits the digital formation of an image, by depicting a value of collected electron intensity as a function of position. Due to the nature of this imaging process, STEM provides inherently multidimensional measurement capacities. Indeed, as each coordinate of the scan window represents a distinct scattering experiment, it can be used to extract several physical signals all at once, in principle without ambiguities on their positions of recording. For instance, X-rays emitted by atoms in the specimen, following a transfer of energy to a core electron and a subsequent transition from the resulting excited state back to the ground state, can be collected at each scan point, while, in parallel, the probing electrons exiting at this location are transferred to a spectrometer and resolved in terms of their losses of energy. This straightforward visualisation of characteristic inelastic scattering events makes the instrument an ideal framework to investigate the local chemical composition [58, 59, 60], as well as to perform more elaborate nano-optical experiments [61, 62, 63, 64, 65].

Alternatively, the complete diffraction patterns can be recorded using a direct electron detector providing fast acquisition capacities [66, 67, 68, 69, 70, 71, 72, 73]. This newly introduced experimental framework, often referred to as momentum-resolved STEM (MR-STEM) or 4D-STEM, enables the direct visualization of an intensity resolved both in real and reciprocal space, and is at the center of this thesis. Moreover, it arguably constitutes one of the most promising current directions of the field and already led to several innovations. Two prominent examples of this are the direct evaluation of atomic electric fields by means of calculating an average momentum transfer [74], and the application of ptychographic algorithms [75, 76, 77, 78, 79, 80] for the direct retrieval of the specimen potential, in conditions permitting super-resolution [81, 82, 83]. Moreover, with the subsequent augmentation in the amount of available diffraction information, comes a need for their improved understanding. In former approaches, where no resolution was available in reciprocal space, and regions of the diffraction pattern were summed at each real-space position [84], little attention was paid to factors affecting the precise intensity distribution, other than elastic or thermal contributions. In that respect, the momentum-resolved set-up constitutes a strong motivation for further theoretical work enabling new measurement methodologies. For instance, an important proportion of electrons diffracted to angles below 40 mrad go through an inelastic scattering event, which results in the formation of a diffuse low-angle component in the accessible intensity [85]. This component is nevertheless not considered in conventional simulation approaches, which in principle prevents the quantitative employment of this region of reciprocal space. At the same time, the generation of multiple STEM signals, resulting from the summation of intensity in distinct angular ranges covering a wide area of diffraction space, has been shown to provide capacities for the extraction of both structural and chemical information from a specimen [84]. This makes the inclusion of energy-loss in simulations a critical aspect of further quantitative STEM developments. On the other hand, the MR-STEM-based methodology consisting in the extraction and use of multiple signals through a single recording requires that the imaging conditions employed are adequate for each of those signals individually. It is therefore critical to determine whether the obtained diffraction data are universally employable for the measurement of different specimen parameters at the same time.

Contents of this thesis

As the first part of this thesis, chapter 1 discusses the state-of-the-art in the field of TEM, from the most basic aspects of the technique to its more advanced concepts. It is then followed by a theoretical description of the dynamical diffraction of high-energy electrons by a crystalline specimen, including the introduction of the multislice model for the simulation of the electron wave function. Chapter 2 then pursues with a presentation of the different existing imaging modes in STEM, and with a general explanation of the processes involved in the treatment of MR-STEM results. Capacities for the flexible tuning of signals are discussed there as well.

Continuing with results pertaining to quantitative investigations, chapter 3 presents a study on the influence of a transfer of energy from the probing electrons to a plasmon mode within the specimen. For this purpose, energy-filtering was combined with momentum-resolution to enable the formation of diffraction patterns with a restriction on the energy range of contributing electrons. The effect of plasmon scattering could thus be observed experimentally, in particular through the independent recordings of the elastically and inelastically scattered electrons. This in turn provided a sense of the relative importance of the resulting diffuse component in diffraction space. As this component represents a limitation for quantitative approaches employing low-angle scattering, including it in calculations is necessary for the development of new quantitative methodologies based on the MR-STEM technique. A new simulation paradigm was thus demonstrated as well. This chapter then pursues on those findings by extending the energy-resolution of previous experiments to investigate the excitation of up to 5 plasmon modes by a given electron in the material. In that manner, an extension of the diffuse plasmon component was observed from one energy window to the next, and a test on the comparability of the successive intensity redistribution processes was done. Specifically, a simplified calculation method was introduced, consisting in the convolution of a simulated intensity with a Lorentzian kernel to reproduce the effects of plasmon scattering.

Another important subject, presented in chapter 4, is the exact role of the imaging conditions on distinct signals obtainable from an MR-STEM dataset. In particular, an interest was taken in the focus of the objective lens of the microscope. For this purpose, the resolution in real-space was supplemented by a focal series approach. The two main findings of this work are, first, that distinct STEM signals display a mismatch in the focus necessary for them to reach a contrast optimum, and, second, that the locations of those optima may show a correspondence to interfaces with vacuum. Whereas the first point has for immediate consequence that a MR-STEM recording is unable to provide universally employable measurement capacities, as the extraction of each quantity of interest may require specific optical conditions, the second one has interesting implications. Specifically, it shows a potential to perform surface retrieval in conditions where the recorded data are otherwise obtained in a projection geometry. In addition to a first experimental demonstration, this prospect is explored more extensively through comprehensive simulations, performed while varying the conditions of recording in supplementary directions.

Through its different chapters, this thesis presents experiments and simulations aiming to explore some of the directions made available by momentum-resolution in STEM. With the findings made on the influence of energy-loss and focus, the objective of complete understanding of low-angle electron diffraction has been brought closer, thus leading to new prospects for the atomic-scale characterization of materials.

Chapter 1

Fundamental aspects of TEM

Summary

The first chapter of this thesis aims at giving the reader a solid basis to understand the few main principles of TEM. Most contents presented here are adapted from references [86, 87, 88, 89]. Other sources are cited where necessary. The following is divided is four parts. First, section 1.1 provides a general presentation of the technique and the instrument, including its two distinct operation geometry: conventional and scanning TEM. The treatment of beam-specimen interaction in the microscope is then presented in section 1.2. In particular, the multislice model is introduced for the simulation of dynamical electron diffraction. Section 1.3 then pursues with a presentation of various optical aspects of the STEM technique, including the criterions for the resolution achieved and the principle of reciprocity with CTEM imaging. Finally, notions relating to wave coherence, inelastic scattering and electron channelling are addressed in section 1.4.

1.1 Instrumentation

1.1.1 Methodological principle

TEM is an experimental technique which consists of illuminating a thin (usually of thickness $t \lesssim 100$ nm) specimen with a beam of high-energy electrons. Those electrons are accelerated and brought to a velocity v using a high-voltage U, which is usually set between 80 and 300 kV. For specific applications, values as low as 30 kV, or as high as 1 MV, may also be used. As those electrons are quantum particles, they are described by a wave function Ψ, whose wavelength is given by de Broglie's equation:

$$\lambda = \frac{h}{p} \quad , \tag{1.1}$$

where h is the Planck constant and p the momentum. With U taken between 80 and 300 kV, λ is found between 4 and 2 pm. This is nevertheless not this wavelength that determines the spatial resolution achieved in the experiment, but the aberrations of the objective lens of the microscope, as well as the degree of coherence in the electron beam. In order to mitigate their effects, a combination of corrector optics and apertures is employed. In that manner, it is possible to routinely achieve a resolution below 50 pm [48].

Upon interacting with a specimen, the wave function Ψ of the illumination is reshaped according to its three-dimensional potential V. This is due to the combination of scattering by atoms and near-field propagation through the distance t. Moreover, because the beam-specimen interaction is dominated by the Coulomb forces created by the positively charged nuclei, scattering events have a higher probability than when other common radiations, such as X-rays or neutrons, are used. Hence, successive scattering events are induced along the whole path of the electrons throughout the depth of the material. For this reason, the interaction of high-energy electrons with a solid specimen has to be considered in a volumetric manner, meaning with inclusion of near-field propagation and multiple scattering. This dynamical diffraction phenomenon in turn requires numerical models for its rigorous interpretation. For this purpose, the multislice method is employed and will be described in details in section 1.2.

As was mentioned in the introduction, the two main varieties of TEM techniques are conventional TEM, or CTEM, and scanning TEM, or STEM. Whereas the first consists of illuminating the specimen with a plane wave and forming an image in the dedicated plane of the objective lens, in a manner similar to visible light microscopy, the second involves the formation of an atomically small probe of electrons by making the beam converge toward the specimen plane. This probe is then scanned laterally, such that an electron intensity is recorded point-wise and plotted as a function of the position to form a digital image. In both cases, the recovered atomically resolved micrographs can be employed to measure material parameters such as the thickness and the chemical composition of the specimen. In this thesis, the term TEM will refer to the technique in general and will thus include both CTEM and STEM.

While this work concentrates especially on diffraction and atomic-resolution imaging of crystalline structures, many different interests and methods exist within the field, employing a wide range of spatial resolutions. Some examples include cryo-EM for the imaging of biological matter [90, 91, 92, 93, 94], off-axis electron holography for the measurement of electromagnetic fields [95, 96, 97, 98], electron energy-loss and X-ray spectroscopies [99, 60, 100], investigations of nano-optical effects [61, 62, 63, 64, 65], electron tomography [101, 102, 103], in-situ TEM [104, 105, 106] or ultrafast TEM [107, 108, 109, 110, 111].

1.1.2 Magnetic lenses and operation modes

From the optical standpoint, a TEM instrument consists of a complex arrangement of lenses and apertures, organized within a column. This column is kept under high vacuum (10^{-7}-10^{-10} Pa). This is mainly for the purpose of letting the electrons propagate through large distances without disturbance, as microscopes are commonly more than two meters tall. High vacuum also permits to avoid damage of the more fragile elements, such as the electron source. Moreover, the instrument can be separated, from top to bottom, in four components: an electron gun, a condenser system, an objective stage and a projection system.

Electron lenses can manipulate the beam by the use of round coils, through which a current circulates. This current results in a magnetic field which is parallel to z in the center of the coil. The lens itself then consists of a collection of those coils, embedded in a structure made out of

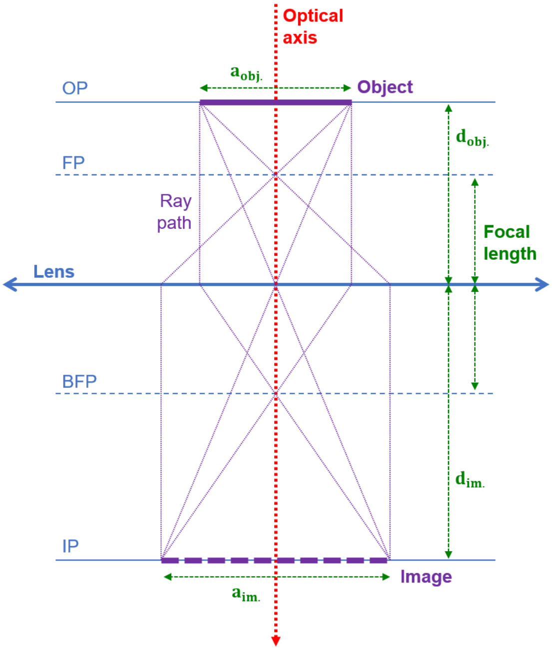

Figure 1.1: Ray diagram of a lens, with indication of the object, image, focal and backfocal planes. The focal length, object distance $d_{obj.}$, image distance $d_{im.}$, object size $a_{obj.}$ and image size $a_{obj.}$ are indicated as well.

an alloy with a high magnetic permeability. A precise manufacturing of this structure allows to accurately guide the field lines in space, and in particular permits the extension of the distance within which they are parallel to the optical axis. This then makes possible the focusing of the high-energy electrons toward z, in a spiraling trajectory having a Larmor frequency equal to $\frac{eB}{2m}$, with B the field strength, e the elementary charge and m the electron mass. In that manner, the device can be treated as a convergent lens, whose focal length is controlled directly by the current passing through its coils. The details of the calculation of magnetic fields generated by the lenses, which often requires numerical simulations, are not discussed further here. To demonstrate the principle of such convergent electron lens, one can employ a simple ray diagram like the one drawn in figure 1.1. This diagram includes, from top to bottom, an object plane (OP), a focal plane (FP), a backfocal plane (BFP) and an image plane (IP). The lens shown at the center then provides a way to transfer all the rays emanating from a point in the OP to another point, in the IP, and thus form an image.

Arguably, the most important part of the microscope is the objective lens (OL). This device is made out of two distinct magnetic lenses, from there on referred to as the lower and upper OL. The specimen is inserted in between them, so that it is immersed in the magnetic field generated by the coils contained in both lenses. An interest of this geometry is that either the upper or the lower OL can be then used as objective. In other words, the choice can be made to make the specimen plane coincide with either the IP or the OP of the device. As a consequence, an instrument equipped with such a lens may be employed in two different illumination modes:

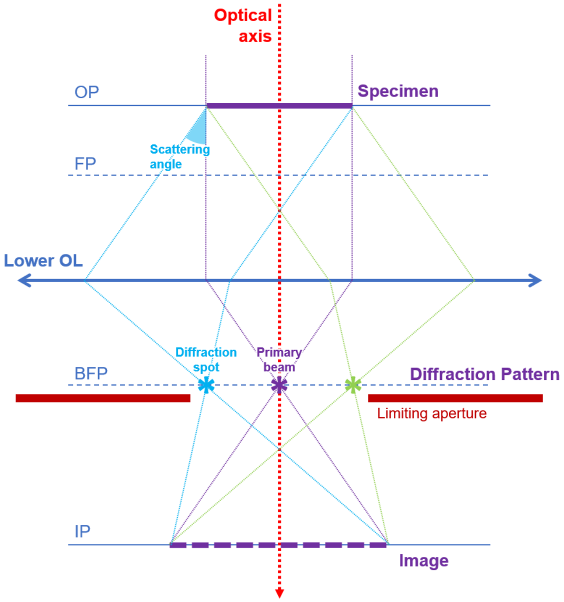

Figure 1.2: Ray path of the parallel illumination mode of the microscope using the lower OL.

parallel and convergent. The parallel illumination mode is the one employed in CTEM, while the convergent illumination mode is employed in STEM. In the CTEM mode schematized in figure 1.2, the specimen is placed in the OP and illuminated by a plane wave. Due to scattering, new plane waves are generated which are inclined by the corresponding scattering angle. They are focused using the lower OL, thus creating a diffraction pattern in the BFP. An image can be then formed in the IP, which results from their interference. This image formation process is in turn responsible for crystallographic contrast contained in the recorded micrograph, due to Bragg scattering [51]. Additionally, an aperture can be inserted in the BFP to impose a limit to the scattering angles that contribute to the process.

On the other hand, in the simplified STEM mode depicted in figure 1.3, the specimen is placed in the IP and an electron probe is created there by convergence of the rays emitted by a point source, up to a semi-convergence angle α determined by a limiting aperture. Like in the previous case, the interaction with the specimen leads to the formation of scattered beams. As the incident electrons follow a convergent trajectory toward the specimen, those diffracted beams are emitted from it in a divergent manner. This can be understood as a result of the fact that this probe formation process is equivalent to a summation of inclined plane waves, with a maximum inclination equal to α. As the interaction occurs, all those plane waves are individually scattered. Bragg scattering then consists of the formation of diffraction disks rather than diffraction spots. A convergent beam electron diffraction (CBED) pattern can be obtained at a known distance below the specimen. This distance is referred to as camera length. In the case where α is larger than a given scattering angle, the corresponding scattered beam overlaps with the primary beam, thus leading to the formation of an interference pattern which is often referred to as a Ronchigram [112]. In most of the work presented in this thesis, semi-convergence angles of 20 to 25 mrad were used, ensuring a complete covering of the primary beam by interference

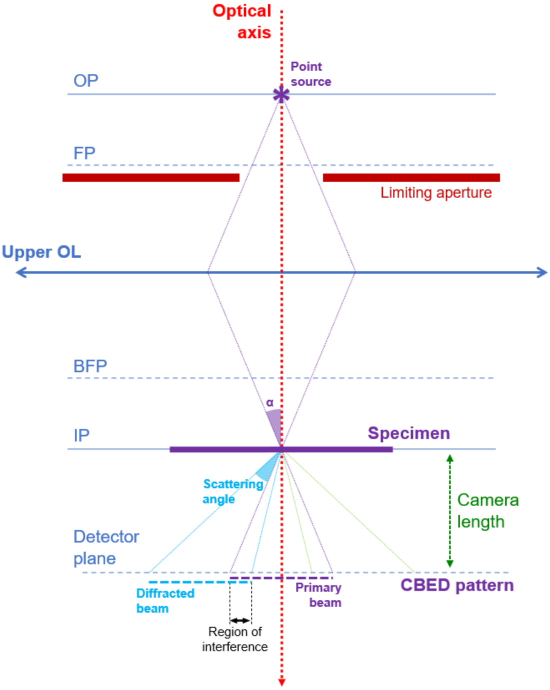

Figure 1.3: Ray path of the convergent illumination mode using the upper OL. This set-up is a simplification from the one actually used in the instruments employed for this work, as is explained further down.

features. When using an instrument that is not aberration-corrected, it is nevertheless common to keep α close to 10 mrad.

At this point, it should also be noted that, in the convergent illumination mode described above, a change in the focal length of the OL may lead to a slight modification of α. This in turn affects the size and distributions of the regions of interference between the primary beam and the diffraction disks. Partly for this reason, the actual set-up of a real electron microscope is more complex than what is displayed in fig. 1.2 and 1.3, in particular due to the presence of the multiple-lens condenser system. As such, in STEM, the probe-forming aperture is in fact located in the BFP of the so-called C2 lens, as shown further down.

In both illumination modes, the diffraction patterns are formed in the far-field. This is noteworthy, as this requires the distance d between the recording plane and the specimen to fulfill $d \gg \frac{{a_{obj.}}^2}{\lambda}$, with $a_{obj.}$ the lateral size of the illuminated object. When considering the imaging of micrometric specimens with high-energy electrons, d can reasonably reach several dozens of meters. This is why, in reality, the far-field condition is ensured by the optics of the instrument. Indeed, lenses contained in the projector system are operated in such a way that their first object plane coincides with a plane of the OL allowing recording in the far-field. The collected rays are then further transmitted, down to a detector, by a series of lenses. In the parallel illumination case, they are additionally responsible for controlling the magnification of the image at the level of the electron camera. In the convergent illumination mode, they determine the camera length, which is used to assign a lateral scaling of the scattering angles in the measured CBED pattern. An important consequence of forming images and diffraction patterns in the far-field is that the waves Ψ_{OP}, Ψ_{FP}, Ψ_{BFP} and Ψ_{IP} formed at the respective planes of the objective lens can be then related by Fourier transforms. Here, by convention, the two-dimensional Fourier transform of a function g of the real-space position $\vec{r}$, defined in the two-dimensional reciprocal space $\vec{q}$, is given by:

$$\mathcal{F}\left[g\left(\vec{r}\right)\right]\left(\vec{q}\right) = \iint g\left(\vec{r}\right) e^{-i2\pi\vec{r}\cdot\vec{q}}\, d^2r = \tilde{g}\left(\vec{q}\right) \quad , \tag{1.2}$$

and the inverse Fourier transform by:

$$\mathcal{F}^{-1}\left[\tilde{g}\left(\vec{q}\right)\right]\left(\vec{r}\right) = \iint \tilde{g}\left(\vec{q}\right) e^{i2\pi\vec{r}\cdot\vec{q}}\, d^2q = g\left(\vec{r}\right) \quad . \tag{1.3}$$

The different planes then fulfill:

$$\begin{aligned} \Psi_{\mathrm{BFP}}\left(\vec{q}_{\mathrm{BFP}}\right) &= \mathcal{F}\left[\Psi_{\mathrm{OP}}\left(\vec{r}_{\mathrm{OP}}\right)\right]\left(\vec{q}_{\mathrm{BFP}}\right) \\ \Psi_{\mathrm{IP}}\left(\vec{r}_{\mathrm{IP}}\right) &= \mathcal{F}^{-1}\left[\Psi_{\mathrm{FP}}\left(\vec{q}_{\mathrm{FP}}\right)\right]\left(\vec{r}_{\mathrm{IP}}\right) \quad . \end{aligned} \tag{1.4}$$

The wave functions at the FP and BFP are thus expressed in reciprocal space, and each of their coordinates is in turn expressed by a spatial frequency $\vec{q}$, which corresponds to an inclination angle equal to $a\sin\left(\lambda \parallel \vec{q} \parallel\right)$.

At the upper side of the OL, the condenser system has the role of providing the objective stage with an initial beam. The general geometry of all the microscopes employed in this work is depicted in figure 1.4.a for the STEM case. It is accompanied, in 1.4.b, by a picture of one of the instruments used for the work presented in this thesis, with indication of all elements mentioned so far. This geometry is made out of a series of four condenser lenses. Here, they will be referred to as C1, C2, C3 and CM, the last one corresponding to the so-called condenser mini-lens. In practice, this notation may differ among manufacturers. Additionally, an aberration corrector is placed between C3 and CM. As was mentioned previously, this ray diagram partly differs from what was shown in figure 1.3, since the rays focused by the OL are not directly emitted from a point source just above it, but are given a parallel trajectory by CM. In practice, this means that the role of the objective of the microscope is assumed not just by the OL, but by its combination with CM. In that way, the effective point source, which is placed in the OP of CM, is an intermediate image of the real electron source and is provided by the rest of the condenser system. Furthermore, the limiting aperture is not placed in the FP of the OL, but in the BFP of C2. Overall, this choice of geometry is justified by the possibility it offers to vary the focus of the OL while conserving a constant and sufficiently high value of semi-convergence angle. Indeed, in this set-up, α can be modified either by changing the size of the limiting aperture, or by vertically moving the intermediate image of the source found between C2 and C3. At the same time, undesired focus-induced variations of α are compensated by displacing the intermediate source image between C3 and CM, which in turn changes the width of the parallel beam created between CM and OL.

1.1.3 Electron sources

At the top of the column lies an electron gun, containing a source. Electrons emitted by this source are focused using an electrostatic gun lens and then brought to a high velocity using an

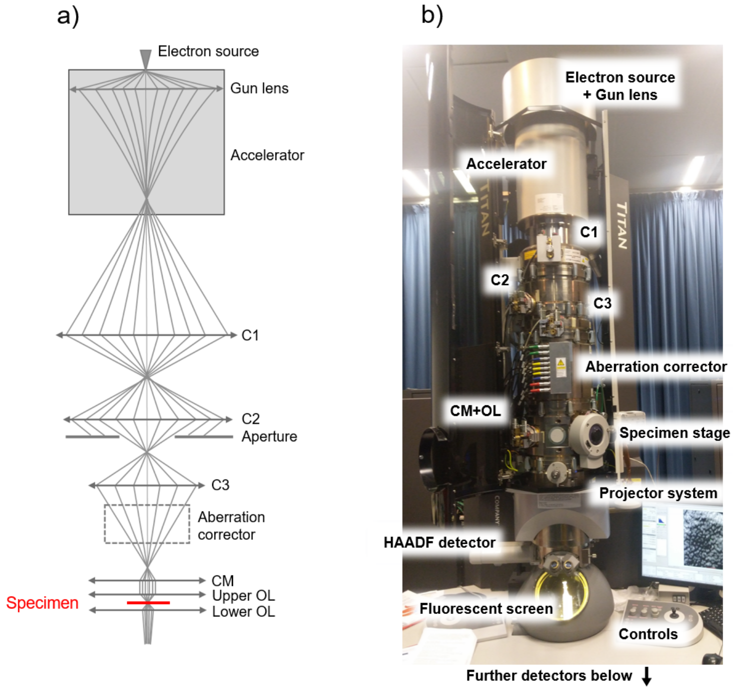

Figure 1.4: a) A schematic of the microscope, with indication of the electron gun, condenser lenses, objective lens, aberration corrector and specimen. The figure is adapted from manufacturer documentation (Thermo Fisher Scientific, FEI Company) [113]. b) Annotated picture of a FEI Titan 80-300 instrument.

accelerator with a potential U. It is noteworthy that the gun lens is the only electrostatic lens present in the column. This is because, in the rest of the optical system, the kinetic energy of the electrons is too important for their practical use, which justifies the employment of round magnetic lenses instead. In general, guns installed in microscopes are found among three different categories: thermionic guns, field-emission guns (FEG, also referred to as Schottky FEG, for reasons clarified further down) and cold field-emission guns (CFEG). Each contains a different type of source with a distinct emission mechanism. For the purpose of accurately modeling the illumination, two aspects of this source are important: its effective size, which affects spatial coherence, and the energy spread of emitted electrons, which affects temporal coherence.

In order to describe the emission of electrons by a source, one has to start from the distribution of occupied states within its material. It is represented by the Fermi-Dirac statistic [115, 116]. The function n, which expresses the probability of occupancy of an energy level E at a temperature T is thus given by:

$$n\left(E\,;\,T\right) = \frac{1}{1+e^{\frac{E-E_F}{k_B T}}} \quad , \tag{1.5}$$

with k_B the Boltzmann constant and E_F the Fermi energy, meaning the highest energy level occupied when $T = 0\,\mathrm{K}$. In figure 1.5.a, the Fermi-Dirac function n is plotted against E for a variety of temperatures T, in pure tungsten. As the temperature increases, n develops a high-

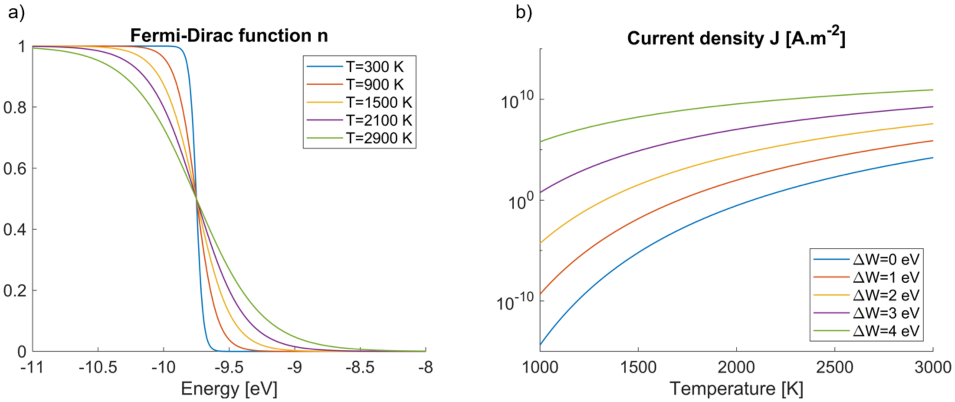

c)

		Thermionic guns		Field-emission guns	
	Units	Tungsten	LaB$_6$	Schottky FEG	Cold FEG
Work function	eV	4.5	2.4	3.0	4.5
Operating temperature	K	2700	1700	1700	300
Current density (at 100 kV)	A/m^2	5	10^2	10^5	10^6
Virtual source diameter	nm	$> 10^5$	10^4	15	3
Brightness (at 100 kV)	A/m^{2}sr	10^{10}	5×10^{11}	5×10^{12}	10^{13}
Energy spread (at 100 kV)	eV	3	1.5	0.7	0.3
Vacuum	Pa	10^{-2}	10^{-4}	10^{-6}	10^{-9}
Lifetime	hr	100	1000	>5000	>5000

Figure 1.5: a) Fermi-Dirac function n, plotted as a function of energy, for several temperatures T. b) Current density J, according to equation 1.8, given as a function of the temperature T, for a variety of ΔW. In both plots, values of $E_F = -9.75\,\text{eV}$ and $W = 5.25\,\text{eV}$, corresponding to tungsten [114], were used. c) Comparison of the characteristics of the different types of electron guns, compiled by D. B. Williams and C. B. Carter [88].

energy tail. For the emission of electrons, an energy equal to the work function W is needed. By increasing the temperature up to a point where electrons may be provided a thermal energy $k_BT > W$, emission into vacuum can occur. This process is the one employed in thermionic guns, and leads to the generation of a current density expressed by the Richardson-Dushman equation [117, 118]:

$$J = C_R T^2 e^{-\frac{W}{k_B T}} = J_T \quad , \tag{1.6}$$

with $C_R = \frac{4\pi m e {k_B}^2}{h^3}$ the Richardson constant. Typically, thermionic emission is ensured by using either a tungsten source with $T = 2700\,\text{K}$ or an LaB$_6$ source with $T = 1700\,\text{K}$. Modern TEM instruments are rarely built with thermionic guns, as they are characterized by a short lifetime due to heat-induced degradation. Furthermore, the strong energy spread and large source size of those sources lead to a rather incoherent illumination, which is undesirable for high-resolution imaging.

Otherwise, an electric field ϵ can be applied between an electrode and the surface of the source, thus lowering the vacuum energy locally. It can be then represented by a barrier potential U_b, given as a function of the distance z_b between the electrode and the source, through:

$$U_b\left(z_b\right) = W - e\epsilon z_b - \frac{e^2}{16\pi\varepsilon_0 z_b} \quad , \tag{1.7}$$

with ε_0 the dielectric permittivity of vacuum. The term $\frac{e^2}{16\pi\varepsilon_0 z_b}$ here represents the Coulomb interaction between the emitted electrons and their mirror images at the surface of the source material. As a result, the work function is lowered by a quantity $\Delta W = \sqrt{\frac{e^3\epsilon}{4\pi\varepsilon_0}}$ at the interface between the source and vacuum. The thermal emission then occurs with a current density equal to:

$$J = C_R T^2 e^{-\frac{W-\Delta W}{k_B T}} = e^{\frac{\Delta W}{k_B T}} J_T \quad . \tag{1.8}$$

This process of field-assisted thermal emission is referred to as Schottky emission [119] and is the emission mechanism employed in a FEG. In such guns, the source is typically made out of a monocrystalline tungsten filament coated with ZrO, with $T = 1800\,\mathrm{K}$ and $\epsilon \approx 1$ V.nm^{-1}. An example of calculation of J is plotted in figure 1.5.b, for the pure tungsten case, as a function of T and for a variety of ΔW.

In addition to the thermionic and Schottky processes, it is also possible for the electrons to reach vacuum by tunnelling through the barrier U_b. In the case of a Schottky FEG, this process is sufficiently improbable to be neglected, owing to the large width of the barrier. In the case of a CFEG, tunnelling is the dominant emission mechanism, as the tungsten source is kept at room temperature and stronger values of ϵ are employed. The effect of the field is further increased by using a much smaller source. The tunnelling-induced current density follows the Fowler-Nordheim equation [120]:

$$\begin{aligned} J &= \frac{4\pi m e}{h^3}\, j\, e^{-\frac{0.6W}{j}} \, \frac{\pi k_B T}{\sin\left(\pi \frac{k_B T}{j}\right)} \\ j &= \frac{e h \epsilon}{4\pi\sqrt{2mW}\left(1 + 0.1107\left(\frac{\Delta W}{W}\right)^{1.33}\right)} \quad . \end{aligned} \tag{1.9}$$

A general comparison of the characteristics of the different types of guns is available in 1.5.c. As can be seen here, the type of gun leading to the highest degree of coherence in the illumination is the CFEG, which constitutes its main advantage in comparison to the Schottky FEG. This is because the lower temperature of the material leads to a reduced spread of energy among the emitted electrons. Furthermore, while the low source size reflects the intent of amplifying the effect of the electric field locally, it also leads to a smaller impact of spatial incoherence. Keeping the source at room temperature nevertheless has the additional consequence of making its tip more susceptible to contamination by adsorption of gas molecules, which leads to damage. This issue is further amplified by the high strength of the imposed electric field, which attracts those gas molecules by Coulomb interaction. For those reasons, a CFEG requires a higher vacuum level than a FEG (of the order of 10^{-9} Pa, instead of 10^{-6} Pa). Nevertheless, even in such high vacuum conditions, contamination still occurs, which has for consequence that the incident intensity decreases throughout the experiment, as the emitting surface is covered by adsorbed molecules. To alleviate this problem, a CFEG has to go through a flashing at regular intervals, meaning that its temperature is increased during a few seconds, so that a desorption of the molecules occurs. This is usually done every 1 to 2 hours. In-between the flashings, the intensity is thus expected to decrease slowly as the contamination layer builds back up. Outside of the actual experiments, the electric field ϵ of the CFEG is turned off to avoid degradation. On the contrary, a Schottky FEG emits electrons constantly. This is because the field induces surface reformations of the ZrO-coated tungsten, which contribute to the efficiency of the emission.

1.1.4 Electron detectors

In TEM, most currently used detectors are made out of a scintillator, which converts the electron intensity into photons, a photomultiplier and a camera, itself made out of a two-dimensional array of photodiodes. The read-out of this camera array is based either on the CCD or the CMOS technology. Alternatively, when the intensity has to be summed in a wide region, a single photodiode may be used. Whereas the employment of such a geometry is a result of the wide availability of digital recording techniques, and made the previously used photographic films obsolete, it has some disadvantages. Their main origin is the necessary conversion of electrons into photons. This leads to a low sensitivity of such devices, as commonly expressed by their detective quantum efficiency (DQE), equal to the ratio of the signal-to-noise ratios (SNR) of the output signal $I_{recorded}$ and the incident electron intensity $I_{physical}$. In addition, as the photomultiplier has a certain thickness, the photon amplitude arising from an electron impact in the scintillator laterally expands from its initial position before reaching the camera. This results in an artificial point spread operation, which is often expressed by a so-called modulation transmission function (MTF) M [121, 122, 123], using:

$$I_{recorded}\left(\vec{r}\right) \;=\; \mathcal{F}^{-1}\left[M\left(\vec{q}\right)\right]\left(\vec{r}\right)\,\otimes_{\vec{r}}\,I_{physical}\left(\vec{r}\right) \quad . \tag{1.10}$$

As $\mathcal{F}^{-1}\left[M\right]$ is a real quantity, M is implied to be symmetric. Furthermore, this quantity also includes the sampling limitation of the intensity by the pixels of the camera.

In order to perform a recording without conversion of the intensity into photons, direct electron detectors (DED) [124, 125, 126] were introduced to the field. The pixels of such cameras consist of PN diodes in which electron-hole pairs are created by the incoming electron beam, and separated by an electric field. Due to this direct recording mechanism, those camera arrays possess a higher DQE than those based on photodiodes. Furthermore, as they are usually combined with fast electronics, and because no photomultiplier decay time has to be accounted for, the recording speed can then range from a few hundreds to a few thousands frames per seconds, depending on the amount of pixels. Though they may be mounted with a CCD or CMOS read-out system, a major subset of those devices is in fact made out of hybrid pixels [66, 127, 128], which have their own read-out electronics and are operated using an energy threshold. This means that, while the measurement is performed by generation of electron-hole pairs, an electron count is registered only when a minimum amount of energy is deposited. The employment of hybrid pixels in a DED therefore leads to an inherent filtering of the shot noise, and to single electron measurement capacities. Finally, it should be noted that, despite its advantages, a DED may still have limitations in terms of MTF. Here, the source of event spreading is nevertheless different, as it comes from the fact that an incoming electron usually deposits energy in more than one pixel of the camera. This so-called double counting phenomenon is due to the stochastic trajectory of the high-energy electron, when going through the semiconductor matter making up the array of pixels, and can be mitigated by specific design choices. Specifically, a sufficiently large pixel size leads to a lower impact of this phenomenon, since it provides a more important space for the movement of the electrons. When using hybrid pixels, this issue may otherwise be fully circumvented by assigning a value above $\frac{eU}{2}$ to the threshold.

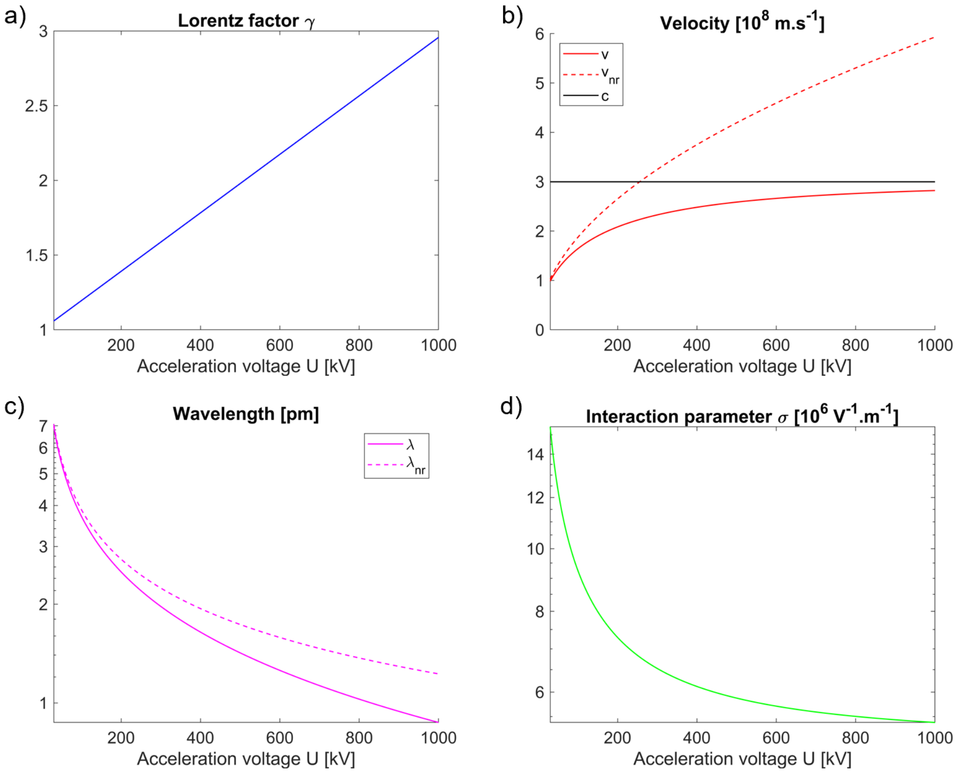

Figure 1.6: Plot of parameters as a function of U. a) The Lorentz parameter γ, b) the relativistic and non-relativistic electron velocities v and v_{nr}, alongside c, c) the relativistic and non-relativistic wavelength λ and λ_{nr}, d) the interaction parameter σ.

This is then at the cost of counting statistics [129]. For the work presented in this thesis, the influence of the MTF was not explicitly considered, as all the procedures applied on the recorded diffraction frames were based on the summation of electron intensity in relatively large areas. As such, the effect of this imaging parameter was not expected to be important.

1.2 Beam-specimen interaction

1.2.1 Relativistic correction

In the range of electron velocities v employed for a TEM experiment, a valid treatment of the diffraction of high-energy electrons requires to account for their relativistic nature. Although the most rigorous path for the derivation of a simulation algorithm for dynamical diffraction would then involve the Dirac equation, the mathematically simpler Schrödinger equation is usually sufficient in this particular range. This nevertheless requires that a relativistic correction is done for the wavelength λ. The Lorentz factor γ then also has to be inserted in the expression of the scattering factors, as well as in the kinetic energy term [130, 131, 132]. In vacuum, those quantities are given by:

$$\begin{aligned} \gamma &= \frac{1}{\sqrt{1-\frac{v^2}{c^2}}} \\ \lambda &= \frac{h}{\gamma m v} \quad , \end{aligned} \tag{1.11}$$

with c the speed of light. The velocity v of the electrons, having been provided with a kinetic energy eU, can be obtained from the relativistic energy-momentum relation:

$$\left(mc^2+eU\right)^2 = (pc)^2 + \left(mc^2\right)^2 \quad , \tag{1.12}$$

and the formula:

$$p = \gamma m v \quad , \tag{1.13}$$

through:

$$\begin{aligned} 1 + \left(\frac{\gamma m v c}{mc^2}\right)^2 &= \left(\frac{mc^2+eU}{mc^2}\right)^2 \\ 1 + \frac{1}{\frac{c^2}{v^2}-1} &= \left(\frac{mc^2+eU}{mc^2}\right)^2 \\ \frac{c^2}{v^2} &= \frac{\left(\frac{mc^2+eU}{mc^2}\right)^2}{\left(\frac{mc^2+eU}{mc^2}\right)^2-1} \\ v &= c\sqrt{1-\left(\frac{mc^2}{mc^2+eU}\right)^2} \quad . \end{aligned} \tag{1.14}$$

For a high-voltage of 300 kV, v is found to reach about 77 % of c. For 80 kV, this number still reaches 50 %. For comparison, in the non-relativistic case, the velocity is given by $v_{nr} = \sqrt{\frac{2eU}{m}}$. By expanding equations 1.11 using 1.14, the following expressions are reached:

$$\begin{aligned} \gamma &= 1 + \frac{eU}{mc^2} \\ \lambda &= \frac{hc}{\sqrt{eU\left(2mc^2+eU\right)}} \quad . \end{aligned} \tag{1.15}$$

On the other hand, the non-relativistic wavelength is given by $\lambda_{nr} = \frac{h}{\sqrt{2meU}}$. Those parameters are plotted in figure 1.6 as a function of U. Fig. 1.6.a depicts the lorentz parameter γ which, when an extreme high-voltage of 1 MV is employed, takes a value of 2.96. Within the more common window of 80 to 300 kV, it is found between 1.16 and 1.59. The relativistic electron velocity is plotted in 1.6.b and shows highly significant differences from the non-relativistic one. The wavelength, depicted in 1.6.c, also shows a clear mismatch between corrected and non-corrected values. In 1.6.d, the interaction parameter σ, given by:

$$\sigma = \frac{2\pi e}{\lambda}\frac{mc^2+eU}{eU\left(2mc^2+eU\right)} = \frac{2\pi\gamma m e\lambda}{h^2} \quad , \tag{1.16}$$

is plotted as well. As will be clarified in a further subsection, this parameter can be understood as a weighting factor for the inclusion of the specimen potential. Finally, since $U \gg V$, the explicit dependence of λ and γ to the specimen potential, which would have to be included in the formalism by means of replacing U by $U+V$ in equation1.15, is neglected. As such, those parameters are considered contant.

1.2.2 Paraxial approximation

In this treatment of the high-energy electrons, it should be noted that their spins are ignored. One more major simplification can be done by treating the interaction as only involving a static crystal, corresponding to the particular snapshot of it interacting with the incident beam at a given time. Indeed, while an electron accelerated by a potential $U = 300\,\mathrm{kV}$ takes approximately 4.30 fs to go through a distance of 1 μm, the typical frequencies of the optical phonon modes of a crystal lattice range close to a few THz [133]. As a consequence, it is reasonable to consider that, within a given interaction, the nuclei remain immobile and that V is fixed. Furthermore, for most TEM applications, the electron current is kept under 10 nA, which means that, for a continuous illumination, the maximum amount of electrons reaching the specimen within one second is equal to 6.24*10^{10}. With the electron velocity v reached when $U = 300\,\mathrm{kV}$, this results in a value of 3.73 mm for the minimal expectation distance between two incident electrons. It is therefore safe to assume that, during the experiment, up to a single probing electron should be present in the specimen at a given time. For those reasons, and by assuming no variations in the specimen, the starting point of the derivation is the stationary Schrödinger equation describing the influence of a fixed specimen potential V on the wave function Ψ of equivalent non-interacting electrons, as written below:

$$\begin{aligned} \left(-\frac{h^2}{8\pi^2\gamma m}\widehat{\Delta} - eV\left(\vec{R}\right)\right)\Psi\left(\vec{R}\right) &= E\Psi\left(\vec{R}\right) \\ \frac{p^2}{2\gamma m} = \frac{1}{2\gamma m}\left(\frac{h}{\lambda}\right)^2 &= E \quad , \end{aligned} \tag{1.17}$$

With E the energy carried by the electron wave, $\vec{R} = [\vec{r}\,,\, z]$ and $\widehat{\Delta} = \widehat{\Delta}_{\vec{r}} + \widehat{\frac{\partial^2}{\partial z^2}}$. Given an incident intensity I_0, Ψ is normalized by:

$$\iiint \mid \Psi\left(\vec{R}\right)\mid^2\, d^3R = \iiint \Psi^*\left(\vec{R}\right)\,\Psi\left(\vec{R}\right)\, d^3R = I_0 \quad . \tag{1.18}$$

Importantly, the interaction described by equation 1.17 is also implied to be elastic. The inclusion of incoherence and inelastic scattering will be treated in section 1.4.

To further simplify the equations, the paraxial approximation can be introduced. It states that, due to the high kinetic energy eU of the incident electrons, their interaction with the specimen does not impact their propagation direction strongly. With the wave vector of Ψ being given by $\vec{K} = \left[\vec{k}\,,\, k_z\right] = [k_x, k_y, k_z]$, and $\parallel \vec{K} \parallel = \frac{1}{\lambda}$, this means that $k_z^2 \gg k_x^2 + k_y^2$. It follows that the variation of Ψ along the dimension z, occurring within the interaction, is low compared to the ones along x and y. This translates into $\mid \widehat{\frac{\partial^2}{\partial z^2}} \mid \ll \mid \frac{2\pi}{\lambda}\widehat{\frac{\partial}{\partial z}} \mid$. In those conditions, it becomes possible to express Ψ as a product of two terms, by:

$$\Psi\left(\vec{R}\right) \equiv \Phi_z\left(\vec{r}\right)\exp\left(i2\pi\frac{z}{\lambda}\right) \quad , \tag{1.19}$$

with $\exp\left(i2\pi\frac{z}{\lambda}\right)$ a phase factor expressing the propagation along the z-axis, and Φ_z the part of the wave function which varies slowly along z. Equation 1.17 can then be expanded as follows:

$$
\begin{aligned}
\left[-\frac{h^2}{8\pi^2\gamma m}\left(\widehat{\Delta}_{\vec{r}}+\widehat{\frac{\partial^2}{\partial z^2}}+i\frac{4\pi}{\lambda}\frac{\widehat{\partial}}{\partial z}-\left(\frac{2\pi}{\lambda}\right)^2\right)-eV\left(\vec{r},\,z\right)\right]\Phi_z\left(\vec{r}\right)=E\Phi_z\left(\vec{r}\right)\\
\left(\widehat{\Delta}_{\vec{r}}+\widehat{\Box}+\zeta\left(\vec{r},\,z\right)\right)\Phi_z\left(\vec{r}\right)=0 \quad .
\end{aligned}
\tag{1.20}
$$

Using the expression for E developed in equations 1.17, the terms $\widehat{\Box}$ and ζ can be clarified to be:

$$
\begin{aligned}
\widehat{\Box} &= \widehat{\frac{\partial^2}{\partial z^2}}+i\frac{4\pi}{\lambda}\frac{\widehat{\partial}}{\partial z} \approx i\frac{4\pi}{\lambda}\frac{\widehat{\partial}}{\partial z}\\
\zeta\left(\vec{r},\,z\right) &= \frac{8\pi^2\gamma m\left(E+eV\left(\vec{r},\,z\right)\right)}{h^2}-\left(\frac{2\pi}{\lambda}\right)^2 = \frac{4\pi\sigma}{\lambda}V\left(\vec{r},\,z\right) \quad .
\end{aligned}
\tag{1.21}
$$

The final expression is thus:

$$
\frac{\partial\Phi_z\left(\vec{r}\right)}{\partial z} = i\frac{\lambda}{4\pi}\widehat{\Delta}_{\vec{r}}\Phi_z\left(\vec{r}\right) + i\sigma V\left(\vec{r},\,z\right)\Phi_z\left(\vec{r}\right) \quad . \tag{1.22}
$$

Equation 1.22 can then be used directly to describe the elastic diffraction of the probing electrons by the specimen, and is the basis for the multislice algorithm. In particular, the interaction with the potential V is weighted by the parameter σ, and occurs concurrently with near-field propagation, which is expressed through the Laplacian operator $\widehat{\Delta}_{\vec{r}}$, itself weighted by $\frac{\lambda}{4\pi}$. It is noteworthy that, in this approach, the backscattering of electrons is neglected.

1.2.3 Potential and scattering factors

The determination of the three-dimensional specimen potential V requires a model for the atomic structure. Here, to a good approximation, each atom of the material can be considered as an isolated elastic scatterer, with scattering factor f_{e^-}. Furthermore, the nuclei can be assimilated to points in the three-dimensional Cartesian space, as the electron wavelength is anyway too large to resolve their inner structure. The influence of bonding between atoms is ignored for most cases. Under the first Born approximation, and in relativistic conditions, the relationship between the scattering factor f_{e^-} of a single atom and its three-dimensional potential distribution V_{atom} is given by:

$$
f_{e^-}\left(\vec{Q}\right) = \frac{\pi\gamma m e}{2h^2}\mathcal{F}_{3D}\left[V_{atom}\left(\vec{R}\right)\right]\left(\vec{Q}\right) \quad , \tag{1.23}
$$

with the three-dimensional Fourier transform:

$$
\begin{aligned}
\mathcal{F}_{3D}\left[g\left(\vec{R}\right)\right]\left(\vec{Q}\right) &= \iiint g\left(\vec{R}\right)\exp\left(-i2\pi\vec{R}\cdot\vec{Q}\right)\,d^3R = \tilde{g}\left(\vec{Q}\right)\\
{\mathcal{F}_{3D}}^{-1}\left[\tilde{g}\left(\vec{Q}\right)\right]\left(\vec{R}\right) &= \iiint \tilde{g}\left(\vec{Q}\right)\exp\left(i2\pi\vec{R}\cdot\vec{Q}\right)\,d^3Q = g\left(\vec{R}\right) \quad .
\end{aligned}
\tag{1.24}
$$

V_{atom} is related to the atomic charge distribution ρ_{atom} by the Poisson equation:

$$
\widehat{\Delta}_{\vec{R}}V_{atom}\left(\vec{R}\right) = -\frac{\rho_{atom}\left(\vec{R}\right)}{\varepsilon_0} \quad , \tag{1.25}
$$

while ρ_{atom} is itself dependent on the nucleus and electron real-space densities d_n and d_e of the atom, by:

$$\rho_{atom} = e\,(d_n - d_e) \quad . \tag{1.26}$$

As the nuclei are considered to be points, the nuclear density can be expressed by $d_n = Z\delta(\vec{R})$. On the other hand, the electron density is conventionally related to the X-ray scattering factor by $f_X\left(\vec{Q}\right) = \mathcal{F}_{3D}\left[d_e\left(\vec{R}\right)\right]\left(\vec{Q}\right)$. It is thus possible to write:

$$\frac{2h^2}{\pi\gamma me}\,\widehat{\Delta}_{\vec{R}}\,\mathcal{F}_{3D}{}^{-1}\left[f_{e^-}\left(\vec{Q}\right)\right] \;=\; -\frac{e}{\varepsilon_0}\,\left(Z\delta(\vec{R}) \;-\; \mathcal{F}_{3D}{}^{-1}\left[f_X\left(\vec{Q}\right)\right]\right) \quad . \tag{1.27}$$

Moreover, using the Fourier derivation theorem, which states that:

$$\mathcal{F}_{3D}\left[\vec{\nabla}\,g\left(\vec{R}\right)\right]\left(\vec{Q}\right) \;=\; i2\pi\vec{Q}\,\tilde{g}\left(\vec{Q}\right) \quad , \tag{1.28}$$

equation 1.27 can be used to obtain the Mott-Bethe relation [134, 135] for the elastic scattering of electrons:

$$\begin{aligned} \parallel i2\pi\vec{Q} \parallel^2 f_{e^-}\left(\vec{Q}\right) &= -\frac{\pi\gamma me}{2h^2}\frac{e}{\varepsilon_0}\left(Z - f_X\left(\vec{Q}\right)\right) \\ f_{e^-}\left(\vec{Q}\right) &= \frac{\gamma me^2}{8\pi h^2\varepsilon_0}\frac{Z - f_X\left(\vec{Q}\right)}{Q^2} \quad . \end{aligned} \tag{1.29}$$

To employ formula 1.29, an expression for the X-ray scattering factor f_X is still required. It can be obtained from the corresponding electron density, which is calculated by numerical methods, such as the relativistic Hartree-Fock model [136]. In practice, tabulated data are available for all elements, which, in the framework of electron diffraction simulations, are often interpolated by parametric functions to build up d_e and thus f_X [137]. For all simulations presented in this thesis, the model introduced in reference [138] was employed, which is based on an interpolation by a collection of hydrogen S-state orbitals. With f_X having been determined, the specimen can then be straightforwardly built in three dimensions from the individual scattering factors f_{e^-}, by linear superposition:

$$V\left(\vec{R}\right) \;=\; \sum_i \mathcal{F}_{3D}^{-1}\left[\frac{2h^2}{\pi\gamma me}\,f_{e^-}^i\left(\vec{Q}\right)\,\exp\left(-i2\pi\vec{Q}\cdot\vec{R}_i\right)\right] \quad . \tag{1.30}$$

$\vec{R}_i$ is here the position of a given atom, having a scattering factor $f_{e^-}^i$. Importantly, in the range of velocities of the electrons, a relativistic correction of the potential is necessary, consisting in a multiplication of the scattering factors by γ, as was mentioned previously.

1.2.4 Multislice solution

With equation 1.22 providing a general description of electron diffraction, it remains to establish a method to solve it numerically for an arbitrary potential V. To this end, the multislice algorithm [139, 140] is introduced. With $\widehat{M_V}$ the multislice operator, one can write:

$$\Psi\left(\vec{r}\,,\,t\right) \;=\; \widehat{M_V}\,\Psi\left(\vec{r}\,,\,0\right) \quad . \tag{1.31}$$

As a starting point to derive the expression of $\widehat{M_V}$, one can perform an integration along the z-axis, within a given distance δz:

$$\frac{\Phi_{z+\delta z}\left(\vec{r}\right)}{\Phi_z\left(\vec{r}\right)} = \exp\left(i\int\limits_{z}^{z+\delta z}\left(\frac{\lambda}{4\pi}\widehat{\Delta}_{\vec{r}} + \sigma V\left(\vec{r}\,,\,z'\right)\right)dz'\right) \quad . \tag{1.32}$$

Through equation 1.32, it is then possible to establish a direct relation between the waves at two vertical locations z and $z+\delta z$. This can be pursued with a separation of the exponential term:

$$\Phi_{z+\delta z}\left(\vec{r}\right) = \widehat{\tau}_{\frac{\delta z}{2}}\left(\vec{r}\right)\,T_{[z\,;\,z+\delta z]}\left(\vec{r}\right)\,\widehat{\tau}_{\frac{\delta z}{2}}\left(\vec{r}\right)\Phi_z\left(\vec{r}\right) + \vartheta \quad , \tag{1.33}$$

with:

$$\begin{aligned} \widehat{\tau}_b\left(\vec{r}\right) &= \exp\left(i\frac{\lambda}{4\pi}\int\limits_{a}^{a+b} dz'\widehat{\Delta}_{\vec{r}}\right) = \exp\left(i\frac{\lambda b}{4\pi}\widehat{\Delta}_{\vec{r}}\right) \\ T_{[a\,;\,a+b]}\left(\vec{r}\right) &= \exp\left(i\sigma\int\limits_{a}^{a+b} V\left(\vec{r}\,,\,z'\right)dz'\right) = \exp\left(i\sigma\mu_{[a\,;\,a+b]}\left(\vec{r}\right)\right) \quad , \end{aligned} \tag{1.34}$$

where a and b are arbitrary vertical distances. The wave functions Φ_z and $\Phi_{z+\delta z}$ are related through a propagation operator $\widehat{\tau}_{\frac{\delta z}{2}}$ and a transmission function $T_{[z\,;\,z+\delta z]}$. This transmission function contains a projected potential $\mu_{[z\,;\,z+\delta z]}$, expressed in V.m and equal to the integration of V between z and $z+\delta z$. It is noteworthy that equation 1.33 also includes an error term ϑ. This is because the Laplacian $\widehat{\Delta}_{\vec{r}}$ does not, in principle, commutate with V. As a consequence, the exponential contained in the expression 1.32 cannot be separated without the introduction of higher-order error factors [141, 142, 143, 140]. In practice, ϑ can nevertheless be omitted, provided that the sampling of the thickness t by δz is high enough. The numerical accuracy is also improved by the Strang splitting of the exponential, meaning the use of two times $\widehat{\tau}_{\frac{\delta z}{2}}$, rather than the Lie splitting, which would result in using one time $\widehat{\tau}_{\delta z}$ [144, 145].

The expression of $\widehat{\tau}_b$ in formulas 1.34 can be shown to be equivalent to the Fresnel propagator $\mathcal{F}^{-1}\left[P_b\left(\vec{q}\right)\right]\left(\vec{r}\right)\otimes_{\vec{r}}$ by use of the Fourier derivation theorem:

$$\begin{aligned} \mathcal{F}\left[\widehat{\tau}_b\left(\vec{r}\right)\right]\left(\vec{q}\right) &= \exp\left(-i\pi\lambda b q^2\right) = P_b\left(\vec{q}\right) \\ \widehat{\tau}_b\left(\vec{r}\right) &= \mathcal{F}^{-1}\left[P_b\left(\vec{q}\right)\right]\left(\vec{r}\right)\otimes_{\vec{r}} \quad , \end{aligned} \tag{1.35}$$

where $\otimes_{\vec{r}}$ represents a convolution along $\vec{r}$, explicitly given by:

$$g\left(\vec{r}\right)\otimes_{\vec{r}} g'\left(\vec{r}\right) = \iint g\left(\vec{r}-\vec{r}\,'\right)g'\left(\vec{r}\,'\right)\,d^2r\,' \quad . \tag{1.36}$$

Equation 1.33, combined with 1.35, is the basis of the multislice model. It thus consists of a separation of the respective influences of near-field propagation and scattering, in discretized increments of the total distance traveled by the electrons in the specimen. As such, the three-dimensional specimen potential V is sliced in a series of two-dimensional $\mu_{[z_{n-1}\,;\,z_n]}$ projected potentials, with $z_n = z_{n-1} + \delta z$ and $n \in [1\,;\,N]$. By convention, $z_0 = 0$ corresponds to the entrance surface of the specimen and $z_N = t$ to the exit surface of the specimen, or simply the maximum thickness available from the calculations. The wave functions Φ_{z_n} are computed for the series of discrete z_n heights, each with dependence on the wave $\Phi_{z_{n-1}}$ calculated at the previous slice. It is noteworthy that the value of δz does not have to be constant and may be chosen in dependence to n in order to refine the sampling in parts of the vertical dimension. Finally, the multislice operator $\widehat{M_V}$ can be written explicitly as:

$$\widehat{M_V} = \prod_{n=1}^{n=N} \mathcal{F}^{-1}\left[P_{\frac{\delta z}{2}}(\vec{q})\right](\vec{r}) \otimes_{\vec{r}} T_{[z_{n-1}\,;\,z_n]}(\vec{r})\, \mathcal{F}^{-1}\left[P_{\frac{\delta z}{2}}(\vec{q})\right](\vec{r}) \otimes_{\vec{r}} \quad . \tag{1.37}$$

Of course, in practice, this expression for $\widehat{M_V}$ consists of a succession of steps rather than in a single mathematical operation. This is because the Fresnel propagator and the transmission functions do not commutate. This also means that, as a result of the simulation, the wave functions of each slice are obtained individually, thus providing thickness-dependent diffraction results. Moreover, rather than by a convolution in real-space, the near-field propagation step is included by use of a succession of Fourier and inverse Fourier transforms, such that:

$$\Phi_{z_n}(\vec{r}) = \mathcal{F}^{-1}\left[P_{\frac{\delta z}{2}}(\vec{q})\, \mathcal{F}\left[T_{[z_{n-1}\,;\,z_n]}(\vec{r})\, \mathcal{F}^{-1}\left[P_{\frac{\delta z}{2}}(\vec{q})\, \mathcal{F}\left[\Phi_{z_{n-1}}(\vec{r})\right](\vec{q})\right](\vec{r})\right](\vec{q})\right](\vec{r}) \quad . \tag{1.38}$$

This choice is made for reasons of computational speed, as it permits the employment of fast Fourier transforms (FFT) schemes [146]. This nevertheless leads to the introduction of a so-called wrap-around error, as explained further in the next subsection.

1.2.5 Numerical sampling

To carry out a multislice simulation while avoiding the appearance of artefacts in the results, the sampling of the object has to be considered carefully. The main source of such artefacts is the wrap-around error due to the FFT method used in the calculations. Indeed, such schemes include a periodicity condition, which in practice means that the first pixel in a given dimension is a neighbour of the last. As a consequence, if a part of the wave amplitude is transferred beyond one of the lateral limits of the simulation frame, it travels back from its opposite side. This may lead to unphysical interferences of the wave function with itself. Moreover, this issue is particularly critical in the case of dynamical diffraction since the wave function can spread significantly, both in real- and reciprocal space, as a result of scattering and propagation. In the reciprocal space window, the first precaution taken to alleviate this wrap-around error is a careful choice of Nyquist frequency for the lateral sampling of real-space. This frequency in turn determines the maximum scattering angle which is considered in the simulation. As the scattering events are repeated at each slice of V, the region of the reciprocal space window containing a significant portion of the total amplitude expands. Therefore, to avoid comparing artefactual simulation results to the experimental ones, the employed region of diffraction space is usually limited to half the Nyquist frequency or less. For thicker specimens, the angular limit may have to be increased accordingly. This limit is also important for the accurate representation of the phenomenological absorption of a portion of the incident electrons, meaning their loss due a scattering beyond the detector range. It is noteworthy that the use of masks, limiting the wave amplitude up to a certain cut-off angle, is also common practice. Another wrap-around artefact may occur in real-space, which is due to the finite size of the electron probe. There, the solution consists of physically extending V. In the case of a bulk specimen, this means using a supercell of the crystal, which is a lateral stacking of several unit cells, such that its periodicity is conserved. Another choice to make, in terms of the sampling of the potential V, is its slicing along the z-axis. Ideally, this should be done at the level of the vertical interatomic distance.

A sub-slicing of the atomic potential may be done in particular cases, for instance where fine atomic shifts are present compared to an ideal crystalline unit cell.

1.2.6 Thin specimen approximations

In equation 1.37, the Fresnel propagator $\mathcal{F}^{-1}\left[P_{\frac{\delta z}{2}}\left(\vec{q}\right)\right]\left(\vec{r}\right)\otimes_{\vec{r}}$ represents the travel of the electrons from one slice of the potential V to the next, while the transmission functions contain the effect of their scattering by the atoms. In that respect, it is interesting to note that those transmission functions do not affect the amplitude of the real-space wave directly, as they only consist of phase factors. Instead, this role is ensured by the propagation. The effect of the projected potentials μ on the amplitude is thus only indirect, as it is induced by the convolution with the function $\mathcal{F}^{-1}\left[P_{\frac{\delta z}{2}}\left(\vec{q}\right)\right]\left(\vec{r}\right)$. More generally, the z-dependent amplitude change is the reason why successive phase variations ensured by the transmission functions cannot, in principle, be assimilated into a single one. In the opposite case, where the effect of near-field propagation is neglected, meaning $P_{\frac{\delta z}{2}}\left(\vec{q}\right) = 1$, then:

$$
\begin{aligned}
\widehat{M}_V \;&=\; \prod_{n=1}^{n=N} \delta\left(\vec{r}\right) \otimes_{\vec{r}} T_{[z_{n-1}\,;\,z_n]}\left(\vec{r}\right)\, \delta\left(\vec{r}\right) \otimes_{\vec{r}} \;=\; \prod_{n=1}^{n=N} T_{[z_{n-1}\,;\,z_n]}\left(\vec{r}\right) \\
&=\; \exp\left(i\sigma \sum_{n=1}^{n=N} \mu_{[z_{n-1}\,;\,z_n]}\left(\vec{r}\right) \right) \;=\; \exp\left(i\sigma\mu_p\left(\vec{r}\right)\right) \;=\; T\left(\vec{r}\right) \quad ,
\end{aligned}
\tag{1.39}
$$

where $\mu_p\left(\vec{r}\right) \;=\; \int_0^t V\left(\vec{r},\, z'\right) dz'$. The neglect of propagation thus means that, outside of the scattering-induced phase variations, the wave incident at each slice remains the same. As such, the projected potentials of each slice add up directly, which permits the assimilation of all the scattering events into a single one. The specimen is then described as a two-dimensional phase object, with a single scattering transmission function T. This is often referred to as the phase object approximation (POA). In practice, this approximation is only valid for specimens whose thickness is below a threshold of a few nm, which depends on the material investigated. This dependence to the material case is due to channelling dynamics, as will be explained in a further subsection.

When it is made from a material with a low atomic number Z, the specimen can be considered to be weakly scattering. If this condition is combined with a sufficiently low thickness, then the weak phase object approximation (WPOA) may be used, which consists of a first order Taylor development of the single scattering transmission function T, by:

$$
T\left(\vec{r}\right) \approx 1 + i\sigma\mu_p\left(\vec{r}\right) \quad . \tag{1.40}
$$

As the WPOA implies both a requirement of low thickness and low scattering strength, it is rigorously applicable only to a few cases [147, 148].

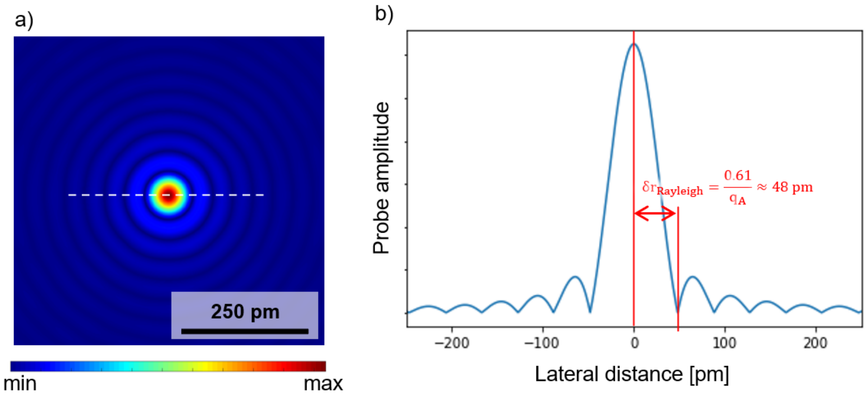

Figure 1.7: a) Depiction of the electron probe Ξ, with $\alpha = 25\,\text{mrad}$ and $U = 300\,\text{kV}$. b) Lateral profile of Ξ along the x-dimension, with $y = 0$, as indicated in a). The value taken by the Rayleigh criterion is given in the plot.

1.3 Optical aspects of STEM

1.3.1 Lateral resolution for a diffraction-limited system

In STEM, the first criterion for the resolution achieved in the experiment is the size of the circular aperture inserted in the focal plane of the OL. It is here modeled by a function $A\left(\vec{q}_{\text{FP}}\right)$, equal to 1 for $\parallel \vec{q}_{\text{FP}} \parallel < q_A$ and 0 otherwise. $q_A = \frac{\sin(\alpha)}{\lambda}$ then represents the highest spatial frequency transmitted by the optical system and $\sin\left(\alpha\right)$ is the radius of its numerical aperture. Given this information transfer limit, the smallest distance able to contribute to the recorded micrograph is expressed by the Abbe criterion for diffraction-limited systems [149, 150]:

$$\delta r_{Abbe} = \frac{1}{2q_A} = \frac{\lambda}{2\,\sin\left(\alpha\right)} \approx \frac{\lambda}{2\,\alpha} \quad . \tag{1.41}$$

Furthermore, the electron probe is given by $\Xi\left(\vec{r}_{\text{IP}}\right) = \mathcal{F}^{-1}\left[A\left(\vec{q}_{\text{FP}}\right)\right]\left(\vec{r}_{\text{IP}}\right)$, which means that its amplitude is equal to the square root of an Airy disk. Whereas it is then highly peaked in its centre, long-range fluctuations are also observed around it. An example obtained with $\alpha = 25\,\text{mrad}$ and $U = 300\,\text{kV}$ is depicted in figure 1.7.a. In order to determine the spatial resolution achievable with such a probe, a supplementary criterion needs to be introduced. By assuming an incoherent imaging of an object $O\left(\vec{r}\right)$ by $\Xi\left(\vec{r}\right)$, meaning that:

$$I_{recorded}\left(\vec{r}\right) = \mid \Xi\left(\vec{r}\right) \mid^2 \otimes_{\vec{r}} \mid O\left(\vec{r}\right) \mid^2 \quad , \tag{1.42}$$

it can be taken equal to the distance between the center of the probe and its first minimum of amplitude. This in turn implies that two points in the STEM micrograph are only distinguishable if the distance between them is larger than this metric. This is the Rayleigh criterion, given by [149, 150]:

$$\delta r_{Rayleigh} = \frac{0.61}{q_A} \approx \frac{0.61\,\lambda}{\alpha} \quad . \tag{1.43}$$

In this way, $\delta r_{Rayleigh} = 1.22\, \delta r_{Abbe}$ can be considered as the practical aberration-free limit of resolution for an incoherent STEM experiment. This is demonstrated in figure 1.7.b, where the lateral profile of Ξ is plotted with indication of the distance covered by the Rayleigh criterion.

1.3.2 Optical aberrations

Whereas the Rayleigh criterion provides a value for the resolution, as expected from the aperture radius q_A, aberrations of the OL constitute a supplementary practical limitation. Indeed, even though manufacturing techniques have largely improved since the beginnings of the field in the 1930's, electron lenses are still highly imperfect, and significant differences in effective focal length can occur among rays collected at different angles from the optical axis. For this reason, images of a point source located in the object plane are formed at heights showing dependence on the angle of collection by the lens. Thus, while the wave created in the image plane is equal to a summation of those angular contributions, each is multiplied by a factor representing a phase shift. This phase shift is commonly expressed using an aberration function $\chi\left(\vec{q}\right)$. Accounting for those geometrical aberrations, the probe function is thus equal to $\Xi\left(\vec{r}_{\mathrm{IP}}\right) = \mathcal{F}^{-1}\left[A\left(\vec{q}_{\mathrm{FP}}\right) e^{-i\chi\left(\vec{q}_{\mathrm{FP}}\right)}\right]\left(\vec{r}_{\mathrm{IP}}\right)$. The aberration function is often expressed as a polynomial [151] of the form:

$$\chi\left(\vec{q}\right) = \frac{2\pi}{\lambda} \sum_{a=1}^{a=\infty} \sum_{b \in B_a} C_{a;b} \, \frac{\left(\lambda \parallel \vec{q} \parallel\right)^{a+1}}{a+1} \, cos\left[b\left(\angle\vec{q} - \beta_{a;b}\right)\right] \quad . \tag{1.44}$$

χ is thus equal to a sum of cosine functions, each identified with a set $[a; b]$ of two integer numbers, and characterized by a modulus $C_{a;b}$, with units of distance, as well as a rotation angle $\beta_{a;b}$. With $a \in [1; \infty]$, the range B_a in which b is defined for a determined a is given by $B_a = \mid 2\,[0; a] - a - 1 \mid$. Importantly, the contribution with $a = 1$ and $b = 0$ is equal to the Fourier transform of the Fresnel propagator, representing the phase change induced by the travel of an electron over a distance $C_{1;0} = \delta z$. In particular, it is here used to include the focus of the microscope by $f \equiv C_{1;0}$. As a consequence, to represent an electron probe focused at a depth z below the the specimen entrance surface, a value $f = -z$ has to be employed.

As the absolute value of χ increases with $\vec{q}$, its impact becomes more important with the maximum spatial frequency included in the probe formation process. The radius $\sin\left(\alpha\right)$ of the numerical aperture is thus chosen to provide the best compromise between the Rayleigh criterion and the necessary elimination of spatial frequencies that are too strongly affected by aberrations. A second strategy, which was first demonstrated at the end of the 20th century [46] and introduced later to the STEM mode [47], is the direct correction of aberrations by using a complex electron-optical system. Thanks to such aberration-correction capacities, and with the larger aperture radius they allow, resolutions of 50 pm and below can be achieved routinely [48]. Nowadays, aberration-correction is increasingly common, and has largely facilitated atomic resolution within the field. In fact, all the work presented in this thesis was done by employing aberration-correction and atomically small electron probes. In figure 1.8.a, a listing of a few aberration types is provided, with inclusion of the corresponding name and notation, following reference [151]. The $\vec{q}$-dependent phase variations obtained for some of those aberrations, as per equation 1.44, are depicted in 1.8.b, for a selection of moduli. Those values were here chosen as a realistic result of aberration-correction. The amplitude of Ξ, obtained for $\alpha = 25\,\mathrm{mrad}$ and $U = 300\,\mathrm{kV}$, is depicted in 1.8.c as well, with inclusion of the aberrations selected in 1.8.b. This probe function can be observed to be distorted from its ideal shape, shown

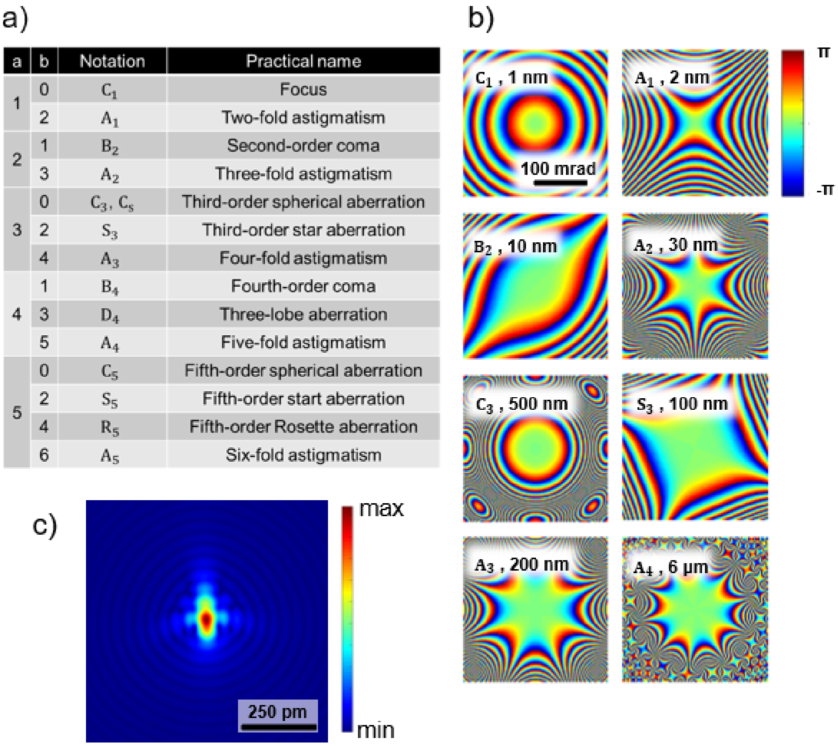

a	b	Notation	Practical name
1	0	C_1	Focus
	2	A_1	Two-fold astigmatism
2	1	B_2	Second-order coma
	3	A_2	Three-fold astigmatism
3	0	C_3, C_s	Third-order spherical aberration
	2	S_3	Third-order star aberration
	4	A_3	Four-fold astigmatism
4	1	B_4	Fourth-order coma
	3	D_4	Three-lobe aberration
	5	A_4	Five-fold astigmatism
5	0	C_5	Fifth-order spherical aberration
	2	S_5	Fifth-order start aberration
	4	R_5	Fifth-order Rosette aberration
	6	A_5	Six-fold astigmatism

Figure 1.8: a) A list of existing aberrations is given up to fifth order, with a notation following reference [151]. b) The phase variations obtained from some of those contributions are depicted, with indication of the aberration modulus. c) The amplitude of the real-space probe, when employing $U = 300\,\mathrm{kV}$ and $\alpha = 25\,\mathrm{mrad}$, depicted with inclusion of the aberrations shown in b).

in figure 1.7.a, in a manner that is usually not precisely known during the experiment, though well-determined by the function χ. In that example, whereas the chosen aberration moduli are within ranges that could be achieved after a routine aberration correction procedure, the variations are still noticeable.

Finally, in addition to the geometrical aberrations expressed by the function χ, an electron lens is also affected by a chromatic aberration C_c. This chromatic aberration results in different focal lengths for electrons having a different energy. In STEM, this effect leads to an incident illumination consisting of an incoherent superposition of probes with a variety of foci. This will be explained in more details in section 1.4. As the severity of this effect is dependent on the energy spread of the electron beam, it can be partly circumvented by adding a monochromator in the column of the instrument. Additionally, and though this was not employed here, capacities have been introduced for the direct correction of the chromatic aberration in the last few years [49]. Such chromatic aberration correctors are nevertheless beyond common applications, and so far have only been installed in a handful of instruments across the world. Their practical use is furthermore currently limited to CTEM. Finally, it is also noteworthy that, for exotic applications where a very small depth of focus is desired, STEM recording has been demonstrated with semi-convergence angles α up to 60 mrad [152]. In such cases, given a precise correction of the geometrical aberrations, C_c becomes the limiting factor for the lateral resolution of the microscope.

1.3.3 Depth of focus

In the wider field of microscopy, two notions exist to characterize the achievable resolution along the depth dimension: the depth of field and the depth of focus [149]. The depth of field is defined as the maximum vertical distance under which the specimen can be displaced without degrading the image, while keeping the focus constant. As such, this quantity characterizes the depth extent, within the imaged material, which can contribute to an image while remaining well focused. On the other hand, the depth of focus is defined as the maximum focus variation which can be performed by the objective lens without losing imaging quality significantly and while keeping the specimen position fixed along the optical axis. Those definitions apply to both CTEM and STEM, although the practical manner in which focus is determined differ, as was explained in details in tprevious sections. Noteworthily, for a state-of-the-art visible light microscope, both depth of field and depth of focus would be determined in relation to the distance between the sensor and the specimen, as well as to the vertical locations of the objective lens.

In a STEM experiment, the depth of focus is the more relevant parameter to consider the depth resolution capacities, as it is further interpreted as the distance beyond which near-field propagation begins to have a significant effect on the lateral amplitude profile of an electron wave. As such, it provides a criterion both for the focusing precision of the optical system and the minimum vertical distance resolvable in a focal series experiment. It is represented by the quantity [149, 153]:

$$\delta z_{DOF} = \frac{\lambda}{2\sin\left(\frac{\alpha}{2}\right)^2} \approx \frac{2\,\lambda}{\alpha^2} \quad , \tag{1.45}$$

and thus depends on the maximum angle α transmitted by the OL and on the wavelength λ. Importantly, this criterion is equal to the distance between two minima of the STEM probe amplitude, along the vertical propagation axis z and around $z = 0$, and is thus analogous to the Rayleigh criterion given in the last subsection [153]. In reality, while this parameter is a useful metric here, finer features may be deciphered along the $z \equiv -f$ dimension in an experiment, in part because of the direct influence of the specimen on the depth-dependent variations of the electron wave, e.g. electron channelling. Other criterions may also be used, which are less conservative [149, 154, 155]. In particular, the value of $\frac{1}{2}\delta z_{DOF}$ is equal to the focus variation under which the z-dependent probe amplitude covers 80 % of its initial profile. In practice, the energy spread of the incident electrons leads to an increment of δz_{DOF}, which becomes the practical limit when employing higher values of α [156, 157, 152].

For further visualisation, it is useful to plot the lateral amplitude profile of the coherent electron probe Ξ, shown previously in figure 1.7.b, in the absence of aberrations, and this time as a function of both x and the focus f. This is done in figure 1.9, for $U = 300\,\text{kV}$ and a selection of semi-convergence angles α. Here, each line of a given plot may be interpreted as the one-dimensional profile of the probe incident on the specimen surface, following a convolution with a Fresnel propagator $\mathcal{F}^{-1}\left[P_f\left(\vec{q}\right)\right]\left(\vec{r}\right) \otimes_{\vec{r}}$. Upon propagating down through the material,

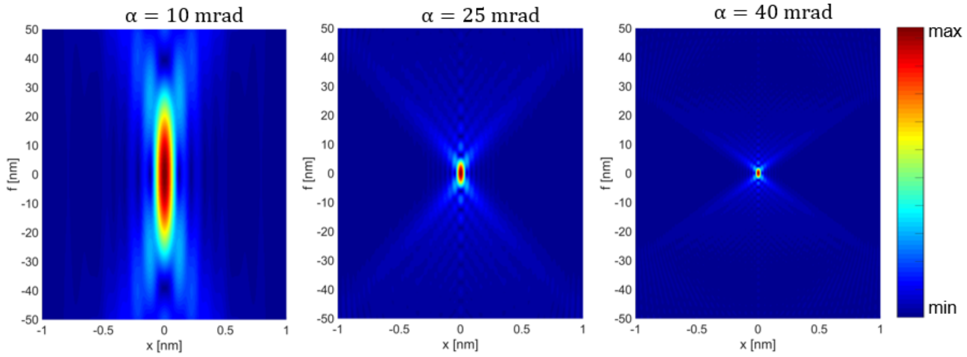

Figure 1.9: Plot of the convergent electron probe amplitude as a function of x, as a function of the focus f, for several different values of α. Calculations were done with $U = 300\,\mathrm{kV}$.

this probe extends in the same manner that it would for an increment of f, albeit with the supplementary influence of the specimen, which leads to channelling effects [158, 159, 160], as explained in a further subsection.

In practice, δz_{DOF} is also strongly affected by the third-order spherical aberration C_s [153, 161]. This is demonstrated in figure 1.10, again depicting the STEM probe as a function of x and f, for a selection of C_s values ranging between -30 μm and +30 μm. As can be seen here, the influence of the third-order spherical aberration is two-fold. First, the focus necessary to reach the smallest probe possible is changed [162]. Second, an asymmetry is induced between the two sides of the f-axis, with one conserving a focused probe for a longer range of focus variations. This in turn demonstrates that this aberration should not only be understood as a limit to the achievable lateral resolution, but also as an important factor for the variations of the electron wave throughout its propagation along the specimen depth.

1.3.4 Principle of reciprocity under the phase object approximation

In order to obtain real-space information in the STEM geometry, the recording is performed while scanning the probe within a two-dimensional raster $\vec{r}_s$, so that a CBED pattern is generated in a collection of positions. An electron probe $\Xi\left(\vec{r}-\vec{r}_s\right) = \mathcal{F}^{-1}\left[A\left(\vec{q}\right)e^{-i\chi(\vec{q})}\,e^{-i2\pi\vec{r}_s\cdot\vec{q}}\right](\vec{r})$ is thus employed with a spatial extension determined by A and χ. On the other hand, in a CTEM experiment, the image is formed directly in the IP of the OL, and the inclination of the incident plane wave can be represented by a spatial frequency $\vec{q}_s$. The illumination is then equal to $e^{i2\pi\vec{r}\cdot\vec{q}_s}$. Moreover, in this case, A and χ participate to the imaging only post-propagation, by insertion at the BFP of the lower OL. The wave functions propagating to the detector, in the CTEM and STEM modes, can be written as:

$$\Psi^{C}_{\vec{q}_s}\left(\vec{r}_{IP}\right) = \mathcal{F}^{-1}\left[A\left(\vec{q}_{BFP}\right)e^{-i\chi(\vec{q}_{BFP})}\,\mathcal{F}\left[\widehat{M}_V\,e^{i2\pi\vec{r}_{OP}\cdot\vec{q}_s}\right]\left(\vec{q}_{BFP}\right)\right]\left(\vec{r}_{IP}\right) \quad , \tag{1.46}$$

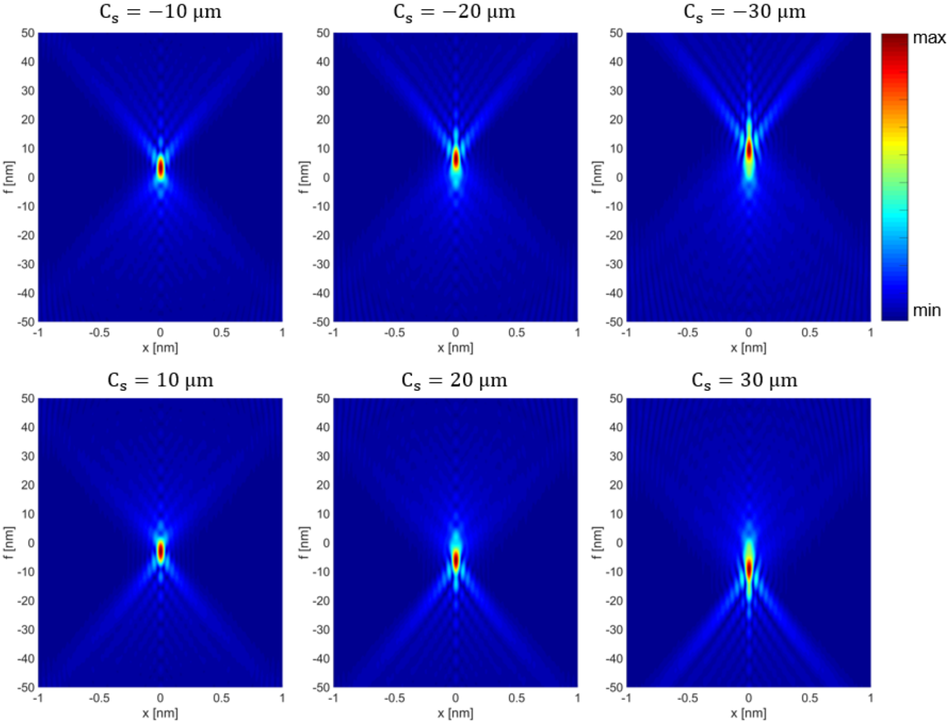
$\mathrm{C_s} = -10\ \mu\mathrm{m}$ $\mathrm{C_s} = -20\ \mu\mathrm{m}$ $\mathrm{C_s} = -30\ \mu\mathrm{m}$

$\mathrm{C_s} = 10\ \mu\mathrm{m}$ $\mathrm{C_s} = 20\ \mu\mathrm{m}$ $\mathrm{C_s} = 30\ \mu\mathrm{m}$

Figure 1.10: Plot of the STEM electron probe amplitude following the same presentation as figure 1.9, this time for several different values of C_s. Calculations were done with $\alpha = 25\,\mathrm{mrad}$ and $U = 300\,\mathrm{kV}$.

for the CTEM case, and:

$$\begin{aligned} \Psi^S_{\vec{r}_s}\left(\vec{q}_{det}\right) &= \mathcal{F}\left[\widehat{M}_V\, \mathcal{F}^{-1}\left[A\left(\vec{q}_{FP}\right) e^{-i\chi\left(\vec{q}_{FP}\right)}\, e^{-i2\pi\vec{r}_s\cdot\vec{q}_{FP}}\right]\left(\vec{r}_{IP}\right)\right]\left(\vec{q}_{det}\right) \\ &= \mathcal{F}\left[\widehat{M}_V\, \Xi\left(\vec{r}_{IP}-\vec{r}_s\right)\right]\left(\vec{q}_{det}\right) \quad , \end{aligned} \tag{1.47}$$

for the STEM case. For the two techniques, the wave function is expressed in a four-dimensional space. The sets of dimensions $\vec{r}$ and $\vec{q}$ then represent the planes where the waves are formed by the lenses. On the other hand, the sets of dimensions $\vec{r}_s$ and $\vec{q}_s$ both represent a series of independent recordings done in distinct illumination conditions. A parallel can thus be made between the two recording geometries, up to the point where an equivalence can be drawn between them. This concept of equivalence is often referred to as the reciprocity principle [163, 164]. Though this reciprocity principle can be further demonstrated by expansion of the multislice model [165], it is easier to do so by using the POA introduced in section 1.2. This results in the substitution of the multislice operator $\widehat{M}_V$ with a multiplication by the single scattering transmission function T. Using this approximation, equations 1.46 and 1.47 become:

$$\begin{aligned} \Psi^C_{\vec{q}_s}\left(\vec{r}_{IP}\right) &= \mathcal{F}^{-1}\left[A\left(\vec{q}_{BFP}\right) e^{-i\chi\left(\vec{q}_{BFP}\right)}\, \mathcal{F}\left[T\left(\vec{r}_{OP}\right)\, e^{i2\pi\vec{r}_{OP}\cdot\vec{q}_s}\right]\left(\vec{q}_{BFP}\right)\right]\left(\vec{r}_{IP}\right) \\ \Psi^S_{\vec{r}_s}\left(\vec{q}_{det}\right) &= \mathcal{F}\left[T\left(\vec{r}_{IP}\right)\, \mathcal{F}^{-1}\left[A\left(\vec{q}_{FP}\right) e^{-i\chi\left(\vec{q}_{FP}\right)}\, e^{-i2\pi\vec{r}_s\cdot\vec{q}_{FP}}\right]\left(\vec{r}_{IP}\right)\right]\left(\vec{q}_{det}\right) \quad . \end{aligned} \tag{1.48}$$

The Fourier convolution theorem can additionally be employed to obtain simplified expressions:

$$\begin{aligned} \Psi^{C}_{\vec{q}_s}\left(\vec{r}\right) &= \mathcal{F}^{-1}\left[A\left(\vec{q}\right)e^{-i\chi(\vec{q})}\right]\left(\vec{r}\right)\,\otimes_{\vec{r}}\,\left(T\left(\vec{r}\right)e^{i2\pi\vec{r}\cdot\vec{q}_s}\right) \\ \Psi^{S}_{\vec{r}_s}\left(\vec{q}\right) &= \mathcal{F}\left[T\left(\vec{r}\right)\right]\left(\vec{q}\right)\,\otimes_{\vec{q}}\,\left(A\left(\vec{q}\right)e^{-i\chi(\vec{q})}e^{-i2\pi\vec{r}_s\cdot\vec{q}}\right) \quad . \end{aligned} \tag{1.49}$$

An explicit expansion of the second equation 1.48 otherwise goes as:

$$\begin{aligned} \Psi^{S}_{\vec{r}_s}\left(\vec{q}_{det}\right) &= \iint T\left(\vec{r}_{IP}\right)\left(\iint A\left(\vec{q}_{FP}\right)e^{-i\chi(\vec{q}_{FP})}\,e^{-i2\pi\vec{r}_s\cdot\vec{q}_{FP}}\,e^{i2\pi\vec{r}_{IP}\cdot\vec{q}_{FP}}\,d^2q_{FP}\right)e^{-i2\pi\vec{r}_{IP}\cdot\vec{q}_{det}}\,d^2r_{IP} \\ &= \iint A\left(\vec{q}_{FP}\right)e^{-i\chi(\vec{q}_{FP})}\left(\iint T\left(\vec{r}_{IP}\right)\,e^{i2\pi\vec{r}_{IP}\cdot\vec{q}_{FP}}\,e^{-i2\pi\vec{r}_{IP}\cdot\vec{q}_{det}}\,d^2r_{IP}\right)e^{-i2\pi\vec{r}_s\cdot\vec{q}_{FP}}\,d^2q_{FP} \quad . \end{aligned} \tag{1.50}$$

The equivalence of formulas 1.48, for the CTEM and STEM geometries, can then be made obvious by finalizing this expansion through the convolution theorem:

$$\begin{aligned} \Psi^{S}_{\vec{r}_s}\left(\vec{q}_{det}\right) &= \mathcal{F}^{-1}\left[A\left(\vec{q}_{FP}\right)e^{-i\chi(\vec{q}_{FP})}\,\mathcal{F}\left[T\left(\vec{r}_{IP}\right)\,e^{-i2\pi\vec{r}_{IP}\cdot\vec{q}_{det}}\right]\left(-\vec{q}_{FP}\right)\right]\left(-\vec{r}_s\right) \\ &= \mathcal{F}^{-1}\left[A\left(\vec{q}'\right)e^{-i\chi(\vec{q}')}\right]\left(-\vec{r}_s\right)\,\otimes_{\vec{r}_s}\,\left(T\left(\vec{r}_s\right)e^{-i2\pi\vec{r}_s\cdot\vec{q}_{det}}\right) \quad . \end{aligned} \tag{1.51}$$

In explicit terms, the reciprocity relation derived in equation 1.51 states that the wave amplitude scattered toward the spatial frequency $\vec{q}$, when using a STEM probe located at a position $\vec{r}_s$, is equal to the one detected at the coordinate $\vec{r}$ of a CTEM image generated with an inclination $-\vec{q}$, at least in conditions where the profile of Ξ used in one geometry is equal to the point inversion of the other. Under this formalism, Ξ furthermore takes the role of a point-spread function (PSF), which expresses the effect of the coherent illumination on the wave reaching the detector, through a convolution with the transmission function.

1.4 Role of wave coherence and energy-loss

1.4.1 Partial coherence and the density matrix

The recording of a STEM intensity is done in a finite time, usually ranging between 10^{-6} and 10^{-3} s for each scan points, depending on the read-out speed of the detector employed. Within this recording time, fluctuations occur among the electrons reaching the detector, which are related to the spatial extension and energy range of the source, as well as to the interaction with the specimen itself [55, 166]. Those specimen-induced changes are due to the vibrations of the crystal lattice and to inelastic scattering. Importantly, and unless specimen damage or other disturbances happen during acquisition, both the slight energy variation of the emitted electrons and lattice vibrations occur as part of a given thermal equilibrium, such that, statistically, electron-specimen interaction remains in a stationary regime. In that context, each new electron detected by the camera is the result of one given electron wave collapsing according to Poisson statistics, and thus leading to Poisson noise. Those electron waves are then affected by the degree of variability in the emission and the specimen. As a result, the diffraction patterns that are realistically being recovered in a MR-STEM experiment can be described as averages among distinct intensity distributions, each being represented by:

$$\begin{aligned} I^n\left(\vec{q}\right) &= \mid \mathcal{F}\left[\Phi^n\left(\vec{r}\right)\right]\left(\vec{q}\right)\mid^2 \\ \Phi^n\left(\vec{r}\right) &= \widehat{M}_{V^n}\,\Xi^n\left(\vec{r}\right) \quad , \end{aligned} \tag{1.52}$$

where $\Phi^n\left(\vec{r}\right)$ is the nth electron wave exiting the specimen within the recording time. Ξ^n and V^n respectively represent the state in which the electron emitted by the source and the specimen are, upon formation of $\Phi^n\left(\vec{r}\right)$. For further theoretical description, it is often useful to introduce the density matrix $\rho\left(\vec{r}\,;\,\vec{r}\,'\right)$ by:

$$\rho\left(\vec{r}\,;\,\vec{r}\,'\right) = \sum_n p_n\,\Phi^{n*}\left(\vec{r}\right)\Phi^n\left(\vec{r}\,'\right) \quad , \tag{1.53}$$

where p_n is the probability of occupancy of the state n. A first important application of the density matrix ρ is the characterization of wave coherence within the intensity reaching the detector, which depends on the degree of phase correlation among the states Φ^n. The higher the energy range and size of the source, or the larger the crystal vibration amplitude, the more variability there is among the electrons detected and the less significant such phase relationship becomes. In particular, the mutual coherence between $\vec{r}$ and $\vec{r}\,'$, which is a measurement of how statistically correlated the electrons found at those positions are, is equal to $\mid \rho\left(\vec{r}\,;\,\vec{r}\,'\right) \mid$ [167, 168]. The situation where a value of 1 is obtained for each couple $[\,\vec{r}\,;\,\vec{r}\,'\,]$ corresponds to a perfect coherence among all electrons. On the other hand, the case where $\mid \rho\left(\vec{r}\,;\,\vec{r}\,'\right) \mid = 0$ unless $\vec{r} = \vec{r}\,'$, meaning where only diagonal elements are not equal to zero, is the one where the electron beam is fully incoherent, thus where there is no phase relationship among the states. The notion of partial coherence, which applies to electron diffraction, corresponds to the situation where $0 < \mid \rho\left(\vec{r}\,;\,\vec{r}\,'\right) \mid < 1$. There, the recovered signals may exhibit coherent as well as incoherent features, with dependence on the spatial frequencies $\vec{q}$ involved in their extraction, as is explained in more details in section 2.1.

Following Van Cittert-Zernike theorem [149], the total intensity recorded in the far-field is found equal to:

$$I^S\left(\vec{q}\right) = \mathcal{F}\left[\iint \rho\left(\vec{r}+\vec{r}\,'\,;\,\vec{r}\,'\right) d^2r\,'\right]\left(\vec{q}\right) = \sum_n p_n\,I^n\left(\vec{q}\right) \quad . \tag{1.54}$$

As such, the diffracted intensity can be thought of as resulting from the interference of all electrons at locations $\vec{r}\,'$ with all electrons at locations $\vec{r}$. The coherence metric $\mid \rho\left(\vec{r};\,\vec{r}\,'\right) \mid$ then acts as a weighting factor for the resulting coherent interference feature in $\vec{q}$-space. In general, the farther away from one another the locations $\vec{r}$ and $\vec{r}$ are, the less coherent they are, and the least they can interfere. For a diffraction pattern obtained from a plane wave, this real-space coherence limit will induce a minimum extension for Bragg spots. When considering only a pure state, relation 1.54 converges back to:

$$I^S\left(\vec{q}\right) = \mid \mathcal{F}\left[\Phi^{exit}\left(\vec{r}\right)\right]\left(\vec{q}\right)\mid^2 = \mid \mathcal{F}\left[\widehat{M}_V\,\Xi\left(\vec{r}\right)\right]\left(\vec{q}\right)\mid^2 \quad . \tag{1.55}$$

In practice, for a STEM simulation, and although methods exist for the direct treatment of electron-specimen interaction based on the density matrix formalism such as the mixed-dynamic form factor [168, 169], calculations are still done involving only single wave states and adding them in terms of intensity, according to equation 1.54. This is because of computational limitations, as the actual storage and treatment of a four-dimensional variable such as ρ is impractical.

1.4.2 Spatial and temporal incoherence of the illumination

The contribution of the incident beam to the incoherence property of the experiment [166, 170, 171] comes in two distinct forms: partial spatial coherence (PSC) and partial temporal coherence (PTC). PSC arises from the effective size Δr of the source, which results in the emission of mutually incoherent electron waves from a variety of lateral positions, with distinct phase offsets corresponding to the added propagation from those positions. PTC, on the other hand, occurs because of the energy spread ΔE of the illumination, which is mostly due to the degree of polychromaticity of the source. A supplementary spread may come from the stochastic Coulomb interaction, or Boersch effect [172], occurring at the level of the first beam cross-over, within the electron gun, where the local density of free electrons is highest [173]. The effect of PTC is often expressed as the incidence of mutually incoherent waves with a variety of foci, using a characteristic focus spread $\Delta f = C_c \frac{\Delta E}{eU}$, which then also expresses the dependence to the chromatic aberration C_c of the objective lens.

In a context where PSC and PTC occur, the illumination thus consists of a range of independent wave components, all having a $\vec{q}$-dependent phase offset in the focal plane [170, 171]. In the case of partial spatial coherence, this phase offset is due to the variety in the lateral positions from which the wave components are emitted, it thus has a shape given by $-2\pi\vec{q}\cdot\vec{r}_m$. The values taken by the emission positions $\vec{r}_m$ follow a Gaussian distribution, whose width is taken equal to the effective source size Δr. Noteworthily, this effective source size does not directly correspond to the actual physical size of the emitting material, but rather accounts for limitation of solid angle imposed by apertures. . On the other hand, partial temporal coherence is due to the energy spread ΔE among the incident electrons and to the chromatic aberration C_c of the lens. The resulting phase offset can be expressed as a variation of focus according to $-\pi\lambda f_m q^2$, where the focus difference f_m is also distributed according to a Gaussian, this time with a width equal to the focus spread $\Delta f = C_c \frac{\Delta E}{eU}$. In this context, performing a multislice STEM simulation while accounting for PSC and PTC consists of calculating:

$$\begin{aligned} \Phi^m_{\vec{r}_s\,;t}(\vec{r}) &= \widehat{M}_V\, \Phi^m_{\vec{r}_s\,;0}(\vec{r}) \\ I^S_{\vec{r}_s}(\vec{q}) &= \sum_m \mid \mathcal{F}\left[\Phi^m_{\vec{r}_s\,;t}(\vec{r})\right](\vec{q}) \mid^2 \quad , \end{aligned} \tag{1.56}$$

with:

$$\begin{aligned} \Phi^m_{\vec{r}_s\,;0}(\vec{r}) &= \mathcal{F}^{-1}\left[e^{-i2\pi\vec{q}\cdot\vec{r}_m}\, e^{-i\pi\lambda f_m q^2}\, A(\vec{q})\, e^{-i\chi(\vec{q})}\, e^{-i2\pi\vec{q}\cdot\vec{r}_s}\right](\vec{r}) \\ &= \omega^m(\vec{r}) \otimes_{\vec{r}} \Xi(\vec{r}-\vec{r}_s) \quad , \end{aligned} \tag{1.57}$$

where $\mathcal{F}\left[\omega^m(\vec{r})\right](\vec{q}) = S^m(\vec{q}) = e^{-i2\pi\vec{q}\cdot\vec{r}_m} e^{-i\pi\lambda f_m q^2}$ is a function representing the phase offset attributed to a given variation of emission position and focus. In turn, the source is described by a collection of ω^m functions. As mentioned in the last paragraph, the probability of a given coordinate $[\vec{r}_m\,;\,f_m]$ is given by:

$$p(\vec{r}_m\,;\,f_m) = p_0\, exp\left[-\frac{\parallel \vec{r}_m \parallel^2}{2\Delta r^2}\right]\, exp\left[-\frac{{f_m}^2}{2\Delta f^2}\right] \quad , \tag{1.58}$$

with p_0 a quantity inserted to ensure the normalisation to the incident intensity I_0. In that context, two strategies may be adopted for the actual calculation: either perform a certain number of simulations with random values of $[\vec{r}_m\,;\,f_m]$, while following the distribution $p(\vec{r}_m\,;\,f_m)$, or doing so in a fixed grid of emission positions and foci, and weighting the distinct calculations

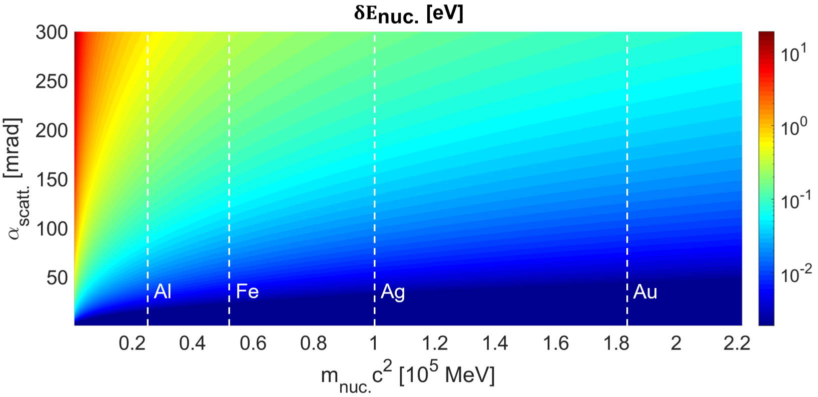

Figure 1.11: Plot of the energy $\delta E_{nuc.}$ exchanged as part of the scattering by a nucleus, given as a function of the scattering angle $\alpha_{scatt.}$ and $m_{nuc.}c^2$. The calculation was done with $U = 300\,\text{kV}$. A few atom types are indicated.

by their probability. The second option is usually the one being favored [171]. Furthermore, as the presence of partial coherence in the illumination leads to a summation of intensities, obtained with electron probes which are both laterally shifted and extended by variation of focus, it in turn causes a certain degree of blurring in real-space. The precise matching of simulated and experimental images thus requires the inclusion of those effects [170]. Similarly, PTC causes a loss of depth resolution in an FS-STEM experiment, which become important when aberrations are otherwise corrected and for large values of α [156, 157]. Nevertheless, in practice, quantitative TEM is usually performed at the level of the unit cell, meaning that signals are averaged in regions of real-space which are defined by a Voronoi segmentation. The quantities obtained through this averaging are then effectively exempt of the effect of feature spreading, whether cause by aberrations or partial coherence, at least within a certain limit [174, 175]. For this reason, the inclusion of PSC and PTC is often omitted.

1.4.3 Lattice vibrations and phonon excitation

Another origin of partial coherence in a TEM experiment is the interaction with the specimen itself. In particular, the scattering of an electron by an atomic nucleus of mass $m_{nuc.}$, toward an angle $\alpha_{scatt.}$, leads to a transfer of energy [86]:

$$\delta E_{nuc.} = \frac{2eU\left(eU + 2mc^2\right)}{m_{nuc.}c^2}\left(\sin\left(\frac{\alpha_{scatt.}}{2}\right)\right)^2 \quad . \tag{1.59}$$

In figure 1.11, $\delta E_{nuc.}$ is depicted with a logarithmic colour scale, as a function of both $\alpha_{scatt.}$ and $m_{nuc.}c^2$, for $U = 300\,\text{kV}$. It should be noted that, although this transfer of energy should in principle be a strong factor of incoherence in an electron diffraction experiment, it remains below a tenth of eV within a wide angular range, and for the most commonly investigated materials. For this reason, it is often neglected for low-angle scattering. There is thus an assumption of elasticity in the description, which implies a conservation of coherence. In reality, when considering high-angle scattering, this assumption breaks, and the energy transferred to the nucleus contributes to atomic vibrations and, in particular, to the phonon modes of the crystal lattice. For this reason, the high-angle region of reciprocal space is largely considered to be made out of so-called thermal diffuse scattering (TDS) contributions [53, 54], which consist of incoherently scattered electrons.

Atomic vibrations in the specimen can be accounted for by using the frozen phonon approximation [176, 177, 178, 179]. In this context, the calculations are performed while using a variety of potentials V^j, all obtained by shifting each individual atom by a given $\delta\vec{r}^{\,j}_{atom}$. The resulting intensities are then summed. In this context, each configuration V^j can be considered to be a snapshot of the vibrating crystal which, following arguments given previously on the high velocity of the incident electrons, is fixed for a given multislice propagation. The resulting STEM intensity is thus given by:

$$\begin{aligned} \Phi^j_{\vec{r}_s\,;\,t}\,(\vec{r}) &= \widehat{M}_{V^j}\,\Phi_{\vec{r}_s\,;\,0}\,(\vec{r}) \\ I^S_{\vec{r}_s}\,(\vec{q}) &= \sum_j \mid \mathcal{F}\left[\Phi^j_{\vec{r}_s\,;\,t}\,(\vec{r})\right](\vec{q}) \mid^2 \quad . \end{aligned} \tag{1.60}$$

Usually, the shifts are only two-dimensional, as to not affect the vertical slicing, and thus conserve the same thickness steps among the different calculations. Furthermore, while a collection of $\delta\vec{r}^{\,j}_{atom}$ is determined using a probability distribution representing the positions occupied by the vibrating atoms during each interaction, it can be obtained from the phonon modes of the crystal lattice directly [176, 177, 178, 180]. In other words, the model can account for correlations of the atomic movements within the specimen. It is noteworthy that, even though each of the individual calculations done with one of the V^j is still elastic, such an approach is equivalent to a time-dependent quantum mechanical calculation, provided that there is no irreversible changes in the crystal structure due to the excitation of phonon modes [179, 181, 182].

For most applications, it is reasonable to only consider uncorrelated atomic movements. There, this is thus a simplification of the frozen phonon approach, often referred to as the frozen lattice approximation, which is used, based on Einstein's model for lattice vibrations [176, 179]. In this context, each set of $\delta\vec{r}^{\,j}_{atom}$ consists of random numbers, following a Gaussian distribution given by:

$$p\left(\delta\vec{r}^{\,j}_{atom}\right) = p_0\,\exp\left[-\frac{\parallel \delta\vec{r}^{\,j}_{atom} \parallel^2}{2\langle\,\delta {r_{atom}}^2\,\rangle}\right] \quad , \tag{1.61}$$

where $\langle\,\delta r^2_{atom}\,\rangle$ represents the average square displacement of a given atom from its rest position. Interestingly, although TDS is inelastic, at least to an extent, the quasi-elastic approach presented here does not explicitly account for the transfer of energy to the phonon modes of the specimen, as they are considered unchanged by the interaction.

Going further, and although it was not used directly here, it is interesting to introduce the so-called Debye-Waller factor [183, 176] $B\,(\vec{q})$ of a given vibrating atom in the specimen, which expresses the resulting $\vec{q}$-dependent damping of coherent scattering features in the far-field intensity. It is given by:

$$B\,(\vec{q}) = \langle\,e^{i2\pi\vec{q}\cdot\delta\vec{r}}\,\rangle^2 = e^{-4\pi^2\langle\delta r^2\rangle\|\vec{q}\|^2} \quad , \tag{1.62}$$

by assuming both harmonicity and isotropy of the atomic potentials. Here, $\delta\vec{r}$ is the time-dependent displacement of an atom from its equilibrium position and $\langle ... \rangle$ is used to denote a time average. In this context, the sum of $1 - B$ over reciprocal space provides the proportion of the incident beam which, upon interacting with the concerned atom, will be redistributed among the TDS electrons. On the other hand B can be used as a metric to estimate the resulting attenuation of Bragg beams.

1.4.4 Inelastic scattering

Whereas atomic vibrations can be accounted for in a quasi-elastic manner using the frozen phonon approximation, the inclusion of other inelastic scattering events requires a more complex treatment method. Such inelastic scattering events are in turn due to a transfer of energy to an electron in the imaged material and involve more important losses of energy. At the level of a single event, the inelastically scattered wave function $\Phi^{eU-\delta E}$ generated from the incident Φ^{eU} with a loss of energy δE, can be expressed by:

$$\Phi^{eU-\delta E}\left(\vec{r}\right) = T^{\delta E}\left(\vec{r}\right)\Phi^{eU}\left(\vec{r}\right) \quad , \tag{1.63}$$

with $T^{\delta E}$ an inelastic transmission function containing the transition potential between the two energy states eU and $eU - \delta E$ [52]. In general, the expression of $T^{\delta E}$ is determined by the dipolar approximation [58, 184, 185] to:

$$T^{\delta E}\left(\vec{r}\right) = \mathcal{F}^{-1}\left[\sqrt{\frac{p_{\delta E}}{{q_{\delta E}}^2 + \parallel \vec{q} \parallel^2}}\right]\left(\vec{r}\right) \quad , \tag{1.64}$$

with $p_{\delta E}$ representing the probability of the transition and $q_{\delta E}$ being a characteristic spatial frequency, given by:

$$q_{\delta E} = \frac{1}{\lambda}\sin\left(\frac{\delta E}{2eU}\right) \quad . \tag{1.65}$$

The single-event inelastic intensity $I^{eU-\delta E}$, recorded in reciprocal space, is in turn equal to:

$$\begin{aligned} I^{eU-\delta E}\left(\vec{q}\right) &= \mid \mathcal{F}\left[\Phi^{eU-\delta E}\left(\vec{r}\right)\right]\left(\vec{q}\right) \mid^2 \\ &= \mid \sqrt{\frac{p_{\delta E}}{{q_{\delta E}}^2 + \parallel \vec{q} \parallel^2}} \otimes_{\vec{q}} \mathcal{F}\left[\Phi^{eU}\left(\vec{r}\right)\right]\left(\vec{q}\right) \mid^2 \\ &\approx L^{\delta E}\left(\vec{q}\right) \otimes_{\vec{q}} I^{eU}\left(\vec{q}\right) \quad , \end{aligned} \tag{1.66}$$

with I^{eU} the $\vec{q}$-distribution of the incident intensity, and:

$$L^{\delta E}\left(\vec{q}\right) = L_c\left(\vec{q}\right)\frac{p_{\delta E}}{{q_{\delta E}}^2 + \parallel \vec{q} \parallel^2} \quad . \tag{1.67}$$

In practice, the dipolar approximation, and thus the Lorentzian shape of the transmission function, is only valid up to a certain spatial frequency $q_c = \frac{\sin(\theta_c)}{\lambda}$, with θ_c a critical angle of 10 to 20 mrad [185]. Consequently, L includes a function L_c, which is equal to L_0 for $\parallel \vec{q} \parallel < q_c$, and 0 otherwise. The quantity L_0 additionally permits the normalisation of the two-dimensional Lorentzian. In the absence of a cut-off, it diverges with the size of the integration region. While equation 1.66 is applicable to the treatment of a loss of energy occurring under the single scattering approximation, it is not sufficient for the more general case, where dynamical diffraction dominates. Then, the inelastic scattering events need to be considered in a volumetric manner, for instance by means of a multislice calculation as explained in the next paragraph. To this end, equation 1.63 is employed directly, with $T^{\delta E}\left(\vec{r}\right) = \mathcal{F}^{-1}\left[\sqrt{L^{\delta E}\left(\vec{q}\right)}\right]\left(\vec{r}\right)$ [186].

For the general understanding of the effect of energy-loss in a context where multiple elastic scattering occurs, it is necessary to consider the depth z at which the electron beam interacts with $T^{\delta E}$. The incident wave function is then equal to Φ_{z_n}, having been elastically propagated, to the slice $z_n = z$, beforehand. In turn, following the inelastic scattering event, electrons are elastically propagated again, down to the thickness t. As a consequence, a complex mixing of elastic and inelastic features occurs in the accessible intensity, which results in the so-called preservation of elastic contrast [187, 188]. Indeed, in general, the real-space contrast originating from inelastic scattering is expected to be delocalized, due to the long-range character of the electrostatic interaction with the atomic electrons [189, 190] and, in the case where plasmon modes of the material are excited, to their collective nature [191]. On the contrary, the elastic scattering by the nuclei is highly localized and, in the case where they are arranged in a crystal lattice, leads to the appearance of Bragg reflections. As such, even within a wave having transferred energy to an electron in the material, the interference of Bragg beams can occur, leading to atomic resolution. Going back to questions of computation, one of the most important aspects of energy-loss is its influence on the degree of incoherence within the electron beam. In the general case, excitations of bound electrons by the incident beam occur independently, which means that the inelastically scattered wave components created at different positions in the volume of the material, as well as the elastically scattered wave function, are all mutually incoherent. As a consequence, the amount of wave states contributing to the accessible intensity increases with the thickness traveled by the electrons. Furthermore, as a given electron can potentially lose energy multiple times during the propagation, it follows that the increment is exponential. In this context, it is clear that the rigorous implementation of energy-loss in a multislice simulation comes at a major cost of computational complexity. In fact, this objective was only recently achieved, as was reported in reference [186], and is the subject of chapter 3.

1.4.5 Channelling dynamics in quasi-elastic conditions

Another important aspect of the interaction of high-energy electrons with a specimen is the phenomenon of channelling, which arises from the geometry in which the experiment is carried out. As the optical axis is chosen to coincide with one of the crystallographic zone axes, the projected atomic columns act as electrostatic guides for the electron wave function [192]. This means that, while they propagate through the thickness of the material, the probing electrons are attracted by the positive charges of the nuclei and, as a result, oscillate around them. This phenomenon can be observed in multislice simulations, where it can be understood as the effect the phase variation by $T_{[z\,;\,z+\delta z]}\left(\vec{r}\right)$ has on the subsequent amplitude change, which arises through the Fresnel propagator $\mathcal{F}^{-1}\left[P_{\delta z}\left(\vec{q}\right)\right]\left(\vec{r}\right)\otimes_{\vec{r}}$. For a direct representation of channelling, in quasi-elastic conditions, and its contribution to the complex shaping of the electron wave within the specimen, a multislice simulation was performed employing the frozen lattice approximation. A real-space intensity was thus obtained as a function of the depth traveled within the specimen, equal to the incoherent summation of waves interacting with 30 different crystal configurations. The square root of this intensity, which can be interpreted as an average real-space amplitude among the configurations, is depicted in figure 1.12.a, as a function of the position along the [010] axis and the thickness t. The calculations were performed using an Au specimen in [100] orientation and an electron probe with $\alpha = 25\,\mathrm{mrad}$ and $U = 300\,\mathrm{kV}$. Six distinct cases are presented, corresponding to two different positions of the probe, one coinciding with an atomic column, the other being between two of them, while staying on the [010] axis, and three different foci. The value of $f = 0\,\mathrm{nm}$ corresponds to an electron probe focused on the entrance surface of the Au supercell, while $f = -30.59\,\mathrm{nm}$ implies a coincidence with the

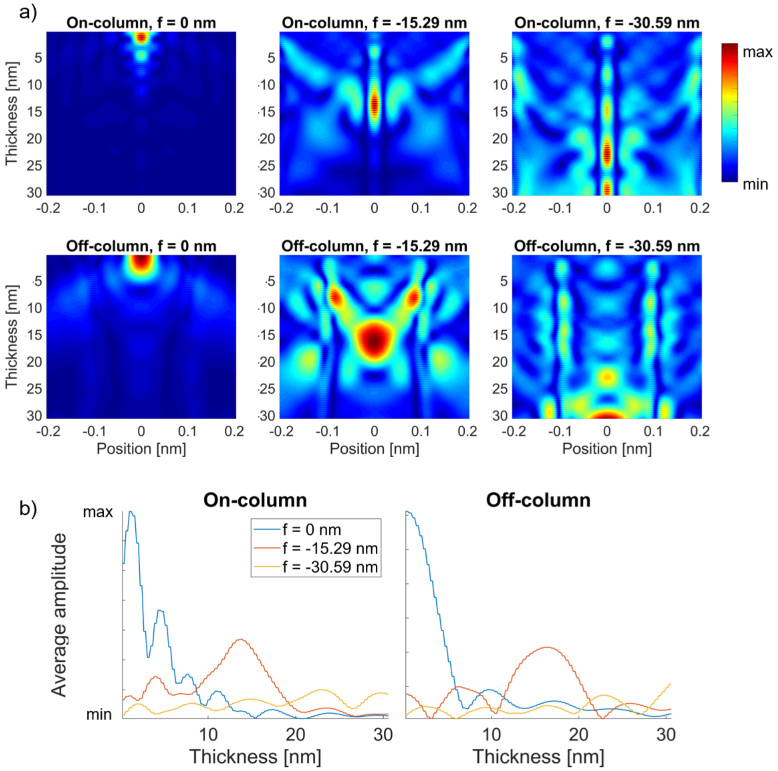

Figure 1.12: a) Depiction of the [010]-profile of the average amplitude of waves propagating through 30 frozen phonon configurations of an Au specimen in [100] orientation, as a function of thickness. The profile is given for two probe position: on an atomic column, and in-between two columns along the [010] axis, and for three values of focus. Calculations were done with $\alpha = 25\,\text{mrad}$ and $U = 300\,\text{kV}$. The lateral scaling in the figures is chosen to cover the length of one unit cell. b) Value of the average amplitude, at the lateral position 0 in a), plotted as a function of thickness for the six cases.

thickness limit of the simulation, and $f = -15.29\,\text{nm}$ with half of it. The amplitude of a wave propagating along the atomic column is observed to laterally oscillate with thickness. Interestingly, the exact manner in which this occurs is also affected by the focus of the electron probe in a non-trivial way. Indeed, whereas the maximum of wave amplitude is indeed found close to a thickness $t = -f$, as expected from arguments given previously, the exact oscillation period, as well as the values reached at the positions of local amplitude maxima along z, vary from one case to the other. This is further confirmed by figure 1.12.b, where the average amplitude at the center of the probe, meaning at $\vec{r} = \vec{r}_s$, is plotted as a function of thickness. As such, a comparison can be made between the case where the probe focus coincides with the entrance of the Au specimen and the one where it coincides with the maximum simulated thickness. Indeed, while $f = 0\,\text{nm}$ leads to sharp maxima of amplitude, and their rapid decrease along the distance traveled by the electrons, $f = -30.59\,\text{nm}$ permits a more constant height among the amplitude peaks. In parallel, placing the probe off-column leads to a spread of the probe amplitude, owing to the attraction by the neighboring atoms, though with a similar oscillation mechanism. Finally, it should be noted that the behavior described here, though useful to acquire an understanding of some of the aspects of dynamical diffraction, does not directly inform on the resulting image contrast. In that regard, while the focus f is, in practice, included in calculations by considering it to be an aberration of the lens, it should rather be understood as a parameter to tune the exact type of contrast observed in a given TEM micrograph, by means of influencing this channelling mechanism. This subject was explored in the frame of a work reported in reference [193], which is at the heart of chapter 4.

1.4.6 Specimen damage and electron dose

A possible consequence of the transfer of energy from the electrons is a degree of damage sustained by the specimen during the experiment [194, 195]. To control the extent under which this phenomenon occurs, two parameters are important. First is the electron dose, meaning the total number of electrons sent to the specimen, during the recording time by units of surface. Second is the dose rate, which represents the increment of dose per units of time. It is interesting to note that a STEM and a CTEM experiments, provided that they lead to the same total dose, do not reach it in the same manner. This is because, in STEM, the probing electrons are concentrated in a small volume and rastered across the specimen surface. This means that a specific part of the specimen receives an electron intensity which is highly peaked in the time dimension. Due to this dose peak, certain damage thresholds can be reached [196], whereas this would not occur in the CTEM mode for which the illumination is homogeneous both in real-space and across the recording time. More generally, the dose and dose rates can be controlled by the incident current [197]. In the CTEM geometry, this current is normally set below a few nA while, in STEM, it is usually kept between 50 and 100 pA. In practice, the exact current used can be adapted according to a few experimental criteria. This includes the beam-sensitivity of the investigated material, the DQE of the employed detector and the proportion of the electrons exiting the specimen which ends up participating in the image formation process. In STEM, this last criterion itself depends on the geometry of the detector.

The most common source of specimen damage is the so-called knock-on of atomic nuclei, which may occur if the energy transfer $\delta E_{nuc.}$ is greater than the displacement energy of the nucleus [198]. This knock-on event may then lead to various defect formation mechanisms [199, 200]. Following equation 1.59, this phenomenon is associated with scattering toward very high angles, backscattering ($\alpha_{scatt.} = \pi$) especially, and is more likely for sufficiently light atoms. It is also noteworthy that, in practice, it can be mitigated by using a lower value of the acceleration voltage U [201]. Furthermore, damage can be induced by other types of inelastic scattering. In particular, a transfer of energy to an electron within the material results in an ionization event and, consequently, in the generation of charge carriers. Besides the case where a recombination occurs immediately, either by radiative or non-radiative process, an ionization can give rise to a wide variety of complex physical and chemical mechanisms within the material [105], thus resulting in changes in both structure and chemical composition. Finally, in the STEM case, as a relatively high number of electrons is concentrated in a small volume, contamination effects may occur at the surface of the specimen [202, 203]. This phenomenon arises from the attraction of organic molecules, initially adsorbed at the surface of the material or present in the microscope column, by the negative charge of the probe due to instantaneous dipole formation. In that way, layers of amorphous carbon may build rapidly, through the polymerization of those molecules, and induce unwanted scattering effects [204, 205].

Discussion

Whereas an exhaustive review of existing TEM methodologies is far beyond the frame of this chapter, aspects relevant to the techniques used in the work presented here could be introduced. This includes the main operational principles of the transmission electron microscope, as well as the concept of the magnetic electron lens and its imperfections. Indeed, whereas optical microscopes nowadays provide a near perfect transfer of spatial frequencies, thanks to longstanding developments in the field of visible light optics, the manufacturing of those lenses is still subject to many issues, owing to the complexity of such devices. As a consequence, experimental TEM micrographs are always affected by a certain degree of aberrations, both geometrical and chromatic, which represents a limit to the achievable resolution. Nevertheless, in large part thanks to advanced capacities in the correction of those aberrations, atomic patterns can nowadays be routinely imaged using the transmission electron microscope.

While the interpretation of TEM micrographs cannot be done, in the general case, using analytical models, numerical solutions exist. The general strategy of quantitative STEM is thus to compare the results of simulations to experimental signals. Among existing simulation methods, the only one employed in the work presented in this thesis, and which was thus explained in details in this chapter, is the multislice algorithm. This method consists of assimilating the dynamical diffraction of electrons to a succession of independent phase grating and near-field propagation steps, while slicing the potential along the optical axis z. Conceptually, this means that the geometry of the experiment remains, in effect, two-dimensional, which is reasonable by virtue of the paraxial approximation. Beyond this aspect, the general description of the electron wave function, and how it interacts with the specimen potential V, is done with the implication that its relativistic nature can be accounted for by means of simple corrections to the Schrödinger equation. Furthermore, owing to the high velocity of the probing electrons, V is considered fixed during the interaction. This last point is, in fact, the justification for the use of the frozen phonon approximation to account for the influence of atomic vibrations on the recorded intensity. In parallel, the degree of partial coherence within the electron beam can be accounted for by repeating calculations with differing incident wave functions, although, in practice, this is often omitted. A more advanced topic in electron diffraction is the occurrence of inelastic scattering within the volume of the specimen, and the transfer of energy to bound electrons. Though the physics describing this type of interaction is well-defined, by use of the dipolar approximation, the actual implementation in a multislice simulation brings new difficulty to the field and, as such, was only tackled recently. Beyond those aspects, the combination of scattering and near-field propagation gives rise to complex shaping of the electron wave while it travels through matter, including its channelling by atomic columns.

Chapter 2

Imaging modes in STEM and processing of four-dimensional data

Summary

Whereas the theoretical aspects, relevant to this work, of electron diffraction were reviewed in chapter 1, several questions were left out with regards to the manner in which an actual image is obtained, in particular in the case of a momentum-resolved STEM experiment. Due to the large amount of information made available by such a multidimensional experiment, data analysis, including the generation of real-space-resolved signals, is not trivial. It will therefore be addressed in this chapter. As such, it is started, in section 2.1, by a review of the conventional imaging modes of STEM. Section 2.2 then pursues toward the direction of 4D-STEM more specifically, with a description of how diffraction space can be mapped, leading to the precise knowledge of the intensity distribution as a function of both spatial frequency and scan position. Furthermore, the details of the integration of the first moment are given in section 2.3. Finally, a new STEM signal, the scalar second moment, introduced to the field by this work, constitutes the subject of section 2.4.

2.1 Imaging modes in STEM and CTEM

2.1.1 Momentum-resolved STEM

The STEM technique is based on the formation of a CBED pattern, resolved in reciprocal space, as a function of the scan position. The electron intensity $I^S_{\vec{r}_s}$, available in the far-field, can then be recorded directly by use of a camera. In that process, a four-dimensional dataset is obtained, providing a direct access to the dependence of the diffracted intensity on both the scan position $\vec{r}_s$ and the spatial frequency $\vec{q}$. Interestingly, the vector $\vec{q}$ expresses a variation of the lateral momentum $\vec{p}$ of the electrons, by use of de Broglie's relation [50]. For this reason, this recording scheme is here referred to as momentum-resolved STEM (MR-STEM). Other terms such as 4D-STEM or pixelated STEM are also common. In practice, the applicability

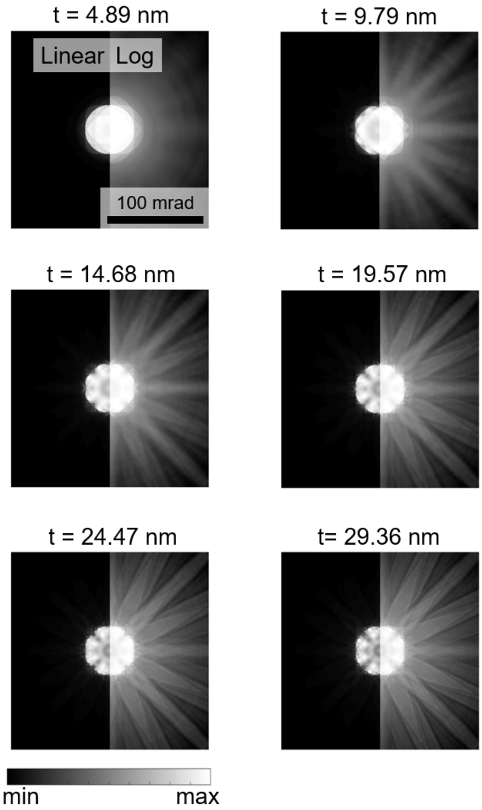

Figure 2.1: PACBED intensity obtained for different thicknesses of an Au specimen, in [100] incidence. For a better visualisation of the high-angle features, which are strongly dependent on TDS, the intensity is also shown in logarithmic colour scale. The simulation was done with $U = 300\,\mathrm{kV}$ and $\alpha = 25\,\mathrm{mrad}$.

of this technique is limited by the recording speed of the camera, especially in the atomically resolved case, as the specimen may be subject to vibrations, lateral drift or damage, while being illuminated. Both a good stability of the instrument and a fast enough detector read-out are therefore necessary for the realistic implementation of high-resolution MR-STEM, with remaining limitations in the number of scan positions. As a consequence, the development of this technique only occurred relatively recently, following the availability of fast direct electron detector arrays [66, 67, 68, 69, 70, 71, 72, 73].

For a first visualisation of the information accessible from a MR-STEM experiment, the position-averaged CBED (PACBED) intensity $I^{PA}(\vec{q}) = \frac{1}{N_{\vec{r}_s}} \sum_{\vec{r}_s} I^{S}_{\vec{r}_s}(\vec{q})$, with $N_{\vec{r}_s}$ the total number of scan points, obtained from a simulation performed with an Au specimen in [100] orientation, is presented in figure 2.1 for a selection of thicknesses t. As was initially explained in section 1.1, the main features of those patterns are a central beam, which reproduces the shape of the convergent, aperture-limited, illumination in the focal plane, and a certain number of Bragg beams overlapping with the central beam. Due to multiple scattering, the respective

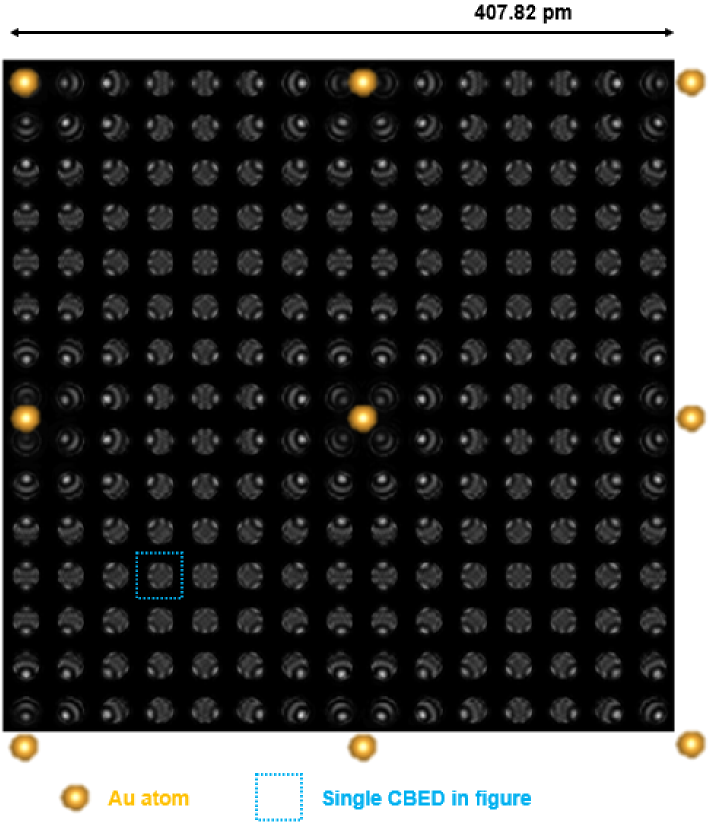

Figure 2.2: The CBED patterns are aligned along the $\vec{r}_s$ dimensions, in order to show their variation within the scan window. The positions of the gold atomic columns in the employed [100] projection are indicated, alongside their distance to one another. The diffraction patterns depicted here are obtained after a propagation through a thickness $t = 4.89\,\mathrm{nm}$.

complex amplitudes of the diffracted beams vary dynamically throughout the propagation, as the electrons are exchanged among them, including toward higher and lower diffraction orders. As a consequence, the resulting diffraction features are very characteristic of specimen thickness, and their formation mechanism is critically affected by any mistilt between the propagation direction and the crystallographic axes. Because of this, PACBED patterns can be used for the determination of both thickness and mistilt [206, 174]. In the absence of extensive preliminary knowledge on the material and its crystallography, it is also possible to employ the diffraction features for the direct determination of crystal symmetries [207, 208]. In this example, it should also be noted that the simulation presented here includes the effects of lattice vibration by use of the frozen phonon approximation [176, 177, 178, 179]. The contribution of TDS, which is especially strong for high scattering angles, thus leads to further complications of the intensity distribution. In particular, its combination with elastic scattering, in dynamical conditions, results in the formation of Kikuchi bands [209, 210, 211], which are also characteristic of crystallography [212]. Furthermore, while the PACBED patterns shown in figure 2.1

provide an accurate depiction of how multiple scattering affects the intensity distribution, they do not indicate how it varies as a function of the scan position. For this purpose, the single CBED patterns are given in figure 2.2, for $t = 4.89\,\text{nm}$. As can be observed, a redistribution of intensity occurs within the central disk toward the lateral positions of the atomic column, along the [100] zone axis. This mechanism is due to the Coulomb attraction of the electrons by the nuclei [74] and can be employed to measure projected atomic electric fields in thin specimens, as explained further down in this section.

2.1.2 CTEM imaging and phase contrast

CTEM imaging consists of measuring electron intensity resulting from the formation of an image by the lower objective lens according to equation 1.46. Consequently, the CTEM intensity is given by:

$$I^C_{\vec{q}_s}(\vec{r}) = \mid \mathcal{F}^{-1}\left[A(\vec{q})\, e^{-i\chi(\vec{q})}\, \mathcal{F}\left[\widehat{M}_V\, e^{i2\pi\vec{q}_s\cdot\vec{r}\,'}\right](\vec{q})\right](\vec{r}) \mid^2 \quad . \tag{2.1}$$

By convention, the case where $\parallel \vec{q}_s \parallel \leq q_A$ is referred to as bright field (BF) imaging, and the one where $\parallel \vec{q}_s \parallel > q_A$ as dark field (DF) imaging. The term DF is also employed to refer to cases where the aperture is displaced from the center of the BFP to encircle a specific selection of diffraction spots.

If the specimen fulfills the POA, I^C becomes:

$$I^C_{\vec{q}_s}(\vec{r}) = \mid \mathcal{F}^{-1}\left[A(\vec{q})\, e^{-i\chi(\vec{q})}\right](\vec{r}) \otimes_{\vec{r}} \left(T(\vec{r})\, e^{i2\pi\vec{q}_s\cdot\vec{r}}\right) \mid^2 = \mid \Xi(\vec{r}) \otimes_{\vec{r}} \left(T(\vec{r})\, e^{i2\pi\vec{q}_s\cdot\vec{r}}\right) \mid^2 \quad . \tag{2.2}$$

Note that $\Xi(\vec{r})$ here represents the PSF of the CTEM imaging mode, as was explained in section 1.3. In routine conditions, a single recording is done with an uninclined plane wave, and thus $\vec{q}_s = \vec{0}$. This results in a direct dependence of the micrograph on the phase variation of the incident plane wave due to the interaction, which, under the POA, is equal to $\sigma\mu_p$. This method is thus often referred to as phase contrast imaging. This phase sensitivity leads to complex real-space variations as a function of specimen thickness, focus and other aberrations, including contrast reversals. For this reason, a CTEM image is often difficult to interprete quantitatively. In the case where an unaberrated lens with infinite angular transmission is employed to image a phase object, the intensity simplifies to:

$$I^C(\vec{r}) = \mid T(\vec{r}) \mid^2 = \mid e^{i\sigma\mu_p(\vec{r})} \mid^2 = 1 \quad . \tag{2.3}$$

What this demonstrates is that, under the POA and in conditions of perfect coherence, employing the best possible resolution in a CTEM experiment, and transferring all spatial frequencies perfectly, implies a loss of image contrast. This is because the propagation of the electrons through the specimen then only affects the phase of the wave function, which is lost in the recording. Therefore, in conditions where the specimen is thin, it is often necessary to employ an intentionally aberrated set-up, for instance by means of varying the focus of the objective lens, to obtain interpretable results. This is usually the approach chosen for the imaging of viruses [93], for instance. Beyond that, methodologies exist which aim at directly extracting the phase of the wave function. This includes, for instance, electron holography [95, 97], which consists of making it interfere with a reference wave, and exploiting the resulting pattern by Fourier analysis. Another example is the focal series reconstruction (FSR) method [213, 214], which consists of calculating the wave from a series of recordings performed with a varying Ξ.

2.1.3 Conventional STEM

Whereas this thesis focuses on the momentum-resolved STEM technique and some of its recent developments, previously introduced implementations of real-space imaging based on the STEM set-up remain important for the interpretation of the four-dimensional diffraction results. Such approaches rely on the summation of intensity within predefined angular ranges, using detectors of annular shapes. Interpretable micrographs are then obtained by plotting the resulting intensity as a function of the scan position. In this work, those methods are referred to as conventional STEM (C-STEM), and are, in principle, fully reproducible through the MR-STEM technique, by employing virtual detectors. In practice, this capacity is nevertheless limited by the sampling of the spatial frequencies by the pixels of the camera, and by the maximum extent of angular space accessible, which is itself determined by the camera length. Whether virtual or physical, the detector can be represented by a function $D\left(\vec{q}\right)$, equal to 1 if $q_{min} \leq \parallel \vec{q} \parallel < q_{max}$ and 0 otherwise. The resulting C-STEM signal is given by:

$$\begin{aligned} I^D\left(\vec{r}_s\right) &= \iint D\left(\vec{q}_{det}\right) \mid \Psi^S_{\vec{r}_s}\left(\vec{q}_{det}\right) \mid^2 \; d^2 q_{det} \\ &= \iint D\left(\vec{q}_{det}\right) \mid \mathcal{F}\left[\widehat{M_V}\, \mathcal{F}^{-1}\left[A\left(\vec{q}_{FP}\right) e^{-i\chi\left(\vec{q}_{FP}\right)}\, e^{-i2\pi\vec{r}_s\cdot\vec{q}_{FP}} \right]\left(\vec{r}_{IP}\right)\right]\left(\vec{q}_{det}\right) \mid^2 \; d^2 q_{det} \quad . \end{aligned} \tag{2.4}$$

Here, it should be noted that, in the MR-STEM case, each of the pixels of the camera can already be considered as a distinct STEM detector, providing access to a corresponding C-STEM signal. This signal is in turn equal to the squared amplitude of the spatial frequency component $\vec{q}$ of the exit wave $\Psi^{exit}_{\vec{r}_s}\left(\vec{r}\right)$. In this condition, the generation of I^D using a virtual detector is inherently done in a discrete $\vec{q}$-space, rather than a continuous one.

It is possible to go further in drawing a relationship between the signal and the specimen potential. When employing the POA in fully coherent conditions, as done in equation 1.50, while assigning:

$$\iint T\left(\vec{r}_{IP}\right) e^{i2\pi\vec{r}_{IP}\cdot\vec{q}_{FP}}\, e^{-i2\pi\vec{r}_{IP}\cdot\vec{q}_{det}}\, d^2 r_{IP} \;=\; \tilde{T}\left(\vec{q}_{det} - \vec{q}_{FP}\right) \quad , \tag{2.5}$$

the expression for the intensity $I^S_{\vec{r}_s}\left(\vec{q}_{det}\right)$ recorded in a STEM experiment can be expanded as:

$$\begin{aligned} I^S_{\vec{r}_s}\left(\vec{q}_{det}\right) \;=\; \iint \iint & A\left(\vec{q}_{FP}\right) A\left(\vec{q}_{FP}{}'\right) e^{-i\left(\chi\left(\vec{q}_{FP}\right) - \chi\left(\vec{q}_{FP}{}'\right)\right)} \\ & \tilde{T}\left(\vec{q}_{det} - \vec{q}_{FP}\right) \tilde{T}^*\left(\vec{q}_{det} - \vec{q}_{FP}{}'\right) e^{-i2\pi\vec{r}_s.\left(\vec{q}_{FP} - \vec{q}_{FP}{}'\right)}\, d^2 q_{FP}\, d^2 q_{FP}{}' \quad . \end{aligned} \tag{2.6}$$

It is then possible to go further by stating that $\Delta\vec{q} = \vec{q}_{FP}{}' - \vec{q}_{FP}$, such that:

$$I^S_{\vec{r}_s}\left(\vec{q}_{det}\right) \;=\; \mathcal{F}^{-1}\left[\tilde{I}^S_{\Delta\vec{q}}\left(\vec{q}_{det}\right)\right]\left(\vec{r}_s\right) \quad , \tag{2.7}$$

and:

$$\begin{aligned} \tilde{I}^S_{\Delta\vec{q}}\left(\vec{q}_{det}\right) \;=\; \iint & A\left(\vec{q}_{FP}\right) A\left(\vec{q}_{FP} + \Delta\vec{q}\right) e^{-i\left(\chi\left(\vec{q}_{FP}\right) - \chi\left(\vec{q}_{FP} + \Delta\vec{q}\right)\right)} \\ & \tilde{T}\left(\vec{q}_{det} - \vec{q}_{FP}\right) \tilde{T}^*\left(\vec{q}_{det} - \vec{q}_{FP} - \Delta\vec{q}\right) d^2 q_{FP} \quad . \end{aligned} \tag{2.8}$$

Equation 2.8 can be further employed to write:

$$I^D\left(\vec{r}_s\right) \;=\; \mathcal{F}^{-1}\left[\tilde{I}^D\left(\Delta\vec{q}\right)\right]\left(\vec{r}_s\right) \quad , \tag{2.9}$$

with:

$$\begin{aligned}\tilde{I}^{D}\left(\Delta\vec{q}\right) = \iint\iint & D\left(\vec{q}_{det}\right)\, A\left(\vec{q}_{FP}\right) A\left(\vec{q}_{FP}+\Delta\vec{q}\right) e^{-i\left(\chi\left(\vec{q}_{FP}\right)-\chi\left(\vec{q}_{FP}+\Delta\vec{q}\right)\right)} \\ & \tilde{T}\left(\vec{q}_{det}-\vec{q}_{FP}\right)\tilde{T}^{*}\left(\vec{q}_{det}-\vec{q}_{FP}-\Delta\vec{q}\right) d^{2}q_{FP}\, d^{2}q_{det} \quad .\end{aligned} \tag{2.10}$$

It is noteworthy that C-STEM methods can be employed, like CTEM imaging, to obtain phase contrast within a micrograph, thus making it directly dependent on the phase variations of the electron wave-function. This condition relies on the reciprocity theorem and therefore requires the detector to cover a small enough angular range. In the opposite case, the summation of intensity within an angular range is equivalent to incoherently summing distinct spatial frequency components of the STEM exit wave, corresponding to the scattering angles. All those components in turn contain a specific dependence to the scan position. In this context, the more variety there is among the scattering angles, the more difference occurs among those contributions, which leads to a damping of the coherent features of the C-STEM image. As such, the angular extent of the STEM detector can be considered as a supplementary factor of incoherence in the recording.

Among existing hardware detectors, one can mention the BF one, named in analogy to the BF-CTEM imaging mode mentioned previously, which sums electrons scattered up to an angular limit below α, thus $q_{min} = 0$ and $q_{max} < q_A$. Other signals are obtained with ring detectors. For instance, the annular bright field (ABF) intensity is generated by summing electrons within an angular interval contained in the outer part of the Ronchigram, usually meaning $q_{min} \geq \frac{q_A}{2}$ and $q_{max} < q_A$. Annular dark field (ADF) signals, on the other hand, are obtained by employment of angles above α, thus $q_{min} \geq q_A$. Depending on the angular range, those are often referred to as low-angle ADF (LAADF) or high-angle ADF (HAADF), which use electrons scattered to angles below and above 40 to 50 mrad, respectively. Examples are provided in figure 2.3, consisting of all imaging modes mentioned in this paragraph. The simulation employed there is the same as presented previously in this section. For all cases, the inner and outer acceptance angles are indicated as subscripts. A CTEM result is depicted as well, obtained by employing intensity within a single pixel of reciprocal space, corresponding to $\vec{q} = \vec{0}$. It is interesting to note that the real-space features of the CTEM image are mostly conserved in BF_5, but are absent in BF_{25}. This is because, in general, the detector size of a given C-STEM mode grants it specific coherence properties, as explained above.

2.1.4 Z-contrast

In STEM, the most common detectors cover angular ranges which are sufficiently extended so that the resulting C-STEM signal does not contain notable phase dependences. In particular, the HAADF imaging mode makes use of electrons which are scattered toward angles above 40 to 50 mrad, up to a limit of 100 to 300 mrad. There, the source of incoherence is two-fold, as it also arises from the predominance of TDS. Since the probability of high-angle scattering displays a dependence on the atomic number Z through the Mott-Bethe relation given in equation 1.29, the HAADF signal is often said to display Z-contrast [215, 216, 217]. Furthermore, as the amount of incoherently scattered electrons becomes higher with the distance traveled within the specimen, such a signal is expected to increase monotonously with the thickness t. The relation to t is nevertheless not linear, and thus requires multislice simulations, including

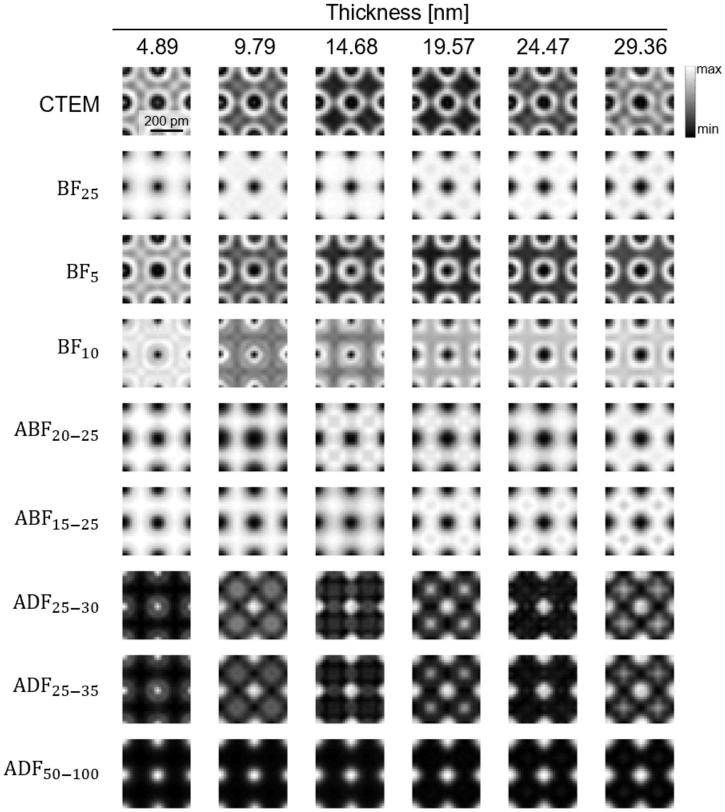

Figure 2.3: Examples of C-STEM micrographs are depicted for a few different specimen thicknesses. This includes several instances of BF, AF, LAADF and HAADF imaging, with acceptance angles indicated as subscripts. The result of the CTEM imaging mode, obtained through the reciprocity relation at $\vec{q} = \vec{0}$, is shown as well. The simulation employed here is the same as for figure 2.2.

TDS, to be known precisely [218, 219, 220]. Importantly, such simulations do not necessarily require the inclusion of further inelastic scattering events such as the excitation of valence electrons and plasmon modes in the specimen, as their impact can be considered, to a large extent, to be only noticeable in the low-angle region of diffraction space [85]. This is an interest of the HAADF imaging mode, compared to the other available C-STEM signals, and one of the main subjects treated in this thesis. It is nevertheless noteworthy that the excitation of core electrons, although they are not responsible for as many events as plasmon excitations, may affect high-angle scattering more significantly [221].

For a qualitative understanding of the behaviors expected from the HAADF signal, the incoherent imaging model [222, 223] can be introduced, by considering that the specimen fulfills the POA. The condition $q_{min} \gg q_A$ is then imposed by the geometry of the detector, and by assuming a small value of α. Starting from equation 2.10, this translates into $\parallel \vec{q}_{det} \parallel \gg \parallel \vec{q}_{FP} \parallel$,

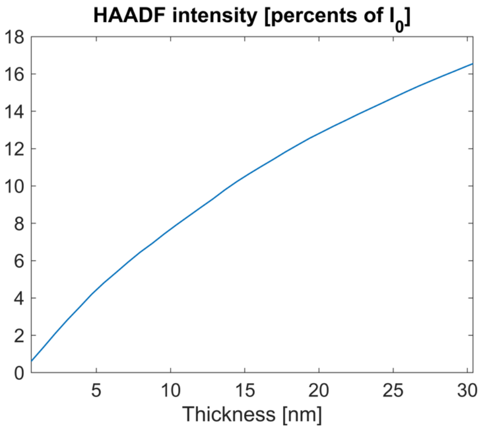

Figure 2.4: An HAADF signal calculated from the same simulation as the one used for figure 2.2. The result of averaging the image among the scan points is plotted as a function of thickness, thus displaying a monotonous dependence.

which allows the separation of the integrals:

$$\tilde{I}^D\left(\Delta\vec{q}\right) \approx \tilde{I}^{inc.}\left(\Delta\vec{q}\right) = \iint A\left(\vec{q}_{FP}\right) A\left(\vec{q}_{FP}+\Delta\vec{q}\right) e^{-i\left(\chi\left(\vec{q}_{FP}\right)-\chi\left(\vec{q}_{FP}+\Delta\vec{q}\right)\right)}\, d^2q_{FP} \iint D\left(\vec{q}_{det}\right)\tilde{T}\left(\vec{q}_{det}\right)\tilde{T}^*\left(\vec{q}_{det}-\Delta\vec{q}\right)\, d^2q_{det} \quad . \tag{2.11}$$

In this context, since:

$$\mathcal{F}^{-1}\left[\iint A\left(\vec{q}_{FP}\right) A\left(\vec{q}_{FP}+\Delta\vec{q}\right) e^{-i\left(\chi\left(\vec{q}_{FP}\right)-\chi\left(\vec{q}_{FP}+\Delta\vec{q}\right)\right)}\, d^2q_{FP}\right]\left(\vec{r}_s\right) = \mid \Xi\left(-\vec{r}_s\right)\mid^2 \quad , \tag{2.12}$$

by the same reasoning as used for equation 2.8, the incoherent intensity $I^{inc.}$ can be expressed by:

$$I^{inc.}\left(\vec{r}_s\right) = \mid \Xi\left(-\vec{r}_s\right)\mid^2 \otimes_{\vec{r}_s} T^{inc.}\left(\vec{r}_s\right) \quad , \tag{2.13}$$

with:

$$T^{inc.}\left(\vec{r}_s\right) = \mathcal{F}^{-1}\left[\iint D\left(\vec{q}_{det}\right)\tilde{T}\left(\vec{q}_{det}\right)\tilde{T}^*\left(\vec{q}_{det}-\Delta\vec{q}\right)\, d^2q_{det}\right]\left(\vec{r}_s\right) \quad . \tag{2.14}$$

Here, $\mid \Xi \mid^2$ translates the influence of the illumination on the incoherent transmission function $T^{inc.}$, which itself depends on the coherent transmission function T and the detector D. Through equations 2.2 and 2.13, the respective characteristics of Z-contrast and phase contrast can be compared. Whereas, in both cases, the detected intensity is obtained through the convolution of a specimen-dependent function by an illumination-dependent function, this convolution involves, for the latter, real quantities, while, for the former, it occurs between complex numbers. As a consequence, the incoherent imaging model permits the removal of phase effects and the potential separation of both contributions, post-recording [224, 225].

For further visualization, a simulated real-space-averaged HAADF intensity, obtained by summing electrons scattered to angles between 50 and 100 mrad, is plotted in figure 2.4 as a function of thickness. As expected, a monotonous variation against t is observed, with the considered average HAADF-STEM signal reaching close to 17 % of the incident intensity I_0 when

$t = 30\,\mathrm{nm}$. Whereas the thickness dependence has interests for materials characterization, done by comparing an experimental result to the simulated one, this relatively small proportion sheds light on another aspect of C-STEM methods: their limitation in terms of dose-efficiency. Indeed, while it was shown here that the HAADF imaging mode has many advantages, its employment may come at a high cost in terms of incident intensity, since only a relatively small part of it eventually contributes to the recorded signal. As a consequence, the imaging of beam-sensitive specimens is often made more difficult by the reliance on incoherent imaging and STEM in general [226, 227]. Furthermore, the strong dependence on Z leads to low contrast from light elements [228]. For those reasons, employing multiple C-STEM signals in a given experiment can be seen as a way to access multiple specimen parameters at once, with higher dose-efficiency.

2.1.5 First moment $\langle\vec{q}\rangle$ and differential phase contrast

Another use of the STEM technique consists of measuring the first moment in diffraction space $\langle\vec{q}\rangle = \iint \vec{q}\, I^S_{\vec{r}_s}(\vec{q})\; d^2q$. This quantity is proportional to the average momentum transfer from the specimen to the electron wave, as expressed by de Broglie's relation [50]. As it is equivalent to the Dirac product $\langle\Psi^S \mid \widehat{\vec{q}} \mid \Psi^S\rangle$, it satisfies:

$$\begin{aligned} \langle\Psi^S \mid \widehat{\vec{q}} \mid \Psi^S\rangle &= \frac{1}{i2\pi}\,\langle\Psi^{exit} \mid \widehat{\vec{\nabla}} \mid \Psi^{exit}\rangle \\ \iint \Psi^{S\,*}_{\vec{r}_s}(\vec{q})\;\vec{q}\,\Psi^S_{\vec{r}_s}(\vec{q})\; d^2q &= \frac{1}{i2\pi}\iint \Psi^{exit*}_{\vec{r}_s}(\vec{r})\;\widehat{\vec{\nabla}}_{\vec{r}}\,\Psi^{exit}_{\vec{r}_s}(\vec{r})\; d^2r \quad , \end{aligned} \tag{2.15}$$

where $\Psi^{exit}_{\vec{r}_s} = \widehat{M_V}\,\Xi(\vec{r}-\vec{r}_s)$ is the wave exiting the specimen when the probe is centered at the scan position $\vec{r}_s$, and $\widehat{\vec{\nabla}}_{\vec{r}} = \left[\frac{\widehat{\partial}}{\partial x}\,;\,\frac{\widehat{\partial}}{\partial y}\right]$. The relation 2.15 can otherwise be justified by the derivation property of the Fourier transform. Under the POA, $\Psi^{exit}_{\vec{r}_s}$ is given by:

$$\Psi^{exit}_{\vec{r}_s}(\vec{r}) = \Xi(\vec{r}-\vec{r}_s)\;T(\vec{r}) = \mathcal{F}^{-1}\left[A(\vec{q})\,e^{-i\chi(\vec{q})}e^{-i2\pi\vec{r}_s\cdot\vec{q}}\right](\vec{r})\;T(\vec{r}) \quad , \tag{2.16}$$

which results in:

$$\begin{aligned} i2\pi\,\langle\Psi^S \mid \widehat{\vec{q}} \mid \Psi^S\rangle &= \iint \Xi^*(\vec{r}-\vec{r}_s)\,T^*(\vec{r})\;\Big(T(\vec{r})\,\widehat{\vec{\nabla}}_{\vec{r}}\,\Xi(\vec{r}-\vec{r}_s) + \Xi(\vec{r}-\vec{r}_s)\,\widehat{\vec{\nabla}}_{\vec{r}}T(\vec{r})\Big)\; d^2r \\ &= \iint \mid T(\vec{r}) \mid^2\;\Xi^*(\vec{r}-\vec{r}_s)\,\widehat{\vec{\nabla}}_{\vec{r}}\,\Xi(\vec{r}-\vec{r}_s)\; d^2r + \iint \mid \Xi(\vec{r}-\vec{r}_s) \mid^2\;T^*(\vec{r})\,\widehat{\vec{\nabla}}_{\vec{r}}T(\vec{r})\; d^2r \quad . \end{aligned} \tag{2.17}$$

Because $\mid T(\vec{r}) \mid^2 = \mid e^{i\sigma\mu_p(\vec{r})} \mid^2 = 1$, the first component of equation 2.17 can be expanded as follows:

$$\begin{aligned} &\frac{1}{i2\pi}\iint \mid T(\vec{r}) \mid^2\;\Xi^*(\vec{r}-\vec{r}_s)\,\widehat{\vec{\nabla}}_{\vec{r}}\,\Xi(\vec{r}-\vec{r}_s)\; d^2r \\ &= \iint\iint\iint \vec{q}\,A(\vec{q})\,A(\vec{q}\,')\,e^{-i(\chi(\vec{q})-\chi(\vec{q}\,'))}e^{-i2\pi\vec{r}_s.(\vec{q}-\vec{q}\,')}\;e^{i2\pi\vec{r}.(\vec{q}-\vec{q}\,')}\,d^2q\,d^2q\,'\,d^2r \\ &= \iint\iint \vec{q}\,A(\vec{q})\,A(\vec{q}\,')\,e^{-i(\chi(\vec{q})-\chi(\vec{q}\,'))}e^{-i2\pi\vec{r}_s.(\vec{q}-\vec{q}\,')}\,\delta(\vec{q}-\vec{q}\,')\;d^2q\,d^2q\,' \\ &= \iint \vec{q}\,A(\vec{q})\; d^2q \\ &= \vec{0} \quad . \end{aligned} \tag{2.18}$$

Then, by using $\widehat{\vec{\nabla}}_{\vec{r}} T\left(\vec{r}\right) = i\sigma T\left(\vec{r}\right) \widehat{\vec{\nabla}}_{\vec{r}} \mu_p\left(\vec{r}\right)$, the derivation can be finalised as [229]:

$$\begin{aligned} \langle\vec{q}\rangle\left(\vec{r}_s\right) &= \langle\Psi^S \mid \widehat{\vec{q}} \mid \Psi^S\rangle = \frac{\sigma}{2\pi} \iint \mid \Xi\left(\vec{r} - \vec{r}_s\right) \mid^2 \mid T\left(\vec{r}\right) \mid^2 \, \widehat{\vec{\nabla}}_{\vec{r}} \mu_p\left(\vec{r}\right) \, d^2 r \\ &= \frac{\sigma}{2\pi} \mid \Xi\left(-\vec{r}_s\right) \mid^2 \otimes_{\vec{r}_s} \left(\widehat{\vec{\nabla}}_{\vec{r}_s} \mu_p\left(\vec{r}_s\right)\right) \quad . \end{aligned} \tag{2.19}$$

Through equation 2.19, it is thus shown that, under the POA, the first moment $\langle\vec{q}\rangle$ in diffraction space is proportional to the convolution of the real-space gradient of $\mu_p\left(\vec{r}_s\right)$ with a function equal to $\mid \Xi\left(-\vec{r}_s\right) \mid^2$. The same result can be obtained by using a quantum mechanical approach, with the Ehrenfest theorem as a starting point [74] or involving an expression based on the probability current of propagating electrons [230]. Here, it is also interesting to establish a parallel with the so-called phase contrast provided by CTEM imaging, which leads to a direct relation with $\mu_p\left(\vec{r}_s\right)$. By comparison, $\langle\vec{q}\rangle$ displays its real-space derivatives, though with a different influence from the illumination [229]. For this reason, this method is often referred to as differential phase contrast (DPC) [231, 232]. By further assuming the specimen to be non-magnetic, one can relate $\langle\vec{q}\rangle$ to the projected electric field $\vec{\epsilon}_p$ [233, 74], expressed in V, through:

$$\begin{aligned} \widehat{\vec{\nabla}}_{\vec{r}_s} \mu_p\left(\vec{r}_s\right) &= -\vec{\epsilon}_p\left(\vec{r}_s\right) \\ \langle\vec{q}\rangle\left(\vec{r}_s\right) &= -\frac{\sigma}{2\pi} \mid \Xi\left(-\vec{r}_s\right) \mid^2 \otimes_{\vec{r}_s} \vec{\epsilon}_p\left(\vec{r}_s\right) \quad . \end{aligned} \tag{2.20}$$

This quantity is itself related to the three-dimensional electric field distribution $\vec{\Theta}$, expressed in V.m^{-1}, by $\vec{\epsilon}_p\left(\vec{r}\right) = \int_0^t \vec{\Theta}\left(\vec{r}, \, z\right) dz$. Moreover, the projected charge density $\rho_p = \varepsilon_0 \widehat{\vec{\nabla}} \cdot \vec{\epsilon}_p$, expressed in C.m, can also be introduced. It is here obtained from the divergence ϱ of the first moment [234, 235], using the derivation rule of convolutions, by:

$$\begin{aligned} \varrho\left(\vec{r}_s\right) &= \widehat{\vec{\nabla}}_{\vec{r}_s} . \langle\vec{q}\rangle\left(\vec{r}_s\right) \\ &= -\frac{\sigma}{2\pi} \mid \Xi\left(-\vec{r}_s\right) \mid^2 \otimes_{\vec{r}_s} \left(\widehat{\vec{\nabla}}_{\vec{r}_s} \cdot \vec{\epsilon}_p\left(\vec{r}_s\right)\right) \\ &= -\frac{\sigma}{2\pi\varepsilon_0} \mid \Xi\left(-\vec{r}_s\right) \mid^2 \otimes_{\vec{r}_s} \rho_p\left(\vec{r}_s\right) \quad . \end{aligned} \tag{2.21}$$

Similarly to μ_p and ϵ_p, ρ_p is related to the three-dimensional charge density Ω, expressed in C, by $\rho_p\left(\vec{r}\right) = \int_0^t \Omega\left(\vec{r}, \, z\right) dz$. Finally, the integral φ of $\langle\vec{q}\rangle$ is related to the projected potential μ_p by:

$$\begin{aligned} \widehat{\vec{\nabla}}_{\vec{r}_s} \varphi(\vec{r}_s) &= \langle\vec{q}\rangle(\vec{r}_s) \\ \varphi(\vec{r}_s) &= \frac{\sigma}{2\pi} \mid \Xi\left(-\vec{r}_s\right) \mid^2 \otimes_{\vec{r}_s} \mu_p\left(\vec{r}_s\right) \quad . \end{aligned} \tag{2.22}$$

The Poisson equation finally leads to:

$$\begin{aligned} -\frac{1}{\varepsilon_0} \rho_p(\vec{r}_s) &= \widehat{\Delta}_{\vec{r}_s} \mu_p(\vec{r}_s) \\ \varrho(\vec{r}_s) &= \widehat{\Delta}_{\vec{r}_s} \varphi(\vec{r}_s) \quad , \end{aligned} \tag{2.23}$$

More information on the practical methods used to derive ϱ and φ from the first moment maps are available in section 2.3.

In its most common implementations, a DPC measurement is carried out by acquiring intensity in a ring-shaped detector, separated in at least four independent azimuthal sections, before

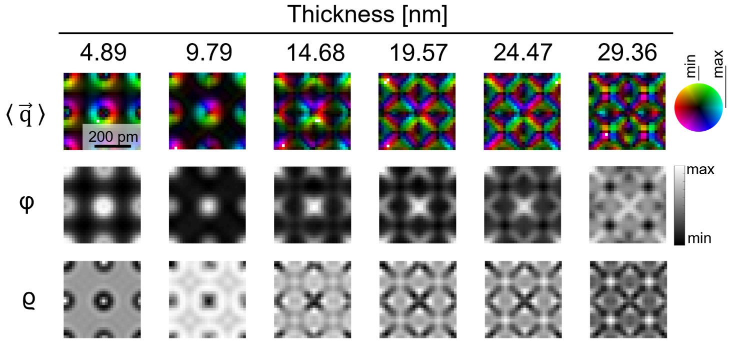

Figure 2.5: $\langle\vec{q}\rangle$, ϱ and φ are plotted for a selection of thicknesses, using the same simulation as for fig. 2.2. As it is a vector map, $\langle\vec{q}\rangle$ is given in colour wheel representation, with the colour representing the orientation of the vector at each scan point, and its modulus being represented by the brightness. $\langle\vec{q}\rangle$ was calculated by using an angular limit of 30 mrad.

subtracting the respective acquisitions of opposite sectors to one another [236]. The intensity difference can thus be expressed as a two-dimensional vector field, given as a function of the scan position. It is then in principle directly related to $\langle\vec{q}\rangle$, although not exactly proportional to it. Non-linearities of the recorded DPC signal against the first moment can occur, which are an inherent characteristic of the geometry of the employed segmented detectors [237, 238]. In this context, momentum-resolution is a more reliable solution for DPC measurements. Using the MR-STEM technique, $\langle\vec{q}\rangle$ is calculated directly by extracting the center of mass (CoM) in the recorded CBED patterns. Going beyond the approach based on the POA, the quantity $\langle\vec{q}\rangle$ can generally be understood as being made out of two distinct contributions [239]. The first arises from redistributions of intensity within the Ronchigram, an example of which is given in figure 2.2, and is due to real-space features which are smaller than, or have a size close to, the spatial extension of the probe [234]. As such, those redistributions are sensitive to high-frequency components of $\vec{\Theta}$, meaning atomic electric fields, and can be used for their measurement [233, 74]. The second contribution comes from lateral shifts of the primary beam itself, independently of its inner structure, and can be attributed to low-frequency components of $\vec{\Theta}$. This includes long-range electromagnetic fields [240, 241, 242] or specimen shape effects [243, 244]. In conditions where the POA is not realised, and where dynamical diffraction effects become impactful, the shift-induced and redistribution-induced variations of $\langle\vec{q}\rangle$ influence one another throughout the path of the wave through the material [239, 244].

An example of a first moment calculation is given in figure 2.5, alongside the divergence ϱ and integral φ, for a selection of thicknesses. There, $\langle\vec{q}\rangle$ is given in colour wheel representation, with the orientation of the vector being represented by the hue of the colour, and the modulus by its brightness. In the cases where $t \leq 10\,\mathrm{nm}$, the resulting images contain clear atomic contrast, with the vectors pointing toward the crystallographic columns, which thus act as sinks of momentum, consistently with the expected Coulomb interaction with the electrons. It is also worth noting that the vector modulus reaches a local minimum close to their centers. This is because, there, the spatial extension of the probe leads to a weighted summation of atomic electric field components pointing toward opposite directions. For higher thicknesses, however, the contrast decays, leading to a loss of the atomic features. This is due to the predominance of complex dynamical diffraction effects, which prevents the direct relation with ϵ_p. High contrast can nevertheless be recovered by means of adapting the probe focus to the thickness of the specimen [245, 246, 247, 193], as is further demonstrated in chapter 4. It can additionally be noted that, even without it consisting in a relation of proportionality, the sensitivity of $\langle \vec{q} \rangle$ to the electric fields remains and can still be employed for the investigation of polarization effects [248, 249], for instance.

2.1.6 Analysis based on multiple micrographs

As was shown previously in this section, the summation of the diffracted intensity in a detector permits the generation of a C-STEM micrograph. It is then dependent on both the angular range covered by the detector and the exact imaging conditions, in a manner that is conditioned by the dynamical nature of electron diffraction. In particular, the tuning of q_{min} and q_{max}, as well as of the focus f, can lead to specific relations of the signal to the structure and chemical composition of the specimen. In that regard, a possibility offered by the STEM technique is the recording of images in varying conditions, thus allowing to gain more information about the specimen than what would be possible from a single one. For this thesis, two particular examples of such methodologies are relevant: angle-resolved STEM (AR-STEM) and focal series STEM (FS-STEM).

First, in the AR-STEM technique, the intensity is summed within intervals of spatial frequency modulus, covered by ring-shaped detectors. In its original instance, this method was implemented using an iris placed over an HAADF detector [84, 250], thus allowing to record signals in a series of upper angular boundaries q_{max}. Subtractions among the distinct micrographs, combined with the availability of different camera lengths, then provide the capacity to generate intensities with flexibility of both q_{min} and q_{max}. In the work described in ref. [84], the variations of intensity due to changes in thickness and proportion of substitutional atoms, in the $\mathrm{Ge}_x\mathrm{Si}_{1-x}$/Si and $\mathrm{GaN}_x\mathrm{As}_{1-x}$/GaAs systems, were determined by simulations for a series of angular ranges. Such simulations were thus done while including static atomic displacements [251, 252, 253] due to local variations of composition, and to the differing covalent radii of substitutional atoms. In that manner, the extraction of those two distinct characteristics, independently from one another, could be demonstrated with atomic column resolution. Limitations were nevertheless reported in terms of simulation accuracy, in the low-angle region of reciprocal space. Those are due to effects not considered in the calculations, inelastic scattering in particular. This is, in fact, the initial motivation for the work presented in chapter 3. Whereas this set-up requires to perform a series of scans using different camera lengths and openings of the iris, MR-STEM grants more versatility in the generation of AR-STEM signals, through the use of virtual detectors and a single scan [186]. An example of this 4D-STEM-based approach is depicted in figure 2.6, using virtual ring detectors, each with 1 mrad of difference between the inner and outer acceptance angles. As can be seen from the micrographs, specific behaviors against variations of the specimen thickness t can be obtained for all different angular ranges, including those contained in the bright field and dark field regions.

Whereas AR-STEM is still a relatively recent technique, FS-STEM, commonly referred to as depth sectioning, is a well-established method consisting in the recording of C-STEM micrographs in a focal series. In the past years, it showed its interests for measuring the position of dopant and impurity atoms within a material [254, 161, 155], but also for observing dislocations and other defects [255, 256], as well as for detecting three-dimensional crystallographic strain [257]. More advanced applications include the retrieval of the large-scale shape of parti-

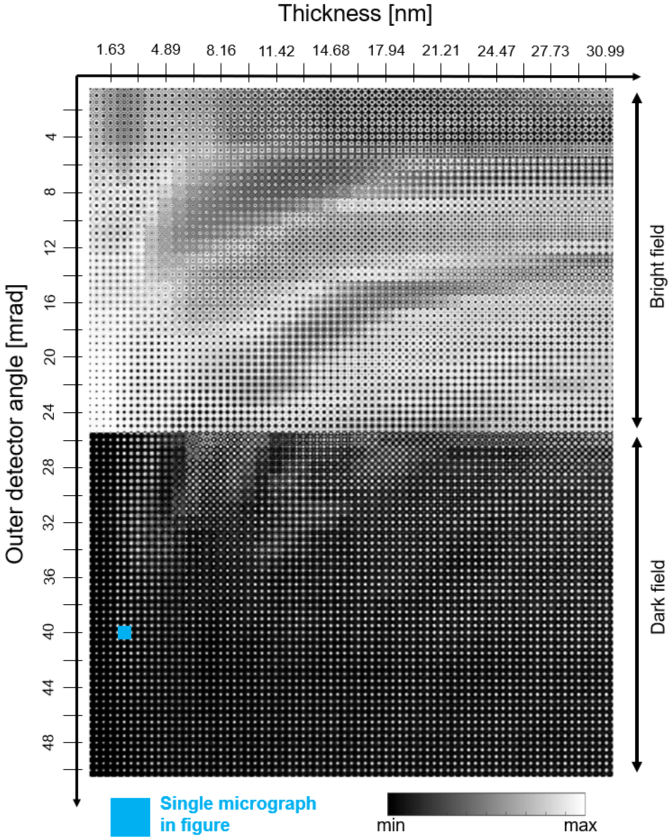

Figure 2.6: AR-STEM images are obtained from the same simulation as for fig. 2.2, at $\alpha = 25\,\text{mrad}$ and $U = 300\text{kV}$, by summing electrons within rings of 1 mrad. The resulting micrographs are depicted as a function of thickness and outer detector angle. Each single image is shown normalized between its particular minimum and maximum intensities.

cles [153, 258], sometimes by combination with further models, treatment methods and signals [259, 260, 261]. This list is of course not exhaustive. More generally, FS-STEM can be understood as providing a sensitivity to a selection of features along the vertical dimension, depending on the exact signal employed. When the vertical cross-over of the probe coincides with such features, this then results in specific, detector-dependent, contrast types. In practice, the exact focus-dependent behavior of different imaging modes needs to be determined by simulations in order to accurately decipher the role of channelling mechanisms. Furthermore, a useful metric for the limit of achievable resolution within the focus dimension is the depth of focus δz_{DOF}. This is nevertheless not necessarily the directing parameter since, for instance, the reconstruction of objects in the depth dimension is done in practice with a $\vec{q}$-dependent depth resolution [258], as is represented by a three-dimensional PSF.

2.2 Self-consistent calibration of diffraction coordinates

2.2.1 Mapping of reciprocal space in the presence of elliptical distortion

In order to generate virtual detectors employing specifically targeted spatial frequencies, it is necessary to attribute an accurate $\vec{q}$-coordinate to each pixel within the recorded frames. This rather fundamental aspect of the evaluation is critical, as a preliminary scaling of the scattering angles, on a given camera, is often not available. Furthermore, distortions of the CBED patterns can occur, owing to the imperfect optics making up the projection system of the instrument [262, 263]. The most accurate method to correct for this effect consists of recording a calibration diffraction pattern and register the locations of the diffraction spots it contains. Provided that the spatial frequencies where those spots occur are previously known from the crystal structure of the material employed, the collection of distances between them is a sufficient basis to fit the distortion function. Nevertheless, although this approach is in principle the most rigorous for reciprocal space mapping, the requirement of an initial calibration recording can be impractical. This is in part because it assumes that there are no differences between the distortion function occurring in the calibration diffraction pattern and the one affecting the CBED patterns detected afterwards. In practice, this is not necessarily true, owing to the rotation of features, at the level of the detector, due to changes in the focal lengths of different lenses. Furthermore, the camera length of the microscope, which controls the scaling of the diffraction pattern at the level of the detector plane, is usually employed as a free parameter to tune the sampling of the recorded frames and the maximum available scattering angle. There is then a need for a calibration for each of those camera lengths.

On the other hand, in the absence of an aberration-corrector below the specimen plane, and while considering only scattering angles of up to a few dozens of mrad, the distortion function remains dominated by a first-order elliptical component [264]. This means that, by assuming the aperture placed in the focal plane of the objective lens to be perfectly round, reciprocal space can be mapped from a single primary beam detected on the camera, by fitting its rim with an ellipse. Such a strategy can in turn be applied on a vacuum measurement, or directly on a PACBED pattern obtained from the MR-STEM data. The workflow of the method employed here for this purpose is illustrated in figure 2.7. The elliptical beam is first passed through a Sobel filter to enhance its edges, after which a first estimation of its shape is performed, by maximising the value of a summation done within an elliptical virtual ring detector. This initial estimation is followed by a cycling of two distinct fitting procedures, the first aiming at varying the center and radius of the ring, and the second the two components of a distortion vector. The succession of both those steps is done a number N_0 of times, while the fittings themselves consist of calculating and substracting a value of numerical gradient, respectively N_1 and N_2 times. As the integration is expected to reach its highest value when the virtual ring detector coincides perfectly with the edges of the beam, this is the state to which the process normally converges. Two examples of beam fitting done through this procedure are shown in figure 2.8, including a Pt [110] specimen and an α-In_2Se_3 specimen. It is noteworthy that, even in conditions where a considerable amount of diffuse scattering occurs around the central beam or where the distortion is relatively strong, the procedure still converges. As a last step, provided that the semi-convergence angle α has also been calibrated, the fitted beam can be used to map the complete set of $\vec{q}$ recorded.

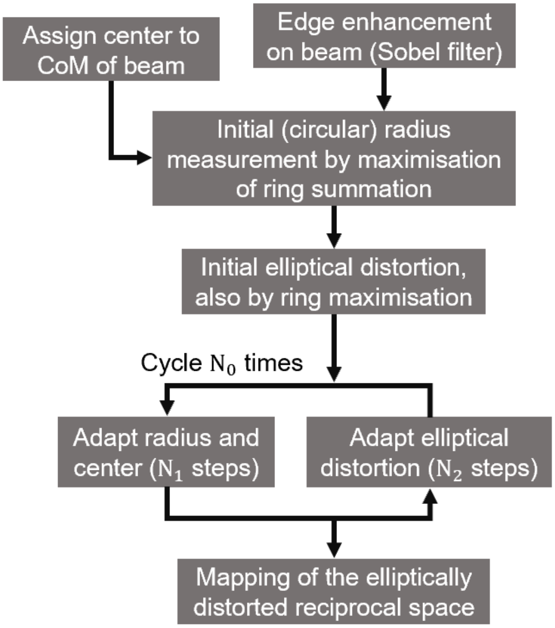

Figure 2.7: Workflow of the elliptical diffraction coordinates mapping method, using a measurement of the incident beam, or of the PACBED pattern.

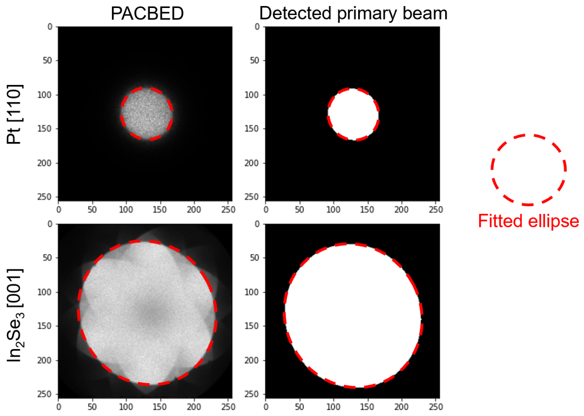

Figure 2.8: Two examples of beam shape retrieval, using a recorded PACBED and the method described by figure 2.7. This includes a bulk Pt specimen in [110] zone axis, in the presence of diffuse low-angle scattering due to amorphous carbon contamination, and an α-In_2Se_3 specimen in [001] zone axis orientation.

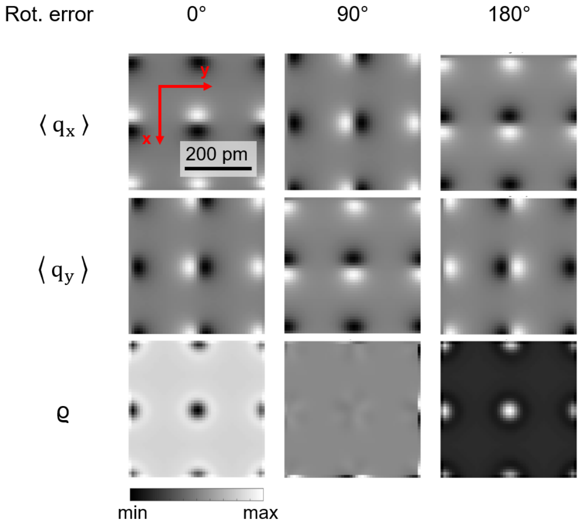

Figure 2.9: Demonstration of the influence of a rotation error of 0°, 90° and 180° on the x- and y-components of $\langle\vec{q}\rangle$, as well as on its divergence ϱ. For this calculation, a simulation of a 0.40782 nm-thick Au layer was imaged with $U = 300\,\mathrm{kV}$ and $\alpha = 25\,\mathrm{mrad}$. The convention taken for the x and y directions is highlighted in red.

2.2.2 Correction of the rotation error

Once the distortions have been accounted for, and a first calibration of diffraction space has been performed, a second important correction needs to be done which consists of a rotation of the camera axes $\vec{q}_{det}$ to match the directions of the scan window $\vec{r}_s$. When employing the microscope to record CBED patterns, a rotation error is common and leads to a wrong correspondence of real-space and diffraction space features. This is exemplified in figure 2.9, where the two components of the vectorial first moment, as well as its divergence, are depicted following rotations error of 0°, 90° and 180°, for a simulated Au layer. In the case where no error is present, the atomic columns act as sinks of momentum, thus leading to a negative divergence. This is consistent with the physical picture under which electrons are attracted by the positively-charged nuclei in the column. In the other hand, under an error of 180°, they appear as sources of momentum, which appears unphysical at first sight, although such an effect could be induced physically due to dynamical diffraction. A demonstration of this can be found in the chapter 4 of this thesis. Finally, in the 90° case, the divergence takes values close to zero, as the vector field erroneously appears to be purely rotational.

In order to correct for the rotation error, a method can be employed based on the use of the first moment $\langle\vec{q}\rangle$, also with no requirement for calibration data. From the vector map, the integral φ is first extracted along the $\vec{r}_s$ scan axes. Upon calculating its gradient, a vector field $\langle\vec{q}\rangle^{int\rightarrow grad}$ is obtained, which should be equal to the initial $\langle\vec{q}\rangle$, albeit with a slight damping of high-frequency features and scan noise. This equality is nevertheless broken if the axes $\vec{r}_s$ are not well aligned with $\vec{q}_{det}$. The strategy for finding the right rotation of $\vec{q}_{det}$ thus consists of minimizing the sum of squared difference between $\langle\vec{q}\rangle^{int\rightarrow grad}$ and $\langle\vec{q}\rangle$ [265], while rotating

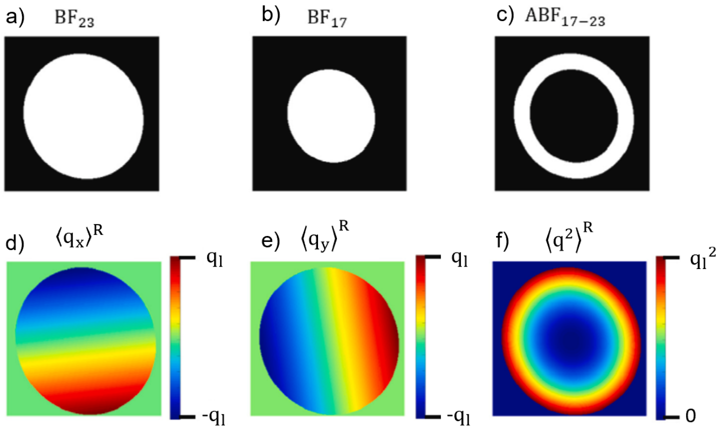

Figure 2.10: Depiction of a collection of virtual detectors. a) Bright field covering the entire primary beam, b) bright field covering angles up to 17 mrad, c) annular bright field covering the outer 6 mrad of the primary beam, d,e) the two components of the raw first moment with an angular cut-off of 27 mrad, f) second moment with the same cut-off.

the first moment before the successive integration and derivation steps. A first limit of this method is found in the existence of a second minimization can be reached when the vector map is rotated by 180° more than the correct value. As is shown in figure 2.9, this results in atomic columns appearing as sources, rather than sinks, of momentum, while still satisfying the criterium of $\langle \vec{q} \rangle^{int \to grad} = \langle \vec{q} \rangle$.

Here, it is noteworthy that recent results [266] also suggested that when specific crystallographic features occur in a thick enough specimen, e.g. geometric phase effects [267], a natural curl component may be induced in the first moment signal. This can potentially lead to errors when using the correction approach proposed here, since the succession of integration and derivation suppresses the curl component. Nevertheless, cases where such considerations become important were not encountered in the work presented in this thesis and are generally outside of common applications.

2.2.3 Signal extraction by virtual detectors

Once the diffraction coordinates have been accurately mapped, it becomes straightforward to generate a collection of virtual detectors covering tailored angular regions. This in turn permits the extraction of C-STEM signals from the MR-STEM dataset, according to equation 2.4, although this then consists of a discrete summation of $\vec{q}$ coordinates, rather than a continuous one. An example is given in figure 2.10 for the diffraction space calibration presented in figure 2.8, specifically the α-In_2Se_3 case, with a semi-convergence angle of 23 mrad. This includes, in 2.10.a,b, the detectors for two BF signals, the first summing electrons up to 23 mrad, meaning the full primary beam, and the second up to 17 mrad. An ABF case equal to their difference is depicted as well in fig. 2.10.c. Furthermore, the two components of the vectorial detector $\vec{q}\,D\,(\vec{q})$, used for the calculation of $\langle \vec{q} \rangle$, are plotted in 2.10.d,e. Finally, the scalar second moment $\langle q^2 \rangle$, which is discussed in section 2.4, is obtained via $q^2\,D\,(\vec{q})$, as shown in fig. 2.10.f.

Although the virtual detectors presented here all possess an annular geometry, in relation to existing hardware-based detection geometries, it is clear that STEM signals can in principle be generated in a wide variety of manners, based on the available diffraction dataset.

2.3 Calculation, derivation and integration of the first moment $\langle\vec{q}\rangle$

2.3.1 Extraction from the MR-STEM data

Going back to arguments given in section 2.1 on the first moment signal, it is important to note that the actual measurement of $\langle\vec{q}\rangle$ was, so far in this thesis, implied as being done through an integration of angular space toward infinity. In practice, and as was already implied by figure 2.10, when extracting this quantity from the MR-STEM data, the summation can only be done up to a spatial frequency limit q_l which cannot exceed the maximum extent of the camera. As a consequence, not the entirety of the incident intensity I_0 is included in the calculation. This means that, for an accurate, standardless, comparison to a simulation, there is a need for a normalisation to the total amount of contributing electrons. The first moment is thus obtained by:

$$\langle\vec{q}\rangle\left(\vec{r}_s\right) = \frac{\langle\vec{q}\rangle^{\mathrm{R}}\left(\vec{r}_s\right)}{\sum\limits_{\vec{q}} D\left(\vec{q}\right) I^S_{\vec{r}_s}\left(\vec{q}\right)} \quad , \tag{2.24}$$

where $\langle\vec{q}\rangle^{\mathrm{R}}$ is a raw counterpart, given by:

$$\langle\vec{q}\rangle^{\mathrm{R}}\left(\vec{r}_s\right) = \sum_{\vec{q}} \vec{q}\, D\left(\vec{q}\right) I^S_{\vec{r}_s}\left(\vec{q}\right) \quad . \tag{2.25}$$

D is then equal to 1 for $\mid \vec{q} \mid \leq q_l$ and 0 otherwise. Although this approach does not fulfill the physical expectation of an integration toward infinity, it is considered sufficient to provide differential phase contrast. This is because $\langle\vec{q}\rangle$ rapidly converges with an increasing q_l, as long as it is taken a few mrad above the radius of the primary beam [234].

2.3.2 Iterative finite differences

Within the work presented in this thesis, the divergence ϱ and integral φ of the first moment vector map $\langle\vec{q}\rangle$ were obtained through a five-point-stencil calculation scheme involving an iterative step [193]. The derivation of this method relies on the explicit expression: $\langle\vec{q}\rangle(x,y) = [\,\langle q_x\rangle(x,y)\,;\,\langle q_y\rangle(x,y)\,]$, and:

$$\begin{aligned} \varrho(x,y) &= \frac{\partial\langle q_x\rangle(x,y)}{\partial x} + \frac{\partial\langle q_y\rangle(x,y)}{\partial y} \\ [\,\langle q_x\rangle(x,y)\,;\,\langle q_y\rangle(x,y)(x,y)\,] &= \left[\frac{\partial\varphi(x,y)}{\partial x}\,;\,\frac{\partial\varphi(x,y)}{\partial y}\right] \quad . \end{aligned} \tag{2.26}$$

Using finite differences, the derivation of $[\,\langle q_x\rangle(x,y)\,;\,\langle q_y\rangle(x,y)\,]$ by $[\,x\,;\,y\,]$ can then be approximated by:

$$\begin{aligned}\frac{\partial\langle q_x\rangle(x,y)}{\partial x} &= \frac{\langle q_x\rangle(x+\delta x,y)-\langle q_x\rangle(x-\delta x,y)}{2\delta x}\\ \frac{\partial\langle q_y\rangle(x,y)}{\partial y} &= \frac{\langle q_y\rangle(x,y+\delta y)-\langle q_y\rangle(x,y-\delta y)}{2\delta y} \quad .\end{aligned} \tag{2.27}$$

In that manner, and while identifying $\delta r = \delta x = \delta y$ to the pixel size of the scan window, the extraction of ϱ can be done in one step by using:

$$\rho = \frac{\langle q_x\rangle(x+\delta r,y)-\langle q_x\rangle(x-\delta r,y)+\langle q_y\rangle(x,y+\delta r)-\langle q_y\rangle(x,y-\delta r)}{2\delta r} \quad . \tag{2.28}$$

The calculation of φ is performed afterward by using the Laplacian relation:

$$\varrho(x,y) = \Delta\varphi(x,y) = \frac{\partial^2\varphi(x,y)}{\partial x^2} + \frac{\partial^2\varphi(x,y)}{\partial y^2} \quad , \tag{2.29}$$

with the second-order derivatives being given by:

$$\begin{aligned}\frac{\partial^2\varphi(x,y)}{\partial x^2} &= \frac{\varphi(x+\delta x,y)-2\varphi(x,y)+\varphi(x-\delta x,y)}{\delta x^2}\\ \frac{\partial^2\varphi(x,y)}{\partial y^2} &= \frac{\varphi(x,y+\delta y)-2\varphi(x,y)+\varphi(x,y-\delta y)}{\delta y^2} \quad .\end{aligned} \tag{2.30}$$

By combination of those formulas, the following expression is reached:

$$\varrho(x,y) = \frac{\varphi(x+\delta r,y)+\varphi(x-\delta r,y)+\varphi(x,y+\delta r)+\varphi(x,y-\delta r)-4\varphi(x,y)}{\delta r^2} \quad . \tag{2.31}$$

$\varphi(x,y)$ can thus be obtained from the previously generated $\varrho(x,y)$ by iterating:

$$\varphi^n(x,y) = \frac{\varphi^{n-1}(x+\delta r,y)+\varphi^{n-1}(x-\delta r,y)+\varphi^{n-1}(x,y+\delta r)+\varphi^{n-1}(x,y-\delta r)-\delta r^2\varrho(x,y)}{4} \tag{2.32}$$

an arbitrary number N of times, with the initial conditions $\left[\,\varphi^0(x,y)=0\,;\,n=1\,\right]$. The first and last pixels along the two dimensions of the scan window are furthermore set to a value of zero at each iteration. This is done to impose a Dirichlet boundary condition to the calculation, which otherwise leads to artefacts.

2.3.3 Fourier integration

An alternative integration method for the vector map $\langle\vec{q}\rangle$ is based on the Fourier derivation theorem. Its derivation goes as follows:

$$\begin{aligned} i2\pi\vec{q}\,\mathcal{F}\left[\varphi\left(\vec{r}_s\right)\right](\vec{q}) &= \mathcal{F}\left[\langle\vec{q}\rangle\left(\vec{r}_s\right)\right](\vec{q})\\ i2\pi q^2\,\mathcal{F}\left[\varphi\left(\vec{r}_s\right)\right](\vec{q}) &= \vec{q}\,.\,\mathcal{F}\left[\langle\vec{q}\rangle\left(\vec{r}_s\right)\right](\vec{q})\\ \varphi\left(\vec{r}_s\right) &= \mathcal{F}^{-1}\left[\frac{\vec{q}\,.\,\mathcal{F}\left[\,\langle\vec{q}\rangle\left(\vec{r}_s\right)\right](\vec{q})}{i2\pi q^2}\right]\left(\vec{r}_s\right) \quad .\end{aligned} \tag{2.33}$$

In parallel, the divergence ϱ may be obtained by:

$$\begin{aligned}\mathcal{F}\left[\varrho\left(\vec{r}_s\right)\right](\vec{q}) &= i2\pi\vec{q}\,.\,\mathcal{F}\left[\langle\vec{q}\rangle\left(\vec{r}_s\right)\right](\vec{q})\\ \varrho\left(\vec{r}_s\right) &= \mathcal{F}^{-1}\left[\,i2\pi\vec{q}\,.\,\mathcal{F}\left[\,\langle\vec{q}\rangle\left(\vec{r}_s\right)\right](\vec{q})\,\right]\left(\vec{r}_s\right) \quad .\end{aligned} \tag{2.34}$$

It is interesting to note that, through the use of an FFT, this integration method imposes a boundary condition to the calculation which consist of an imposed periodicity.

2.4 Scalar second moment $\langle q^2 \rangle$

2.4.1 Calculation of $\langle q^2 \rangle$ in diffraction space

The scalar second moment $\langle q^2 \rangle$ in diffraction space was introduced in the field in reference [193], and thus as part of the work presented in this thesis. It can be obtained in a manner similar to $\langle \vec{q} \rangle$. Following the same arguments as those given in section 2.1, this quantity is equivalent to the product $\langle \Psi^S \mid \widehat{\vec{q}}.\widehat{\vec{q}} \mid \Psi^S \rangle$, and:

$$\begin{aligned} \langle \Psi^S \mid \widehat{\vec{q}}.\widehat{\vec{q}} \mid \Psi^S \rangle &= -\frac{1}{4\pi^2} \langle \Psi^{exit} \mid \widehat{\Delta} \mid \Psi^{exit} \rangle \\ \iint \Psi^{S\,*}_{\vec{r}_s}\left(\vec{q}\right)\, \vec{q}\cdot\vec{q}\, \Psi^{S}_{\vec{r}_s}\left(\vec{q}\right)\, d^2q &= -\frac{1}{4\pi^2} \iint \Psi^{exit*}_{\vec{r}_s}\left(\vec{r}\right)\, \widehat{\Delta}_{\vec{r}}\, \Psi^{exit}_{\vec{r}_s}\left(\vec{r}\right)\, d^2r \quad , \end{aligned} \tag{2.35}$$

Using the POA and $\Psi^{exit}_{\vec{r}_s}\left(\vec{r}\right) = \Xi\left(\vec{r}-\vec{r}_s\right)\, T\left(\vec{r}\right)$, this expression can be expanded such that:

$$\begin{aligned} &-4\pi^2 \langle \Psi^S \mid \widehat{\vec{q}}.\widehat{\vec{q}} \mid \Psi^S \rangle = \iint \Xi^*\left(\vec{r}-\vec{r}_s\right) T^*\left(\vec{r}\right)\, \widehat{\vec{\nabla}}_{\vec{r}}. \left(T\left(\vec{r}\right) \widehat{\vec{\nabla}}_{\vec{r}} \Xi\left(\vec{r}-\vec{r}_s\right) + \Xi\left(\vec{r}-\vec{r}_s\right) \widehat{\vec{\nabla}}_{\vec{r}} T\left(\vec{r}\right) \right) d^2r \\ &= \iint \Xi^*\left(\vec{r}-\vec{r}_s\right) T^*\left(\vec{r}\right) \left(T\left(\vec{r}\right) \widehat{\Delta}_{\vec{r}} \Xi\left(\vec{r}-\vec{r}_s\right) + 2\widehat{\vec{\nabla}}_{\vec{r}} \Xi\left(\vec{r}-\vec{r}_s\right) .\widehat{\vec{\nabla}}_{\vec{r}} T\left(\vec{r}\right) + \Xi\left(\vec{r}-\vec{r}_s\right) \widehat{\Delta}_{\vec{r}} T\left(\vec{r}\right) \right) d^2r \\ &= 2\iint \left(\Xi^*\left(\vec{r}-\vec{r}_s\right) \widehat{\vec{\nabla}}_{\vec{r}} \Xi\left(\vec{r}-\vec{r}_s\right) \right) . \left(T^*\left(\vec{r}\right) \widehat{\vec{\nabla}}_{\vec{r}} T\left(\vec{r}\right) \right) d^2r \\ &\quad + \iint \mid \Xi\left(\vec{r}-\vec{r}_s\right) \mid^2\ T^*\left(\vec{r}\right) \widehat{\Delta}_{\vec{r}} T\left(\vec{r}\right)\, d^2r \\ &\quad + \iint \Xi^*\left(\vec{r}-\vec{r}_s\right) \widehat{\Delta}_{\vec{r}} \Xi\left(\vec{r}-\vec{r}_s\right)\ \mid T\left(\vec{r}\right) \mid^2\ d^2r \quad . \end{aligned} \tag{2.36}$$

The first term of $\langle \Psi^S \mid \widehat{\vec{q}}.\widehat{\vec{q}} \mid \Psi^S \rangle$ contained in equation 2.36 can be expanded as follows:

$$\begin{aligned} &-\frac{1}{2\pi^2} \iint \left(\Xi^*\left(\vec{r}-\vec{r}_s\right) \widehat{\vec{\nabla}}_{\vec{r}} \Xi\left(\vec{r}-\vec{r}_s\right) \right) . \left(T^*\left(\vec{r}\right) \widehat{\vec{\nabla}}_{\vec{r}} T\left(\vec{r}\right) \right) d^2r \\ &= -\frac{1}{2\pi^2} \iint \left(i2\pi \iint \iint \vec{q}\, A\left(\vec{q}\right) A\left(\vec{q}\,'\right) e^{-i(\chi(\vec{q})-\chi(\vec{q}\,'))} e^{-i2\pi\vec{r}_s.(\vec{q}-\vec{q}\,')}\, e^{i2\pi\vec{r}.(\vec{q}-\vec{q}\,')}\, d^2q\, d^2q\,' \right) \\ &\qquad . \left(i\sigma \mid T\left(\vec{r}\right) \mid^2 \widehat{\vec{\nabla}}_{\vec{r}} \mu_p\left(\vec{r}\right) \right) d^2r \\ &= \frac{\sigma}{\pi} \iint \iint A\left(\vec{q}\right) A\left(\vec{q}\,'\right) e^{-i(\chi(\vec{q})-\chi(\vec{q}\,'))} e^{-i2\pi\vec{r}_s.(\vec{q}-\vec{q}\,')}\, \vec{q}\,.\, \mathcal{F}\left[\widehat{\vec{\nabla}}_{\vec{r}} \mu_p\left(\vec{r}\right) \right] \left(\vec{q}\,' - \vec{q} \right)\, d^2q\, d^2q\,' \\ &= \frac{\sigma}{\pi} \iint \iint A\left(\vec{q}\right) A\left(\vec{q}\,'\right) e^{-i(\chi(\vec{q})-\chi(\vec{q}\,'))} e^{-i2\pi\vec{r}_s.(\vec{q}-\vec{q}\,')}\, \vec{q}\,.\, \left(i2\pi \left(\vec{q}\,' - \vec{q} \right) \tilde{\mu}_p\left(\vec{q}\,' - \vec{q} \right) \right)\, d^2q\, d^2q\,' \quad . \end{aligned} \tag{2.37}$$

By assigning $\vec{q}\,' = \vec{q} + \Delta\vec{q}$, in a manner similar to what was done in equation 2.8, one can go further by:

$$\begin{aligned}
&(2.37)\\
&= \frac{\sigma}{\pi} \iint \iint A(\vec{q})\, A(\vec{q}+\Delta\vec{q})\, e^{-i(\chi(\vec{q})-\chi(\vec{q}+\Delta\vec{q}))} e^{i2\pi\vec{r}_s.\Delta\vec{q}}\ (i2\pi\vec{q}\,.\,\Delta\vec{q})\ \tilde{\mu}_p(\Delta\vec{q})\ d^2q\, d^2\Delta q\\
&= \frac{\sigma}{\pi} \mathcal{F}^{-1}\left[i2\pi\Delta\vec{q}\,.\left(\iint \vec{q}\, A(\vec{q})\, A(\vec{q}+\Delta\vec{q})\, e^{-i(\chi(\vec{q})-\chi(\vec{q}+\Delta\vec{q}))}\, d^2q \right) \tilde{\mu}_p(\Delta\vec{q}) \right](\vec{r}_s) \qquad (2.38)\\
&= \frac{\sigma}{\pi} \left(\widehat{\vec{\nabla}}_{\vec{r}_s}\,.\,\mathcal{F}^{-1}\left[\iint \vec{q}\, A(\vec{q})\, A(\vec{q}+\Delta\vec{q})\, e^{-i(\chi(\vec{q})-\chi(\vec{q}+\Delta\vec{q}))}\, d^2q \right](\vec{r}_s) \right) \otimes_{\vec{r}_s} \mu_p(\vec{r}_s) \quad ,
\end{aligned}$$

with:

$$\begin{aligned}
&\widehat{\vec{\nabla}}_{\vec{r}_s}\,.\,\mathcal{F}^{-1}\left[\iint \vec{q}\, A(\vec{q})\, A(\vec{q}+\Delta\vec{q})\, e^{-i(\chi(\vec{q})-\chi(\vec{q}+\Delta\vec{q}))}\, d^2q \right](\vec{r}_s)\\
&= \widehat{\vec{\nabla}}_{\vec{r}_s}\,.\left(\Xi^*(-\vec{r}_s) \left(\frac{1}{-i2\pi} \widehat{\vec{\nabla}}_{\vec{r}_s} \Xi(-\vec{r}_s) \right) \right)\\
&= i\frac{1}{2\pi} \left(\widehat{\vec{\nabla}}_{\vec{r}_s} \Xi^*(-\vec{r}_s)\,.\,\widehat{\vec{\nabla}}_{\vec{r}_s} \Xi(-\vec{r}_s) + \Xi^*(-\vec{r}_s)\, \widehat{\Delta}_{\vec{r}_s} \Xi(-\vec{r}_s) \right)\\
&= i\frac{1}{2\pi} \left(\frac{1}{2} \left(\widehat{\Delta}_{\vec{r}_s} \mid \Xi(-\vec{r}_s) \mid^2 - \Xi(-\vec{r}_s)\, \widehat{\Delta}_{\vec{r}_s} \Xi^*(-\vec{r}_s) - \Xi^*(-\vec{r}_s)\, \widehat{\Delta}_{\vec{r}_s} \Xi(-\vec{r}_s) \right) + \Xi^*(-\vec{r}_s)\, \widehat{\Delta}_{\vec{r}_s} \Xi(-\vec{r}_s) \right) \quad .
\end{aligned} \tag{2.39}$$

Using the expression found in 2.39, and the derivation property of convolutions, the expansion of the first term can be finalized by:

$$\begin{aligned}
&(2.37)\\
&= i\frac{\sigma}{4\pi^2} \left(\widehat{\Delta}_{\vec{r}_s} \mid \Xi(-\vec{r}_s) \mid^2 + \Xi^*(-\vec{r}_s)\, \widehat{\Delta}_{\vec{r}_s} \Xi(-\vec{r}_s) - \Xi(-\vec{r}_s)\, \widehat{\Delta}_{\vec{r}_s} \Xi^*(-\vec{r}_s) \right) \otimes_{\vec{r}_s} \mu_p(\vec{r}_s)\\
&= i\frac{\sigma}{4\pi^2} \left(\mid \Xi(-\vec{r}_s) \mid^2 \otimes_{\vec{r}_s} \widehat{\Delta}_{\vec{r}_s} \mu_p(\vec{r}_s) + i2\,\mathrm{Im}\left[\Xi^*(-\vec{r}_s)\, \widehat{\Delta}_{\vec{r}_s} \Xi(-\vec{r}_s) \right] \otimes_{\vec{r}_s} \mu_p(\vec{r}_s) \right) \quad ,
\end{aligned} \tag{2.40}$$

Pursuing the expansion of equation 2.36, the second term is equal to:

$$\begin{aligned}
&-\frac{1}{4\pi^2} \iint \mid \Xi(\vec{r}-\vec{r}_s) \mid^2\ T^*(\vec{r})\, \widehat{\Delta}_{\vec{r}} T(\vec{r})\ d^2r\\
&= -\frac{1}{4\pi^2} \iint \mid \Xi(\vec{r}-\vec{r}_s) \mid^2\ T^*(\vec{r}) \left(-\sigma^2 T(\vec{r}) \mid \widehat{\vec{\nabla}}_{\vec{r}} \mu_p(\vec{r}) \mid^2 + i\sigma T(\vec{r})\, \widehat{\Delta}_{\vec{r}} \mu_p(\vec{r}) \right) d^2r\\
&= \frac{\sigma}{4\pi^2} \iint \mid \Xi(\vec{r}-\vec{r}_s) \mid^2 \left(\sigma \mid \widehat{\vec{\nabla}}_{\vec{r}} \mu_p(\vec{r}) \mid^2 - i\widehat{\Delta}_{\vec{r}} \mu_p(\vec{r}) \right) d^2r\\
&= \frac{\sigma}{4\pi^2} \mid \Xi(-\vec{r}_s) \mid^2 \otimes_{\vec{r}_s} \left(\sigma \mid \widehat{\vec{\nabla}}_{\vec{r}_s} \mu_p(\vec{r}_s) \mid^2 - i\widehat{\Delta}_{\vec{r}_s} \mu_p(\vec{r}_s) \right) \quad ,
\end{aligned} \tag{2.41}$$

and the third term to:

$$\begin{aligned}
&-\frac{1}{4\pi^2}\iint \Xi^*\left(\vec{r}-\vec{r}_s\right)\widehat{\Delta}_{\vec{r}}\,\Xi\left(\vec{r}-\vec{r}_s\right)\ \mid T\left(\vec{r}\right)\mid^2\ d^2r \\
&= -\frac{1}{4\pi^2}\iint\left(-4\pi^2\iint\iint q^2\,A\left(\vec{q}\right)A\left(\vec{q}\,'\right)e^{-i(\chi(\vec{q})-\chi(\vec{q}\,'))}e^{-i2\pi\vec{r}_s.(\vec{q}-\vec{q}\,')}\,e^{i2\pi\vec{r}.(\vec{q}-\vec{q}\,')}\,d^2q\,d^2q\,'\right)d^2r \\
&= \iint\mathcal{F}^{-1}\left[\iint q^2\,A\left(\vec{q}\right)A\left(\vec{q}+\Delta\vec{q}\right)e^{-i(\chi(\vec{q})-\chi(\vec{q}+\Delta\vec{q}))}\,d^2q\,e^{-i2\pi\vec{r}.\Delta\vec{q}}\right]\left(\vec{r}_s\right)\,d^2r \\
&= \mathcal{F}^{-1}\left[\iint q^2\,A\left(\vec{q}\right)A\left(\vec{q}+\Delta\vec{q}\right)e^{-i(\chi(\vec{q})-\chi(\vec{q}+\Delta\vec{q}))}\,d^2q\,\delta\left(\Delta\vec{q}\right)\right]\left(\vec{r}_s\right) \\
&= \iint q^2\,A\left(\vec{q}\right)\,d^2q \\
&= \frac{\pi {q_A}^4}{2} \quad .
\end{aligned} \tag{2.42}$$

Upon combining the three terms, a final expression for the scalar second moment is obtained:

$$\begin{aligned}
\langle q^2\rangle\left(\vec{r}_s\right) = \langle\Psi^S\mid\widehat{\vec{q}}.\widehat{\vec{q}}\mid\Psi^S\rangle = &\frac{\pi {q_A}^4}{2} \\
&+\frac{\sigma^2}{4\pi^2}\ \mid\Xi\left(-\vec{r}_s\right)\mid^2\ \otimes_{\vec{r}_s}\ \mid\widehat{\vec{\nabla}}_{\vec{r}_s}\,\mu_p\left(\vec{r}_s\right)\mid^2 \\
&-\frac{\sigma}{2\pi^2}\ \mathrm{Im}\left[\Xi^*\left(-\vec{r}_s\right)\widehat{\Delta}_{\vec{r}_s}\Xi\left(-\vec{r}_s\right)\right]\ \otimes_{\vec{r}_s}\ \mu_p\left(\vec{r}_s\right) \quad .
\end{aligned} \tag{2.43}$$

From equation 2.43, $\langle q^2\rangle$ can thus be expected to carry a dependence to both the projected potential μ_p and the squared modulus of its real-space gradient, though both those contributions are affected differently by the illumination characteristics. As a consequence, in conditions where the POA holds, this signal would provide a mixture of phase contrast and differential phase contrast. In practice, its extraction is performed using a camera, and thus a limited angular range. In a manner similar to the first moment, the scalar second moment $\langle q^2\rangle$ is then obtained by:

$$\begin{aligned}
\langle q^2\rangle(\vec{r}_s) &= \frac{\langle q^2\rangle^{\mathrm{R}}(\vec{r}_s)}{\sum\limits_{\vec{q}} D\left(\vec{q}\right)\,I_{\vec{r}_s}\left(\vec{q}\right)} \\
\langle q^2\rangle^{\mathrm{R}}(\vec{r}_s) &= \sum_{\vec{q}} q^2\,D\left(\vec{q}\right)\,I_{\vec{r}_s}\left(\vec{q}\right) \quad .
\end{aligned} \tag{2.44}$$

Whereas the first moment converges rapidly to the value it would have for an integration toward infinite spatial frequency [234], this is not true for the scalar second moment [193]. Indeed, as is shown in the next two subsections, the necessity of calculating $\langle q^2\rangle$ with an angular cut-off q_l may be problematic, as the signal diverges with an increasing q_l, at least under the limit of spatial frequencies which are accessible in a simulation. As such, the properties derived in equation 2.43 cannot be strictly expected from the recorded signal. Nevertheless, a secondary consequence of this divergence is found in the fact that the dependences to the specimen and illumination parameters can be tuned by precise assignation of the cut-off angle, as this parameter determines the amount of incoherently scattered electrons contributing to the signal.

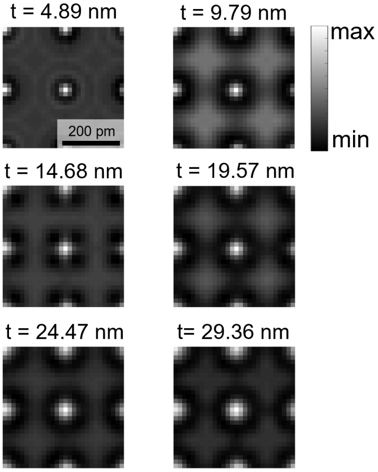

Figure 2.11: The scalar second moment $\langle q^2 \rangle$ is depicted for a selection of thicknesses, using the same simulation as for figure 2.2. The quantity was calculated by using an angular limit of 30 mrad.

An example of a second moment calculation is depicted in figure 2.11, using the same Au simulation as employed in section 2.1. An interpretable image with atomic contrast is obtained for all thicknesses depicted, without the complications seen in figure 2.5 for the vectorial first moment. It is noteworthy that, for this particular calculation, an angular cut-off of 30 mrad was chosen, thus only 5 mrad above α. As a consequence, most of the electrons contributing to the depicted micrographs are coherently scattered by the specimen. An in-depth presentation of how the real-space features vary, both along the thickness and focus dimensions, as a function of q_l is available in chapter 4.

2.4.2 Prediction of convergence properties by Mott scattering

Whereas extensive simulations are needed to calculate the angular distribution of scattered electrons quantitatively, abstract analytical considerations can often be employed to provide some understanding for some of the more general aspects of the scattered intensity. Here, an interest is taken in the convergence of $\langle q^2 \rangle_{q_l}$ for a spatial frequency cut-off $q_l \to \infty$, and thus for an increasingly dominating incoherent high-angle component made of TDS. In those conditions, the scattered intensity can be regarded as being equal to the incoherent summation over single atomic scattering events, following arguments provided in section 2.1. As a consequence, it is sufficient to consider electron scattering by a single atom to obtain the main characteristics of $\langle q^2 \rangle_{q_l \to \infty}$. As was explained in the last chapter, the elastic scattering of electrons by an atom can be expressed by using the Mott-Bethe relationship, given in equation 1.29. For high-angle scattering, which is composed mostly of the interaction with the unscreened nuclear potential, the term f_X, being the Fourier transform of the electronic charge density, can be neglected. What remains is then the simpler Mott relation [135], expressing the scattering

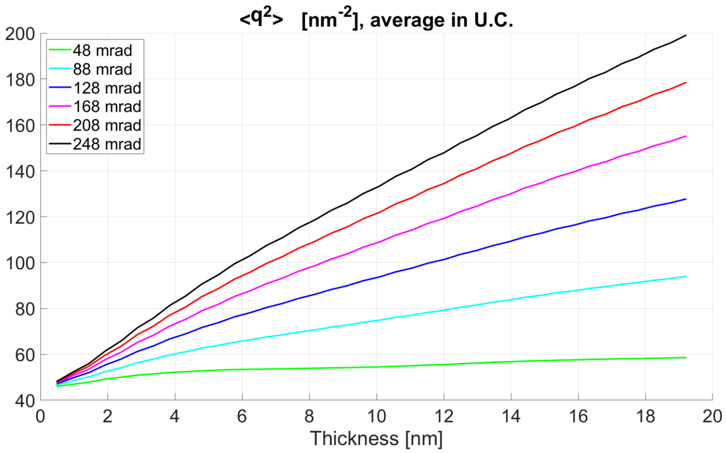

Figure 2.12: Result of the real-space average of $\langle q^2 \rangle$ images, within one projected unit cell, for increasing specimen thickness. The measurement was done with a varying cut-off angle.

factor for electrons toward three-dimensional spatial frequencies $\vec{Q}$:

$$f_{e^-}\left(\vec{Q}\right) = \frac{eZ}{4\pi^2\epsilon_0 Q^2} \quad . \tag{2.45}$$

Including only single atomic events, f_{e^-} can be projected in the two-dimensional coordinate $\vec{q}$. By considering the numerical aperture radius q_A to be sufficiently smaller than q_l, the illumination can be understood to be a plane wave, thus leading to an intensity given by:

$$I_{Mott}\left(\vec{q}\right) = \frac{Z^2 e^2}{16\pi^4 \varepsilon_0^2 q^4} = \frac{C_1}{q^4} \quad , \tag{2.46}$$

with introduction of a constant C_1. For the second moment, this translates into:

$$\langle q^2 \rangle_{q_l}^{\mathrm{R}} = C_0 + 2\pi C_1 \int\limits_{q_m}^{q_l} \frac{1}{q^4}\, q^2\, q\, dq = C_0 + 2\pi C_1 \log\left(\frac{q_l}{q_m}\right) \tag{2.47}$$

with introduction of a lower integration limit $q_m > 0$, justified by the approximation of pure high-angle scattering. For lower angles, f^X would need to be taken into account to avoid the divergence at $q \to 0$. Here, the integral from $q = 0$ to $q = q_m$ is included in the constant C_0. Most importantly, according to equation 2.47, the scalar second moment can be expected to display a logarithmic divergence with increasing values of the cut-off angle.

2.4.3 Verification by multislice simulation

The neglect of low-angle details of the scattered intensity and multiple scattering, as well as the assumption of plane wave incidence, done in the previous subsection, lead to the compact analytical expression 2.47. Whereas such a finding carries some interests for its simplicity, validation should be sought from simulations. For this purpose, calculations were done using

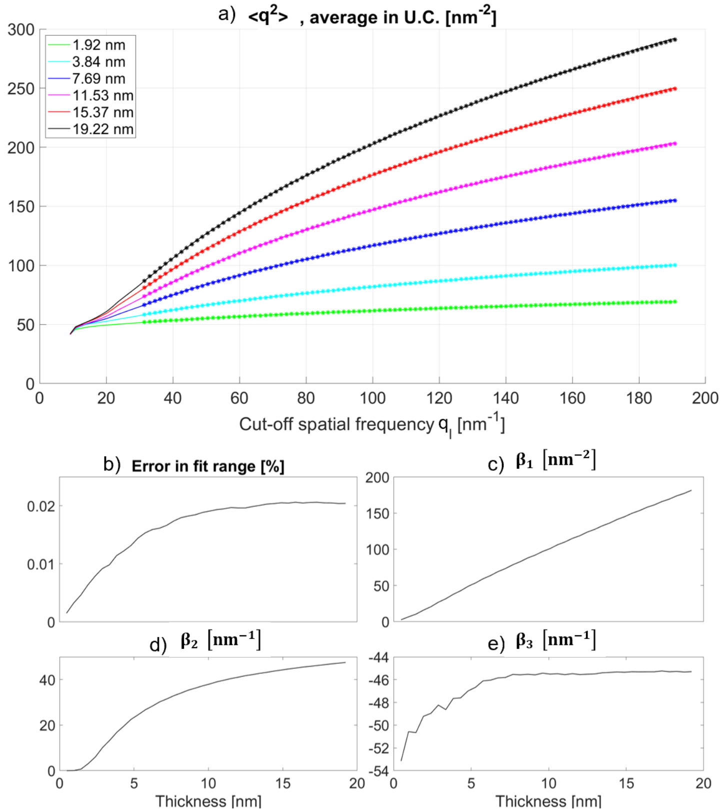

Figure 2.13: a) Results of the real-space average of $\langle q^2 \rangle$ images, within one projected unit cell, for increasing cut-off spatial frequencies q_l. The measurement is done with varying thickness. The curves are fitted with the parametric function given in equation 2.48, depicted as dot curves. b) Values taken by the fitting parameters α, β and δ, as well as the average quadratic error within the considered range, plotted as functions of thickness.

an α-In$_2$Se$_3$ specimen in [001] incidence. Employed imaging parameters were $U = 200\,\mathrm{kV}$ and $\alpha = 23\,\mathrm{mrad}$. The frozen lattice approximation was employed to account for atomic vibrations, with 15 different configurations, and an average was performed among the collection of scan positions within the projected unit cell. First, in order to assess the thickness-dependence in conditions where the high-angle contribution becomes important, the value taken by this real-space average is plotted in figure 2.12, as a function of the specimen thickness t and for a selection of cut-off angles. Results display a monotonous variation against increments of t, which is a mark of the predominance of TDS electrons in the signal. Furthermore, taking an interest in the influence of the angular cut-off directly, $\langle q^2 \rangle$ was extracted while varying it from 23 mrad to 499 mrad in steps of 4 mrad. The values taken by the real-space average are plotted against q_l in figure 2.13.a, for a selection of thicknesses. The curves were fitted [265] using a parametric function of the form

$$\langle q^2 \rangle_{\theta_l} : \quad f(q_l) = \beta_1 \log\left(\frac{q_l - \beta_3}{\beta_2}\right) \quad , \tag{2.48}$$

while using β_1, β_2 and β_3 as fit parameters. This parametric function was chosen consistently with equation 2.47, while including a spatial frequency offset β_3 to allow the error minimization process to adapt the region of fitting by a lateral shift. Furthermore, the data points employed in the error minimization process were restricted to a high-angle region covering cut-off angles above 80 mrad. The fitted parametric function is plotted in figure 2.13.a as well, as a dotted curve given for each employed thickness. Evidently, the logarithmic characteristics are confirmed by the multislice results. To prove it, the quadratic relative error of the fit, averaged among the data points included within the fitting window, is plotted in figure 2.13.b as a function of thickness, and is observed to remain below 0.02 %. It however increases systematically with thickness, which is likely related to the added number of multiply scattered elastic electrons in the high-angle region, which were not included in the previous analytical considerations. A plateau is reached at about 15 nm in thickness, which in turn could be due to the high-angle region being then overall dominated by TDS, independently of considerations of multiple scattering. The values taken by the parameters $\beta_{1,2,3}$ are additionally plotted against thickness in figure 2.13.c,d,e. A remarkable linearity is found for the thickness-dependence displayed by the parameter β_1. This, consistently with results shown in figure 2.12, demonstrates an HAADF-like characteristic of the signal, which could potentially make it suitable for further quantitative STEM applications. Furthermore, whereas the parameters β_2 and β_3 can be understood as offsets in the horizontal and vertical axes of figure 2.13.a, they act as additional degrees of freedom for the fitting process. In that respect, the dependences shown by these two parameters reflect the quality of fit assessed in 2.13.b.

Discussion

To exploit the information caught by the electron wave as part of its propagation through the imaged material, several imaging modes are available, for both the CTEM and STEM recording geometries. Among those, the one at the focus of this work is MR-STEM, which consists of the recording of a CBED pattern as a function of scan position in a STEM experiment. In that manner, a four-dimensional dataset is obtained, which, in principle, can be used to reproduce all conventional STEM signals, post-recording. More generally, the image formation process in STEM is dependent on the contributions of different spatial frequency coordinates, which carry specific real-space information. In that context, the size of the employed detector can be seen as an artificial source of incoherence in the micrograph.

The practical treatment of the diffraction datasets generated during a MR-STEM experiment requires a precise workflow, with a criterion of reliability. In particular, it is important that a mapping of spatial frequency coordinates is done with correction of both the projection-induced elliptical distortions and the rotation error. The methods presented here for spatial frequency mapping, as well as for the subsequent C-STEM and AR-STEM analysis, were thus developed with the goal of self-consistency and reproducibility. To obtain the results presented in this thesis, softwares were thus developed employing both the matlab and python languages. In particular, the latest iteration of software capacity, including all methods presented in this thesis, was developed with reliance on the pytorch environment [268], providing a highly efficient framework for multidimensional data, parallelization and the use of graphic processing units (GPU) for the acceleration of treatment methods.

With the knowledge on reciprocal space, virtual detectors can be generated covering known diffraction coordinates. In particular, the calculation of both $\langle\vec{q}\rangle$ and $\langle q^2\rangle$ is done with the use of finite detectors, which may condition the features they carry. Moreover, the newly introduced $\langle q^2\rangle$ signal, now available thanks to momentum-resolution, shows relevance for future material characterization work. This is due to its high-angle characteristics, which can be understood in an analytical manner through a simple logarithmic model. Specifically, a linear dependence to the thickness of the specimen was found for the parameter β_1 in equation 2.47, which is attractive for the measurement of thickness. In that respect, this imaging mode has the additional advantage that it is, due to the normalization to the total intensity measured below the angular cut-off, independent of the incident intensity and can be thus compared to a simulation directly. In contrast, quantitative HAADF requires additional care in employing the linear range of the detector and measuring the incident intensity independently [269]. To go further than the Z-contrast-like features shown by $\langle q^2\rangle$ when employing the high-angle region of diffraction space, it is also relevant to note that conserving low values of q_l leads to very different behaviors. In particular, surface sensitivity occurs within the dependence of the signal to probe focus, which is a result of the more prevalent role of coherent scattering. This argument is further developed in chapter 4.

Chapter 3

Influence of plasmon scattering on low-angle electron diffraction

Summary

This chapter aims at presenting work performed to demonstrate the influence of inelastic scattering, due to the excitation of volume plasmon modes, on the diffracted electron intensity. The results shown here were published in references [186] and [270]. The chapter begins with section 3.1, where the general motivations of this study are reviewed. This is followed, in section 3.2, by a presentation of experiments, consisting in the combination of energy-filtering and momentum resolution to image a bulk Pt specimen. Continuing, section 3.3 introduces some simulation results including single plasmon-losses. The rest of the chapter extends the topic of inelastic scattering by including the subject of multiple plasmon excitation. As a first step, motivations for this are presented in section 3.4. Experiments performed using thick bulk Al are then described in section 3.5. Finally, a model for the energy-loss-induced intensity redistribution, based on a convolutional approach, is presented in section 3.6.

3.1 Importance of inelastic scattering for momentum-resolution

In the framework of the multislice method, although a quasi-elastic approach is common for the inclusion of phonon excitations, most inelastic processes contributing to the experimental diffraction distribution are omitted. In that manner, the electron wave function is propagated coherently throughout each individual crystal configuration V^j, which is convenient for computation purposes. Nevertheless, in reality, energy-loss plays a major role in the field of TEM, in particular for spectroscopic methods, where it provides a reliable source of knowledge on the chemical composition of the specimen investigated [58], for instance. When detected as a function of the spatial frequency $\vec{q}$, rather than the energy-loss δE, the general assumption is however that the intensity distribution does not vary strongly among the various contributing wave states. This is justified by the fact that the redistribution caused by inelastic scattering events is represented by the convolution with a Lorentzian function $L(\vec{q})$, as expressed in equation 1.66. In particular, this Lorentzian function is often considered to be sufficiently sharp, owing to the generally low values taken by the characteristic spatial frequency $q_{\delta E}$ [184, 185], to ensure that the elastically and inelastically scattered electrons have nearly the same distribution in reciprocal space, at least given the experimental precision on $\vec{q}$. As a consequence, they should not be distinguishable on the detector, independently of their mutual incoherence. From this, it follows that no specific treatment of inelastic scattering should be necessary for electron diffraction simulations. In reality, the assumption of identical intensity distribution often turns out to be inconsistent with experimental results [271, 85], where an important diffuse scattering component may be observed in the low-angle region of diffraction space. Indeed, whereas $L\left(\vec{q}\right)$ generally has a small width, it still possesses long-range tails below the critical angle θ_c, which are responsible for a strong intensity spread effect, in addition to the general blurring of diffraction features [186]. In bulk materials, the main component of this intensity spread is the excitation of volume plasmon modes, because of its high probability of occurrence.

In practice, even if quasi-elastic simulations are insufficient for the accurate modeling of low-angle scattering, it should be noted that this topic is less problematic for conventional quantitative STEM approaches. This is because most of them were developed based on the employment of Z-contrast, and thus with a restriction to electrons scattered toward high angles, owing to their convenient incoherent properties [218]. In particular, the representation of TDS through the frozen phonon model is equivalent to a time-dependent quantum mechanical calculation [179, 181, 182], which results in accurate simulation capacities for this phenomenon. Incoherent imaging via HAADF-STEM nevertheless presents some limitations. This includes its general lack of dose-efficiency, as most of the electrons sent to the specimen are then discarded, but also its uniqueness in terms of its sensitivity to variations of thickness and chemical composition. While the monotonous dependences on t and Z are the main interests of this signal, one given micrograph may only provide information about one parameter at a time, which is why interest has been taken in employing multiple detectors, providing different dependences, for instance in the framework of an AR-STEM experiment [84]. In that respect, enlarging the range of angles usable for that purpose is a critical step toward enabling chemical quantification for more material systems and more chemical elements. For those reasons, several investigations aiming at achieving a better understanding of the role of energy-loss in low-angle electron diffraction were initiated recently [272, 273, 186, 250, 221, 270], which led to new simulation paradigms.

3.2 Energy-filtered MR-STEM of Pt in [110] orientation

3.2.1 Experimental set-up

In order to establish a baseline in the understanding of how the complex diffraction features observed in a given CBED pattern are affected by plasmon-loss, experiments were performed while combining energy-filtering and momentum-resolution. For those energy-filtered MR-STEM (EF-MR-STEM) measurements, an aberration-corrected JEOL JEM2200FS instrument equipped with an in-column JEOL Omega filter [274] and a 264^2 pixels PNCCD camera [71] were employed, such that MR-STEM datasets of 256^2 scan positions could be recorded. Note that this camera consists in an array of DED pixels, connected to a common CCD read-out system. Since the accumulated charge is measured directly, rather than a quantified amount of counts determined by thresholding, as done by hybrid pixels [66, 127, 128], this camera is

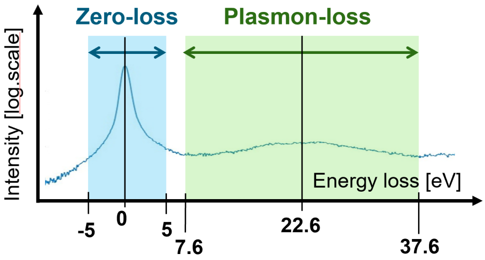

Figure 3.1: Energy spectrum obtained with the Pt specimen, given in logarithmic scale, with indication of the energy windows employed for the experiments.

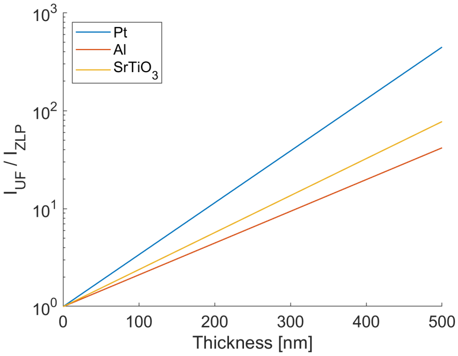

Figure 3.2: Plot of the ratio of unfiltered intensity over zero-loss intensity, given as a function of thickness for Pt, Al and $SrTiO_3$, with $U = 200\,\text{kV}$.

affected both by an imperfect MTF and the common read-out artefacts affecting CCD systems. Whereas the first of those two issues was not believed to be problematic for data analysis, given the use of large virtual detectors, the second was corrected as part of data treatment. By placing windows in specific regions of the energy axis, in combination to the MR-STEM recordings, the formation of diffraction patterns was enabled while restricting the energy range of the contributing electrons, thus allowing a comparison of the reciprocal space features carried by the corresponding collections of wave states. The dwell time of a given scan position was set to 1 ms, such that the total recording time of each energy-dependent dataset was approximately 66 s. Furthermore, the lateral scan interval was set to about 18 pm, and the instrument was operated with an acceleration potential U of 200 kV and a semi-convergence angle α of 15.1 mrad, ensuring a Rayleigh resolution $\delta r_{Rayleigh}$ of about 101 pm. Finally, the electron diffraction acquisitions were quantified in terms of the incident intensity I_0, through a supplementary recording performed in vacuum.

For those experiments, a Pt specimen was imaged in [110] incidence, in two different regions, from here on referred to as regions A and B. As presented in figure 3.1, two energy windows were employed, the first having a width of 10 eV and being centered on the zero-loss peak, and the second being 30 eV wide and centered on the first plasmon peak, meaning at $\delta E = 22.6\,\text{eV}$. In the rest of the text, those two cases are termed ZLP and PL. In addition, an unfiltered MR-STEM acquisition was done, which is referred to as UF. For all individual scans, an HAADF detector was also employed, which was situated above the Omega filter in the column. As such, an unfiltered HAADF-STEM signal was also made available as a complement to each energy window. The thickness t of the specimen in the regions of interest was estimated through the log-ratio approach [275, 276], stating that the ratio of the total unfiltered intensity I_{UF} over the total zero-loss intensity I_{ZLP} obeys:

$$\frac{I_{UF}}{I_{ZLP}} = \exp\left(\frac{t}{\Lambda}\right) \quad , \tag{3.1}$$

where Λ is the inelastic mean free path of the electrons in a given material, for a given incident energy. This is exemplified in figure 3.2. For Pt at $U = 200\,\mathrm{kV}$, the value of $\Lambda = 82\,\mathrm{nm}$ was taken from ref. [277]. By applying this approach on the recorded diffraction patterns, summed in reciprocal space and averaged across the scan window, the thicknesses of the regions of interest A and B were thus determined to be, respectively, 13 and 51 nm. Those values were additionally confirmed by comparison of simulated and experimental PACBED. It is also noteworthy that the recordings done in region A were affected by a specimen mistilt of 5.2 mrad.

The effect of energy-loss was first observed by means of extracting the angular dependence, meaning the result of summing the diffracted intensity azimuthally in diffraction space, from the EF-STEM data. It is then expressed in three dimensions only, including the scan position $\vec{r_s}$. In practice, this is done by employing virtual ring detectors, equivalently to a hardware-based AR-STEM experiment. This analysis was further reduced to a unique angular dimension by averaging across $\vec{r_s}$, as justified by the fact that the influence of plasmon excitation is delocalized in the imaged area, due to the collective nature of the vibration modes among the conduction electrons. For its compact depiction, the angle-resolved intensities were additionally divided by the interval of solid angle per azimuth, so that they were then expressed as a proportion of I_0 per Sr. Finally, since one of the objectives of the experiment is to demonstrate a distinct angular distribution among different energy ranges, the ratio between plasmon-loss and zero-loss intensity was also extracted in order to observe its possible non-uniformities along the angular dimension.

3.2.2 Determination of a common interval of thickness

As part of the normal employment of the in-column Omega filter, delays of up to a few minutes occurred between each energy-filtered acquisition. A consequence of this is a certain amount of sample drift, which implies that the recordings were likely not all done in the exact same area. As the experiments aim at comparing diffraction features arising strictly from energy-loss, in an otherwise fixed set of conditions, it is important to ensure that the same range of thickness is used from an energy window to the next. This issue was here solved by restricting the scan pixels used for the extraction of angular dependences to the atomic sites included within an interval of thickness common to the different recordings. In order to determine this interval of thickness and exclude the regions outside of it, the method depicted in figure 3.3 was introduced. It makes use of the fact that, for the three cases introduced, UF, ZLP and PL, an unfiltered HAADF signal was obtained in parallel to the diffraction recordings, as shown in 3.3.a. Given the high angular range of the detector employed for its acquisition, this signal is expected to display a monotonous dependence to thickness. The three micrographs were thus divided in Voronoi cells centered on the atomic sites, as depicted in 3.3.b, such that all the scan pixels could be individually attributed to one. Local averages within the cells then

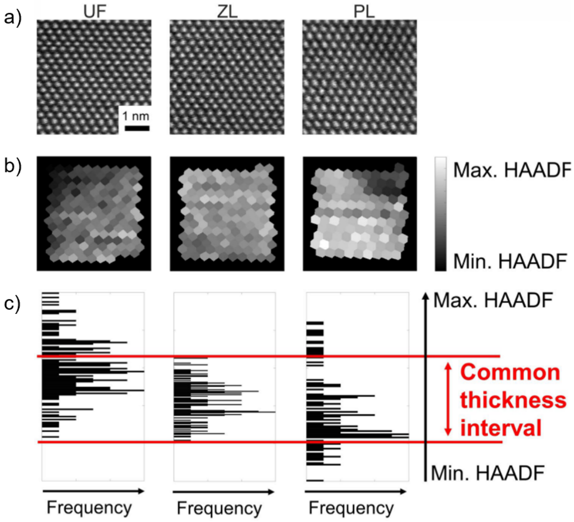

Figure 3.3: a) Unfiltered HAADF images for each recording done in the region B. The variation in thickness from one recording to another is measured using b) a Voronoi segmentation which allows to find the c) thickness interval common to the three recordings and finally make sure that further analysis are done using Voronoi-integrated diffraction patterns only from this common thickness interval.

permitted to attribute an incoherent intensity to each site, which is thus expected to share a monotonous relation to the length of the corresponding column. Upon plotting those intensities in an histogram, as shown in 3.3.c, a common interval of values could be found, which in turn corresponds to the thickness range needed. The real-space-averaged angular dependences were therefore calculated while only using the diffraction patterns recorded at scan positions found within the concerned Voronoi cells.

3.2.3 Results and analysis

The results obtained in region A are presented in figure 3.4. In particular, the real-space-averaged angular dependences are displayed in logarithmic scale in 3.4.a, for the three cases investigated. The ratio of the PL over the ZLP angle-dependent intensities is plotted as well, in 3.4.b, and displays rather strong variations. This constitutes a first confirmation of the fact that the PL and ZLP intensities do not share the same dependence on the scattering angle, and thus of the inability of a routine quasi-elastic simulation to reproduce the low-angle dark field region satisfyingly. The previously mentioned unfiltered HAADF images are displayed in 3.4.c, alongside BF micrographs obtained by summing all intensity within the primary beam detected with the camera. In the three cases, those BF images display atomic resolution, which is due to the phenomenon of preservation of elastic contrast, as explained in section 1.4. Indeed, the co-occurrence of inelastic scattering with the diffraction by the atomic lattice ensures that, within a given energy-dependent wave state resulting from the excitation of a plasmon mode, interference of the Bragg beams still happens, which leads to the appearance of crystallo-

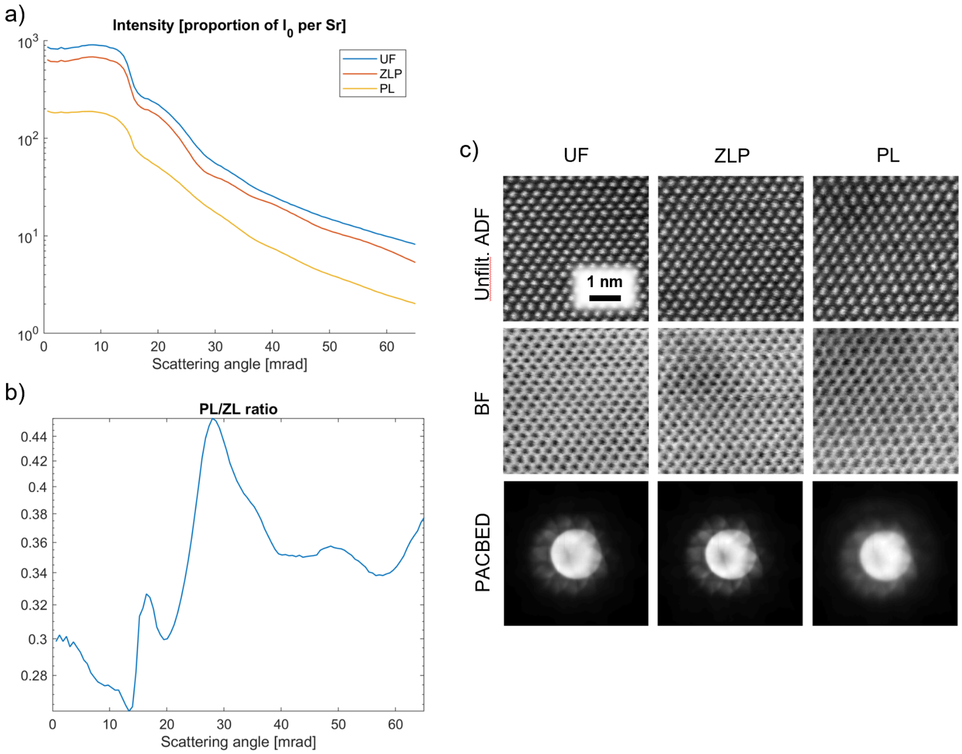

Figure 3.4: Results of the EF-MR-STEM experiment performed on region of interest A. a) Angular dependences, expressed as a proportion of I_0 by units of solid angle, shown by the unfiltered, zero-loss-filtered and plasmon-filtered intensity, extracted by azimuthal summation in diffraction space, and average in real-space. b) Angle-dependent ratio of plasmon-loss by zero-loss intensity. c) Unfiltered HAADF, BF and PACBED results obtained for the three cases.

graphic features in real-space. Nevertheless, the complex distribution of intensity in diffraction space, in addition to its simpler azimuthal integration, is strongly impacted. As a proof of this, a collection of PACBED patterns is additionally depicted. It is relevant to note that such patterns display the effect of specimen mistilt in the form of a shift of the primary beam from the origin of the Bragg beams. This angular shift, which is thus equal to the inclination of the optical axis compared to the crystallographic [110] zone axis was measured to be 5.2 mrad. More importantly, a comparison of the three patterns makes clear that a spreading of the intensity, from the primary beam toward the low-angle dark field, occurs in the PL case, and not in the ZLP case. This redistribution effect can in turn be interpreted as being due to the long-range tails of the function L, as discussed. Going back to the ratio curves in figure 3.4.b, a dip is seen at an angle just below α and a peak just above, thus representing the blurring of the primary beam. This blurring is induced by the small width of the Lorentzian, independently of the tails. Another, higher and broader, peak is additionally observed at approximately 28 mrad, pinpointing the portion of the low-angle region that is favored by the transfer of intensity from ZLP to PL. In addition to this obvious feature, the intensity redistribution effect can be further observed in the form of a generally higher ratio above angles of approximately 40 mrad, com-

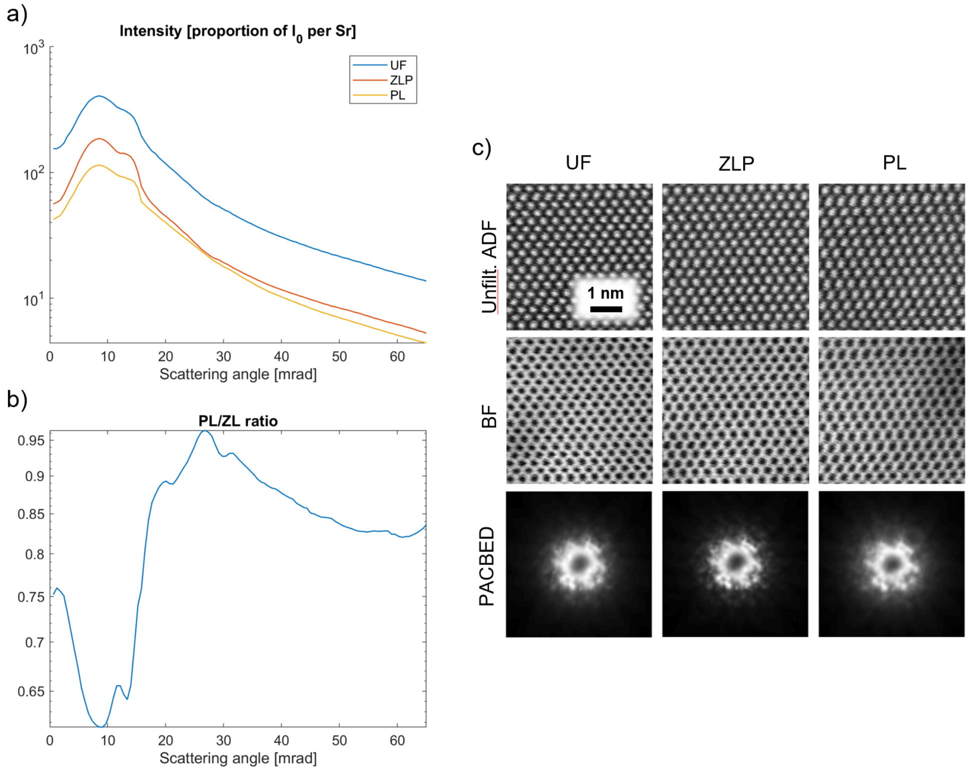

Figure 3.5: Results of the EF-MR-STEM experiment performed on region of interest B of thickness 51 nm, following the same presentation model as figure 3.4.

pared to angles below $\alpha = 15.1\,\text{mrad}$. Indeed, whereas a diffuse intensity component appears in the low-angle dark field due to inelastic scattering, the electrons that make it up are taken primarily from the primary beam. Finally, it is interesting to note that, at its lowest value, the ratio is found just below 26 % and that, at its highest point, it goes beyond 44 %. This shows that, even for a small thickness of 13 nm, the impact of plasmon scattering in the overall CBED pattern, when compared to the elastic intensity, is not negligible.

Further results were obtained in the region B of the Pt specimen, with a much higher thickness of 51 nm, and a near perfect zone axis incidence. They are presented in figure 3.5, following the same outline as figure 3.4. As before, atomic resolution was achieved and PACBED patterns were extracted, displaying a similar blurring effect of diffraction features, as well as the redistribution of intensity due to the tails of L. In particular, the intensity ratio plotted in 3.5.b shows an accumulation of electrons in the low-angle dark field, with a peak at about 28 mrad, and a depletion of the primary beam. The reasoning given for region A on the impact of plasmon scattering also applies to the case of region B. In fact, due to the higher distance traveled within the specimen, the relative amount of plasmon-scattered electrons is here much higher. This is observed in the ratio curve, whose lowest and highest values are found close to 61 and 96 %, respectively. Reported to the UF case, the overall proportion of PL electrons, within an

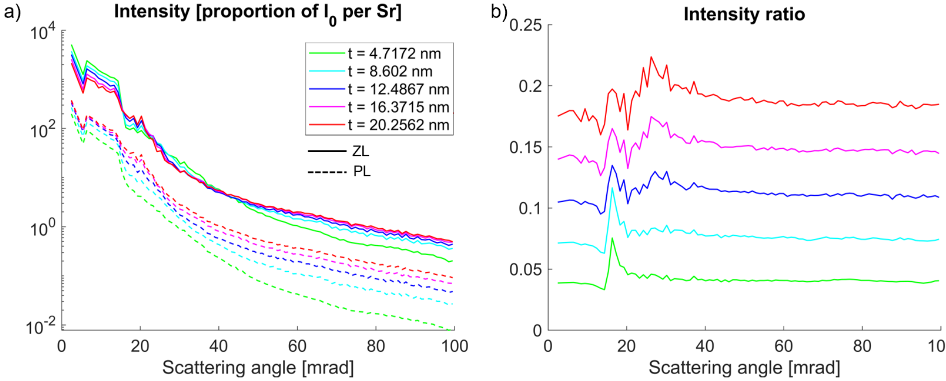

Figure 3.6: Results of the simulation done including single plasmon excitation, using the same tilt as detected in region A, and an analogous thickness range. a) Real-space averaged angular dependences, for several thicknesses and the ZLP/PL cases. b) Corresponding ratios.

angular range of 60 mrad, reaches 31 %. Given this large percentage of plasmon-loss electrons in the recorded intensity, it is clear that, for the investigation of bulk materials using low-angle electron scattering, the inclusion of plasmon-loss is necessary.

3.3 Multislice simulation model including single plasmon-losses

Following the experimental investigation, it is relevant to pursue with simulations. For this purpose, the STEMsim software [278] was adapted to include single plasmon-losses. The necessary theoretical work, implementation and other programming efforts were carried out by collaborators in Universität Bremen. Consequently, simulation results depicted in this section were obtained by application of a ready-to-use version of the software.

In this new implementation, the multislice model was provided a supplementary interaction step with an inelastic transfer function $T^{\delta E}\left(\vec{r}\right)$, following the multiplication by the elastic transfer function $T_{z_n}\left(\vec{r}\right)$ at each slice z_n. To accurately represent the delocalization of the plasmon modes, a total of 50 interactions with $T^{\delta E}\left(\vec{r}-\vec{r}_p\right)$ were performed at each slices, with $\vec{r}_p$ being a random shift used for all events. Each of the emergent waves was then propagated down to the maximum thickness considered, independently of all the others. As only single plasmon-losses were included, no second interaction of a given inelastically scattered wave with a $T^{\delta E}$ function was performed. Even then, in this model, the number of mutually incoherent states to account for increases by 50 at each height z_n, which makes the complete process computationally expensive. It is noteworthy that a normalisation among the elastic wave function and the inelastic components emerging from it is done at each slice, according to an interaction probability $p_{\delta E}$. More implementation details are available in ref. [186]. The simulations were repeated for 10 different phonon configurations, determined by use of the Einstein model imposing random atomic shifts. As a result of the calculations, a real-space-averaged angular dependence is obtained for the ZLP and PL cases, in analogy to the experimental recordings.

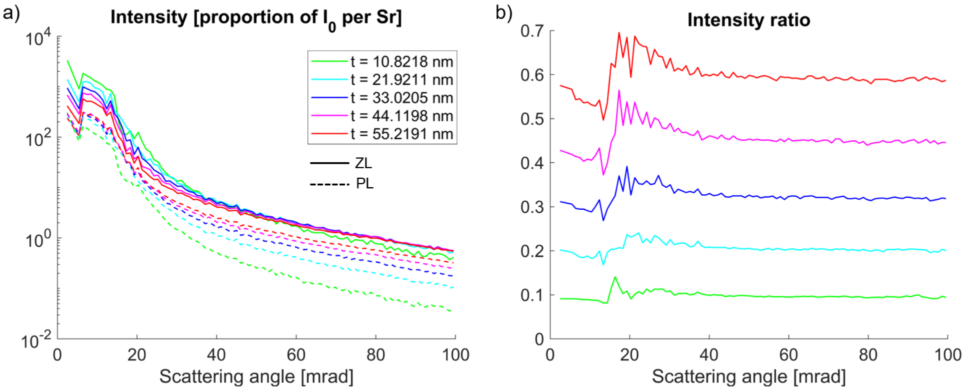

Figure 3.7: Results of the simulation done including single plasmon excitation, using a thickness range analogous to region B. The general presentation is the same as for figure 3.6.

In figure 3.6, the results of a first simulation, reproducing the experimental parameters for the imaging of region A, are shown. In particular, the mistilt of 5.2 mrad against the [110] zone axis was included by modification of the Fresnel propagator [279]. In 3.6.a, the resulting real-space-averaged angular dependences are plotted for a collection of thicknesses, from 4.72 to 20.26 nm, both for the PL and ZLP cases. From those angular dependences, the ratio can be obtained as well, both as a function of thickness and scattering angle, as plotted in 3.6.b. Remarkably, here, the same general features which were observed in figure 3.4.b are present, including the blurring at the edge of the central disk and the redistribution of intensity from the primary beam to the low-angle dark field. Nevertheless, beyond this qualitative agreement, the range in which the ratios are found does not correspond to experimental expectations. The same arguments can be made with regards to the second set of simulation results, shown in figure 3.7. There, no mistilt was introduced and higher thicknesses were made available, relating to the experimental results obtained in the region B. For this second case as well, while the general variations of the ratio against the scattering angle reproduce the experimental findings rather well, a quantitative agreement is not achieved. Generally, the mismatch in the range in which the ratios are found can either be interpreted as an underestimation, by the simulation model, of the overall amount of inelastically scattered electrons, or as resulting from the absence of more contributions affecting low-angle diffraction [250]. This point is detailed in the discussion.

3.4 Role of multiple plasmon excitation

The EF-MR-STEM experiments presented in the last sections consisted of three distinct recordings: an unfiltered intensity, a quasi-elastic intensity and an inelastic intensity. Through these few collections of CBED patterns, important conclusions could be made on the overall effect of plasmon excitation on a dynamically diffracted beam of electron, which both confirmed the importance of energy-loss for quantitative STEM and provided a basis for the comparison to new simulation methods. Nevertheless, this work was still performed with an inherent limitation with regards to more complex energy-loss mechanisms. Indeed, as only a single plasmon peak was available, it was not possible to conclude on the effect of successive plasmon-losses. In particular, a series of recordings done with energy windows centered around several successive plasmon peaks would be necessary to establish the extent to which the redistribution of intensity observed from the zero-loss to the first plasmon-loss is comparable to the one observed from first to second plasmon-loss, for instance.

Going back to aspects of simulation, it was already explained that the inclusion of inelastic scattering by plasmon excitation, in a multislice simulation, is relatively impractical, owing to the large number of wave components to be generated at each slice. Even then, the restriction of the model to single inelastic scattering events [186] ensures that the increment in the number of wave components remains constant for all heights z_n, whereas allowing multiple losses would require this number to increase exponentially with the number of slices traveled through. As a consequence, the rigorous inclusion of multiple plasmon scattering in a multislice simulation remains out of the range of currently available computation capacities, at least in the absence of a new paradigm for the representation of the inelastic electron scattering occurring in the microscope. Importantly, beyond the question of mutual incoherence, the necessity to generate wave components at each slice can be also thought as a consequence of the non-commutativity of the Fresnel propagator $\mathcal{F}^{-1}\left[P_b\left(\vec{q}\right)\right]\left(\vec{r}\right)\otimes_{\vec{r}}$ with the inelastic transfer function $T^{\delta E}\left(\vec{r}\right)$. In other words, the overall influence of a given loss of energy on a diffraction pattern depends, at least in principle, on the exact depth z at which it occurs.

At the same time, when considering specifically the influence of volume plasmons, it should also be understood that the recorded diffracted intensity is affected by a high number of distinct plasmon-losses, occurring at many different positions in the path of the electrons through the specimen. Furthermore, $T^{\delta E}\left(\vec{r}\right)=\mathcal{F}^{-1}\left[\sqrt{L^{\delta E}\left(\vec{q}\right)}\right]\left(\vec{r}\right)$ displays a high extension in real-space, which makes it so that distinct plasmon excitations are in fact not differentiable in terms of their effects. In this context, a new approximation could be introduced, under which the interaction with the transition potential is reported to the end of the elastic propagation and only done once [280, 186, 270], by use of equation 1.66. The plasmon-loss intensity $I_{\vec{r}_s}^{PL}\left(\vec{q}\right)$ could be then directly extracted from the intensity $I_{\vec{r}_s}^{FP}\left(\vec{q}\right)$ obtained from a conventional quasi-elastic simulation. This prospect is particularly attractive for quantitative STEM, as the use of such an approximation would lower the required amount of calculations rather dramatically.

3.5 EF-MR-STEM employing multiple energy windows

3.5.1 Experimental set-up

A 256^2 pixels Medipix fast camera [67, 69, 281] was installed within a CEOS energy-filtering and imaging device (CEFID) [282], itself placed at the end of an aberration-corrected Hitachi HF5000 microscope equipped with a CFEG. Importantly, this camera consists in an array of hybrid DED pixels [66, 127, 128], as explained in section 1.1, each equipped with its own reading electronics. As part of the recording process, a number of counts could be extracted from each pixels by means of thresholding the energy deposited by incident electrons, rather than by measuring the total charge directly, as was the case for the PNCCD [71]. It is noteworthy that the Medipix camera was here operated with a threshold of 80 keV, meaning that, in order to be detected, an electron had to deposit at least this quantity of energy in a given pixel. As was explained in section 1.1, this results in a certain probability of double counting and thus in a

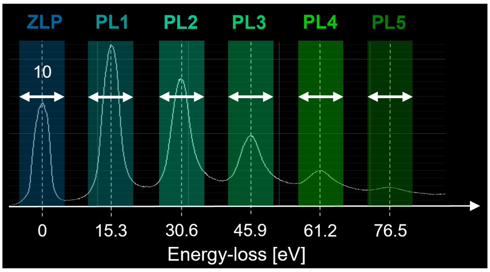

Figure 3.8: Energy spectrum obtained with the Al specimen with indication of the energy windows employed for the experiments.

slightly imperfect MTF. This choice was made as a trade-off between this effect and the DQE of the detector, thus leading to an overall improved recording condition. Like in section 3.2, MR-STEM datasets of 256^2 scan positions were recorded while restricting the energy range of the contributing electrons. The spatial scan interval was set to approximately 22 pm, and the dwell time of a single scan pixel to 1 ms, such that the total recording time of each energy-dependent dataset was approximately 66 s. The acceleration potential U and semi-convergence angle α were respectively set to 200 kV and 20.0 mrad. As such, the resulting Rayleigh criterion was close to $\delta r_{Rayleigh} = 76\,\text{pm}$.

Thick bulk Al was employed for the experiments, being imaged in two distinct sites and in [100] incidence. The thicknesses of those two regions, from here on referred to as A and B, were estimated, again using the log-ratio approach [275, 276] described in equation 3.1 and illustrated by figure 3.2, to 74 and 360 nm, respectively. In particular, with $U = 200\,\text{kV}$, an inelastic mean free path of $\Lambda = 134\,\text{nm}$ [277] was used. The energy windows were chosen as centered on the respective zero-loss and multiple plasmon peaks, with $\delta E = 15.3\,\text{eV}$, obtained in each case, and were given widths of 10 eV. An example of energy-loss spectrum is shown in figure 3.8, which was obtained at a site neighboring region B. Following the extreme distance traveled by the electrons within the material, the first five plasmon peaks, referred to as PL1-5 in further parts of the text, are here all clearly visible and can each be used for a respective recording. The strong plasmonic response observed in this spectrum can be related to the high density of conduction electrons in an Al crystal, in addition to the thickness. This is in turn due to the fact that an Al atom possesses three valence electrons, while Pt, for instance, only has one. This material is therefore very well-suited for the present study.

Due to the different geometry of the energy-filter and better stability of the instrument, the specimen drift issue encountered for the experiments presented in section 3.2 did not occur in those new recordings. As such, the EF-MR-STEM datasets employed here were individually obtained in a fixed location, and with time intervals of a few seconds at most.

3.5.2 Measurement of incident electron intensity emitted by a CFEG

In order to quantify the electron intensity in terms of proportion of I_0, it is necessary to record a non-interacting electron beam. Due to the employment of a CFEG, a series of measurement was thus also required to ensure that the incident intensity would not change strongly from

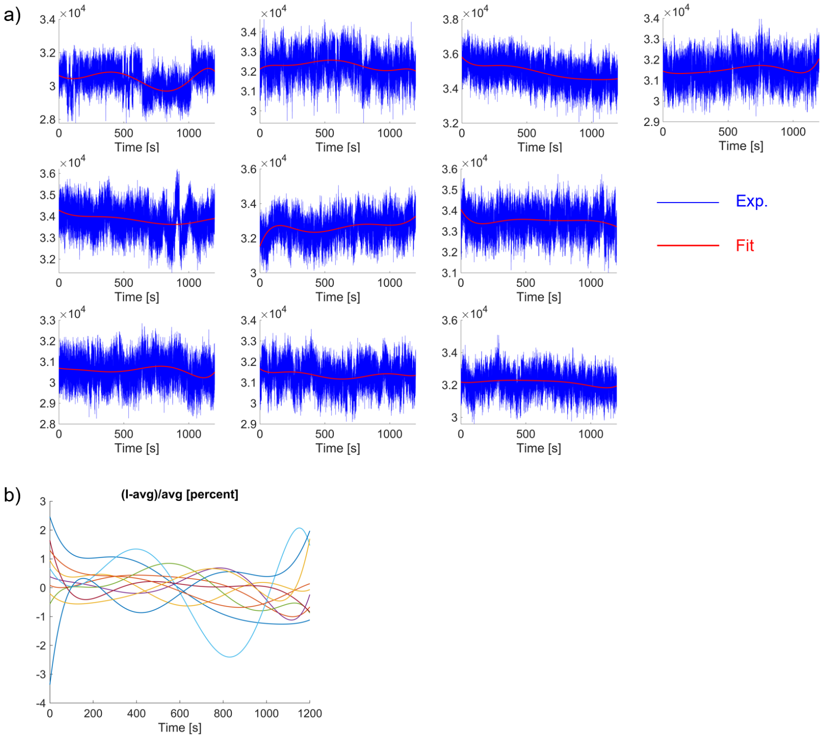

Figure 3.9: a) Recording of intensity done using the diffraction camera. Frames were acquired with a dwell time of 1 ms each, during a total of 20 minutes, repeated 10 times with a flashing done before each one. The curves presented here show the total of each frame as a function of time, for each of the 10 recordings individually. A fitting of the curves was additionally done with a polynomial function, whose results are superposed to the raw curves. b) From the fitted polynomial functions, the proportions of variations, within the long-range trend of the fluctuations in incident intensity, are extracted and plotted against time.

a recording to the next. As was explained in section 1.1, while the use of a cold field-effect source results in a lower energy spread of the incident electron beam, which is especially attractive for experiments involving energy-dependence, it may also create problems relating to the instability of the electron flux. In particular, a CFEG has to be flashed regularly, and thus briefly elevated to a high temperature, to remove contaminants. Here, a choice was made to do it once before each series of energy-dependent recordings and to measure I_0 as part of the actual EF-MR-STEM dataset, as its value is then likely specific to the particular flashing of the source, due to possible remaining contaminants. From that point, it nevertheless remains to determine the extent under which the intensity fluctuates within the total recording time and beyond, due to the slow re-building of the contamination layer. To this end, the non-interacting electron beam was recorded with the Medipix camera, using the same dwell time of 1 ms as for the energy-filtered data, for a total of 20 minutes, and thus well above the duration of a complete series of acquisitions done in a given region of the specimen. This operation was repeated 10 times. For each of those measurements, the total intensity is plotted in figure 3.9.a as a function of time. As the resulting curves indeed display a high amount of fluctuations, due to the counting statistics of the camera, it was convenient to perform a fitting [265] using a 6th-order polynomial function in order to access the long-range trend within the recording time. The fitted functions, here superposed to each curve, can be seen to successfully encompass those trends. In figure 3.9.b, the proportions of variations within the polynomial functions, meaning their time-dependent value minus and then divided by their mean, are plotted as well. This proportion of variations is here observed to remain between -3.2 % and +2.5 % for all cases. This window can thus be understood as representing the maximum impact of the long-range variations in the intensity curves shown in 3.9.a. More importantly, no obvious systematic decrease is observed within the considered time window. This in turn means that the expected loss of incident intensity, due to adsorption of contaminants, will only begin to occur well after the recordings are concluded.

3.5.3 Results and analysis

The results obtained from the region A of the Al specimen are displayed in figure 3.10. In particular, the real-space-averaged angular dependences are plotted in 3.10.a, alongside the ratios of successive energy-losses in 3.10.b, denoted by Rn = $\frac{\text{PLn}}{\text{PLn-1}}$, with PL0=ZLP. Here, a first observation to make is that all those ratios differ from one another. This is significant of the fact that, as was one of the initial questions for this study, each distinct plasmon-scattered intensity possesses its own particular angular profile. This in turn constitutes a first proof that, even when including single plasmon-losses in calculations, multiple excitations may be responsible for a supplementary mismatch when considering the unfiltered intensity. Interestingly, in the framework of those recordings, atomic resolution could be obtained, as verified by the BF images shown in 3.10.c, though a decrease in real-space contrast, from the ZLP to the PL5 recording, can be observed. This loss of contrast can be related to the overall reduction in recorded intensity, visible in 3.10.a. Moreover, the PACBED patterns, shown in 3.10.d for the different cases, display a rather strong redistribution of intensity, which is amplified at each energy-loss. In particular, the angular region where an important inelastic diffuse component is present expands from one case to the next. Furthermore, the blurring of diffraction features is directly visible in the angular dependences plotted in 3.10.a, with the curve being less and less well-defined at the level of the primary beam radius. Going back to the intensity ratios in figure 3.10.b, typical low-angle redistribution features can be observed in each curve, similar to those reported in section 3.2. Specifically, the ratios display a peak in the low-angle dark field, accompanied by a depletion of the primary beam. From energy window to energy window, this redistribution peak is both shifted toward higher angles, specifically from about 27 mrad by a constant step of approximately 2 mrad, and broadened. This behavior, though it is described only qualitatively here, constitutes a rather strong hint that the redistribution of intensity toward higher angles follows a constant mechanism. Beyond the peak, the ratio remains constant, consistently with the damping of the diffuse inelastic component.

Continuing, the results obtained in the 360 nm-thick region B of the specimen are given in figure 3.11. Essentially, the same conclusions can be drawn for this case as for region A, though the total PL intensity is of course much higher, relatively to the UF case, in those conditions of high specimen thickness. In this context, it is remarkable that, while the PL1, the PL2 and the PL3 intensities are stronger than the ZLP one, high resolution is still achievable. This can be interpreted as a rather extreme example of preservation of elastic contrast. This capacity is nevertheless hindered by the low amount of electrons remaining in the employed angular range, as made evident by the low contrast observed in the BF images and the PACBED patterns, especially for the higher levels of energy-loss. This is due to the high amount of electrons being scattered outside of the available part of reciprocal space, which is related especially to TDS. In that respect, it should be understood that the high thickness of region B places it beyond common applications of TEM, in particular because of this important loss of incident intensity. It is also interesting to note that, while the difference in thickness affects the proportions of inelastically scattered electrons contributing to the respective energy-dependent measurements, it does not affect the redistribution mechanism itself, as is expressed by the Lorentzian function L.

3.6 Convolutional model for the inclusion of plasmon scattering

3.6.1 Concept and implementation

Through section 3.5, a general understanding of the features resulting from multiple plasmon scattering was gained. In particular, each given inelastic event intervening in the dynamical diffraction process provokes a redistribution of intensity toward the low-angle dark field. Those events occur successively as a function of energy-loss. Going further, it is expected that the directing inelastic transfer function $T^{\delta E}$ remains the same for all of them. This is because the amount of energy δE lost by an electron through the excitation of a plasmon mode in bulk Al is only 15.3 eV, which is small enough, compared to eU, to consider that the characteristic spatial frequency $q_{\delta E} = \frac{1}{\lambda} \sin\left(\frac{\delta E}{2eU}\right)$ conserves the same value of 0.015 nm^{-1} for all losses. For the same reason, both the elastically and inelastically scattered waves share the same wavelength and thus propagate through the same Fresnel operator. Beyond that aspect, it remains that $T^{\delta E}$ and $\mathcal{F}^{-1}\left[P_b\left(\vec{q}\right)\right]\left(\vec{r}\right) \otimes_{\vec{r}}$ do not commute with one another, at least in principle. This is the reason why, in the first place, a rigorous treatment of inelastic scattering requires the generation of mutually incoherent wave states from several positions in the specimen volume. Nevertheless, as was explained in section 3.4, the argument can be drawn that, due to the large extension of the inelastic transfer function in real-space, and because the several position-dependent plasmon excitations are not distinguishable in terms of their distinct effects on the diffracted intensity, a reasonable substitution to this approach would consist of reporting the inclusion of inelastic scattering to the end of a complete elastic propagation. In this context, the plasmon-loss intensity is given by:

$$I^{PL}\left(\vec{q}\right) = L\left(\vec{q}\right) \otimes_{\vec{q}} I^{FP}\left(\vec{q}\right) = \left(p_{\delta E}\, L_c\left(\vec{q}\right) \frac{1}{q^2 + {q_{\delta E}}^2}\right) \otimes_{\vec{q}} I^{FP}\left(\vec{q}\right) \quad , \tag{3.2}$$

where I^{FP} designates a simulation result obtained through a multislice simulation employing the frozen phonon approximation. Under equation 3.2, the role of the propagation of several independent waves is thus effectively neglected and a direct dependence of the plasmon-loss intensity on the quasi-elastic intensity is established through a convolution with the Lorentzian function L. In particular, the probability $p_{\delta E}$ then corresponds to the total amount of generated inelastic electrons, compared to the incident elastic intensity. Consequently, it can be obtained from the log-ratio rule [275, 276] used previously to estimate the thicknesses in regions A and B, and is thus given by:

$$p_{\delta E} = 1 - \exp\left(-\frac{t}{\Lambda_P}\right) \quad , \tag{3.3}$$

where $\Lambda_P = 160\,\text{nm}$ is the plasmon mean free path obtained in bulk Al for $U = 200\,\text{kV}$ [277]. Reported to the experimental cases, $p_{\delta E}$ reaches about 37 % for a thickness of 74 nm and 89 % for 360 nm. With I^{PL} having been determined by equation 3.2, the zero-loss intensity is otherwise given by:

$$I^{ZLP}(\vec{q}) = (1 - p_{\delta E})\, I^{FP}(\vec{q}) \quad . \tag{3.4}$$

Going further, the calculation of the multiple plasmon-loss intensities can be performed by:

$$I^{PL\,;\,n}(\vec{q}) = L(\vec{q}) \otimes_{\vec{q}} I^{PL\,;\,n-1}(\vec{q}) \quad . \tag{3.5}$$

Under this model, each new plasmon-loss intensity distribution is obtained from the previous one, by convolution and with a weighting $p_{\delta E}$. Of course, this also implies a need to account for the loss of weight in the pre-loss intensity, similarly to the zero-loss case in formula 3.4. Thus, the following step is also required in the algorithm:

$$I^{PL\,;\,n-1}(\vec{q}) = (1 - p_{\delta E})\, I^{PL\,;\,n-1}(\vec{q}) \quad . \tag{3.6}$$

Finally, the total unfiltered intensity can be accessed by a simple summation of all terms according to:

$$I^{UF}(\vec{q}) = \sum_{n=0}^{n=N} I^{PL\,;\,n}(\vec{q}) \quad , \tag{3.7}$$

with $I^{PL\,;\,0} = I^{ZLP}$. N then represents the maximum number of successive losses to be considered under this convolutional model.

3.6.2 Verification through a simulation

As was mentioned in the last subsection, when $t = 360\,\text{nm}$, $p_{\delta E} = 0.89$. Consequently, in the conditions of high thickness corresponding to the recordings done in region B, the plasmon-loss components dominate, and the zero-loss intensity only accounts for 11 % of the detected electrons. This is thus a very suitable example to verify the applicability of the convolutional approach through a simulation. To this end, multislice calculations were made with the same parameters as in the experiment, employing a frozen phonon scheme and an Al specimen in [100] orientation. The resulting real-space-averaged angular dependences are plotted in figure 3.12.a, including the initial simulation result, all the calculated plasmon-loss cases, as well as the final unfiltered curve. The Lorentzian L employed here was obtained with the theoretical characteristic spatial frequency $q_{\delta E} = 0.015\,\text{nm}^{-1}$, corresponding to a length of 5 pixels in the simulation, and a critical angle $\theta_c = 15\,\text{mrad}$. As expected from the experimental results, the successive plasmon-loss intensities display a decay according to ${p_{\delta E}}^n$, as well as an angular broadening from the edge of the primary beam accompanied by an increment in the low-angle dark field. Both the magnitudes of the components and the general features they carry show agreement with the angular dependences shown in figure 3.11, although differences remain in the scaling of the various cases compared to one another. This can nevertheless be related to the small width of the energy windows, which do not include the entire range of the respective plasmon peaks, as shown by figure 3.8.

As $p_{\delta E}$, and thus the respective weightings of each energy-dependent components, carries a dependence on thickness, so does the requirement on the number N of excitations which is necessary to consider in this model. To verify this in more details, an additional study was done, as presented in figure 3.12.b. Specifically, the angular dependences were calculated for thicknesses of 90, 180, 270 and 360 nm, and while including 0 to 4 plasmon scattering events through the convolutional approach. Owing to the spectrum shown in figure 3.8, it can be considered that the intensity reaches a convergence for $N = 5$, in the range of thicknesses $t \leq 360\,\mathrm{nm}$. As such, the relative difference between the unfiltered intensity calculated with the desired number of losses and the one obtained with $N = 5$ can be considered to provide a criterion on the error made when not enough inelastic events are included. It is here plotted in the figure as a function of the scattering angle and for the selection of thicknesses. A first observation to be made from those plots is that, in all cases, not accounting for any plasmon excitations results in errors of up to 50 % in the low-angle region. Beyond that, taking only 1-2 losses into account may be already sufficient for the thickness of 90 nm, whereas, with increasing thicknesses, the inclusion of at least 3 losses becomes a necessity. It is of course important to note that such requirements are dependent on the material an in particular on its plasmon mean free path Λ_P.

3.6.3 Application to the experimental data

With a general demonstration having been done by means of quasi-elastic simulations, it is relevant to pursue with a verification employing the experimental data directly. Specifically, as the recorded PACBED patterns are identified to the respective $I^{PL\,;\,n}$ intensities, they can be used to perform a fitting via a minimization of the squared differences of successive cases, one being convolved with L, and by varying the characteristic spatial frequency $q_{\delta E}$ [265]. In that respect, although the convolution was performed using the two-dimensional PACBED patterns, the actual difference to minimize was obtained from the one-dimensional angular dependences, to ensure the absence of errors due to possible differences in the centering and rotation of the diffraction frames. Like in the simulation case, the angular cut-off θ_c was set to 15 mrad. It is noteworthy that, because of the loss of intensity due to the small width of the energy windows, as mentioned previously, it is not expected to obtain a perfect agreement in the value of $p_{\delta E}$, excitation-wise. For this reason, the fitted Lorentzian was multiplied by a coefficient, itself being adjusted for each individual transition. Values extracted for $q_{\delta E}$ are 0.0221 nm^{-1} in region A and 0.0214 nm^{-1} in region B, the fitting being concluded with an average relative error of (A) 3.92 % and (B) 6.38 %. Importantly, those experimentally determined characteristic scattering angles only lead to a marginal improvement of 0.5 % of the fit as compared to the theoretical value of 0.015 nm^{-1}. In fact, this slight difference can be related to the finite sampling of diffraction space by the pixels of the camera. It is therefore possible to conclude that the convolution-based model provides a satisfying representation of the experimental results. Furthermore, the quality of fit is generally higher for the data obtained in region A, which is likely because of the higher intensity of the corresponding diffraction patterns. This is in turn due to the lower thickness traveled by the electrons within the material, ensuring that a smaller proportion of those contribute to TDS.

Discussion

In this chapter, the EF-MR-STEM technique was introduced and experiments presented in order to decipher the influence of plasmon-loss on the CBED intensity distribution. It was shown that a blurring of the diffraction features, as well as a redistribution of electrons toward the low-angle dark field region of reciprocal space accompanied by a depletion of the primary beam, were the main components of this effect. As explained previously, those two aspects can be associated to the small width of the Lorentzian L and to its long-range tails below the critical angle θ_c, respectively. Beyond this distinction, such features, which are not reproducible by means of conventional quasi-elastic simulations, account for a rather large part of the detected electrons. For instance, in the case of 51 nm-thick Pt, the plasmon-loss intensity was found to reach almost a third of the total unfiltered intensity, below a scattering angle of 60 mrad.

Whereas, for the purpose of establishing a quantitative STEM method, the blurring effect itself could potentially be alleviated by means of a careful summation strategy in diffraction space, it is clear that such an approach cannot be applied to alleviate the redistribution-induced low-angle diffuse intensity. In this context, the inclusion of plasmon-loss becomes a strict requirement for the quantitative employment of low-angle scattering. Some initial attempts at doing this were presented in section 3.3, and otherwise reported recently in the literature [272, 186, 273]. Nevertheless, such inelastic simulations still present limitations, among which their inherent computational complexity. Furthermore, even with the inclusion of plasmon excitation, mismatches remain which may be due to further contributions still not considered here [250, 221]. Among those, one can cite surface strain [283, 284], or Huang scattering [285] caused by static atomic displacement [251, 252, 253], which, due the local modifications of the crystal lattice, affect the exact distribution and amplitude of the Bragg beams. Beyond that, the presence of an amorphous layer of material at the surfaces of the specimen is also known to cause an accumulation of intensity in the low-angle region, due to Mott-Bethe scattering by the randomly located atoms [204, 205]. Finally, the use of the Einstein model of uncorrelated atomic shifts, as part of the implementation of the frozen lattice approximation, can be questioned as well [178, 180].

Despite the mismatch in terms of the range of PL/ZLP ratio, it is important to note that the general angular features expected from the experiments described in section 3.2 were still observed in the simulation. Consequently, the results presented in section 3.3 provide a proof-of-concept for the generalized inclusion of energy-loss in multislice simulations, which is an important topic for TEM in general.

In the second study presented in this chapter, the data recording scheme went from two to six energy windows. The high flexibility of the EF-MR-STEM technique was thus exploited to investigate the influence of multiple plasmon-losses. As an extension to the arguments made previously on the inability of conventional simulation methods to describe inelastic low-angle scattering, it was found that the angular dependences of respective energy-dependent recordings differ from one another. This means that, even when single plasmon-losses are included in calculations, an error can still potentially occur when multiple plasmon excitations become probable, as in the case of a material with high plasmonic response such as Al. In that respect, it is also important to understand that, whereas plasmon scattering leads to intensity being redistributed toward higher angles, repeated plasmon-losses can extend the angular range in which a large proportion of inelastic electrons are found. In other words, while high-angle scattering is relatively insensitive to a given inelastic scattering event, electrons having gone though more than one of such events may end up having a significant role on it. For those reasons, it is clear that the inclusion of multiple plasmon excitations in a multislice simulation, rather than just the single loss case, is desirable, at least in certain cases. While the rigorous implementation of such mechanisms is currently beyond available computational capacities, the convolutional approach described in section 3.6 may provide a satisfying, albeit approximative, solution. Through the example of Al, this model was shown to successfully encompass the features expected from experiments, thus making it a viable substitution to the more rigorous approach.

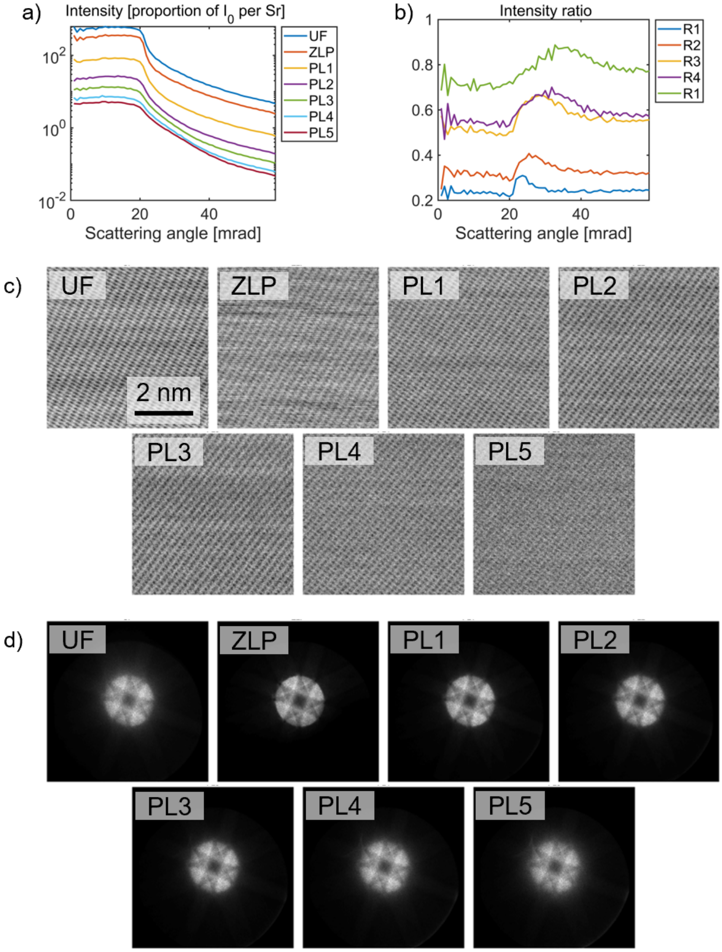

Figure 3.10: Results of the EF-MR-STEM experiment performed on the region of interest A of the Al specimen, with a thickness equal to 74 nm. a) Angular dependences, expressed as a proportion of I_0 by units of solid angle, shown by the unfiltered, zero-loss-filtered and plasmon-filtered intensities, extracted by azimuthal summation in diffraction space, and averaged in real-space. b) Angle-dependent ratio of successive inelastic intensities, denoted by Rn=$\frac{\text{PLn}}{\text{PLn-1}}$. c) PACBED patterns obtained for all cases. d) BF images obtained for all cases.

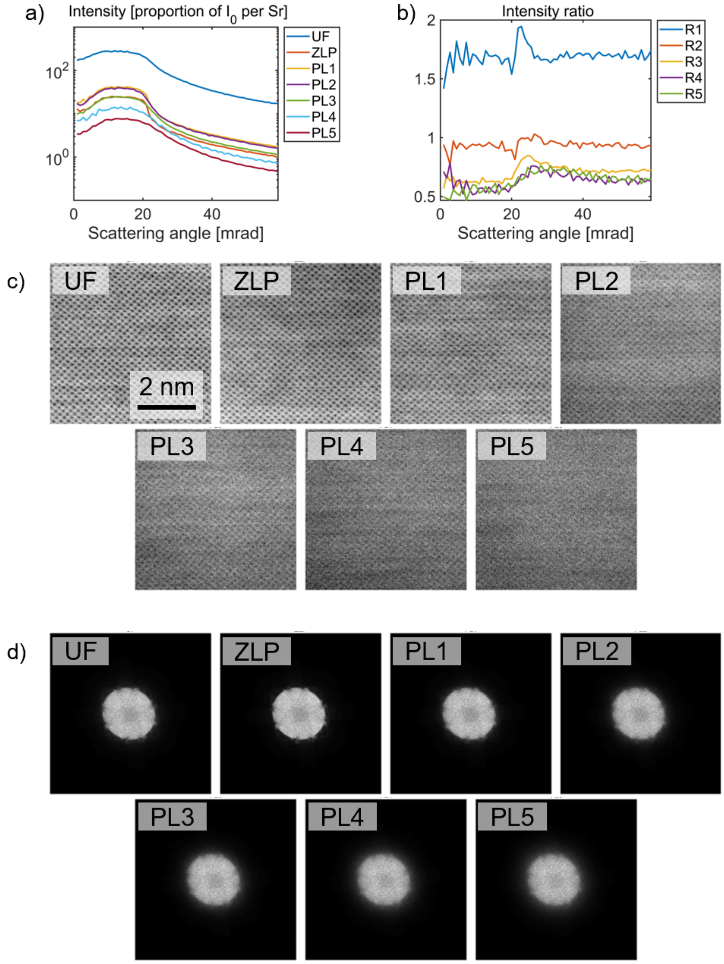

Figure 3.11: Results of the EF-MR-STEM experiment performed on the region of interest B of the Al specimen, with a thickness equal to 360 nm. The outline is the same as for figure 3.10.

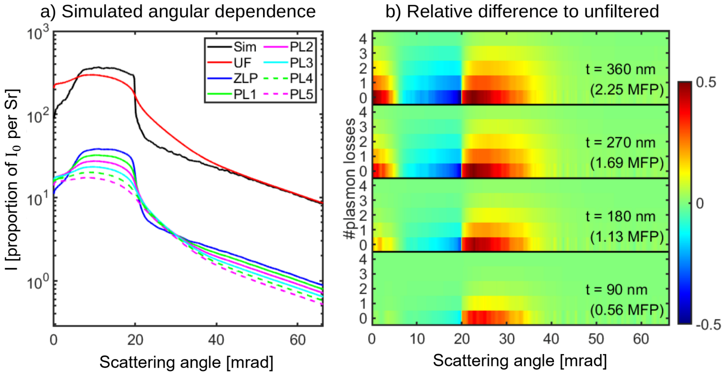

Figure 3.12: a) Simulated angular dependences for a bulk Al specimen, with a thickness of 360 nm specimen thickness. The displayed cases are the result of a multislice quasi-elastic simulation, the several plasmon-loss intensities obtained using the convolutional approach, and an unfiltered intensity, meaning the result of their summation. The employed Lorentzian parameters were $q_{\delta E} = 0.015\text{nm}^{-1}$ and $\theta_c = 15\,\text{mrad}$. b) Relative error of the simulation, using the convolutional method to add the effect of plasmon-loss, when 0 to 4 plasmon excitations are included. The depiction is done in dependence to scattering angle and thickness. The case with 5 plasmon excitations included is considered as unfiltered.

Chapter 4

Focus-dependence of STEM signals and prospects for surface detection

Summary

In this chapter, a study is presented on the influence of probe focus on distinct signals obtainable from a MR-STEM dataset. Most results presented here were included in reference [193]. The chapter starts with section 4.1, where motivations for this work are given in the context of the FS-STEM methodology. Then, in section 4.2, a microscopy set-up aiming at providing an experimental demonstration of focus mismatch effects is discussed, alongside the results obtained. Their interpretation is supplemented with section 4.3, where an extensive simulation study is presented. It is pursued with a simulated bulk Au specimen, in section 4.4. The rest of the chapter continues on the prospects of using the findings on focus-dependences of STEM signals to perform surface detection in materials. In particular, the experimental requirements of such a measurement are explored by means of simulations. This is explained in more details in section 4.5. Further sections follow with the influencing factors to be investigated, including the depth of focus δz_{DOF}, aberrations, partial coherence of the incident electron beam, specimen tilt, carbon contamination, temperature, and finally the atomic number Z of the material investigated.

4.1 Limitations of conventional depth sectioning approaches

While the STEM technique can nowadays be used routinely to obtain atomic contrast in the lateral dimensions [48], it remains inherently limited by its transmission geometry. As a consequence, information relating to the vertical axis of the specimen are not accessible directly. To circumvent this limitation, methods exist which consist of the recording of a series of micrographs in varying conditions. This includes, for instance, STEM tomography [102], which consists of tilting the specimen in a variety of angles and use the various resulting projections to perform a reconstruction of the specimen. Another example is FS-STEM, more generally referred to as depth sectioning, where the probe focus is varied through a series of scans. The resulting images then display a specifically targeted contrast type when the focus f coincides with a feature the selected STEM signal is sensitive to. In that respect, examples of investigations done using FS-STEM were already given in section 2.1. More generally, the appearance of employable focus-dependent features is conditioned by channelling mechanisms, and thus displays a non-trivial dependence on the range of spatial frequencies collected in the C-STEM signal employed, as well as on the exact specimen being illuminated. Results obtained a depth sectioning investigation are therefore case-specific.

Beyond the first limitation on the depth of focus, which was discussed in chapter 2, conventional FS-STEM approaches were so far mostly restricted to the use of the HAADF-STEM imaging mode. Although it is conventionally favored for its incoherent properties, this signal may lack in sensitivity to light atoms, and does not inherently provide a clear distinction between variations of intensity due to either changes of composition, thickness or strain [251, 284, 220]. In that respect, and for the reasons given in the last paragraph, it is clear that the recording of multiple STEM signals as a function of focus has the potential to provide additional sources of information. In particular, imaging modes employing the low-angle region of diffraction space were shown to provide a strong sensitivity to channelling and coherence-dependent effects [286, 287, 288, 289, 290, 291, 292, 293, 294], leading to new opportunities in C-STEM analysis.

In that context, an exploratory experiment was performed where a focal series recording was combined with MR-STEM, thus allowing the simultaneous investigation of several STEM signals as a function of f. A first finding obtained from this work is a mismatch of optimal focus among the different signals, which in turn constitutes the first subject of the present chapter.

4.2 Case study on α-In$_2$Se$_3$

4.2.1 Experimental set-up

A focal series MR-STEM (FS-MR-STEM) experiment was performed using an FEI Titan 80-300 instrument, as was depicted in figure 1.4.b, equipped with a 256^2 pixels Medipix fast camera [67, 69, 281]. This camera was also used to obtain the experimental results presented in section 3.5 and, here too, was operated with an threshold of 80 keV. The focal series was implemented via a python-based script acting on the interface of the microscope via its component object model. 21 recordings consisting of 64^2 scan pixels, with a focus step of 1.5 nm, were performed, thus covering a focus range of 30 nm. The lateral scan interval was 31 pm. As the dwell time of a single scan pixel was set to 0.5 ms, the total recording time was approximately 43 s. The acceleration voltage U and semi-convergence angle α were assigned values of 200 kV and 23.0 mrad, respectively. Those values in turn ensured a lateral resolution $\delta r_{Rayleigh} = 66\,\text{pm}$ and a depth of focus $\delta z_{DOF} = 9.48\,\text{nm}$. Here, of course, it is important to note that the definition of δz_{DOF} given in chapter 1 corresponds to the distance between two minima of the amplitude profile along the f-axis. As such, finer features can in practice be resolved within a focal series recording, as is demonstrated by the results presented here. Furthermore, as was mentioned in section 1.3, the focus axis, although the physical location of its zero is unknown, is conventionally determined as opposite to the propagation direction of the probing electrons. A coincidence of the probe cross-over with the entrance surface of the specimen is thus obtained for a focus $f = 0$ and with its exit surface for $f = -t$.

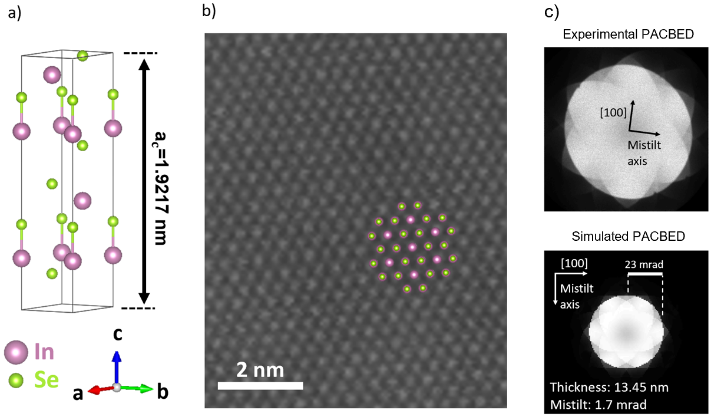

Figure 4.1: a) The unit cell of an α-In$_2$Se$_3$ crystal, represented using the Vesta software [295]. b) HAADF image of the specimen in [001] projection, following a). c) Comparison between experimental and simulated PACBED patterns to determine thickness and mistilt of the specimen.

For this experiment, an α-In$_2$Se$_3$ [296] specimen was prepared by exfoliation from a bulk crystal, and dispersed on a carbon TEM grid. For reference, the unit cell of the specimen is depicted in figure 4.1.a. In figure 4.1.b, a HAADF image recorded in [001] projection is additionally shown, alongside the projected atomic pattern. The thickness of 13.45±1.92 nm, meaning 7±1 stacked unit cells, as well as a 1.7 mrad mistilt between the propagation direction and the [001] zone axis, were obtained by direct comparison of the experimental and simulated PACBED patterns. This is demonstrated in figure 4.1.c. From the recorded CBED patterns, a selection of STEM signals were obtained, including two bright field cases, BF$_{23}$ and BF$_{17}$, summing electrons up to maximum scattering angles of 23 and 17 mrad, respectively, as well as an annular bright field mode $\mathrm{ABF}_{17-23} = \mathrm{BF}_{23} - \mathrm{BF}_{17}$. Furthermore, $\langle\vec{q}\rangle^{\mathrm{R}}$, $\langle\vec{q}\rangle$, $\langle q^2\rangle^{\mathrm{R}}$ and $\langle q^2\rangle$ were measured using an angular limit of 27 mrad. The divergence ϱ and integral φ of the first moment vector map $\langle\vec{q}\rangle$ could be then extracted as well, using the finite difference method explained in section 2.3. Finally, in parallel to the diffraction patterns, a HAADF signal was obtained from a dedicated detector covering scattering angles between 39 and 230 mrad. With those various imaging modes available as a function of both the scan position $\vec{r}_s$ and the probe focus f, it is in turn possible to sample the variations displayed by their respective real-space contrast as a function of the z coordinate. In the following, the standard deviation within the scan window is taken as contrast metric.

4.2.2 Results and analysis

The contrast curves are plotted in figure 4.2, between their respective minimum and maximum values. As becomes immediately visible from this result, a great variability in focus-dependence can exist among different STEM signals, in particular with maxima of contrast coinciding with different values of f. More specifically, the focus of maximum contrast obtained for $\langle\vec{q}\rangle^{\mathrm{R}}$ and $\langle\vec{q}\rangle$, and which is here shared with BF$_{17}$ and $\langle q^2\rangle$, is found to be located 3 nm below the one obtained for HAADF and BF$_{23}$. Additionally, ABF$_{17-23}$ and $\langle q^2\rangle^{\mathrm{R}}$ here display two distinct local contrast maxima, distant of 13.5 nm from another. It is interesting

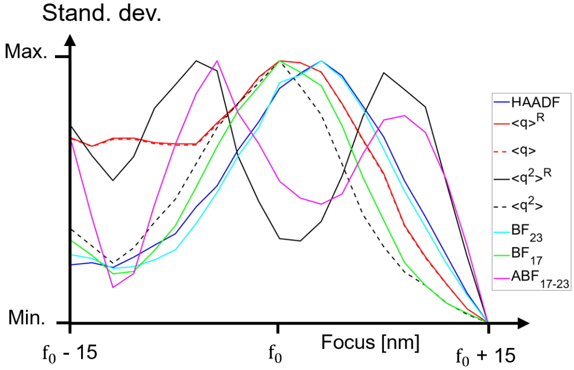

Figure 4.2: Real-space standard deviation plotted against focus for all signals of interest. Each curve is scaled between its minimum and maximum.

to note that this distance corresponds well to the thickness of the specimen, which suggests a coincidence between those maxima and the specimen surfaces. This is further verified in section 4.3. For a better visualisation of the variations in image features, the micrographs are displayed as a function of focus in figure 4.3. The foci where contrast maxima occur are highlighted in red. A visual inspection of those images confirms the points made so far, with the additional observation that the two optima displayed by ABF_{17-23} and $\langle q^2\rangle^{\mathrm{R}}$ are accompanied by a contrast reversal mechanism. The atomic columns then appear either as local maxima or minima of value for the two foci. Additionally, the HAADF and BF_{23} signals display a large region of atomic contrast, in fact covering the entire focal range visible here, while BF_{17} is well-contrasted only in a sharply peaked area. In the case of $\langle\vec{q}\rangle$ and its byproducts, atomic visibility is conserved in a large focus extent as well, while decaying close to the point attributed to the entrance surface.

4.3 Interpretation of experimental results through simulation

4.3.1 Simulation parameters and focus-dependences

A comprehensive quasi-elastic multislice simulation study was performed to further interpret the results presented in section 4.2, as well as to extend the frame of the study in terms of specimen thickness. For this purpose, the same imaging parameters as those employed for the experiment were used, including U, α, the scan interval and the focus interval. Additionally, the measured tilt of 1.7 mrad was included by modification of the Fresnel propagator [279]. The size of the supercell was chosen to be 9×5 unit cells, thus corresponding to a surface of 3.62×3.48 nm^2, in order for it to remain large enough to contain all probe extension arising both from the propagation through matter and variations of focus. 15 phonon configurations were employed, assuming uncorrelated atomic movements. From the simulated diffraction patterns, the real-space standard deviation was obtained as a function of both focus and thickness for the several signals investigated here. To those signals, a LAADF mode, resulting from the summation of electrons scattered to angles between 23 and 29 mrad, was

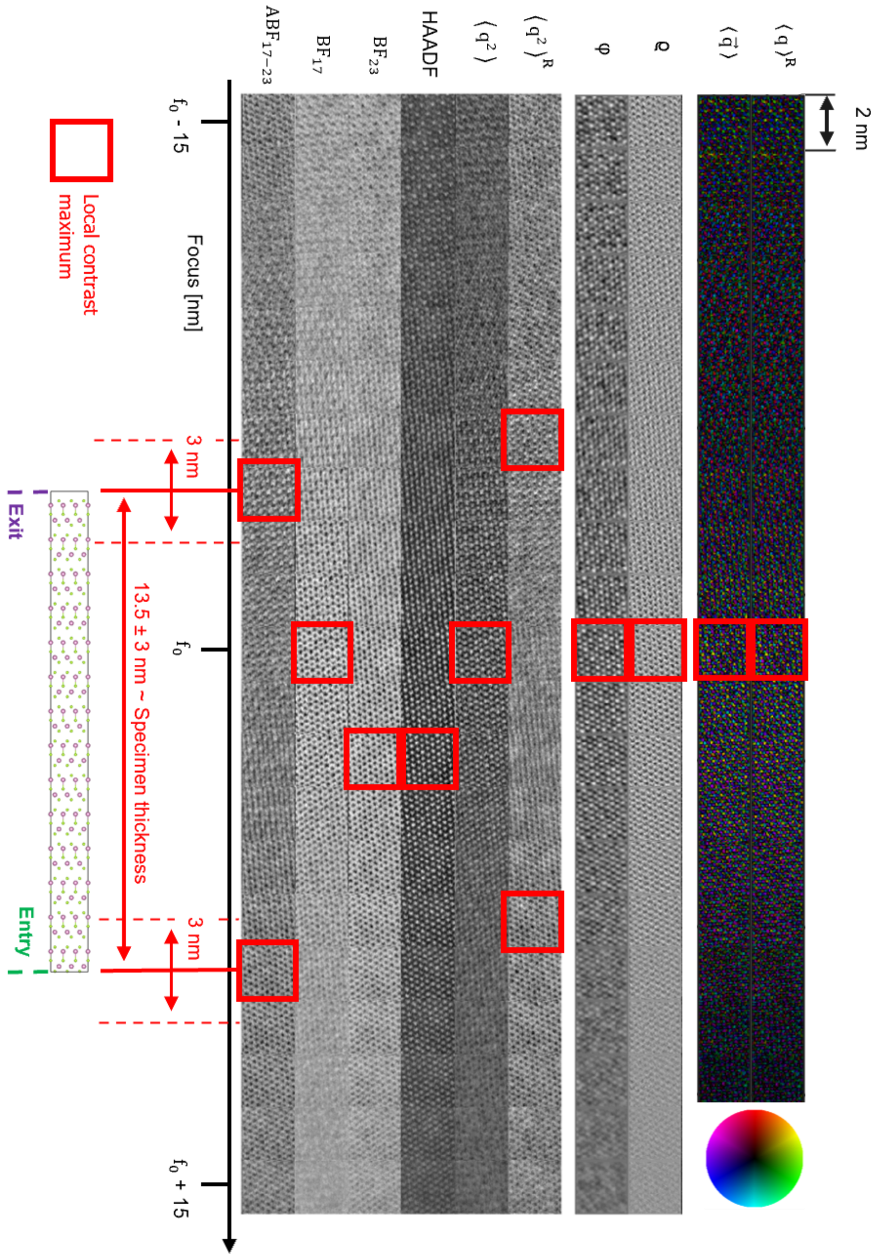

Figure 4.3: The experimental images calculated for each focus coordinate. The size of the field of view is equal to 2 nm. The images displaying contrast optima are highlighted in red. The vectorial quantities $\langle \vec{q} \rangle^{\mathrm{R}}$ and $\langle \vec{q} \rangle$ are given in colour wheel representation. The specimen, with its interfaces with vacuum, is depicted next to the images.

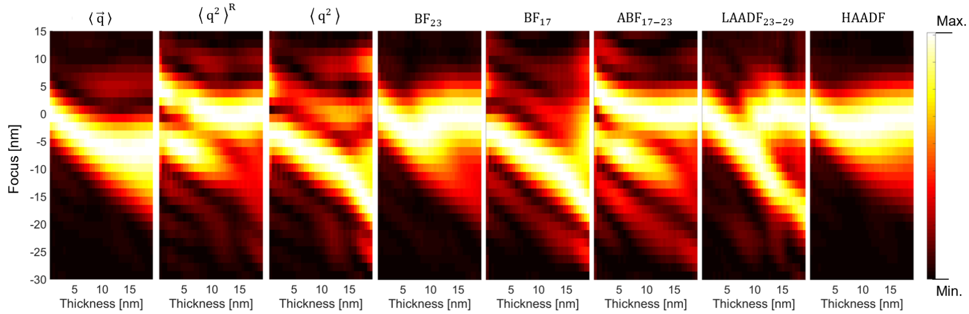

Figure 4.4: Contrast profiles obtained for the various signals extracted from the simulated CBED patterns. The real-space standard deviation is given scaled between the minimum and maximum values reached for a given thickness, meaning at the level of each column of the graph. This choice is made to visually separate the contrast variation that would be due to changes in focus, which is the object of the investigation, from the one that is due to thickness increments.

added for completeness of the argumentation. The standard deviation is plotted in figure 4.4, with normalization done between the minimum and maximum values obtained at each given thickness. A first confirmation is thus obtained for the mismatch of optimum focus among the different signals, as they indeed display very different focus-dependences, which additionally show thickness specificity. In the following, those dependences are detailed for each signal of interest. It is noteworthy that, among those, a distinction is made between $\langle q^2 \rangle$ and its raw counterpart $\langle q^2 \rangle^{\mathrm{R}}$, whereas it is not made for $\langle \vec{q} \rangle$, since no important differences are found between the normalized and raw cases.

4.3.2 C-STEM signals

The C-STEM results are plotted in figure 4.5 as a function of both thickness and focus. The positions of the entrance and exit surfaces on the f-axis are additionally indicated, alongside the experimentally available thickness. The bright field signals BF$_{23,17}$, in figure 4.5.a,b, exhibit complex features depending on detector acceptance angles, focus and thickness. Consistently to the experimental results shown in figure 4.3, foci that geometrically lie inside the specimen lead to negative contrast. Furthermore, while the BF$_{23}$ changes weakly within an extended region of f, BF$_{17}$ shows a significantly sharper contrast maximum shifted closely to the exit surface. Similarly, the ABF$_{17-23}$ mode, displayed in figure 4.5.c, shows sharp peaks at both specimen surfaces. This is in agreement with the experimental results, as well as the observed negative to positive contrast change when focusing through the specimen. A further observation is the existence of additional, smaller, local optima at foci a few nanometers above and below the surfaces. Not unlike the ABF case, scattering into the low-angle dark field, assessed by the LAADF$_{23-29}$ signal given in figure 4.5.d, exhibits a pronounced contrast maximum for foci close to the exit surface. Another one is seen at the entrance, for thicknesses above a value of approximately 10 nm, though with no contrast reversal then. Finally, in the case of the HAADF mode shown in figure 4.5.e, a broad region of atomic visibility is observed at foci a few nm below the surface, which is also consistent with the experimental results.

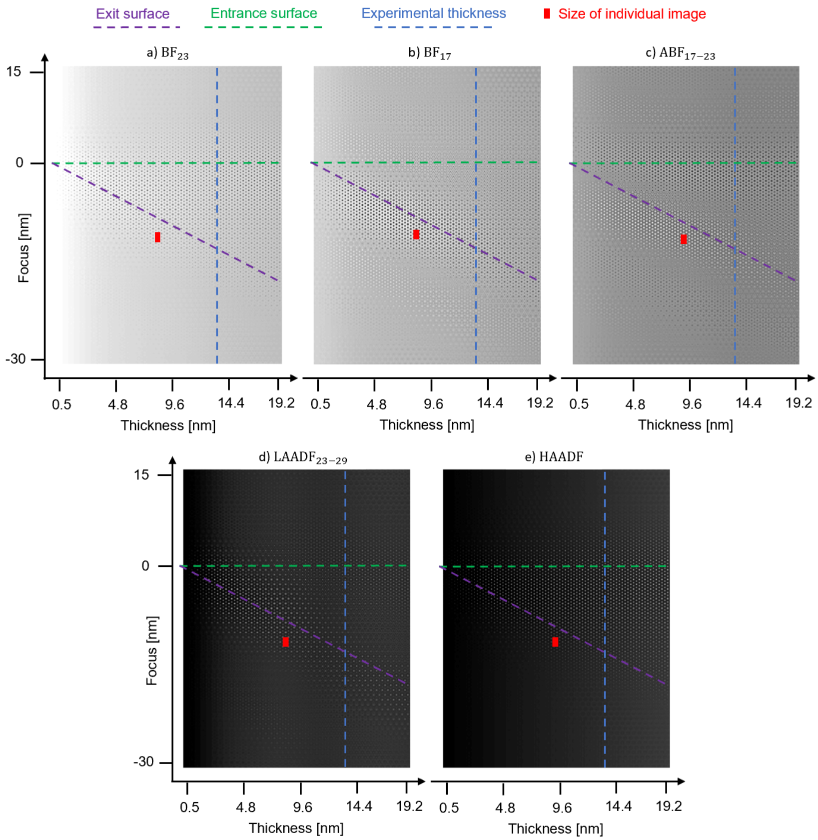

Figure 4.5: Conventional STEM signals extracted from the simulation. Data is given as a function of specimen thickness and probe focus, the latter being equal to zero at the entrance surface. The positions of the entrance and exit surfaces on the focus axis are indicated as well. The size of an single image in the graph is denoted as a red rectangle.

4.3.3 MR-STEM-specific signals

Pursuing from the last subsection, attention is now given to the MR-STEM-specific signals, meaning to the first and second moments in diffraction space. They are compiled in figure 4.6, following the same general presentation as figure 4.5. $\langle \vec{q} \rangle$, depicted in 4.6.a, is found to reach its contrast maximum when focusing into the specimen, with a tendency to follow the exit surface for thicknesses below 8 nm. Above this value, the focus-dependence neither follows the bright nor the dark field characteristics, but conserves an optimum at a constant depth below the entrance surface, independently of the total distance traveled through the specimen. For those sufficiently large thicknesses, the consequence is then a mismatch of optimum recording condition between investigations aiming at obtaining electric field characteristics through $\langle \vec{q} \rangle$ or chemical composition through Z-contrast. As for the previous cases, this observation is consistent with the experimental results displayed in figure 4.3. Furthermore, the focus-dependence

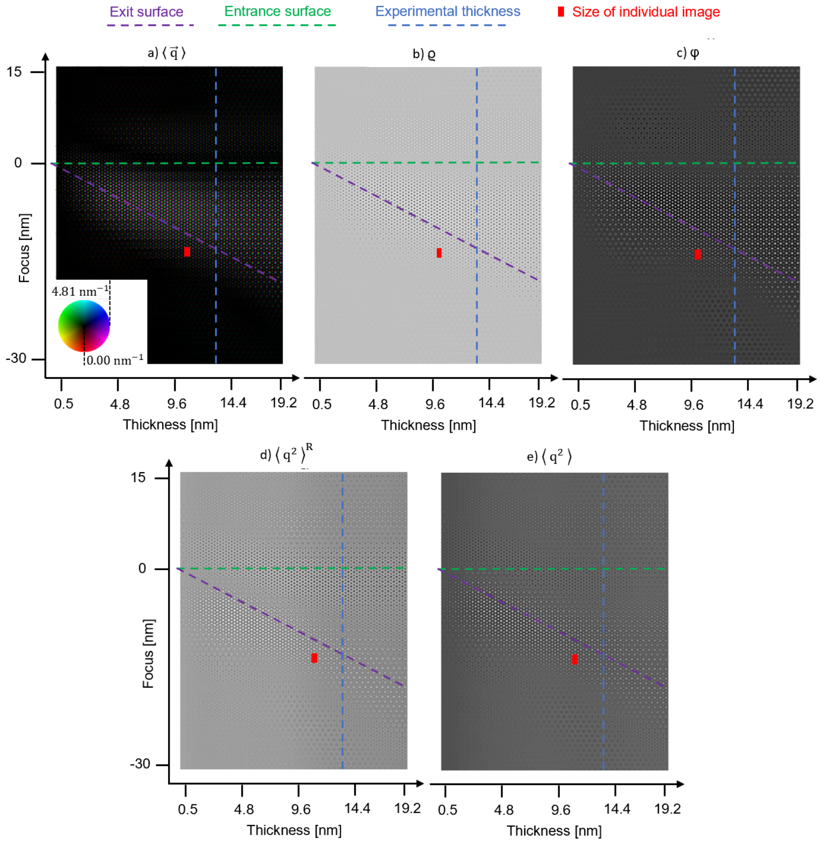

Figure 4.6: MR-STEM-specific signals, including $\langle \vec{q} \rangle$, $\langle q^2 \rangle^{\mathrm{R}}$ and $\langle q^2 \rangle$. Vectorial quantities are given using a colour wheel representation. The presentation is the same as in figure 4.5.

observed for the quantities ϱ and φ, shown in figure 4.6.b,c, follows the same pattern as $\langle \vec{q} \rangle$. For the $\langle q^2 \rangle^{\mathrm{R}}$ signal, presented in figure 4.6.d, two focus optima are found, with negative and positive atomic contrast at the entrance and exit surfaces, respectively. In particular, significant similarity to the ABF_{17-23} behaviour is observed. The normalized counterpart $\langle q^2 \rangle$, in figure 4.6.e, shows a similar focus-dependence, but with slightly increased contrast close to the exit.

4.3.4 Role of acceptance angle in the behavior of $\langle q^2 \rangle$

Although the newly available signals $\langle q^2 \rangle^{\mathrm{R}}$ and $\langle q^2 \rangle$ display interesting features in the focus dimension, relating to the geometry of the specimem, such features were obtained given a particular choice of cut-off angle, itself determined by the experiment. In that respect, for other STEM signals employing low-angle intensity, it is known that different dynamical behaviors can occur as a function of the detector radii [286, 289]. It is thus relevant to investigate the focus-dependence of the second moment as a function of its angular cut-off, as was previously

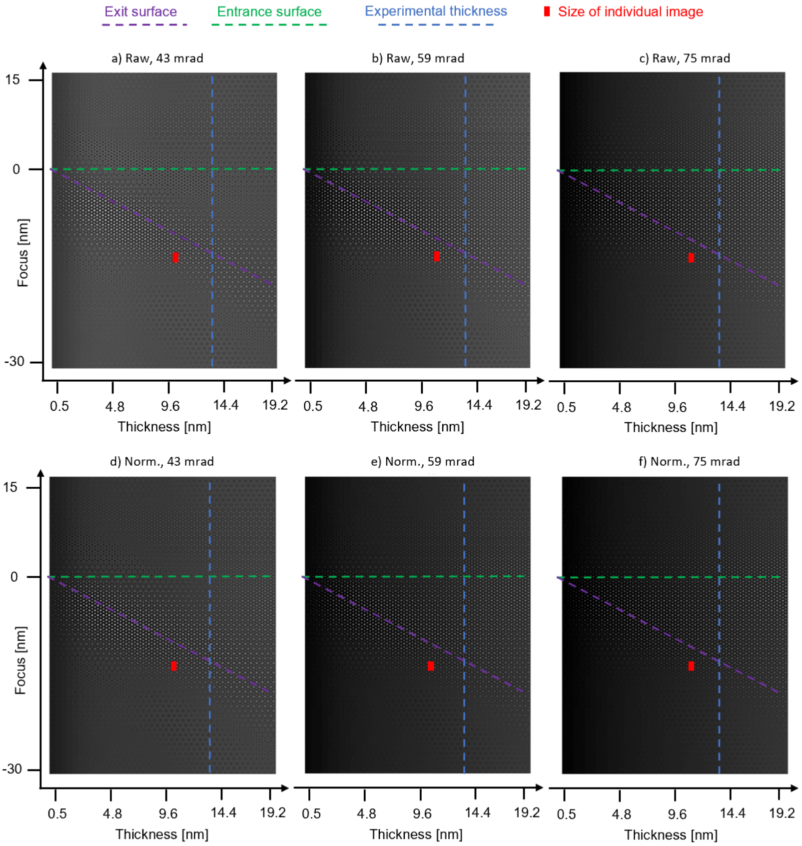

Figure 4.7: $\langle q^2 \rangle^{\mathrm{R}}$ and $\langle q^2 \rangle$ signals for increasing cut-off angles, as indicated. The presentation is the same as in figure 4.5.

done in section 2.4 for the thickness-dependence. To this end, the extraction is performed with cut-off angles of 43 mrad, as shown in figure 4.7.a,d, 59 mrad, in 4.7.b,e, and 75 mrad, in 4.7.c,f. Like in the previous subsection, a distinction is made between the normalized case $\langle q^2 \rangle$ and the raw one $\langle q^2 \rangle^{\mathrm{R}}$. As can be observed immediately for the 43 mrad case, the two contrast maxima are still present, though faintly, thus demonstrating the conservation of surface sensitivity for a large angular range, up to values above 40 mrad. As a consequence, surface detection through the use of the second moment is shown to be possible with robustness against variations of this parameter. For the two further cases studied, 59 mrad and 75 mrad, a transition occurs toward new focus-dependences, bearing similarities with the ADF imaging modes presented in figure 4.5.d,e. Atomic contrast then remains positive, with local maxima coinciding with the positions of atomic columns. In the 59 mrad case, higher intensity is seen close to the exit surface, whereas, in the 75 mrad case, it goes through a smooth decay across specimen thickness and reaches a peak close to the entrance. This transition from an ABF-like to a LAADF-like, and finally to an HAADF-like, profile is very interesting, as it confirms that the behavior of the scalar second moment can be tuned by use of the cut-off angle, not only in terms of thickness-dependence, but also with regards to more complex coherence-induced features. In particular,

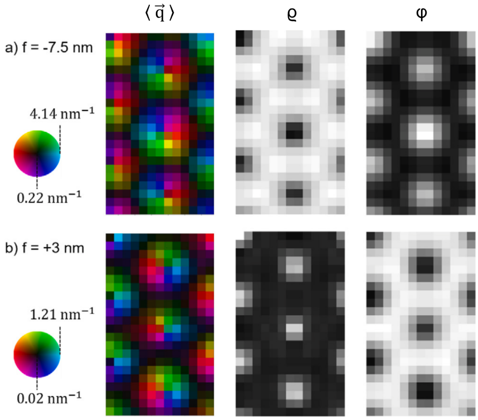

Figure 4.8: The simulated $\langle \vec{q} \rangle$ vector field for a thickness of 13.45 nm, and a focus of a) -7.5 nm and b) +3 nm. The vectors are depicted using the colour wheel representation. The integral φ and divergence ϱ are shown as well.

this can be related to the controlled proportion of incoherently scattered electrons participating in the signal, similarly to arguments made in section 2.4.

4.3.5 Inversion of $\langle \vec{q} \rangle$ across the focus axis

At the contrast maximum of $\langle \vec{q} \rangle$, atomic columns act as sinks of momentum transfer, and thus display a negative divergence. This is shown in figure 4.8.a, for the experimental thickness of 13.45 nm, where the first moment map, alongside ϱ and φ, is depicted. Such features are consistent with the intuitive physical interpretation under which the electrons are attracted by the positive charge carried by the nuclei, which therefore induces a shift of the center of mass of the diffraction patterns towards the center of the atomic site [74]. However, although the contrast is fairly low at foci close to the top surface, a faint optimum is observed above it. Interestingly, the momentum transfer vectors are then pointing away from the atomic sites, now being sources rather than sinks of momentum transfer. This is exemplified in figure 4.8.b. Whereas the mismatch of optimum foci between $\langle \vec{q} \rangle$, HAADF and BF is confirmed experimentally, such a reversal of the vector map for foci above the entrance surface is more difficult to see in the experimental vector field. This is due to the counting statistics of the camera, and in particular to the short dwell time employed. More generally, this feature can be related to the optical inversion of reciprocal space occurring as a result of the probe cross-over.

4.4 Multislice simulation of bulk Au

Whereas previous sections focused on the case of α-In_2Se_3 and found general agreement between behaviors observed in experiment and simulation, it remains relevant to add a further case to the study, and thus verify the consistency of the findings across different materials. For this purpose, an additional series of simulations was performed using bulk Au in [100] orientation, with a calculation window of 13×13 horizontally stacked unit cells, thus representing an area of (5.31 nm)^2, and a maximum simulated thickness of 75 vertically stacked unit cells, which is 30.59 nm. The scan window of 15×15 points was chosen to cover one unit cell of gold in the projection, with a scan interval of about 27 pm. The semi-convergence angle α and acceleration voltage U were set to 25 mrad and 300 kV, respectively. The results are depicted using the same general layout as in section 4.3, while employing a series of different STEM signals. Following the same terminology as used in previous sections, the selected signals consist of two bright field cases, BF_{25} and ABF_{20-25}, a low-angle and high-angle annular dark field signals, ADF_{25-30} and ADF_{50-100}, and a first and second moment, $\langle \vec{q} \rangle$ and $\langle q^2 \rangle$, obtained with an angular cut-off of 30 mrad. The real-space standard deviation profiles, plotted as functions of thickness and focus, are given as insets of the figures.

The images obtained for BF_{25} and ABF_{20-25} are compiled in figure 4.9. In both cases, a high contrast is obtained for probe depths close to the entrance surface of the specimen. As is more visible in the case of ABF_{20-25}, shown in 4.9.b, a second local contrast maximum is observed for a focus close to the exit surface, which is opposite to the one obtained at the entrance. While BF_{25} and ABF_{20-25} share a fair amount of features, a higher discrepancy is observed between the two considered annular dark field imaging modes, shown in figure 4.10, as was also the case in section 4.3. This is due to the difference in angular range, with ADF_{25-30} representing a particular choice of LAADF signal, and ADF_{50-100} being a HAADF signal, suitable for Z-contrast imaging. In the case of ADF_{50-100}, shown in 4.10.b, a single high-contrast region is observed, spanning a wide range of focus. For thicknesses lower than approximately 11 nm, atomic visibility is thus obtained for any probe depth laying within the specimen. On the other hand, ADF_{25-30}, displayed in figure 4.10.a, appears to follow a more complex focus dependence. Below the thickness of about 11 nm, dominant sites of atomic contrast close to the exit surface can nevertheless be seen. For thicknesses above this value, multiple contrast maxima are obtained across the focus axis. Such a complex collection of contrast maxima across the t-axis can be related to the channelling of the electron beam by the atomic columns of the specimen, since it is conditioned by the focus of the incident probe, as was shown in section 1.4. On the other hand, micrographs obtained for the vectorial first moment $\langle \vec{q} \rangle$ are compiled in figure 4.11.a and depicted in colour wheel representation. The integral φ is shown as well in figure 4.11.b. For this imaging mode, as in the case of α-$\mathrm{In_2Se_3}$, a dependence distinct from the ones observed for the BF and ADF modes is obtained. Indeed, the contrast is found to reach a maximum for a focus close to the exit surface, for thicknesses up to about 11 nm, and then at a constant depth, for thicknesses above that value. $\langle q^2 \rangle$, as displayed in figure 4.12, is characterized by a very strong local contrast maximum close to the exit surface, and another one at the entrance surface, thus showing the sensitivity of the signal to interfaces with vacuum.

4.5 Surface retrieval using a focal series

Whereas the discussions done in the previous sections were mostly concentrated on the discrepancies in the focus of optimum contrast among different STEM signals, another important finding was the possibility of using the experimentally determined focus-dependence to extract structural information. In particular, it was found that the positions of contrast maxima, in the focus axis, coincide with the vertical locations of interfaces between the material and vacuum, at least for signals employing the low-angle region of diffraction space. This prospect

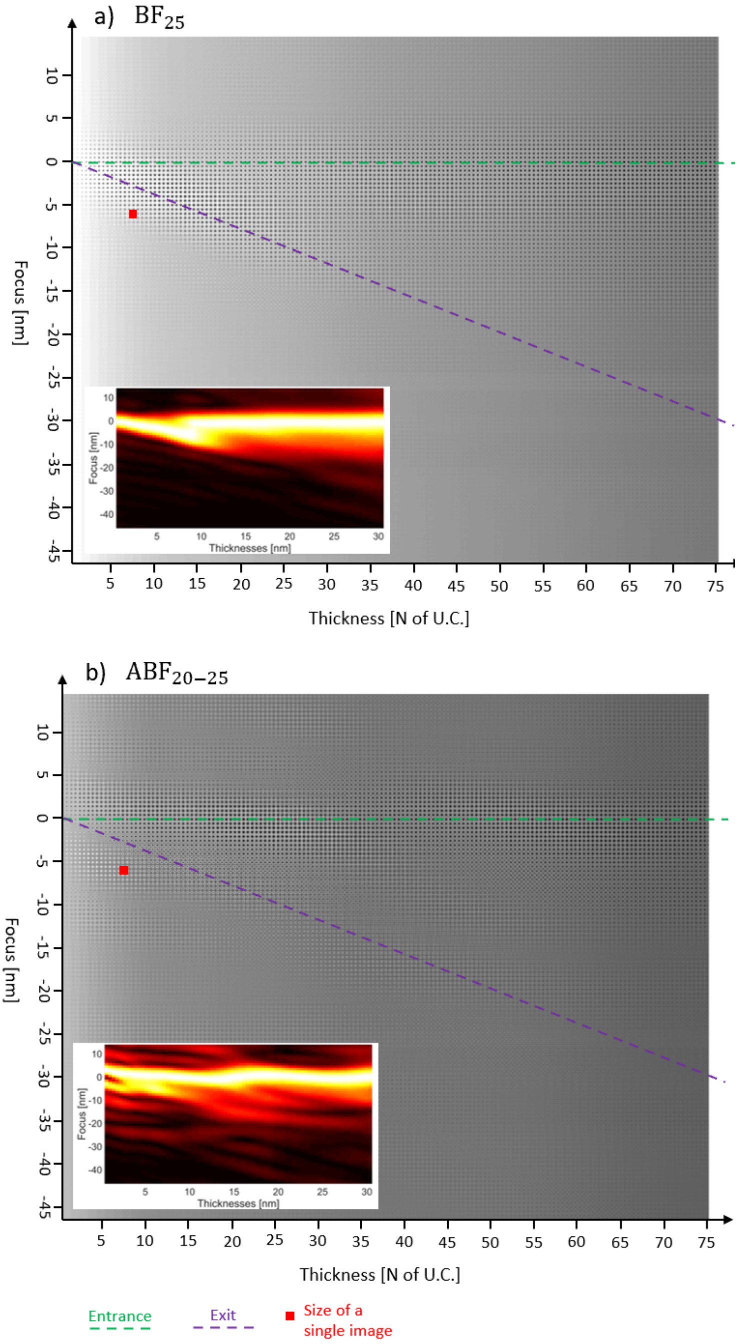

Figure 4.9: The real-space resolved a) BF_{25} and b) ABF_{20-25} signals are stacked along the focus and thickness dimensions. The positions of the entrance and exit surfaces on the focus axis are indicated as two lines, while the size of one given image is given as a red square. For each case, an inset depicts the real-space standard deviation plotted as a function of both thickness and focus. Each column of the inset figures is normalized to its minimum and maximum.

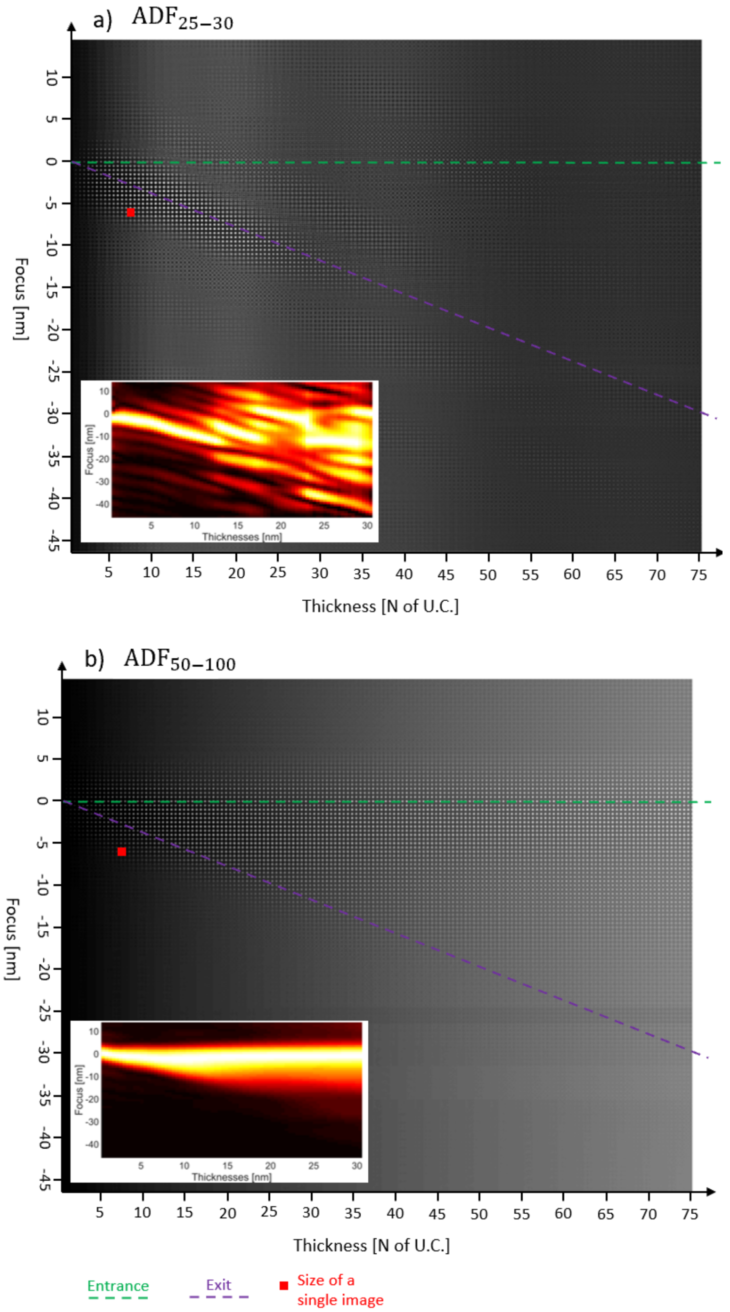

Figure 4.10: The real-space resolved a) ADF$_{25-30}$ and b) ADF$_{50-100}$ are stacked are displayed following the same model as in figure 4.9.

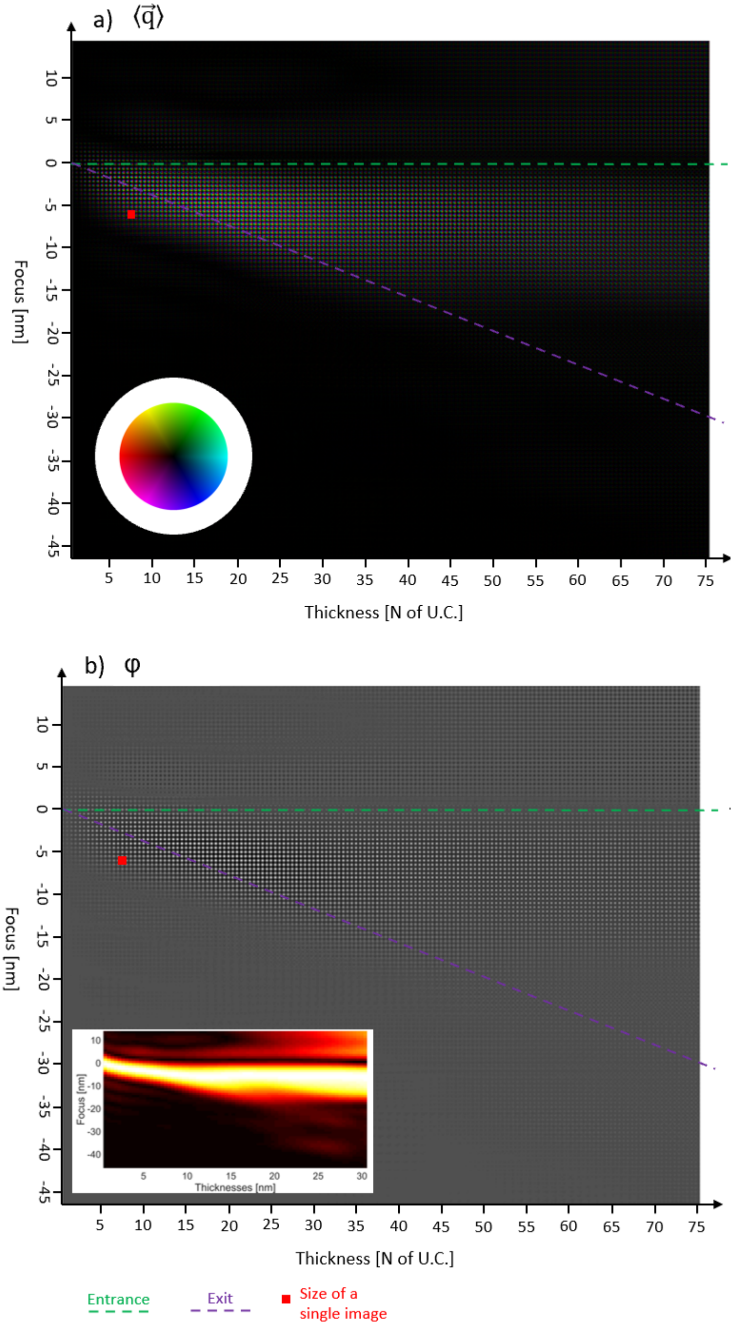

Figure 4.11: The real-space resolved a) $\langle\vec{q}\rangle$ signal and b) its integral φ are displayed following the same model as in figure 4.9. $\langle\vec{q}\rangle$ is given in vectorial colour wheel representation

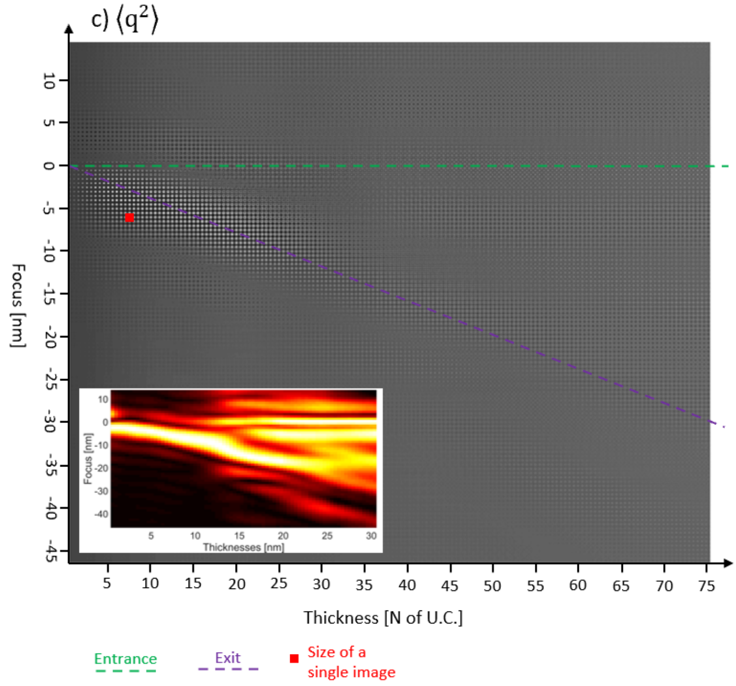

Figure 4.12: The real-space resolved $\langle q^2 \rangle$ signal is displayed following the same model as in figure 4.9.

is especially interesting for future investigations of the surface topography of specimens, or even for particle shape retrieval applications. Although a qualitative agreement was established between experiment and simulation, no information was available on the exact aberration function and partial coherence properties of the employed illumination. The simulations were thus done in perfect experimental conditions, save for the inclusion of specimen tilt, and no attention was paid to the possible influence of further unknown parameters.

The rest of this chapter therefore aims at filling this gap, and pursuing from the simulation results presented in chapter 4, by means of comparing the focus-dependences obtained in different conditions. For this work, bulk Au in [100] zone axis incidence was chosen as model, for its crystallographic simplicity. The basic simulated case, as well as the selection of STEM signals, are the same as used in section 4.4. Further simulations and treatments were performed to account for the factors considered here, and for the comparisons done thereafter. Throughout the following sections, the main objective remains the interpretability of the focus-dependences, such that the positions of the surfaces can still be extracted straightforwardly.

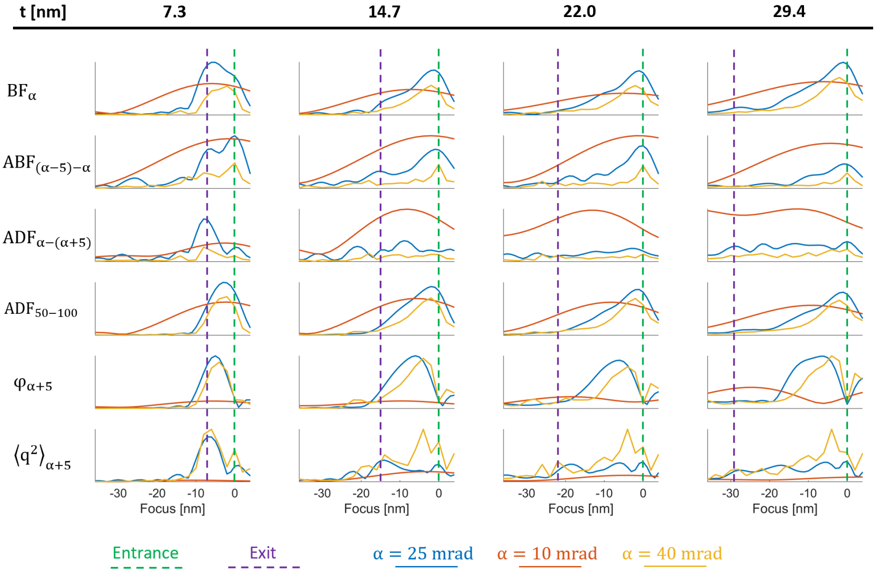

Figure 4.13: The real-space standard deviation is given as a function of focus, for the six signals considered, and for a selection of four different thicknesses, equal to 18, 36, 54 and 72 times the unit cell thickness of 0.40782 nm. In each plot, the curves obtained for semi-convergence angles of 25, 10 and 40 mrad are depicted. The positions of the entrance and exit surfaces in the focus axis are indicated as well.

4.6 Focus-dependence for different depths of focus

When employing focus-dependent features in STEM, obtaining a sufficient resolution in the depth dimension is of high importance. In the STEM measurement geometry, and in the absence of aberrations, this parameter is generally determined by the numerical aperture radius $\sin(\alpha)$ and the wavelength λ. Indeed, as the phase shift induced by the free-space Fresnel propagator, used to insert the probe focus f in the formalism, increases with $|\vec{q}|^2$, the inclusion of higher spatial frequencies in the formation of the real-space probe results in a larger impact of a given focus change. Those concepts are encompassed by the depth of focus δz_{DOF}. In order to investigate the influence of δz_{DOF} in a signal-dependent manner, simulations were thus performed with semi-convergence angles α of 10 and 40 mrad. The signals of interest were then calculated, as well as their real-space contrast, as shown in figure 4.13. This was done as a function of focus, for thicknesses equal to 7.3, 14.7, 22.0 and 29.4 nm, corresponding to a vertical stacking of 18, 36, 54 and 72 unit cells. At this point, it is important to note that the signals considered here, contrary to those shown in further sections, are not actually the same among the three different cases. This is, of course, because the intuitive division of diffraction space into high-angle, low-angle, bright field and dark field regions is dependent on the size of the primary beam. For this reason, the signals are here explicitly defined as a function of α, with the exception of ADF_{50-100}, which can be considered to represent a high-angle ADF signal in all cases. A qualitative comparison among the cases is then still possible. As taken from figure 4.13, the large depth of focus obtained from the low value of $\alpha = 10\,\text{mrad}$ is here observed to

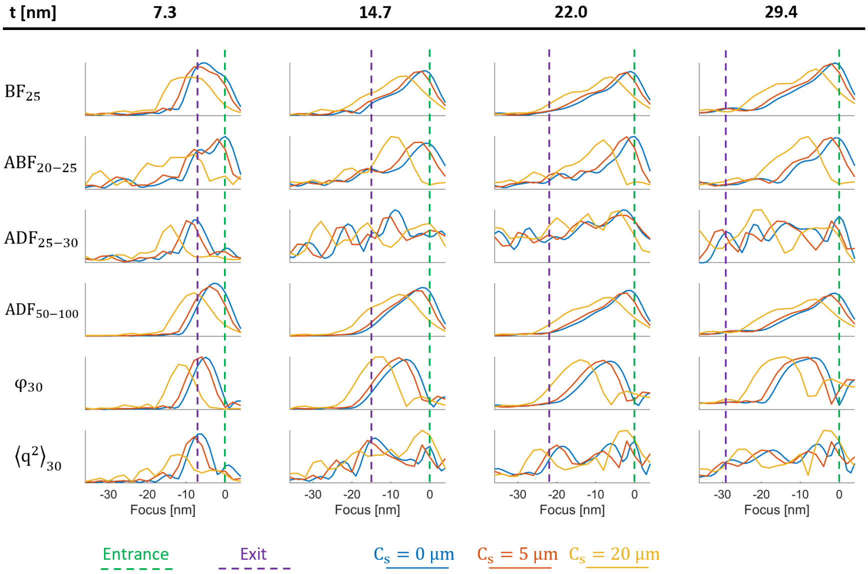

Figure 4.14: The real-space standard deviation is depicted following the same template as in figure 4.13. In each plot, the curves obtained for the unaberrated case and a spherical aberration C_s of 5 and 20 μm, are depicted.

be sufficient to erase all the complex focus behaviors observed when $\alpha = 25$ mrad. In this case, and for all considered signals, the focus-dependence consists of a broad curve, which thus only contains one contrast optimum. Interestingly, it can be observed that, among the signals, large mismatches of several nm still occur. The case where $\alpha = 40$ mrad, On the other hand, results in a conservation of the entrance and exit surface peaks, though with some displacement along the focus axis, and some variations of the peak ratios. Finer contrast features are additionally present.

4.7 Role of geometrical aberrations

4.7.1 Third-order spherical aberration

Continuing, given that the focus is inserted in the general formalism by modification of the function χ, it is relevant to investigate how a dependence of the depth features to aberrations can be then induced. This is here initiated by the third-order spherical aberration C_s. As it was explained in section 1.3, the main effect of C_s on the electron probe, and its focus-induced variations, is a displacement of the point of maximum amplitude across the focus axis. Here, this can be expected to result in a simple displacement of image features across the focus axis. To verify this, two additional simulations were performed, with respective values of 5 and 20 μm for C_s, whose results are plotted in figure 4.14. For all signals, the influence of a positive third-order spherical aberration is mostly observed in the form of a shift of contrast peaks

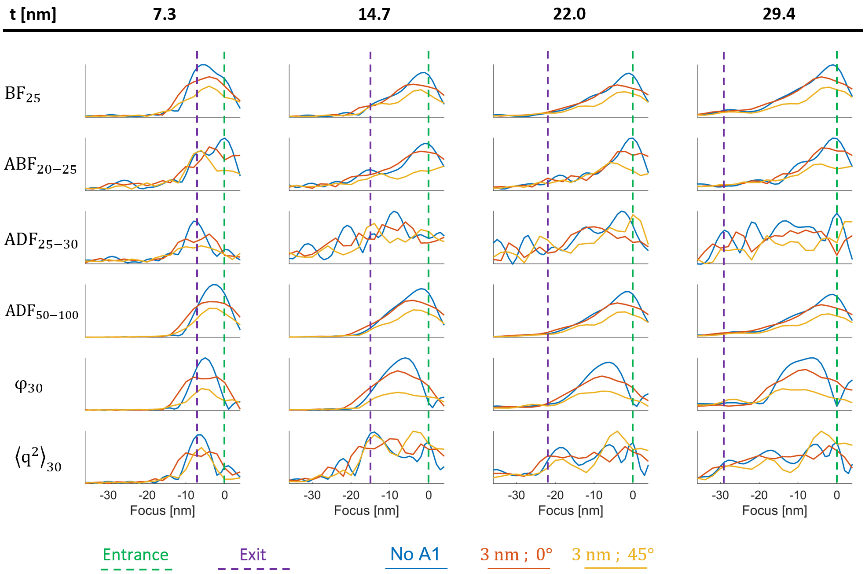

Figure 4.15: The real-space standard deviation is depicted following the same template as in figure 4.13. In each plot, the curves obtained for the unaberrated case, a first-order astigmatism A_1 with modulus of 3 nm and rotation of 0°, and a rotation of 45°, are depicted.

towards negative foci, as expected. Some small variations in the overall shape and height of the contrast peaks are additionally seen, which can be related to more complex variations of the focus-profile of the incident probe, as was shown in figure 1.10.

4.7.2 First-order astigmatism

Simulations were also done with two different settings of the first-order astigmatism A_1. Specifically, a modulus of $C_{1,2} = 3\,\text{nm}$ was chosen, with two different angular offsets $\beta_{1;2}$ of 0° and 45°, respectively. The resulting curves are given in figure 4.15. Beyond the overall loss of contrast across the whole f-axis, the influence of A_1 is observed to be lowest on the focus-dependences obtained for the BF$_{25}$ and ADF$_{50-100}$ signals, for which only a slight shift of the contrast peak occurs. This is not unexpected, as the employment of a large angular range results in a generally more incoherent signal, as explained in section 2.1, and thus in less sensitivity to aberrations. The influence on φ is also fairly minor, except for lower thicknesses, and specifically for the 45° rotation case, where the contrast peak appears to be widened. Such a feature is more difficult to interprete intuitively, but may be related to the stronger channelling by the atomic columns along the [110] crystalline axis, occurring due to the extension of the probe in the corresponding direction. The effects of A_1 are generally more important in the cases of ABF$_{20-25}$, ADF$_{25-30}$ and $\langle q^2 \rangle$, where the overall appearance of the focus-dependence is modified in a way such that the relation to existing geometrical features can potentially be occluded. This in turn shows the importance of accurately correcting this aberration when attempting to use coherent signals in a STEM analysis.

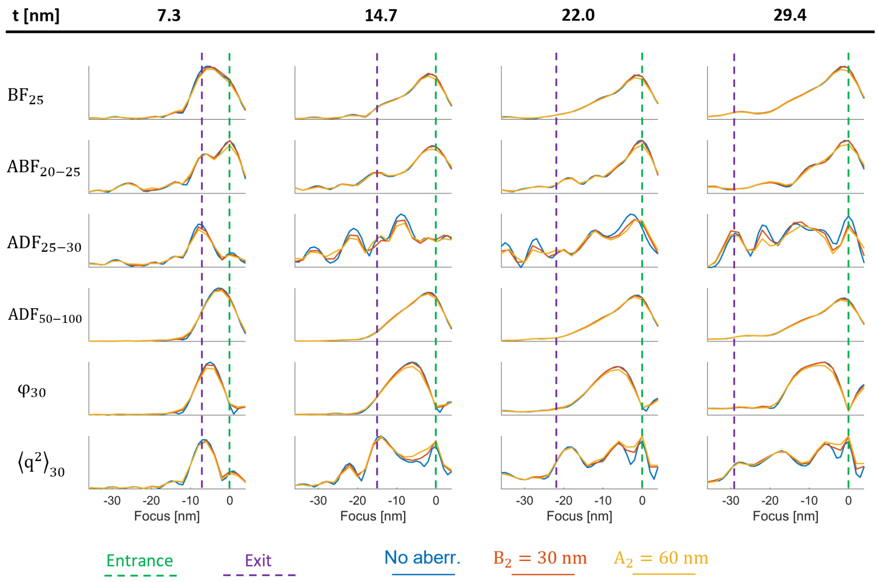

Figure 4.16: The real-space standard deviation is depicted following the same template as in figure 4.13. In each plot, the curves obtained for the unaberrated case, a second-order coma B_2 with modulus of 30 nm and a second-order astigmatism A_2 with modulus of 60 nm, are depicted.

4.7.3 Second-order coma and astigmatism

Additional simulations were done, including a second-order astigmatism A_2 of 60 nm in modulus, and a second-order coma B_2 of modulus 30 nm, meaning within values above what would be targeted in an aberration-corrected STEM experiment. The focus-dependences obtained in those cases, as depicted in figure 4.16, are found to be largely unchanged compared to the unaberrated case. This demonstrates that, whereas A_1 is critical for the conservation of the focus-dependent features, second-order aberrations do not induce any further complications for FS-STEM, outside of the expected distortion of a given image owing to the resulting PSF.

4.8 Influence of the partial spatial and temporal coherence

As was explained in section 1.4, to accurately model a diffraction dataset affected by partial coherence, each diffraction pattern is replaced by a weighted average done within real-space to model PSC, and within the f-axis to model PTC [166, 170, 171]. These averages are here performed with a sampling equal to 27 pm in the scan dimensions, and 1 nm in the focus dimension, using Gaussian weightings with respective widths equal to the effective source size Δr and to the focus spread Δf. In figure 4.17, results obtained with $\Delta f = 1.274\,\text{nm}$, and $\Delta r = 21.233\,\text{pm}$, respectively, are presented. Note that those numbers were chosen as they lead to Gaussian full widths at half-maximum of 3 nm, for PTC, and 50 pm, for PSC. As can

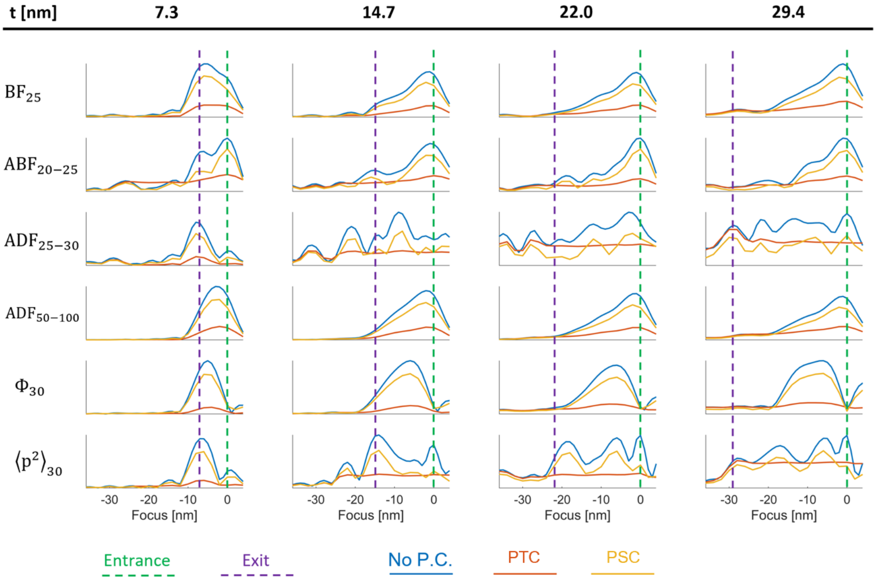

Figure 4.17: The real-space standard deviation is depicted following the same template as in figure 4.13. In each plot, the curves obtained for the fully coherent case, partial temporal coherence and partial spatial coherence, respectively obtained with a Gaussian FWHM of 3 nm, and 50 pm, are depicted.

be observed, the focus-dependences obtained for BF_{25}, ADF_{50-100} and φ are nearly unaffected by the inclusion of partial coherence. This is however not the case for the other signals which, at least for higher thicknesses, lose some of their characteristics. As in the case of the coherent broadening due to aberrations, this state of fact can be explained by detector size arguments. For ABF_{20-25}, the influence of PSC nevertheless does not go much further than a variation of the entrance peak height, which still represents the overall maximum of achievable contrast. On the other hand, the influence of PTC appears stronger, with the loss of the exit surface contrast peak, although not occurring for higher thicknesses. In the cases of ADF_{25-30} and $\langle q^2 \rangle$, similar observations can be made with regards to the influence of PSC, though some peaks then tend to vanish for higher thicknesses. The influence of PTC is, there as well, more important, as it leads to a loss of the entrance surface peak.

4.9 Other factors relating to the specimen

4.9.1 Specimen tilt

The effect of specimen tilt is additionally investigated, owing to its general importance in understanding dynamical diffraction and image formation in STEM [297, 298, 247]. Two simulations were performed, representing two distinct cases of a tilted specimen, by including the inclination directly in the Fresnel propagator [279]. In particular, a tilt magnitude of 5 mrad was

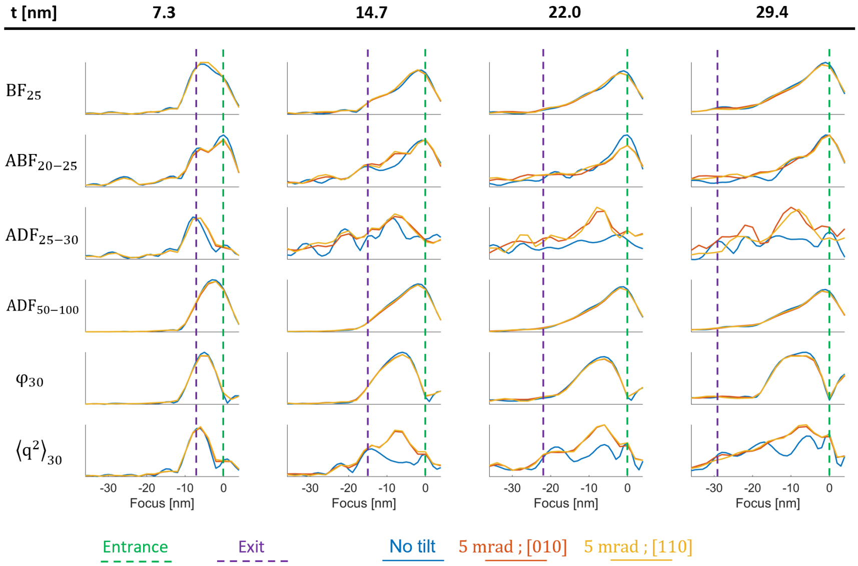

Figure 4.18: The real-space standard deviation is depicted following the same template as in figure 4.13. In each plot, the curves obtained for the untilted case, a tilt of 5 mrad toward the [100] zone axis and a tilt of the same magnitude, but toward the [110] axis, are depicted.

chosen, with two distinct orientations. The first corresponds to a tilt toward the [010] axis and the second toward the [110] axis. The focus-dependences obtained for these two simulations are given in figure 4.18. As is immediately observed, the influence of tilt, at least in this range, is nearly unnoticeable in the case of the BF_{25}, ADF_{50-100} and φ signals. It also remains low for ABF_{20-25}, although its lower contrast peaks, observed close to the exit surface and within the specimen thickness, are still affected. In the case of ADF_{25-30}, and at least from a certain thickness on, shifts are seen in the contrast peaks as well as changes in their relative heights. For $\langle q^2 \rangle$, and again except for the smallest considered thickness, the peaks at the entrance and exit surfaces vanish, while a unique peak appears a few nm below the entrance. Whereas the reduced impact of mistilt for low thicknesses is expected, since the propagation through matter is then less important overall, it is also interesting that no deep difference is here observed between the effects of the two orientations tested here, even though they are not crystallographically equivalent.

4.9.2 Carbon contamination

Since the detection of surfaces relies on the use of electrons scattered toward low angles, it can be expected to display a sensitivity to factors affecting primarily the low-angle dark field. One of those factors is the scattering by an amorphous layer of carbon contamination [204, 205]. In order to faithfully represent the influence of such a layer on the diffraction data, the electron probe was propagated through an amorphous carbon cell before reaching the specimen. To obtain a realistic atomic distribution in three dimensions, this cell was obtained by relaxation of a $(100\,\mathrm{nm})^3$ cube filled with C atoms initially placed at random positions, using Tersoff poten-

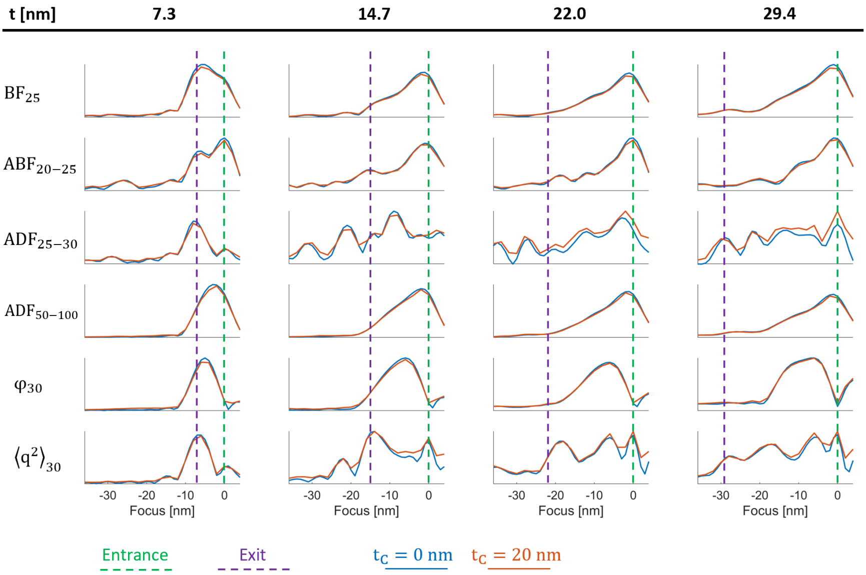

Figure 4.19: The real-space standard deviation is depicted following the same template as in figure 4.14. In each plot, the curves obtained for the uncontaminated case and a carbon thickness of 20 nm are depicted

tials [299], as implemented within the LAMMPS software [300, 301]. Note that this LAMMPS relaxation was performed by collaborators in the University of Antwerp. The results of the STEM simulation are given in figure 4.19, for which a carbon thickness of 20 nm, divided in slices of 2 nm each, was employed. As expected, the direct influence of this layer is only visible in signals employing the low-angle annular dark field region of diffraction space. This effect is however limited to a slight change in the peak heights for ADF_{25-30} and $\langle q^2 \rangle$.

4.9.3 Temperature

Another important aspect of the surface detection approach is its reliance on coherent properties of the employed imaging modes. In turn, it can be supposed that surface visibility is improved at lower specimen temperatures or worsened at higher ones. Since the focus-dependent features observed here so far were calculated only at room temperature, it is relevant to investigate whether and how they are conserved for further cases. Whereas the governing parameter of the frozen lattice approximation is the mean squared thermal displacement, changing its value before the generation of the configurations V^j allows to obtain temperature-dependent diffraction patterns. In figure 4.20, the focus-dependences obtained at room temperature, the liquid N_2 temperature of 77 K, as well as the higher values of 190 and 400 K, are depicted. As it turns out, only minor variations, notably in peak ratios, occur from one curve to another. A slight change is nevertheless observed in the shape of the contrast peak obtained for ADF_{50-100}, when going toward liquid nitrogen temperature. This can be interpreted as the result of a lower TDS contribution when the vibration amplitude of the atoms is kept low. Otherwise, the ab-

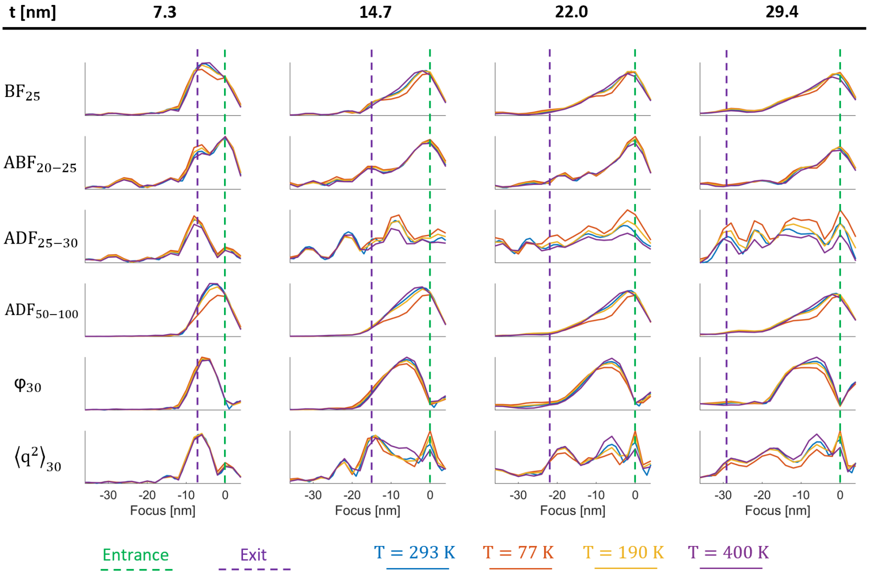

Figure 4.20: The real-space standard deviation is depicted following the same template as in figure 4.13. In each plot, the curves obtained for 293 K (room temperature), 77 K (liquid N_2 temperature), 190 K and 400 K, are depicted.

sence of a clear temperature-dependence of the focus-induced surface contrast is interesting as it shows that the requirement for the method, rather than being on the general coherence properties of the experiment, is only critical for the illumination, as was demonstrated by figure 4.17.

4.10 Comparison with other materials

Finally, while requirements could be derived both on the properties of the illumination and on possible imperfections of the specimen, it remains to provide a sense of their specificity to the Au case, used as model so far. For the simulations presented in this section, two more face-centered cubic metals, Ag and Cu, were thus employed with a goal to compare the dependences obtained, for the same thicknesses and signals. The results are given in figure 4.21. Overall, similar features are observed for all the signals considered, including contrast peaks at the entrance and exit surfaces of the specimens. Nevertheless, minor variations can be noticed in the height and exact positions of the peaks, from one material to the next. Furthermore, in the case of the BF_25, ABF_{20-25} and ADF_{25-30} signals, a stronger contrast is obtained at the exit position, for the Cu and Ag specimens, than for the Au specimen. Interestingly, in the case of φ, and for both Cu and Ag, a doubling of the contrast peak is also seen, with one maximum being located a few nm above the exit surface, and the other remaining at the same position as for the Au case. In general, while lower local values of contrast can be related to the atomic number Z, as the interatomic distances are close among the three materials used, more complex differences, such as the shifts in the positions of optima, can be related to the induced changes

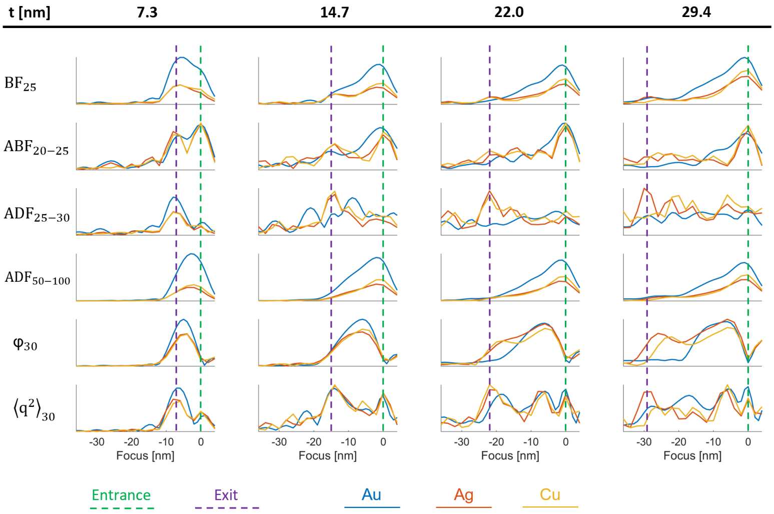

Figure 4.21: The real-space standard deviation is depicted following the same template as in figure 4.13. In each plot, the curves obtained for Au, Ag and Cu are depicted.

in the exact channelling mechanism. Overall, since the observed features are still not inherently different from one case to the other, the general validity of the method is confirmed.

Discussion

Through the results presented in this chapter, it was found that different imaging modes in STEM are affected by probe focus in a specific manner, that is itself dependent on the thickness of material traveled through. In particular, the focus for which a maximum of real-space contrast is attained is inherently signal-specific. With regards to the interpretation of STEM results, this observation can appear fairly counter-intuitive, as it implies that the best condition for imaging is not necessarily the one for which the incident electron probe has the lowest extension in real-space. Instead, it was determined that the optimal recording condition is specific on the type of recording that is performed, and thus depends on the complex image formation mechanisms involved in obtaining a specific STEM signal. An application of this principle can be found, for instance, in the mismatch of focus between $\langle\vec{q}\rangle$ and HAADF, and thus between a measurement of the average momentum transfer and Z-contrast. Such considerations are critical for MR-STEM techniques, as they may make it difficult to obtain multiple signals simultaneously while conserving an optimum image quality. In other words, a fast electron camera does not necessarily provide universally employable data.

Another aspect of those questions, with regards to C-STEM signals, is the role of detector radii. As is shown both experimentally and through simulation, both the BF and ADF signals can display very different dependences for varying detector sizes. This can be understood, to a large extent, through the fact that the integration of intensity within an angular range is equivalent to an incoherent summation of the corresponding spatial frequency components of the real-space electron wave exiting the specimen. The more pixels a virtual detector contain, the more of those components are summed, and the more damping of the coherent features of the real-space image occur. This is for this reason, for instance, that contrast reversal mechanisms tend to be more strongly visible in BF signals obtained with a rather small angular range.

Furthermore, as a response to the potential issue of unequal signal quality, the FS-MR-STEM approach provides further flexibility with regards to imaging conditions. This is nevertheless at the cost of experimental practicability, since the specimen is required to remain stable while several scans are performed in the same area. Additionally, this approach has the advantage of yielding geometrical information, including the position of the interfaces between the specimen and vacuum, along the depth dimension. This measurement was here shown to be best performed using $\langle q^2 \rangle$, due to its robustness against limited variations of the angular cut-off. This prospect was further explored by a series of simulations aiming at establishing experimental requirements for such a measurement.

The first factor studied here was the depth of focus δz_{DOF}, controlled by the semi-convergence angle. Upon employing a low enough α, such that the value taken by the depth of focus gets close to the specimen thickness or above, the complex features contained in the focus-dependence tend to vanish, although mismatches of maximum contrast remain among the signals. This is interesting given that, in the absence of an aberration-corrector, STEM experiments are often performed with semi-convergence angles close to 10 mrad. On the other hand, when using higher values of α, surface contrast remains.

This study was continued with the impact of several aberrations. The first of those was the third-order spherical aberration C_s. In otherwise perfect conditions, this aberration was not found to cause problems for the interpretation of focus-dependences, given that its main effect, at least in a limited range of values, is a shift of the features along the focus dimension. On the other hand, the influence of a reasonable value of first-order astigmatism A_1 was found to be more difficult to predict, though less problematic for the most common signals. In particular, the low sensitivity of BF$_{25}$ shows that measuring the position of the entrance surface should still be possible in the presence of non-zero A_1. The detection of the exit surface, On the other hand, which would be performed using the LAADF, ABF or $\langle q^2 \rangle$ modes then becomes more challenging. Finally, the second-order coma B_2 and second-order astigmatism A_2 were found to not affect the focus-dependences strongly.

Going beyond the coherent spreading of the electron probe through the aberration function χ, its incoherent spreading by PTC and PSC was also investigated, for a high-quality, albeit still realistic [156, 152], source. As it turns out, the dependences displayed by ADF$_{50-100}$, BF$_{25}$ and $\langle \vec{q} \rangle$ are left nearly intact by both PSC and PTC, which again saves the possibility to infer the position of the entrance surface. The signals showing mostly coherent features, ADF$_{25-30}$, ABF$_{20-25}$ and $\langle q^2 \rangle$, are however affected in a non-negligible manner. It nevertheless seems that, at least in a specific range of thickness, ADF$_{25-30}$ and $\langle q^2 \rangle$ would still be usable to detect the exit surface.

Leaving aside the factors pertaining to the illumination, specimen tilt was also introduced as a relevant factor to study the focus-dependences. Here, its influence on the dependences obtained for ADF$_{50-100}$, BF$_{25}$ and $\langle \vec{q} \rangle$ was found to be fairly low. This, again, signifies a conservation of the capacities for the retrieval of the entrance surface. ABF$_{20-25}$ also does not display a lot of variations, though some of the finer features within the specimen depth tend to be modified. ADF_{25-30} and $\langle q^2 \rangle$, On the other hand, lose their exit surface peaks, at least for higher thicknesses. In that context, it is clear that, whereas the retrieval of the exit surface could still be possible under low specimen tilts, the criterion for the thickness range would then become stricter. Moreover, a thick amorphous carbon layer of 20 nm was found to have only a low influence on all the signals investigated. In that respect, this contribution is not expected to be a strong limitation to the detection of interfaces between a metallic specimen and vacuum or, in that case, carbon. In addition to elements that were here considered strictly as limiting factors, variations of temperature were furthermore carried out in simulations. Those variations led to the conclusion that temperature only has a low influence on the focus-dependences, which is interesting when compared to the results obtained with a partially coherent probe. Indeed, this shows that the requirement of coherence for surface contrast, while remaining important with regards to the size of the detector and the illumination, is less strict with regards to lattice vibrations.

Finally, a comparison among different metallic materials with a face-centered cubic unit cell, specifically Au, Ag and Cu, was done. There, it was possible to establish that a different atomic number Z can lead to different levels of contrast at the exit surface, at least for a fixed STEM signal. This in turn can be linked to the exact channelling mechanism occurring within the specimen illuminated. Furthermore, the behavior of the first moment was also found to vary in an interesting manner as a function of the observed material. Even then, the few main targeted aspects of the focus-dependences remain present, which is important for the application of surface detection to a wide range of objects.

General discussion

Scalar second moment $\langle q^2 \rangle$

The scalar second moment $\langle q^2 \rangle$, introduced in section 2.4 of this thesis, is a physical quantity representing the average square modulus of the lateral momentum transfer of the probing electrons, following the interaction with the specimen. It is part of the many new signals that can be flexibly extracted from the diffraction measurements done in the frame of a 4D-STEM experiment, and it possesses properties which make it attractive for material characterization. Those properties are dependent on the exact cut-off spatial frequency q_l chosen for the extraction, and thus on the relative impact of TDS over coherently scattered electrons, which can thus be used as a degree of freedom in tailoring the resulting contrast. In particular, by making the angular limit relatively small, meaning just a few mrad more than the semi-convergence angle, focus-dependent features appear, enabling surface detection. Otherwise, a Z-contrast-like behavior can be induced by making the incoherent high-angle intensity dominant, which provides opportunities for thickness measurement, for instance. Finally, a logarithmic divergence is observed when q_l goes toward infinity, which can be predicted by means of employing the Mott relation.

Role of inelastic scattering in dynamical electron diffraction

The interplay of elastic diffraction features with the multiple inelastic contributions resulting from excitations occurring within the specimen, while the electron beam travels though it, is an important factor for the development of STEM methodologies. Nevertheless, the topic of energy-loss itself is by no means new, and has been largely explored in the framework of routine spectroscopic measurements. In fact, the existence of a diffuse inelastic component in electron diffraction has long been reported. Solutions for its exclusion were thus already proposed years ago, in the context of structure retrieval methods based on CBED measurements, through energy-filtering [271]. In the field of quantitative STEM, however, interest is usually taken in the TDS component, due to its incoherent characteristics and linearity against relevant parameters such as thickness, rather than in low-angle scattering. Beyond the inherent qualities shown by Z-contrast, this state of fact can also be explained by the difficulty of accurately and efficiently simulating energy-dependent electron diffraction. Furthermore, contrary to the case where crystallographic features are employed directly in structure refinement procedures [207, 208], energy-filtering is not an obvious solution here. This is because the restriction to the zero-loss peak, and thus to the elastically and quasi-elastically scattered electrons, would result in a loss of intensity from the incident beam, expressed by a quantity $exp\left(\frac{t}{\Lambda}\right)$. As this quantity is dependent both on the thickness of the material imaged and on its chemical composition, due to the variety of inelastic scattering processes contributing to the mean free path Λ, all attempts at a rigorous characterization would be then prevented. In this context, it is clear that the inclusion of energy-loss in a simulation is a strict requirement for the application of quantitative STEM to low-angle scattering.

In chapter 3, work was thus presented on the influence of the excitation of volume plasmons by the probing electrons, which usually represents the strongest component of the energy-loss spectrum of bulk metals. For this purpose, the EF-MR-STEM methodology was introduced, where diffraction patterns are formed while restricting the contributing electrons to the quasi-elastic and inelastic cases, thus allowing the immediate visualization of the diffraction features carried by the corresponding collections of wave states. In particular, a redistribution process could be observed where the diffraction features are blurred, and intensity is transferred toward the low-angle dark field, mainly through a depletion of the primary beam. Those results were used for further interpretation involving multislice simulations including single plasmon excitations. Though this model did not provide fully quantitative information, likely due to even further factors not included then [250], a qualitative reproduction of the features could be achieved.

In a second time, experiments were performed while making use of multiple plasmon peaks, occurring in a material with high thickness. There, it was possible to demonstrate a comparability between the successive redistribution processes, in particular through the convolution with a Lorentzian kernel. This last point was made in the context of testing an approximation based on reporting the interaction with the inelastic transfer function down to the end of the propagation, thus effectively eliminating the entire physical process involving the generation and travel of mutually incoherent waves. In that manner, a direct relationship could be established among the intensity distributions obtained for each energy window. Although this approach is based on an inherently unrealistic inelastic interaction model, it was found to be successful in both the theoretical and experimental frameworks. This in turn can be largely related to the collective nature of plasmon modes in the illuminated material. As such, the method is likely inapplicable to the excitation of core electrons, for instance. Beyond that, a suggestion to implement plasmon scattering in an empirical manner, by use of known Lorentzian parameters, can be made with the purpose of drastically reducing calculation times. In particular, such a model would enable the easy representation of multiple plasmon-loss, and would thus permit the measurement of chemical composition even in materials with high plasmonic activity.

Influence of probe focus on a variety of MR-STEM signals

While momentum-resolution provides an opportunity for the investigation of further contributions to low-angle scattering, it also constitutes a framework for an analysis based on the extraction of a collection of signals, and the employment of their dependences to distinct physical quantities. A first example of such an approach is the combination of the measurement of the average momentum transfer, which has applications for the retrieval of electric and polarization fields [74, 249], and of incoherent high-angle scattering, which varies monotonously with thickness and atomic number [218, 219, 220]. For such an analysis to be performed in the best conditions, all the signals are expected to display high contrast, and thus to have reached an optimal, atomically-resolved, sensitivity to the quantities to measure. Nevertheless, STEM signals often reach this optimal contrast in specific conditions, including a carefully chosen probe focus. In chapter 4 of this thesis, it was thus shown, both experimentally using the newly introduced FS-MR-STEM methodology and through simulations, that the focus of maximum contrast is indeed different from signal to signal, even when obtained from a single diffraction recording. For this reason, momentum-resolution may not provide universal quality and precision in the multiple information extracted using it. What those findings also demonstrate, with regards to the technique, is that a lot of care should be taken in the interpretation of differently extracted micrographs, and that tuning the electron probe for the intended measurement can be necessary for later analysis. Alternatively, the direct acquisition of a focal series can be seen as a solution to this potential issue, though demanding experimentally.

The FS-MR-STEM approach was also found to have an supplementary interest, thanks to the presence of inherent structural information in the behavior displayed by certain imaging modes against focus variations. Indeed, the scalar second moment, as well as other signals, was found to possess a focus-dependence containing multiple local contrast maxima, coinciding with geometrical features of the specimen. Therefore, when employing $\langle q^2 \rangle$, ABF or LAADF imaging, high contrast can be obtained when the probe is focused at certain heights, which include the entrance and exit surfaces of the specimen. This behavior, which was initially reported in simulations of LAADF images [289], can be generalized to all signals obtained using the low-angle region of reciprocal space. With this finding, an opportunity thus arises to perform a direct measurement of surface locations by means of a depth sectioning experiment, combined with momentum-resolution or an annular detector covering a specific angular range. This prospect was further explored through a large range of simulations, in order to provide a more precise picture of the experimental requirements for such an experiment. In that context, the influence of further illumination conditions, such as the depth of focus, aberrations and partial coherence, was investigated. The effects of a tilt from a perfect crystallographic alignment, carbon contamination, temperature and the atomic number were additionally studied. Overall, it was found that the requirements for the generation of focus-dependent surface contrast include a careful correction of geometrical aberrations, as well as a limited degree of incoherence in the illumination. Conditions related to the state of the specimen, such as lattice vibrations or surface contamination, seem to be less strict, which is encouraging for the application of this prospective method to a wide range of material systems.

Conclusion

Through the work presented in this thesis, distinct advances have been made toward the goal of quantitatively analysing low-angle electron diffraction. In that respect, a specific interest was taken in the roles of inelastic scattering and the focus of the objective lens. Furthermore, new possibilities for materials imaging and characterization were presented, through the combined employment of multiple recording dimensions, including the real-space position, momentum, energy and probe focus. Such multidimensional electron diffraction measurements represent a very rich basis for new methodologies aiming to investigate solid matter at the atomic level.

Among the developments reported here, models to include the excitation of plasmon modes, as a part of dynamical diffraction simulations, were introduced, including a simplified approach for cases where such energy transfers occur multiple times for single electrons. Furthermore, some insights on the dynamics of the variety of imaging modes available through the acquisition of intensity were provided, alongside prospects for their employment toward the detection of surfaces.

With this work reaching a conclusion, it is interesting to note that, whereas a large volume of information can be made available experimentally, by using a fast diffraction camera, its interpretation remains far from trivial. In fact, the quantitative employment of the detected electron intensity presents a challenge where conventional models fail. The momentum-resolved STEM technique is thus not only a powerful tool to solve complex materials science problems, but also a great motivation for the improvement of state-of-the-art methodologies and theoretical capacities.

Prospects

Topography mapping and quantitative analysis via focal series

In chapter 4, the combination of depth sectioning with momentum-resolution was presented both as a practical solution to the non-universality of the focus of maximum contrast in STEM, and as a new surface retrieval method. This approach could in principle be applied to the measurement of local surface topography in a given specimen, for which some of the recording requirements have been explored as well. Such an experiment in turn presents interests for a wide variety of material systems, in which the precise knowledge of the three-dimensional structure and surface states become relevant. In particular, nanomaterials and nanoparticles would provide a good collection of application candidates for this purpose. Such work is thus part of future prospects. Beyond this, one could make an argument to consider probe focus as an additional degree of freedom for the comparison of experimental and simulated features. As such, it could be integrated into quantitative methodologies as a new manner of investigating probe-dependent real-space variations which, by themselves, are potentially dependent on relevant specimen parameters.

Imaging of weakly scattering and dose-sensitive objects

One of the most important strengths of MR-STEM is the minimal loss of electron intensity, from the incident beam, in the employable diffraction features. Indeed, as the primary source of contrast in transmission electron microscopy is scattering, the recorded diffraction patterns are expected to contain all the electrons sent on the specimen, at least under the limits imposed by the maximum scattering angle accessible by the camera, as well as its DQE. For this reason, MR-STEM is an inherently dose-efficient technique, making it highly suitable for the observation of weakly scattering, or otherwise dose-sensitive, specimens [302, 303]. In particular, ptychographic methods led to advances in that direction, due to the manner in which they allow the employment of all available intensity at once [304, 305, 306, 307], leading to high sensitivity to both light and heavy atoms [308, 309]. In fact, work was recently published demonstrating the application of electron ptychography to the imaging of viruses [310] which, in the framework of structural biology, are usually investigated using a parallel illumination set-up [93]. In this context, it is highly relevant to pursue work aiming to apply ptychographic methods, and multidimensional STEM techniques in general, to light matter. Though work was initiated by this thesis' author in that direction, this project is currently being pursued in the framework of another doctoral project.

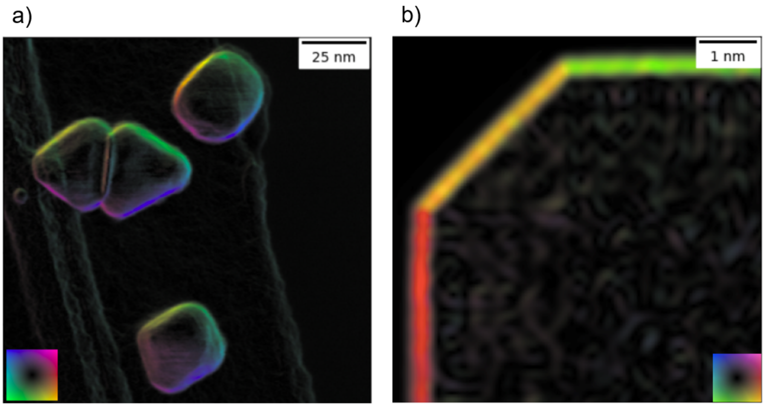

Figure 4.22: Demonstration of shape sensitivity in $\langle\vec{q}\rangle$. a) Experimental 1st moment micrograph displaying Au particles standing on an amorphous carbon strip. Imaging conditions were $\alpha = 3.74\,\mathrm{mrad}$ and $U = 300\,\mathrm{kV}$. b) Simulated 1st moment micrograph obtained from a truncated gold nanocube presenting [100] and [110] facets. Imaging conditions were $\alpha = 5\,\mathrm{mrad}$ and $U = 300\,\mathrm{kV}$. The images are depicted in colour wheel format.

Shape sensitivity in first moment STEM

As was explained in chapter 1 of this thesis, the first moment $\langle\vec{q}\rangle$ measured in reciprocal space can be related to the electromagnetic fields experienced by the electrons when traveling through the specimen. Furthermore, since the imaged specimens are finite in the depth dimension, propagation and dynamical diffraction effects condition the influence of those fields which, in most cases, prevents the direct proportionality between their vertical projection and the vector map. Additional contributions may be caused by long-range aspects of the field distribution, such as the interface between two volumes with different mean inner potentials [244]. This brings a further dependence to the three-dimensional shape of the specimen investigated. Work was thus initiated (as part of a Master thesis project supervised by this thesis' author) to understand this shape-sensitivity and determine possibilities for its practical employment. As it turns out, for the observation of three-dimensional objects, this effect appears superposed to the atomic-resolution image, as part of a supplementary low-frequency component. In a first approach, this component can be understood as depending solely on the orientations of surfaces and not on atomic-level diffraction effects, and may therefore be expressed through the interaction of the beam with a continuous medium. This in turn only allows refraction-like momentum transfers between the electrons and the specimen. This interpretation goes of course against the complex, dynamical, nature of the interaction between the electron beam and the specimen, and leads to errors in crystalline matter, depending on the exact thickness traveled through. Nevertheless, considering only the qualitative level, or using amorphous specimens, an agreement could be obtained when fulfilling imaging conditions leading to the suppression of high-frequency components in the image. Such imaging conditions correspond to a low value of semi-convergence angle, thus ensuring a nm-wide probe and a large depth of focus.

An example of shape sensitivity is displayed in figure 4.22, where gold particles were imaged experimentally, as shown in 4.22.a, or by simulation, in 4.22.b. Owing to the low semi-convergence angles used, respectively 3.74 and 5 mrad, the recordings were performed with nm-wide electron probes, thus permitting the domination of long-range features in the resulting vector maps and the apparent loss of atomic features. As such, the edges of the particles, as well as the inclination of their exposed surfaces, appear clearly. In reality, it can further be shown that, in dependence to thickness, dynamical diffraction limits the quantitative application of such a shape retrieval method. Those findings will be published in a scientific article, currently in preparation.

New detectors for the direct measurement of momentum transfer

Whereas the measurement of the average momentum transfer in STEM is usually performed using a segmented annular detector [236], this geometry leads to a non-linearity between the recorded signal and the underlying physical quantities [237, 238]. A solution to this issue can be found in the extraction of the first moment from a prealably acquired MR-STEM dataset. This is nevertheless at the cost of flexibility for the scan operation and the size of the image. This is because the dwell time then has to be extended, owing to the frame rate of the camera. There is thus a motivation to introduce new hardware providing an accurate measurement of $\langle \vec{q} \rangle$, while allowing large fields of view without a loss of the detailed real-space information. This was recently realized by a new type of position-sensitive detector, adapted to the STEM instrument [311]. This prototype having been provided by the group responsible for its creation, some initial experiments were performed, and preliminary work was done for the interpretation of the results.

Bibliography

[1] P. Yang, J. M. Tarascon, Towards systems materials engineering, Nature Materials 11 (7) (2012) 560–563. `doi:10.1038/nmat3367`.
URL `http://dx.doi.org/10.1038/nmat3367`

[2] W. Schilling, Self-interstitial atoms in metals, Journal of Nuclear Materials 69-70 (C) (1978) 465–489. `doi:10.1016/0022-3115(78)90261-1`.

[3] A. V. Granato, Interstitialcy model for condensed matter states of face-centered-cubic metals, Physical Review Letters 68 (7) (1992) 974–977. `doi:10.1103/PhysRevLett.68.974`.

[4] M. A. Green, Intrinsic concentration, effective densities of states, and effective mass in silicon, Journal of Applied Physics 67 (6) (1990) 2944–2954. `doi:10.1063/1.345414`.

[5] P. M. Koenraad, M. E. Flatté, Single dopants in semiconductors, Nature Materials 10 (2) (2011) 91–100. `doi:10.1038/nmat2940`.
URL `http://dx.doi.org/10.1038/nmat2940`

[6] X. Lin, B. Wegner, K. M. Lee, M. A. Fusella, F. Zhang, K. Moudgil, B. P. Rand, S. Barlow, S. R. Marder, N. Koch, A. Kahn, Beating the thermodynamic limit with photo-activation of n-doping in organic semiconductors, Nature Materials 16 (12) (2017) 1209–1215. `doi:10.1038/nmat5027`.

[7] R. W. Siegel, Vacancy concentrations in metals, Journal of Nuclear Materials 69-70 (C) (1978) 117–146. `doi:10.1016/0022-3115(78)90240-4`.

[8] R. W. Cahn, Measures of crystal vacancies, Nature 397 (6721) (1999) 656–657. `doi:10.1038/17701`.

[9] J. Zhang, R. J. Perez, E. J. Lavernia, Dislocation-induced damping in metal matrix composites, Journal of Materials Science 28 (3) (1993) 835–846. `doi:10.1007/BF01151266`.

[10] N. Bassiri-Gharb, I. Fujii, E. Hong, S. Trolier-Mckinstry, D. V. Taylor, D. Damjanovic, Domain wall contributions to the properties of piezoelectric thin films, Journal of Electroceramics 19 (1) (2007) 47–65. `doi:10.1007/s10832-007-9001-1`.

[11] B. P. Uberuaga, L. J. Vernon, E. Martinez, A. F. Voter, The relationship between grain boundary structure, defect mobility, and grain boundary sink efficiency, Scientific Reports 5 (2015) 1–9. `doi:10.1038/srep09095`.

[12] M. J. Pitkethly, Nanometerials - The driving force, Materials Today 7 (12 SUPPL.) (2004) 20–29. `doi:10.1016/S1369-7021(04)00627-3`.
URL `http://dx.doi.org/10.1016/S1369-7021(04)00627-3`

[13] E. Roduner, Size matters: Why nanomaterials are different, Chemical Society Reviews 35 (7) (2006) 583–592. `doi:10.1039/b502142c`.

[14] Z. Guo, L. Tan, Fundamentals and applications of nanomaterials, 2010.

[15] S. Jesse, A. Y. Borisevich, J. D. Fowlkes, A. R. Lupini, P. D. Rack, R. R. Unocic, B. G. Sumpter, S. V. Kalinin, A. Belianinov, O. S. Ovchinnikova, Directing Matter: Toward Atomic-Scale 3D Nanofabrication, ACS Nano 10 (6) (2016) 5600–5618. `doi:10.1021/acsnano.6b02489`.

[16] F. Fang, N. Zhang, D. Guo, K. Ehmann, B. Cheung, K. Liu, K. Yamamura, Towards atomic and close-to-atomic scale manufacturing, International Journal of Extreme Manufacturing 1 (1) (2019). `doi:10.1088/2631-7990/ab0dfc`.

[17] J. Morley, K. Widdicks, M. Hazas, Energy Research and Social Science Digitalisation, energy and data demand : The impact of Internet traffic on overall and peak electricity consumption, Energy Research and Social Science 38 (August 2017) (2018) 128–137. `doi:10.1016/j.erss.2018.01.018`.
URL `https://doi.org/10.1016/j.erss.2018.01.018`

[18] A. P. Malshe, K. P. Rajurkar, K. R. Virwani, C. R. Taylor, D. L. Bourell, G. Levy, M. M. Sundaram, J. A. McGeough, V. Kalyanasundaram, A. N. Samant, Tip-based nanomanufacturing by electrical, chemical, mechanical and thermal processes, CIRP Annals - Manufacturing Technology 59 (2) (2010) 628–651. `doi:10.1016/j.cirp.2010.05.006`.

[19] X. Liu, T. Xu, X. Wu, Z. Zhang, J. Yu, H. Qiu, J. H. Hong, C. H. Jin, J. X. Li, X. R. Wang, L. T. Sun, W. Guo, Top-down fabrication of sub-nanometre semiconducting nanoribbons derived from molybdenum disulfide sheets, Nature Communications 4 (2013) 1–6. `doi:10.1038/ncomms2803`.

[20] A. N. Abbas, G. Liu, B. Liu, L. Zhang, H. Liu, D. Ohlberg, W. Wu, C. Zhou, Patterning, characterization, and chemical sensing applications of graphene nanoribbon arrays down to 5 nm using helium ion beam lithography, ACS Nano 8 (2) (2014) 1538–1546. `doi:10.1021/nn405759v`.

[21] S. U. Engelmann, R. L. Bruce, M. Nakamura, D. Metzler, S. G. Walton, E. A. Joseph, Challenges of Tailoring Surface Chemistry and Plasma/Surface Interactions to Advance Atomic Layer Etching, ECS Journal of Solid State Science and Technology 4 (6) (2015) N5054–N5060. `doi:10.1149/2.0101506jss`.

[22] L. Chen, J. Wen, P. Zhang, B. Yu, C. Chen, T. Ma, X. Lu, S. H. Kim, L. Qian, Nanomanufacturing of silicon surface with a single atomic layer precision via mechanochemical reactions, Nature Communications 9 (1) (2018) 1–7. `doi:10.1038/s41467-018-03930-5`.
URL `http://dx.doi.org/10.1038/s41467-018-03930-5`

[23] S. M. George, Atomic layer deposition: An overview, Chemical Reviews 110 (1) (2010) 111–131. `doi:10.1021/cr900056b`.

[24] N. P. King, J. B. Bale, W. Sheffler, D. E. McNamara, S. Gonen, T. Gonen, T. O. Yeates, D. Baker, Accurate design of co-assembling multi-component protein nanomaterials, Nature 510 (7503) (2014) 103–108. `doi:10.1038/nature13404`.

[25] R. W. Johnson, A. Hultqvist, S. F. Bent, A brief review of atomic layer deposition: From fundamentals to applications, Materials Today 17 (5) (2014) 236–246. `doi:10.1016/j.mattod.2014.04.026`.
URL `http://dx.doi.org/10.1016/j.mattod.2014.04.026`

[26] Q. Luo, C. Hou, Y. Bai, R. Wang, J. Liu, Protein Assembly: Versatile Approaches to Construct Highly Ordered Nanostructures, Chemical Reviews 116 (22) (2016) 13571–13632. `doi:10.1021/acs.chemrev.6b00228`.

[27] M. N. Baibich, J. M. Broto, A. Fert, F. N. Van Dau, F. Petroff, P. Eitenne, G. Creuzet, A. Friederich, J. Chazelas, Giant magnetoresistance of (001)Fe/(001)Cr magnetic superlattices, Physical Review Letters 61 (21) (1988) 2472–2475. `doi:10.1103/PhysRevLett.61.2472`.

[28] G. Binasch, P. Grünberg, F. Saurenbach, W. Zinn, Enhanced magnetoresistance in layered magnetic structures with antiferromagnetic interlayer exchange, Physical Review B 39 (7) (1989) 4828–4830. `doi:10.1103/PhysRevB.39.4828`.

[29] K. Gabriel, J. Jarvis, W. Trimmer, N. S. F. (U.S.), Small Machines, Large Opportunities: A Report on the Emerging Field of Microdynamics : Report of the Workshop on Microelectromechanical Systems Research ; Sponsored by the National Science Foundation, AT & T Bell Laboratories, 1988.
URL `https://books.google.be/books?id=7lKytgAACAAJ`

[30] J. Åkerman, Toward a universal memory, Science 308 (5721) (2005) 508–510. `doi:10.1126/science.1110549`.

[31] R. N. Hall, G. E. Fenner, J. D. Kingsley, T. J. Soltys, R. O. Carlson, Coherent Light Emission From GaAs Junctions, Physical Review Letters 9 (9) (1962) 366–368. `doi:10.1103/PhysRevLett.9.366`.
URL `https://link.aps.org/doi/10.1103/PhysRevLett.9.366`

[32] S. Sharma, K. K. Jain, A. Sharma, Solar Cells: In Research and Applications—A Review, Materials Sciences and Applications 06 (12) (2015) 1145–1155. `doi:10.4236/msa.2015.612113`.

[33] N. Suresh Kumar, K. Chandra Babu Naidu, A review on perovskite solar cells (PSCs), materials and applications, Journal of Materiomics 7 (5) (2021) 940–956. `doi:10.1016/j.jmat.2021.04.002`.
URL `https://doi.org/10.1016/j.jmat.2021.04.002`

[34] K. S. Novoselov, A. Mishchenko, A. Carvalho, A. H. Castro Neto, 2D materials and van der Waals heterostructures, Science 353 (6298) (2016). `doi:10.1126/science.aac9439`.

[35] V. Garcia, M. Bibes, Ferroelectric tunnel junctions for information storage and processing, Nature Communications 5 (2014) 4289. `doi:10.1038/ncomms5289`.
URL `http://dx.doi.org/10.1038/ncomms5289`

[36] V. B. Mbayachi, E. Ndayiragije, T. Sammani, S. Taj, E. R. Mbuta, A. ullah Khan, Graphene synthesis, characterization and its applications: A review, Results in Chemistry 3 (2021) 100163. `doi:10.1016/j.rechem.2021.100163`.
URL `https://doi.org/10.1016/j.rechem.2021.100163`

[37] G. Pilania, C. Wang, X. Jiang, S. Rajasekaran, R. Ramprasad, Accelerating materials property predictions using machine learning, Scientific Reports 3 (2013) 1–6. `doi:10.1038/srep02810`.

[38] N. Marzari, Materials modelling: The frontiers and the challenges, Nature Materials 15 (4) (2016) 381–382. `doi:10.1038/nmat4613`.
URL `http://dx.doi.org/10.1038/nmat4613`

[39] J. P. Janet, H. J. Kulik, Predicting electronic structure properties of transition metal complexes with neural networks, Chemical Science 8 (7) (2017) 5137–5152. `arXiv:1702.05771`, `doi:10.1039/c7sc01247k`.

[40] I. M. Robertson, C. A. Schuh, J. S. Vetrano, N. D. Browning, D. P. Field, D. J. Jensen, M. K. Miller, I. Baker, D. C. Dunand, R. Dunin-Borkowski, B. Kabius, T. Kelly, S. Lozano-Perez, A. Misra, G. S. Rohrer, A. D. Rollett, M. L. Taheri, G. B. Thompson, M. Uchic, X. L. Wang, G. Was, Towards an integrated materials characterization toolbox, Journal of Materials Research 26 (11) (2011) 1341–1383. `doi:10.1557/jmr.2011.41`.

[41] T. Heine, Grand challenges in computational materials science: From description to prediction at all scales, Frontiers in Materials 1 (July) (2014) 1–3. `doi:10.3389/fmats.2014.00007`.

[42] J. L. Provis, Grand challenges in structural materials, Frontiers in Materials 2 (April) (2015) 8–11. `doi:10.3389/fmats.2015.00031`.

[43] M. Knoll, E. Ruska, Das Elektronenmikroskop, Zeitschrift für Physik 78 (5-6) (1932) 318–339. `doi:10.1007/BF01342199`.
URL `http://dx.doi.org/10.1007/BF01342199`

[44] H. Rose, Correction of aberrations, a promising means for improving the spatial and energy resolution of energy-filtering electron microscopes, Ultramicroscopy 56 (1-3) (1994) 11–25. `doi:10.1016/0304-3991(94)90142-2`.

[45] M. Haider, G. Braunshausen, E. Schwan, Correction of the spherical aberration of a 200 kV TEM by means of a hexapole-corrector, Optik 99 (1995) 167–179.

[46] M. Haider, S. Uhlemann, E. Schwan, G. Rose, B. Kabius, K. Urban, H. Rose, B. Kabius, K. Urban, Electron microscopy image enhanced, Nature 392 (6678) (1998) 768–769. `doi:10.1038/33823`.
URL `http://dx.doi.org/10.1038/33823`

[47] P. E. Batson, N. Dellby, O. L. Krivanek, Sub-angstrom resolution using aberration corrected electron optics, Nature 418 (6898) (2002) 617–620. `doi:10.1038/nature00972`.
URL `http://www.nature.com/articles/nature01058http://www.nature.com/articles/nature00972http://dx.doi.org/10.1038/nature00972`

[48] R. Erni, M. D. Rossell, C. Kisielowski, U. Dahmen, Atomic-Resolution Imaging with a Sub-50-pm Electron Probe, Phys. Rev. Lett. 102 (9) (2009) 96101. `doi:10.1103/PhysRevLett.102.096101`.
URL `http://link.aps.org/doi/10.1103/PhysRevLett.102.096101`

[49] M. Haider, P. Hartel, H. Mller, S. Uhlemann, J. Zach, H. Müller, S. Uhlemann, J. Zach, Information Transfer in a TEM Corrected for Spherical and Chromatic Aberration, Microscopy and Microanalysis 16 (4) (2010) 393–408. `doi:10.1017/S1431927610013498`.
URL `https://doi.org/10.1017/S1431927610013498`

[50] L. de Broglie, A tentative theory of light quanta, The London, Edinburgh, and Dublin Philosophical Magazine and Journal of Science 47 (278) (1924) 446–458. `doi:10.1080/14786442408634378`.

[51] W. H. Bragg, W. L. Bragg, The reflection of X-rays by crystals, Proc. Roy. Soc. Lond. A 88 (1913) 428–438.

[52] H. Yoshioka, Effect of Inelastic Waves on Electron Diffraction, Journal of the Physical Society of Japan 12 (6) (1957) 618–628. `doi:10.1143/JPSJ.12.618`.
URL `https://journals.jps.jp/doi/10.1143/JPSJ.12.618http://jpsj.ipap.jp/link?JPSJ/12/618/`

[53] C. R. Hall, The scattering of high energy electrons by the thermal vibrations of crystals, Philosophical Magazine 12 (118) (1965) 815–826. `doi:10.1080/14786436508218919`.
URL `http://www.tandfonline.com/doi/abs/10.1080/14786436508218919`

[54] C. R. Hall, P. B. Hirsch, Effect of Thermal Diffuse Scattering on Propagation of High Energy Electrons Through Crystals, Proc. Roy. Soc. Lond. A 286 (1405) (1965) 158–177. `doi:10.1098/rspa.1965.0136`.
URL `http://rspa.royalsocietypublishing.org/content/286/1405/158.abstract`

[55] J. Fertig, H. Rose, A reflection on partial coherence in electron microscopy, Ultramicroscopy 2 (1977) 269–279.

[56] M. von Ardenne, Das Elektronen-Rastermikroskop, Zeitschrift für Physik 109 (9) (1938) 553–572. `doi:10.1007/BF01341584`.
URL `https://doi.org/10.1007/BF01341584`

[57] A. Crewe, J. Wall, L. M. Welter, A High-Resolution Scanning Transmission Electron Microscope, J. Appl. Phys. 39 (1968) 5861–5868.

[58] R. F. Egerton, Electron Energy-loss Spectroscopy in the Electron Microscope, 1986. `doi:10.1080/09500348714550571`.

[59] K. Suenaga, M. Tencé, C. Mory, C. Colliex, H. Kato, T. Okazaki, H. Shinohara, K. Hirahara, S. Bandow, S. Iijima, Element-selective single atom imaging, Science 290 (5500) (2000) 2280–2282. `doi:10.1126/science.290.5500.2280`.

[60] P. Longo, P. Thomas, A. Aitouchen, B. Schaffer, R. D. Twesten, Simultaneous EELS/EDS Composition Mapping at Atomic Resolution Using Fast STEM Spectrum-Imaging, Microscopy Today 21 (4) (2013) 36–40. `doi:10.1017/s1551929513000643`.

[61] G. M. Vanacore, I. Madan, G. Berruto, K. Wang, E. Pomarico, R. J. Lamb, D. McGrouther, I. Kaminer, B. Barwick, F. J. García De Abajo, F. Carbone, Attosecond coherent control of free-electron wave functions using semi-infinite light fields, Nature Communications 9 (1) (2018). `doi:10.1038/s41467-018-05021-x`.
URL `http://dx.doi.org/10.1038/s41467-018-05021-x`

[62] G. M. Vanacore, G. Berruto, I. Madan, E. Pomarico, P. Biagioni, R. J. Lamb, D. McGrouther, O. Reinhardt, I. Kaminer, B. Barwick, H. Larocque, V. Grillo, E. Karimi, F. J. García de Abajo, F. Carbone, Ultrafast generation and control of an electron vortex beam via chiral plasmonic near fields, Nature Materials 18 (6) (2019) 573–579. `arXiv:1806.00366`, `doi:10.1038/s41563-019-0336-1`.
URL `http://dx.doi.org/10.1038/s41563-019-0336-1`

[63] A. Polman, M. Kociak, F. J. García de Abajo, Electron-beam spectroscopy for nanophotonics, Nature Materials 18 (11) (2019) 1158–1171. `doi:10.1038/s41563-019-0409-1`.

[64] A. Konečná, V. Di Giulio, V. Mkhitaryan, C. Ropers, F. J. García De Abajo, Nanoscale Nonlinear Spectroscopy with Electron Beams, ACS Photonics 7 (5) (2020) 1290–1296. `arXiv:1912.01539`, `doi:10.1021/acsphotonics.0c00326`.

[65] N. Talebi, Quantum optics with swift electrons, Light: Science and Applications 10 (1) (2021) 9–11. `doi:10.1038/s41377-021-00530-9`.
URL `http://dx.doi.org/10.1038/s41377-021-00530-9`

[66] G. McMullan, D. Cattermole, S. Chen, R. Henderson, X. Llopart, C. Summerfield, L. Tlustos, A. Faruqi, Electron imaging with Medipix2 hybrid pixel detector, Ultramicroscopy 107 (4-5) (2007) 401–413. `doi:10.1016/j.ultramic.2006.10.005`.
URL `https://linkinghub.elsevier.com/retrieve/pii/S0304399106001963`

[67] R. Ballabriga, M. Campbell, E. Heijne, X. Llopart, L. Tlustos, W. Wong, Medipix3: A 64k pixel detector readout chip working in single photon counting mode with improved spectrometric performance, Nuclear Instruments and Methods in Physics Research Section A: Accelerators, Spectrometers, Detectors and Associated Equipment 633 (SUPPL. 1) (2011) S15–S18. `doi:10.1016/j.nima.2010.06.108`.
URL `https://linkinghub.elsevier.com/retrieve/pii/S0168900210012982`

[68] K. Müller, H. Ryll, I. Ordavo, S. Ihle, L. Strüder, K. Volz, J. Zweck, H. Soltau, A. Rosenauer, Scanning transmission electron microscopy strain measurement from millisecond frames of a direct electron charge coupled device, Appl. Phys. Lett. 101 (21) (2012) 212110. `doi:10.1063/1.4767655`.
URL `http://dx.doi.org/10.1063/1.4767655`

[69] R. Plackett, I. Horswell, E. N. Gimenez, J. Marchal, D. Omar, N. Tartoni, Merlin: a fast versatile readout system for Medipix3, Journal of Instrumentation 8 (1) (2013) C01038. `doi:10.1088/1748-0221/8/01/C01038`.
URL `http://iopscience.iop.org/article/10.1088/1748-0221/8/01/C01038/meta`

[70] K. Müller-Caspary, A. Oelsner, P. Potapov, Two-dimensional strain mapping in semiconductors by nano-beam electron diffraction employing a delay-line detector, Appl. Phys. Lett. 107 (7) (2015) 72110. `doi:10.1063/1.4927837`.
URL `http://scitation.aip.org/content/aip/journal/apl/107/7/10.1063/1.4927837`

[71] H. Ryll, M. Simson, R. Hartmann, P. Holl, M. Huth, S. Ihle, Y. Kondo, P. Kotula, A. Liebel, K. Müller-Caspary, A. Rosenauer, R. Sagawa, J. Schmidt, H. Soltau, L. Strüder, A pnCCD-based, fast direct single electron imaging camera for TEM and STEM, J. Instrum. 11 (04)

(2016) P04006. doi:10.1088/1748-0221/11/04/P04006.
URL http://stacks.iop.org/1748-0221/11/i=04/a=P04006

[72] M. W. Tate, P. Purohit, D. Chamberlain, K. X. Nguyen, R. Hovden, C. S. Chang, P. Deb, E. Turgut, J. T. Heron, D. G. Schlom, D. C. Ralph, G. D. Fuchs, K. S. Shanks, H. T. Philipp, D. A. Muller, S. M. Gruner, High Dynamic Range Pixel Array Detector for Scanning Transmission Electron Microscopy, Microsc. Microanal. 22 (1) (2016) 237–249. arXiv:1511.03539, doi:10.1017/S1431927615015664.
URL http://journals.cambridge.org/article_S1431927615015664

[73] G. McMullan, A. Faruqi, R. Henderson, Direct Electron Detectors, in: Methods in Enzymology, Vol. 579, Academic Press Inc., 2016, pp. 1–17. doi:10.1016/bs.mie.2016.05.056.
URL https://linkinghub.elsevier.com/retrieve/pii/S0076687916300921

[74] K. Müller, F. F. Krause, A. Beche, M. Schowalter, V. Galioit, S. Löffler, J. Verbeeck, J. Zweck, P. Schattschneider, A. Rosenauer, A. Béché, M. Schowalter, V. Galioit, S. Löffler, J. Verbeeck, J. Zweck, P. Schattschneider, A. Rosenauer, Atomic electric fields revealed by a quantum mechanical approach to electron picodiffraction, Nature Communications 5 (2014) 5653:1–8. doi:10.1038/ncomms6653.
URL http://dx.doi.org/10.1038/ncomms6653

[75] J. M. Rodenburg, R. H. T. Bates, The theory of super-resolution electron microscopy via Wigner-distribution deconvolution, Philosophical Transactions of the Royal Society of London. Series A: Physical and Engineering Sciences 339 (1655) (1992) 521–553. doi:10.1098/rsta.1992.0050.
URL https://royalsocietypublishing.org/doi/10.1098/rsta.1992.0050

[76] J. Rodenburg, B. McCallum, P. Nellist, Experimental tests on double-resolution coherent imaging via STEM, Ultramicroscopy 48 (3) (1993) 304–314. doi:10.1016/0304-3991(93)90105-7.
URL https://linkinghub.elsevier.com/retrieve/pii/0304399193901057

[77] P. D. Nellist, B. C. McCallum, J. M. Rodenburg, Resolution beyond the 'information limit' in transmission electron microscopy (1995). doi:10.1038/374630a0.

[78] P. D. Nellist, J. M. Rodenburg, Electron Ptychography. I. Experimental Demonstration Beyond the Conventional Resolution Limits, Acta Crystallographica Section A: Foundations of Crystallography 54 (1) (1998) 49–60. doi:10.1107/S0108767397010490.

[79] J. M. Rodenburg, H. M. Faulkner, A phase retrieval algorithm for shifting illumination, Applied Physics Letters 85 (20) (2004) 4795–4797. doi:10.1063/1.1823034.

[80] H. M. Faulkner, J. M. Rodenburg, Movable aperture lensless transmission microscopy: A novel phase retrieval algorithm, Physical Review Letters 93 (2) (2004) 2–5. doi:10.1103/PhysRevLett.93.023903.

[81] A. M. Maiden, M. J. Humphry, F. Zhang, J. M. Rodenburg, Superresolution imaging via ptychography, Journal of the Optical Society of America A 28 (4) (2011) 604. doi:10.1364/josaa.28.000604.

[82] M. J. Humphry, B. Kraus, A. C. Hurst, A. M. Maiden, J. M. Rodenburg, Ptychographic electron microscopy using high-angle dark-field scattering for sub-nanometre resolution imaging, Nature Communications 3 (2012) 730. `doi:10.1038/ncomms1733`.
URL `http://dx.doi.org/10.1038/ncomms1733`

[83] Y. Jiang, Z. Chen, Y. Han, P. Deb, H. Gao, S. Xie, P. Purohit, M. W. Tate, J. Park, S. M. Gruner, V. Elser, D. A. Muller, Electron ptychography of 2D materials to deep sub-ångström resolution (jul 2018). `doi:10.1038/s41586-018-0298-5`.
URL `http://www.nature.com/articles/s41586-018-0298-5`

[84] K. Müller-Caspary, O. Oppermann, T. Grieb, F. F. Krause, A. Rosenauer, M. Schowalter, T. Mehrtens, A. Beyer, K. Volz, P. Potapov, Materials characterisation by angle-resolved scanning transmission electron microscopy, Scientific Reports 6 (April) (2016) 1–9. `doi:10.1038/srep37146`.
URL `http://dx.doi.org/10.1038/srep37146`

[85] K. A. Mkhoyan, S. E. MacCagnano-Zacher, M. G. Thomas, J. Silcox, Critical role of inelastic interactions in quantitative electron microscopy, Physical Review Letters 100 (2) (2008) 1–4. `doi:10.1103/PhysRevLett.100.025503`.
URL `http://link.aps.org/doi/10.1103/PhysRevLett.100.025503https://link.aps.org/doi/10.1103/PhysRevLett.100.025503`

[86] P. SchattSchneider, Fundamentals of inelastic electron scattering, Springer Nature, 1986. `doi:10.1007/bf01080838`.

[87] M. De Graef, Introduction to Conventional Transmission Electron Microscopy, 1st Edition, Cambridge University Press, 2003. `doi:10.1016/s1369-7021(03)00636-9`.

[88] D. B. Williams, C. B. Carter, Transmission Electron Microscopy, A Textbook for Materials Science, 2nd Edition, Springer, 2009.

[89] E. J. Kirkland, Advanced Computing in Electron Microscopy, Springer US, 2013. `doi:10.1007/978-1-4757-4406-4`.

[90] K. A. Taylor, R. M. Glaeser, Electron Diffraction of Frozen , Hydrated Protein Crystals Sunday and Workday Variations in Photochemical Air Pollutants in New Jersey and New York, Science 186 (April) (1974) 1036–1037.

[91] P. N. Unwin, Three-dimensional model of membrane-bound ribosomes obtained by electron microscopy, Nature 269 (5624) (1977) 118–122. `doi:10.1038/269118a0`.

[92] R. Henderson, J. Baldwin, T. Ceska, F. Zemlin, E. Beckmann, K. Downing, Baldwin, J.M. Ceska, T.A. Zemlin, F. Beckmann, E. Downing, K.H. Model for the structure of bacteriorhodopsin based on high-resolution electron cryo-microscopy, Journal of Molecular Biology 213 (4) (1990) 899–929.
URL `http://linkinghub.elsevier.com/retrieve/pii/S0022283605802712`

[93] N. A. Ranson, P. G. Stockley, Cryo-electron microscopy of viruses, Emerging Topics in Physical Virology (I) (2010) 1–33. `doi:10.1142/9781848164666_0001`.

[94] X. chen Bai, G. McMullan, S. H. Scheres, How cryo-EM is revolutionizing structural biology, Trends in Biochemical Sciences 40 (1) (2015) 49–57. `doi:10.1016/j.tibs.2014.10.005`.
URL `http://dx.doi.org/10.1016/j.tibs.2014.10.005`

[95] D. GABOR, A New Microscopic Principle, Nature 161 (4098) (1948) 777–778. `doi:10.1038/161777a0`.
URL `https://www.nature.com/articles/161777a0`

[96] T. Matsuda, S. Hasegawa, M. Igarashi, T. Kobayashi, M. Naito, H. Kajiyama, J. Endo, N. Osakabe, A. Tonomura, R. Aoki, Magnetic field observation of a single flux quantum by electron-holographic interferometry, Phys. Rev. Lett. 62 (21) (1989) 2519–2522. `doi:10.1103/PhysRevLett.62.2519`.

[97] R. E. Dunin-Borkowski, T. Kasama, A. Wei, S. L. Tripp, M. J. Hytch, E. Snoeck, R. J. Harrison, A. Putnis, M. J. Hÿtch, E. Snoeck, R. J. Harrison, A. Putnis, Off-axis electron holography of magnetic nanowires and chains, rings, and planar arrays of magnetic nanoparticles, Microsc. Res. Tech. 64 (5-6) (2004) 390–402. `doi:10.1002/jemt.20098`.
URL `http://dx.doi.org/10.1002/jemt.20098`

[98] H. Lichte, M. Lehmann, Electron holography—basics and applications, Rep. Prog. Phys. 71 (1) (2008) 16102.
URL `http://stacks.iop.org/0034-4885/71/i=1/a=016102`

[99] H. Tan, S. Turner, E. Yücelen, J. Verbeeck, G. Van Tendeloo, 2D atomic mapping of oxidation states in transition metal oxides by scanning transmission electron microscopy and electron energy-loss spectroscopy, Physical Review Letters 107 (10) (2011) 1–4. `doi:10.1103/PhysRevLett.107.107602`.

[100] O. L. Krivanek, T. C. Lovejoy, N. Dellby, T. Aoki, R. W. Carpenter, P. Rez, E. Soignard, J. Zhu, P. E. Batson, M. J. Lagos, R. F. Egerton, P. A. Crozier, Vibrational spectroscopy in the electron microscope, Nature 514 (7521) (2014) 209–212. `doi:10.1038/nature13870`.

[101] K. P. De Jong, A. J. Koster, Three-dimensional electron microscopy of mesoporous materials - Recent strides towards spatial imaging at the nanometer scale, ChemPhysChem 3 (9) (2002) 776–780. `doi:10.1002/1439-7641(20020916)3:9<776::AID-CPHC776>3.0.CO;2-E`.

[102] S. Bals, G. Van Tendeloo, C. Kisielowski, A New Approach for Electron Tomography: Annular Dark-Field Transmission Electron Microscopy, Adv. Mater. 18 (7) (2006) 892–895. `doi:10.1002/adma.200502201`.
URL `http://dx.doi.org/10.1002/adma.200502201`

[103] R. Xu, C. C. Chen, L. Wu, M. C. Scott, W. Theis, C. Ophus, M. Bartels, Y. Yang, H. Ramezani-Dakhel, M. R. Sawaya, H. Heinz, L. D. Marks, P. Ercius, J. Miao, Three-dimensional coordinates of individual atoms in materials revealed by electron tomography, Nature Materials 14 (11) (2015) 1099–1103. `doi:10.1038/nmat4426`.

[104] N. De Jonge, F. M. Ross, Electron microscopy of specimens in liquid, Nature Nanotechnology 6 (11) (2011) 695–704. `doi:10.1038/nnano.2011.161`.

[105] F. M. Ross (Ed.), Liquid Cell Electron Microscopy, Cambridge University Press, 2016. `doi:10.1017/9781316337455`.
URL `https://www.cambridge.org/core/product/identifier/9781316337455/type/book`

[106] G. C. Egan, T. T. Li, J. D. Roehling, J. T. McKeown, G. H. Campbell, In situ dynamic TEM characterization of unsteady crystallization during laser processing of amorphous germanium, Acta Materialia 143 (2018) 13–19. `doi:10.1016/j.actamat.2017.10.003`.
URL `http://dx.doi.org/10.1016/j.actamat.2017.10.003`

[107] W. E. King, G. H. Campbell, A. Frank, B. Reed, J. F. Schmerge, B. J. Siwick, B. C. Stuart, P. M. Weber, Ultrafast electron microscopy in materials science, biology, and chemistry, J. Appl. Phys. 97 (11) (2005) 111101. `doi:http://dx.doi.org/10.1063/1.1927699`.
URL `http://scitation.aip.org/content/aip/journal/jap/97/11/10.1063/1.1927699`

[108] T. LaGrange, G. H. Campbell, B. W. Reed, M. Taheri, J. B. Pesavento, J. S. Kim, N. D. Browning, Nanosecond time-resolved investigations using the in situ of dynamic transmission electron microscope (DTEM), Ultramicroscopy 108 (11) (2008) 1441–1449. `doi:10.1016/j.ultramic.2008.03.013`.

[109] R. J. D. Miller, Femtosecond Crystallography with, High Viscosity Microstream Sample Delivery for Serial Femtosecond Crystallography 1108 (March) (2014) 1108–1116.
URL `http://dx.doi.org/10.1039/9781849731003-00337`

[110] A. Feist, N. Bach, N. Rubiano da Silva, T. Danz, M. Möller, K. E. Priebe, T. Domröse, J. G. Gatzmann, S. Rost, J. Schauss, S. Strauch, R. Bormann, M. Sivis, S. Schäfer, C. Ropers, Ultrafast transmission electron microscopy using a laser-driven field emitter: Femtosecond resolution with a high coherence electron beam, Ultramicroscopy 176 (November 2016) (2017) 63–73. `doi:10.1016/j.ultramic.2016.12.005`.
URL `http://dx.doi.org/10.1016/j.ultramic.2016.12.005`

[111] V. Di Giulio, M. Kociak, F. J. G. de Abajo, Probing quantum optical excitations with fast electrons, Optica 6 (12) (2019) 1524. `arXiv:1905.06887`, `doi:10.1364/optica.6.001524`.

[112] V. Ronchi, Due nuovi metodi per lo studio delle superficie e dei sistemi ottici, Il Nuovo Cimento (1911-1923) 26 (1) (1923) 69–71. `doi:10.1007/BF02959347`.
URL `https://doi.org/10.1007/BF02959347`

[113] Titan condenser manual (Thermofischer scientific, FEI company), Tech. rep. (2005).

[114] N. E. Christensen, B. Feuerbacher, Volume and surface photoemission from tungsten. I. Calculation of band structure and emission spectra, Physical Review B 10 (6) (1974) 2349–2372. `doi:10.1103/PhysRevB.10.2349`.

[115] E. Fermi, Zur Quantelung des idealen einatomigen Gases, Zeitschrift für Physik 36 (11-12) (1926) 902–912. `doi:10.1007/BF01400221`.

[116] P. Dirac, On the theory of quantum mechanics, Proceedings of the Royal Society of London. Series A, Containing Papers of a Mathematical and Physical Character 112 (762) (1926) 661–677. `doi:10.1098/rspa.1926.0133`.
URL `https://royalsocietypublishing.org/doi/10.1098/rspa.1926.0133`

[117] O. Richardson, K. T. Compton, LIII. The photoelectric effect, The London, Edinburgh, and Dublin Philosophical Magazine and Journal of Science 24 (142) (1912) 575–594. `doi:10.1080/14786441008637361`.

URL https://www.tandfonline.com/doi/full/10.1080/14786441008637361

[118] S. Dushman, Electron Emission from Metals as a Function of Temperature, Physical Review 21 (6) (1923) 623–636. doi:10.1103/PhysRev.21.623.
URL https://link.aps.org/doi/10.1103/PhysRev.21.623

[119] E. L. Murphy, R. H. Good, Thermionic Emission, Field Emission, and the Transition Region, Physical Review 102 (6) (1956) 1464–1473. doi:10.1103/PhysRev.102.1464.

[120] R. H. FOWLER, L. NORDHEIM, Electron emission in intense electric fields, Proceedings of the Royal Society of London. Series A, Containing Papers of a Mathematical and Physical Character 119 (781) (1928) 173–181. doi:10.1098/rspa.1928.0091.
URL http://www.worldscientific.com/doi/abs/10.1142/9789814503464_0087https://royalsocietypublishing.org/doi/10.1098/rspa.1928.0091

[121] E. J. van Zwet, H. W. Zandbergen, Measurement of the modulation transfer function of a slow-scan CCD camera on a TEM using a thin amorphous film as test signal, Ultramicroscopy 64 (1-4) (1996) 49–55. doi:DOI:10.1016/0304-3991(96)00014-9.
URL http://www.sciencedirect.com/science/article/B6TW1-3VT9GP7-H/2/42c2c1da2ee9bb518250977eb66e1805

[122] R. R. Meyer, A. Kirkland, Characterisation of the signal and noise transfer of CCD cameras for electron detection, Microsc. Res. Tech. 49 (2000) 269–280.

[123] R. S. Ruskin, Z. Yu, N. Grigorieff, Quantitative characterization of electron detectors for transmission electron microscopy, Journal of Structural Biology 184 (3) (2013) 385–393. doi:10.1016/j.jsb.2013.10.016.
URL http://dx.doi.org/10.1016/j.jsb.2013.10.016https://linkinghub.elsevier.com/retrieve/pii/S1047847713002815

[124] A. R. Faruqi, D. M. Cattermole, R. Henderson, B. Mikulec, C. Raeburn, Evaluation of a hybrid pixel detector for electron microscopy, Ultramicroscopy 94 (3-4) (2003) 263–276. doi:10.1016/S0304-3991(02)00336-4.

[125] A.-C. Milazzo, P. Leblanc, F. Duttweiler, L. Jin, J. C. Bouwer, S. Peltier, M. Ellisman, F. Bieser, H. S. Matis, H. Wieman, P. Denes, S. Kleinfelder, N.-H. Xuong, Active pixel sensor array as a detector for electron microscopy, Ultramicroscopy 104 (2) (2005) 152–159. doi:http://dx.doi.org/10.1016/j.ultramic.2005.03.006.
URL http://www.sciencedirect.com/science/article/pii/S0304399105000513

[126] A.-C. Milazzo, G. Moldovan, J. Lanman, L. Jin, J. C. Bouwer, S. Klienfelder, S. T. Peltier, M. H. Ellisman, A. I. Kirkland, N.-H. Xuong, Characterization of a direct detection device imaging camera for transmission electron microscopy, Ultramicroscopy 110 (7) (2010) 741–744. doi:10.1016/j.ultramic.2010.03.007.
URL http://www.sciencedirect.com/science/article/pii/S0304399110000859

[127] B. Plotkin-Swing, G. J. Corbin, S. De Carlo, N. Dellby, C. Hoermann, M. V. Hoffman, T. C. Lovejoy, C. E. Meyer, A. Mittelberger, R. Pantelic, L. Piazza, O. L. Krivanek, Hybrid pixel direct detector for electron energy loss spectroscopy, Ultramicroscopy 217 (July) (2020)

113067. `doi:10.1016/j.ultramic.2020.113067`.
URL `https://doi.org/10.1016/j.ultramic.2020.113067`

[128] K. A. Paton, M. C. Veale, X. Mu, C. S. Allen, D. Maneuski, C. Kübel, V. O'Shea, A. I. Kirkland, D. McGrouther, Quantifying the performance of a hybrid pixel detector with GaAs:Cr sensor for transmission electron microscopy, Ultramicroscopy 227 (April) (2021) 113298. `arXiv:2009.14565`,`doi:10.1016/j.ultramic.2021.113298`.
URL `https://doi.org/10.1016/j.ultramic.2021.113298`

[129] D. Pennicard, R. Ballabriga, X. Llopart, M. Campbell, H. Graafsma, Simulations of charge summing and threshold dispersion effects in Medipix3, Nuclear Instruments and Methods in Physics Research Section A: Accelerators, Spectrometers, Detectors and Associated Equipment 636 (1) (2011) 74–81. `doi:10.1016/j.nima.2011.01.124`.
URL `https://linkinghub.elsevier.com/retrieve/pii/S0168900211002105http://dx.doi.org/10.1016/j.nima.2011.01.124`

[130] K. Fujiwara, Relativistic Dynamical Theory of Electron Diffraction, Journal of the Physical Society of Japan 16 (11) (1961) 2226–2238. `doi:10.1143/JPSJ.16.2226`.
URL `https://journals.jps.jp/doi/10.1143/JPSJ.16.2226`

[131] H. A. Ferwerda, B. J. Hoenders, C. H. Slump, C. H. Slump, Fully relativistic treatment of electron-optical image formation based on the Dirac equation, Opt. Acta 33 (2) (1986) 145–157. `doi:10.1080/713821923`.

[132] R. Jagannathan, R. Simon, E. C. Sudarshan, N. Mukunda, Quantum theory of magnetic electron lenses based on the Dirac equation, Physics Letters A 134 (8-9) (1989) 457–464. `doi:10.1016/0375-9601(89)90685-3`.

[133] D. J. Lockwood, G. Yu, N. L. Rowell, Optical phonon frequencies and damping in AlAs, GaP, GaAs, InP, InAs and InSb studied by oblique incidence infrared spectroscopy, Solid State Communications 136 (7) (2005) 404–409. `doi:10.1016/j.ssc.2005.08.030`.

[134] H. Bethe, Über die Streuung von Elektronen an Krystallen, Die Naturwissenschaften 15 (1927) 786–788. `doi:10.1007/BF01504661`.
URL `http://www.springerlink.com/content/Q8160663J6475318`

[135] N. F. Mott, The Scattering of Electrons by Atoms, Proc. Roy. Soc. Lond. A 127 (806) (1930) 658–665. `doi:10.1098/rspa.1930.0082`.
URL `http://rspa.royalsocietypublishing.org/content/127/806/658.short`

[136] M. A. Coulthard, A relativistic Hartree-Fock atomic field calculation, Proceedings of the Physical Society 91 (1) (1967) 44–49. `doi:10.1088/0370-1328/91/1/309`.
URL `https://iopscience.iop.org/article/10.1088/0370-1328/91/1/309`

[137] A. Weickenmeier, H. Kohl, Computation of absorptive form factors for high-energy electron diffraction, Acta Crystallogr., Sect. A 47 (5) (1991) 590–597. `doi:10.1107/S0108767391004804`.
URL `http://dx.doi.org/10.1107/S0108767391004804`

[138] I. Lobato, D. Van Dyck, An accurate parameterization for scattering factors, electron densities and electrostatic potentials for neutral atoms that obey all physical constraints, Acta Crystallographica Section A Foundations and Advances 70 (6) (2014) 636–649.

doi:10.1107/S205327331401643X.
URL http://scripts.iucr.org/cgi-bin/paper?S205327331401643X

[139] J. M. Cowley, A. F. Moodie, The scattering of electrons by atoms and crystals. I. A new theoretical approach, Acta Crystallographica 10 (10) (1957) 609–619. doi:10.1107/s0365110x57002194.
URL http://dx.doi.org/10.1107/S0365110X57002194

[140] P. Goodman, A. F. Moodie, Numerical evaluations of N-beam wave functions in electron scattering by the multi-slice method, Acta Crystallographica Section A 30 (2) (1974) 280–290. doi:10.1107/S056773947400057X.

[141] R. P. Feynman, An Operator Calculus Having Applications in Quantum Electrodynamics, Physical Review 84 (1) (1951) 108–128. doi:10.1103/PhysRev.84.108.
URL https://link.aps.org/doi/10.1103/PhysRev.84.108

[142] G. H. Weiss, A. A. Maradudin, The Baker-Hausdorff Formula and a Problem in Crystal Physics, Journal of Mathematical Physics 3 (4) (1962) 771–777. doi:10.1063/1.1724280.
URL http://aip.scitation.org/doi/10.1063/1.1724280

[143] R. M. Wilcox, Exponential Operators and Parameter Differentiation in Quantum Physics, Journal of Mathematical Physics 8 (4) (1967) 962–982. doi:10.1063/1.1705306.
URL http://aip.scitation.org/doi/10.1063/1.1705306

[144] G. Strang, On the Construction and Comparison of Difference Schemes, SIAM Journal on Numerical Analysis 5 (3) (1968) 506–517. doi:10.1137/0705041.
URL https://doi.org/10.1137/0705041

[145] R. E. Omer, E. B. Bashier, A. I. Arbab, Numerical Solutions of a System of ODEs Based on Lie-Trotter and Strang Operator-splitting Methods, Universal Journal of Computational Mathematics 5 (2) (2017) 20–24. doi:10.13189/ujcmj.2017.050202.

[146] P. Duhamel, M. Vetterli, Fast fourier transforms: A tutorial review and a state of the art, Signal Processing 19 (4) (1990) 259–299. doi:10.1016/0165-1684(90)90158-U.

[147] J. M. Gibson, Breakdown of the weak-phase object approximation in amorphouse objects and measurement of high resolution electron optical parameters, Ultramicroscopy 56 (1-3) (1994) 26–31.

[148] M. H. Ho, B. K. Jap, R. M. Glaeser, Validity domain of the weak-phase-object approximation for electron diffraction of thin protein cystals, Acta Crystallographica Section A 44 (6) (1988) 878–884. doi:10.1107/S0108767388002831.

[149] M. Born, E. Wolf, Principles of Optics - M.Born, E. Wolf.pdf (1986).

[150] S. Van Aert, D. Van Dyck, A. J. den Dekker, S. V. Aert, D. V. Dyck, A. J. D. Dekker, S. Van Aert, D. Van Dyck, A. J. den Dekker, Resolution of coherent and incoherent imaging systems reconsidered - Classical criteria and a statistical alternative, Optics Express 14 (9) (2006) 3830. doi:10.1364/oe.14.003830.
URL http://www.opticsexpress.org/abstract.cfm?URI=oe-14-9-3830https://opg.optica.org/oe/abstract.cfm?uri=oe-14-9-3830

[151] D. Typke, K. Dierksen, Determination of Image Aberrations in High-resolution Electron Microscopy using Diffractogram and Cross-correlation Methods, Optik 99 (1995) 155–166.

[152] H. Brown, R. Ishikawa, G. S´anchez-Santolino, N. Shibata, Y. Ikuhara, L. Allen, S. Findlay, Large angle illumination enabling accurate structure reconstruction from thick samples in scanning transmission electron microscopy, Ultramicroscopy 197 (2019) 112–121. `doi:10.1016/j.ultramic.2018.12.010`.
URL `https://linkinghub.elsevier.com/retrieve/pii/S030439911830336X`

[153] A. Y. Borisevich, A. R. Lupini, S. J. Pennycook, Depth sectioning with the aberration-corrected scanning transmission electron microscope, Proceedings of the National Academy of Sciences of the United States of America 103 (9) (2006) 3044–3048. `doi:10.1073/pnas.0507105103`.

[154] L. Reimer, H. Kohl, Transmission Electron Microscopy - Physics of Image Formation, 5th Edition, Springer, 2008.

[155] R. Ishikawa, N. Shibata, T. Taniguchi, Y. Ikuhara, Three-Dimensional Imaging of a Single Dopant in a Crystal, Physical Review Applied 13 (3) (2020) 1. `doi:10.1103/PhysRevApplied.13.034064`.
URL `https://doi.org/10.1103/PhysRevApplied.13.034064`

[156] R. Ishikawa, A. R. Lupini, Y. Hinuma, S. J. Pennycook, Large-angle illumination STEM: Toward three-dimensional atom-by-atom imaging, Ultramicroscopy 151 (1) (2015) 122–129. `doi:10.1016/j.ultramic.2014.11.009`.
URL `http://dx.doi.org/10.1016/j.ultramic.2014.11.009`

[157] R. Ishikawa, S. J. Pennycook, A. R. Lupini, S. D. Findlay, N. Shibata, Y. Ikuhara, Single atom visibility in STEM optical depth sectioning, Applied Physics Letters 109 (16) (2016). `doi:10.1063/1.4965709`.
URL `http://dx.doi.org/10.1063/1.4965709`

[158] D. Van Dyck, G. Van Tendeloo, S. Amelinckx, Direct interpretation of high resolution electron images of substitutional alloy systems with a column structure, Ultramicroscopy 10 (3) (1982) 263–280. `doi:10.1016/0304-3991(82)90047-X`.
URL `https://linkinghub.elsevier.com/retrieve/pii/030439918290047X`

[159] D. Van Dyck, M. Op de Beeck, A simple intuitive theory for electron diffraction, Ultramicroscopy 64 (1-4) (1996) 99–107. `doi:10.1016/0304-3991(96)00008-3`.
URL `https://linkinghub.elsevier.com/retrieve/pii/0304399196000083`

[160] S. Van Aert, A. J. Den Dekker, D. Van Dyck, A. Van Den Bos, Optimal experimental design of STEM measurement of atom column positions, Ultramicroscopy 90 (4) (2002) 273–289. `doi:10.1016/S0304-3991(01)00152-8`.

[161] A. Y. Borisevich, A. R. Lupini, S. Travaglini, S. J. Pennycook, Depth sectioning of aligned crystal with the aberration-corrected scanning transmission electron microscope, Journal of Electron Microscopy 55 (1) (2006) 7–12. `doi:10.1093/jmicro/dfi075`.

[162] C. Mory, C. Colliex, J. Cowley, Optimum defocus for stem imaging and microanalysis, Ultramicroscopy 21 (2) (1987) 171–177. `doi:10.1016/0304-3991(87)90083-0`.
URL `https://linkinghub.elsevier.com/retrieve/pii/0304399187900830`

[163] J. M. Cowley, IMAGE CONTRAST IN A TRANSMISSION SCANNING ELECTRON MICROSCOPE, Applied Physics Letters 15 (2) (1969) 58–59. `doi:10.1063/1.1652901`.
URL `http://aip.scitation.org/doi/10.1063/1.1652901`

[164] H. Rose, Phase Contrast in Scanning Transmission Electron Microscopy. (1974).

[165] F. F. Krause, A. Rosenauer, Reciprocity relations in transmission electron microscopy: A rigorous derivation, Micron 92 (Supplement C) (2017) 1–5. `doi:10.1016/j.micron.2016.09.007`.
URL `http://www.sciencedirect.com/science/article/pii/S0968432816301421`

[166] D. Van Dyck, Persistent misconceptions about incoherence in electron microscopy, Ultramicroscopy 111 (7) (2011) 894–900. `doi:10.1016/j.ultramic.2011.01.007`.
URL `http://www.sciencedirect.com/science/article/pii/S0304399111000222https://linkinghub.elsevier.com/retrieve/pii/S0304399111000222`

[167] P. Schattschneider, M. Nelhiebel, B. Jouffrey, Density matrix of inelastically scattered fast electrons, Physical Review B 59 (16) (1999) 10959–10969. `doi:10.1103/PhysRevB.59.10959`.
URL `http://link.aps.org/doi/10.1103/PhysRevB.59.10959https://link.aps.org/doi/10.1103/PhysRevB.59.10959`

[168] P. Schattschneider, M. Nelhiebel, H. Souchay, B. Jouffrey, The physical significance of the mixed dynamic form factor, Micron 31 (4) (2000) 333–345. `doi:10.1016/S0968-4328(99)00112-2`.
URL `https://linkinghub.elsevier.com/retrieve/pii/S0968432899001122`

[169] H. Lourenço-Martins, A. Lubk, M. Kociak, Bridging nano-optics and condensed matter formalisms in a unified description of inelastic scattering of relativistic electron beams, SciPost Physics 10 (2) (2021) 1–54. `arXiv:2007.02773`, `doi:10.21468/SCIPOSTPHYS.10.2.031`.

[170] A. Beyer, J. Belz, N. Knaub, K. Jandieri, K. Volz, Influence of spatial and temporal coherences on atomic resolution high angle annular dark field imaging, Ultramicroscopy 169 (2016) 1–10. `doi:10.1016/j.ultramic.2016.06.006`.
URL `http://dx.doi.org/10.1016/j.ultramic.2016.06.006https://linkinghub.elsevier.com/retrieve/pii/S0304399116300845`

[171] M. P. Oxley, O. E. Dyck, The importance of temporal and spatial incoherence in quantitative interpretation of 4D-STEM, Ultramicroscopy 215 (January) (2020) 113015. `doi:10.1016/j.ultramic.2020.113015`.
URL `https://doi.org/10.1016/j.ultramic.2020.113015https://linkinghub.elsevier.com/retrieve/pii/S0304399120300255`

[172] H. Boersch, Experimentelle Bestimmung der Energieverteilung in thermisch ausgelösten Elektronenstrahlen, Zeitschrift für Physik 139 (2) (1954) 115–146. `doi:10.1007/BF01375256`.
URL `http://link.springer.com/10.1007/BF01375256`

[173] W. Knauer, Boersch Effect in Electron-Optical Instruments., Journal of vacuum science and technology 16 (6) (1979) 1676–1679. `doi:10.1116/1.570271`.
URL `http://avs.scitation.org/doi/10.1116/1.570271`

[174] J. M. LeBeau, S. D. Findlay, L. J. Allen, S. Stemmer, Position averaged convergent beam electron diffraction: Theory and applications, Ultramicroscopy 110 (2) (2010) 118–125. `doi:10.1016/j.ultramic.2009.10.001`.
URL `http://www.sciencedirect.com/science/article/pii/S0304399109002186`

[175] D. T. Nguyen, S. D. Findlay, J. Etheridge, The spatial coherence function in scanning transmission electron microscopy and spectroscopy, Ultramicroscopy 146 (2014) 6–16. `doi:10.1016/j.ultramic.2014.04.008`.
URL `http://dx.doi.org/10.1016/j.ultramic.2014.04.008`

[176] R. F. Loane, P. Xu, J. Silcox, Thermal vibrations in convergent-beam electron diffraction, Acta Crystallographica Section A 47 (3) (1991) 267–278. `doi:10.1107/S0108767391000375`.

[177] Z. L. Wang, Dynamics of thermal diffuse scattering in high-energy electron diffraction and imaging: Theory and experiments, Philos. Mag. B 65 (1992) 559–587. `doi:10.1080/13642819208207650`.

[178] Z. L. Wang, Dynamical theories of dark-field imaging using diffusely scattered electrons in STEM and TEM, Acta Crystallogr., Sect. A 51 (4) (1995) 569–585. `doi:10.1107/S0108767395002066`.
URL `http://dx.doi.org/10.1107/S0108767395002066`

[179] Z. L. Wang, The 'Frozen-Lattice' Approach for Incoherent Phonon Excitation in Electron Scattering. How Accurate Is It?, Acta Crystallographica Section A: Foundations of Crystallography 54 (4) (1998) 460–467. `doi:10.1107/S0108767398001457`.
URL `http://dx.doi.org/10.1107/S0108767398001457`

[180] D. A. Muller, B. Edwards, E. J. Kirkland, J. Silcox, Simulation of thermal diffuse scattering including a detailed phonon dispersion curve, Ultramicroscopy 86 (86) (2001) 371–380.

[181] D. Van Dyck, Is the frozen phonon model adequate to describe inelastic phonon scattering?, Ultramicroscopy 109 (6) (2009) 677–682. `doi:10.1016/j.ultramic.2009.01.001`.

[182] D. Van Dyck, I. Lobato, F. R. Chen, C. Kisielowski, Do you believe that atoms stay in place when you observe them in HREM?, Micron 68 (2015) 158–163. `doi:10.1016/j.micron.2014.09.003`.

[183] I. Waller, Die Einwirkung der Wärmebewegung der Kristallatome auf Intensität, Lage und Schärfe der Röntgenspektrallinien, Ann. Phys. 83 (1927) 153–183.

[184] R. F. Egerton, K. Wong, Some practical consequences of the Lorentzian angular distribution of inelastic scattering, Ultramicroscopy 59 (1–4) (1995) 169–180. `doi:10.1016/0304-3991(95)00026-W`.
URL `https://doi.org/10.1016/0304-3991(95)00026-W`

[185] R. F. Egerton, R. A. Mcleod, M. Malac, Validity of the dipole approximation in TEM-EELS studies, Microscopy Research and Technique 77 (10) (2014) 773–778. `doi:10.1002/jemt.22398`.
URL `http://dx.doi.org/10.1002/jemt.22398`

[186] A. Beyer, F. F. Krause, H. L. Robert, S. Firoozabadi, T. Grieb, P. Kükelhan, D. Heimes, M. Schowalter, K. Müller-Caspary, A. Rosenauer, K. Volz, Influence of plasmon excitations on atomic-resolution quantitative 4D scanning transmission electron microscopy, Scientific Reports 10 (1) (2020) 17890. `doi:10.1038/s41598-020-74434-w`.
URL `https://www.nature.com/articles/s41598-020-74434-whttps://doi.org/10.1038/s41598-020-74434-w`

[187] P. Stallknecht, H. Kohl, Computation and interpretation of contrast in crystal lattice images formed by inelastically scattered electrons in a transmission electron microscope, Ultramicroscopy 66 (3-4) (1996) 261–275. `doi:10.1016/S0304-3991(97)00007-7`.
URL `https://linkinghub.elsevier.com/retrieve/pii/S0304399197000077`

[188] K. W. Urban, J. Mayer, J. R. Jinschek, M. J. Neish, N. R. Lugg, L. J. Allen, Achromatic Elemental Mapping Beyond the Nanoscale in the Transmission Electron Microscope, Phys. Rev. Lett. 110 (18) (2013) 185507. `doi:10.1103/PhysRevLett.110.185507`.
URL `https://link.aps.org/doi/10.1103/PhysRevLett.110.185507`

[189] A. Howie, Aberration correction: Zooming out to overview, Philosophical Transactions of the Royal Society A: Mathematical, Physical and Engineering Sciences 367 (1903) (2009) 3859–3870. `doi:10.1098/rsta.2009.0104`.

[190] R. F. Egerton, A. M. Blackburn, R. A. Herring, L. Wu, Y. Zhu, Direct measurement of the PSF for Coulomb delocalization – a reconsideration, Ultramicroscopy 230 (August) (2021) 10–12. `doi:10.1016/j.ultramic.2021.113374`.

[191] R. A. Ferrell, Characteristic energy loss of electrons passing through metal foils. II. Dispersion relation and short wavelength cutoff for plasma oscillations, Physical Review 107 (2) (1957) 450–462. `doi:10.1103/PhysRev.107.450`.

[192] M. V. Berry, K. E. Mount, Semiclassical approximations in wave mechanics, Reports on Progress in Physics 35 (1) (1972) 315–397. `doi:10.1088/0034-4885/35/1/306`.

[193] H. Robert, I. Lobato, F. Lyu, Q. Chen, S. Van Aert, D. Van Dyck, K. Müller-Caspary, Dynamical diffraction of high-energy electrons investigated by focal series momentum-resolved scanning transmission electron microscopy at atomic resolution, Ultramicroscopy 233 (October 2021) (2022) 113425. `doi:10.1016/j.ultramic.2021.113425`.
URL `https://doi.org/10.1016/j.ultramic.2021.113425https://linkinghub.elsevier.com/retrieve/pii/S030439912100200X`

[194] R. F. Egerton, P. Li, M. Malac, Radiation damage in the TEM and SEM, Micron 35 (6) (2004) 399–409. `doi:10.1016/j.micron.2004.02.003`.

[195] R. F. Egerton, Radiation damage to organic and inorganic specimens in the TEM, Micron 119 (January) (2019) 72–87. `doi:10.1016/j.micron.2019.01.005`.
URL `https://doi.org/10.1016/j.micron.2019.01.005`

[196] N. Jiang, J. C. Spence, On the dose-rate threshold of beam damage in TEM, Ultramicroscopy 113 (2012) 77–82. `doi:10.1016/j.ultramic.2011.11.016`.
URL `http://dx.doi.org/10.1016/j.ultramic.2011.11.016`

[197] R. F. Egerton, Dose measurement in the TEM and STEM, Ultramicroscopy 229 (June) (2021) 113363. `doi:10.1016/j.ultramic.2021.113363`.
URL `https://doi.org/10.1016/j.ultramic.2021.113363`

[198] W. E. King, R. Benedek, K. Merkle, M. Meshii, Damage effects of high energy electrons on metals, Ultramicroscopy 23 (3-4) (1987) 345–353. `doi:10.1016/0304-3991(87)90245-2`.
URL `https://linkinghub.elsevier.com/retrieve/pii/0304399187902452`

[199] L. W. Hobbs, F. W. Clinard, S. J. Zinkle, R. C. Ewing, Radiation effects in ceramics, Journal of Nuclear Materials 216 (C) (1994) 291–321. `doi:10.1016/0022-3115(94)90017-5`.

[200] L. W. Hobbs, The role of topology and geometry in the irradiation-induced amorphization of network structures, Journal of Non-Crystalline Solids 182 (1-2) (1995) 27–39. `doi:10.1016/0022-3093(94)00574-5`.
URL `https://linkinghub.elsevier.com/retrieve/pii/0022309394005745`

[201] A. Bachmatiuk, J. Zhao, S. M. Gorantla, I. G. G. Martinez, J. Wiedermann, C. Lee, J. Eckert, M. H. Rummeli, Low voltage transmission electron microscopy of Graphene, Small 11 (5) (2015) 515–542. `doi:10.1002/smll.201401804`.

[202] P. Hirsch, M. Kässens, M. Püttmann, L. Reimer, Contamination in a scanning electron microscope and the influence of specimen cooling, Scanning 16 (2) (1994) 101–110. `doi:10.1002/sca.4950160207`.

[203] S. Hettler, M. Dries, P. Hermann, M. Obermair, D. Gerthsen, M. Malac, Carbon contamination in scanning transmission electron microscopy and its impact on phase-plate applications, Micron 96 (2017) 38–47. `doi:10.1016/j.micron.2017.02.002`.
URL `http://dx.doi.org/10.1016/j.micron.2017.02.002`

[204] T. Yamazaki, K. Watanabe, N. Nakanishi, I. Hashimoto, Role of surface amorphous film in high-resolution high-angle annular dark field STEM imaging, Ultramicroscopy 99 (2-3) (2004) 125–135. `doi:10.1016/j.ultramic.2003.12.001`.

[205] K. A. Mkhoyan, S. E. Maccagnano-Zacher, E. J. Kirkland, J. Silcox, Effects of amorphous layers on ADF-STEM imaging, Ultramicroscopy 108 (8) (2008) 791–803. `doi:10.1016/j.ultramic.2008.01.007`.

[206] J. M. LeBeau, S. D. Findlay, L. J. Allen, S. Stemmer, Standardless Atom Counting in Scanning Transmission Electron Microscopy, Nano Letters 10 (11) (2010) 4405–4408. `doi:10.1021/nl102025s`.
URL `https://pubs.acs.org/doi/10.1021/nl102025s`

[207] M. Tanaka, R. Saito, H. Sekii, Point-group determination by convergent-beam electron diffraction, Acta Crystallogr., Sect. A 39 (3) (1983) 357–368. `doi:10.1107/S010876738300080X`.
URL `http://dx.doi.org/10.1107/S010876738300080X`

[208] M. Tanaka, Convergent-beam electron diffraction, Acta Crystallogr., Sect. A 50 (3) (1994) 261–286. `doi:10.1107/S0108767393010426`.
URL `http://dx.doi.org/10.1107/S0108767393010426`

[209] S. NISHIKAWA, S. KIKUCHI, Diffraction of Cathode Rays by Mica, Nature 121 (3061) (1928) 1019–1020. `doi:10.1038/1211019a0`.
URL `https://www.nature.com/articles/1211019a0`

[210] K. Artmann, Zur Theorie der Kikuchi-Bänder, Zeitschrift für Physik A Hadrons and Nuclei 125 (4) (1948) 225–249.
URL `http://dx.doi.org/10.1007/BF01454893`

[211] H. Hashimoto, A. Howie, M. J. Whelan, Anomalous electron absorption effects in metal foils: theory and comparison with experiment, Proceedings of the Royal Society of London. Series A. Mathematical and Physical Sciences 269 (1336) (1962) 80–103. `doi:10.1098/rspa.1962.0164`.

[212] P. Fraundorf, W. Qin, P. Moeck, E. Mandell, Making sense of nanocrystal lattice fringes, Journal of Applied Physics 98 (11) (2005) 0–10. `arXiv:0212281`, `doi:10.1063/1.2135414`.

[213] W. Coene, G. Janssen, M. Op De Beeck, D. Van Dyck, Phase retrieval through focus variation for ultra-resolution in field-emission transmission electron microscopy, Physical Review Letters 69 (26) (1992) 3743–3746. `doi:10.1103/PhysRevLett.69.3743`.

[214] A. Thust, Focal-Series Reconstruction, in: Transmission Electron Microscopy, Springer International Publishing, Cham, 2016, pp. 233–266. `doi:10.1007/978-3-319-26651-0_9`.
URL `http://link.springer.com/10.1007/978-3-319-26651-0_9`

[215] S. J. Pennycook, D. E. Jesson, High-resolution Z-contrast imaging of crystals, Ultramicroscopy 37 (1991) 14–38.

[216] M. M. Treacy, Z dependence of electron scattering by single atoms into annular dark-field detectors, Microscopy and Microanalysis 17 (6) (2011) 847–858. `doi:10.1017/S1431927611012074`.

[217] S. Yamashita, J. Kikkawa, K. Yanagisawa, T. Nagai, K. Ishizuka, K. Kimoto, Atomic number dependence of Z contrast in scanning transmission electron microscopy, Scientific Reports 8 (1) (2018) 1–7. `doi:10.1038/s41598-018-30941-5`.
URL `http://dx.doi.org/10.1038/s41598-018-30941-5`

[218] J. M. LeBeau, S. Stemmer, Experimental quantification of annular dark-field images in scanning transmission electron microscopy, Ultramicroscopy 108 (2008) 1653–1658. `doi:10.1016/j.ultramic.2008.07.001`.

[219] J. M. LeBeau, S. D. Findlay, X. Wang, A. J. Jacobson, L. J. Allen, S. Stemmer, High-angle scattering of fast electrons from crystals containing heavy elements: Simulation and experiment, Physical Review B 79 (21) (2009) 214110. `doi:10.1103/PhysRevB.79.214110`.
URL `https://link.aps.org/doi/10.1103/PhysRevB.79.214110`

[220] A. Rosenauer, K. Gries, K. Müller, A. Pretorius, M. Schowalter, A. Avramescu, K. Engl, S. Lutgen, Measurement of specimen thickness and composition in Alx Ga1 - x N / GaN using high-angle annular dark field images, Ultramicroscopy 109 (9) (2009) 1171–1182. `doi:10.1016/j.ultramic.2009.05.003`.
URL `http://www.sciencedirect.com/science/article/B6TW1-4W91PY1-2/2/377d9008104d5889aa5e83786389aaaa`

[221] J. Barthel, L. J. Allen, Role of ionization in imaging and spectroscopy utilizing fast electrons that have excited phonons, Physical Review B 104 (10) (2021) 1–13. `doi:10.1103/PhysRevB.104.104108`.

[222] S. Pennycook, D. Jesson, High-resolution incoherent imaging of crystals, Physical Review Letters 64 (8) (1990) 938–941. `doi:10.1103/PhysRevLett.64.938`.
URL `http://link.aps.org/doi/10.1103/PhysRevLett.64.938https://link.aps.org/doi/10.1103/PhysRevLett.64.938`

[223] P. Nellist, S. Pennycook, The principles and interpretation of annular dark-field Z-contrast imaging, 2000, pp. 147–203. `doi:10.1016/S1076-5670(00)80013-0`.
URL `https://linkinghub.elsevier.com/retrieve/pii/S1076567000800130`

[224] K. Watanabe, Y. Kotaka, N. Nakanishi, T. Yamazaki, I. Hashimoto, M. Shiojiri, Deconvolution processing of HAADF STEM images, Ultramicroscopy 92 (3-4) (2002) 191–199. `doi:10.1016/S0304-3991(02)00132-8`.

[225] N. Nakanishi, T. Yamazaki, A. Rečnik, M. Čeh, M. Kawasaki, K. Watanabe, M. Shiojiri, Retrieval process of high-resolution HAADF-STEM images, Journal of Electron Microscopy 51 (6) (2002) 383–390. `doi:10.1093/jmicro/51.6.383`.

[226] J. P. Buban, Q. Ramasse, B. Gipson, N. D. Browning, H. Stahlberg, High-resolution low-dose scanning transmission electron microscopy, Journal of Electron Microscopy 59 (2) (2010) 103–112. `doi:10.1093/jmicro/dfp052`.

[227] D. Nicholls, J. Lee, H. Amari, A. J. Stevens, B. L. Mehdi, N. D. Browning, Minimising damage in high resolution scanning transmission electron microscope images of nanoscale structures and processes, Nanoscale 12 (41) (2020) 21248–21254. `doi:10.1039/d0nr04589f`.

[228] M. Varela, A. R. Lupini, K. Van Benthem, A. Y. Borisevich, M. F. Chisholm, N. Shibata, E. Abe, S. J. Pennycook, Materials characterization in the aberration-corrected scanning transmission electron microscope, Annual Review of Materials Research 35 (2005) 539–569. `doi:10.1146/annurev.matsci.35.102103.090513`.

[229] F. Winkler, J. Barthel, R. E. Dunin-Borkowski, K. Müller-Caspary, Direct measurement of electrostatic potentials at the atomic scale: A conceptual comparison between electron holography and scanning transmission electron microscopy, Ultramicroscopy 210 (September 2019) (2020) 112926. `doi:10.1016/j.ultramic.2019.112926`.
URL `https://doi.org/10.1016/j.ultramic.2019.112926`

[230] A. Lubk, J. Zweck, Differential phase contrast: An integral perspective, Phys. Rev. A 91 (2) (2015) 23805. `doi:10.1103/PhysRevA.91.023805`.
URL `http://link.aps.org/doi/10.1103/PhysRevA.91.023805`

[231] N. H. Dekkers, H. de Lang, Differential Phase Contrast in a STEM, Optik 41 (1974) 452–456.
URL `http://xrm.phys.northwestern.edu/research/pdf_papers/1974/dekkers_optik_1974.pdf`

[232] H. Rose, Nonstandard imaging methods in electron microscopy, Ultramicroscopy 2 (1) (1977) 251–267. `doi:10.1016/S0304-3991(76)91538-2`.

URL https://linkinghub.elsevier.com/retrieve/pii/S0304399176915382https://doi.org/10.1016/S0304-3991(76)91538-2

[233] N. Shibata, S. D. Findlay, Y. Kohno, H. Sawada, Y. Kondo, Y. Ikuhara, Differential phase-contrast microscopy at atomic resolution, Nat. Phys. 8 (8) (2012) 611–615. doi:10.1038/nphys2337.
URL http://dx.doi.org/10.1038/nphys2337

[234] K. Müller-Caspary, F. F. Krause, T. Grieb, S. Löffler, M. Schowalter, A. Béché, V. Galioit, D. Marquardt, J. Zweck, P. Schattschneider, J. Verbeeck, A. Rosenauer, Measurement of atomic electric fields and charge densities from average momentum transfers using scanning transmission electron microscopy, Ultramicroscopy 178 (2017) 62–80. doi:10.1016/j.ultramic.2016.05.004.
URL http://www.sciencedirect.com/science/article/pii/S0304399116300596

[235] K. Müller-Caspary, M. Duchamp, M. Rösner, V. Migunov, F. Winkler, H. Yang, M. Huth, R. Ritz, M. Simson, S. Ihle, H. Soltau, T. Wehling, R. E. Dunin-Borkowski, S. Van Aert, A. Rosenauer, Atomic-scale quantification of charge densities in two-dimensional materials, Physical Review B 98 (12) (sep 2018). doi:10.1103/PhysRevB.98.121408.

[236] M. Lohr, R. Schregle, M. Jetter, C. Wächter, T. Wunderer, F. Scholz, J. Zweck, Differential phase contrast 2.0-Opening new "fields" for an established technique, Ultramicroscopy 117 (2012) 7–14. doi:10.1016/j.ultramic.2012.03.020.

[237] K. Müller-Caspary, F. F. Krause, F. Winkler, A. Béché, J. Verbeeck, S. Van Aert, A. Rosenauer, S. VanAert, A. Rosenauer, Comparison of first moment STEM with conventional differential phase contrast and the dependence on electron dose, Ultramicroscopy accepted (August 2018) (2018) in print. doi:10.1016/j.ultramic.2018.12.018.
URL http://www.sciencedirect.com/science/article/pii/S0304399118302730https://doi.org/10.1016/j.ultramic.2018.12.018

[238] Z. Li, J. Biskupek, U. Kaiser, H. Rose, Integrated Differential Phase Contrast (IDPC)-STEM Utilizing a Multi-Sector Detector for Imaging Thick Samples, Microscopy and Microanalysis 28 (3) (2022) 611–621. doi:10.1017/S1431927622000289.

[239] T. Grieb, F. F. Krause, K. Müller-Caspary, R. Ritz, M. Simson, J. Schörmann, C. Mahr, J. Müßener, M. Schowalter, H. Soltau, M. Eickhoff, A. Rosenauer, 4D-STEM at interfaces to GaN: Centre-of-mass approach and NBED-disc detection, Ultramicroscopy 228 (December 2020) (2021) 113321. doi:10.1016/j.ultramic.2021.113321.
URL https://linkinghub.elsevier.com/retrieve/pii/S0304399121001066

[240] N. Shibata, S. D. Findlay, H. Sasaki, T. Matsumoto, H. Sawada, Y. Kohno, S. Otomo, R. Minato, Y. Ikuhara, Imaging of built-in electric field at a p-n junction by scanning transmission electron microscopy, Sci. Rep. 5 (2015) 10040.

[241] I. MacLaren, L. Q. Wang, D. McGrouther, A. J. Craven, S. McVitie, R. Schierholz, A. Kovács, J. Barthel, R. E. Dunin-Borkowski, On the origin of differential phase contrast at a locally charged and globally charge-compensated domain boundary in a polar-ordered material, Ultramicroscopy 154 (2015) 57–63. doi:10.1016/j.ultramic.2015.03.016.
URL http://dx.doi.org/10.1016/j.ultramic.2015.03.016

[242] A. Beyer, M. S. Munde, S. Firoozabadi, D. Heimes, T. Grieb, A. Rosenauer, K. Müller-Caspary, K. Volz, Quantitative Characterization of Nanometer-Scale Electric Fields via Momentum-Resolved STEM, Nano Letters 21 (5) (2021) 2018–2025. `doi:10.1021/acs.nanolett.0c04544`.

[243] M. Wu, E. Spiecker, Correlative micro-diffraction and differential phase contrast study of mean inner potential and subtle beam-specimen interaction, Ultramicroscopy 176 (2017) 233–245. `doi:10.1016/j.ultramic.2017.03.029`.
URL `http://dx.doi.org/10.1016/j.ultramic.2017.03.029`

[244] C. Mahr, T. Grieb, F. F. Krause, M. Schowalter, A. Rosenauer, Towards the interpretation of a shift of the central beam in nano-beam electron diffraction as a change in mean inner potential, Ultramicroscopy 236 (March) (2022) 113503. `doi:10.1016/j.ultramic.2022.113503`.
URL `https://doi.org/10.1016/j.ultramic.2022.113503`

[245] R. Close, Z. Chen, N. Shibata, S. D. Findlay, Towards quantitative, atomic-resolution reconstruction of the electrostatic potential via differential phase contrast using electrons, Ultramicroscopy 159 (2015) 124–137. `doi:10.1016/j.ultramic.2015.09.002`.
URL `http://dx.doi.org/10.1016/j.ultramic.2015.09.002http://www.sciencedirect.com/science/article/pii/S0304399115300255`

[246] C. Addiego, W. Gao, X. Pan, Thickness and defocus dependence of inter-atomic electric fields measured by scanning diffraction, Ultramicroscopy 208 (September 2019) (2020) 112850. `doi:10.1016/j.ultramic.2019.112850`.
URL `https://doi.org/10.1016/j.ultramic.2019.112850`

[247] J. Bürger, T. Riedl, J. K. Lindner, Influence of lens aberrations, specimen thickness and tilt on differential phase contrast STEM images, Ultramicroscopy 219 (February) (2020) 113118. `doi:10.1016/j.ultramic.2020.113118`.
URL `https://doi.org/10.1016/j.ultramic.2020.113118`

[248] B. Bauer, J. Hubmann, M. Lohr, E. Reiger, D. Bougeard, J. Zweck, Direct detection of spontaneous polarization in wurtzite GaAs nanowires, Applied Physics Letters 104 (21) (2014) 211902. `doi:10.1063/1.4880209`.
URL `http://aip.scitation.org/doi/10.1063/1.4880209http://scitation.aip.org/content/aip/journal/apl/104/21/10.1063/1.4880209`

[249] K. Müller-Caspary, T. Grieb, J. Müßener, N. Gauquelin, P. Hille, J. Schörmann, J. Verbeeck, S. Van Aert, M. Eickhoff, A. Rosenauer, Electrical Polarization in AlN/GaN Nanodisks Measured by Momentum-Resolved 4D Scanning Transmission Electron Microscopy, Physical Review Letters 122 (10) (2019) 2–8. `doi:10.1103/PhysRevLett.122.106102`.
URL `https://doi.org/10.1103/PhysRevLett.122.106102https://link.aps.org/doi/10.1103/PhysRevLett.122.106102`

[250] T. Grieb, F. F. Krause, K. Müller-Caspary, S. Firoozabadi, C. Mahr, M. Schowalter, A. Beyer, O. Oppermann, K. Volz, A. Rosenauer, Angle-resolved STEM using an iris aperture: Scattering contributions and sources of error for the quantitative analysis in Si, Ultramicroscopy 221 (October 2020) (2021) 113175. `doi:10.1016/j.ultramic.2020.113175`.
URL `https://doi.org/10.1016/j.ultramic.2020.113175`

[251] V. Grillo, E. Carlino, F. Glas, Influence of the static atomic displacement on atomic resolution Z-contrast imaging, Phys. Rev. B 77 (2008) 54103.

[252] K. Müller, M. Schowalter, A. Rosenauer, O. Rubel, K. Volz, Effect of bonding and static atomic displacements on composition quantification in $In_xGa_{1-x}N_yAs_{1-y}$, Phys. Rev. B 81 (7) (2010) 75315. `doi:10.1103/PhysRevB.81.075315`.
URL `https://link.aps.org/doi/10.1103/PhysRevB.81.075315`

[253] V. Grillo, K. Müller, K. Volz, F. Glas, T. Grieb, A. Rosenauer, Strain, composition and disorder in ADF imaging of semiconductors, J. Phys.: Conf. Ser. 326 (1) (2011) 12006. `doi:10.1088/1742-6596/326/1/012006`.
URL `http://stacks.iop.org/1742-6596/326/i=1/a=012006`

[254] K. van Benthem, A. R. Lupini, M. Kim, H. S. Baik, S. Doh, J.-H. Lee, M. P. Oxley, S. D. Findlay, L. J. Allen, J. T. Luck, S. J. Pennycook, Three-dimensional imaging of individual hafnium atoms inside a semiconductor device, Applied Physics Letters 87 (3) (2005) 034104. `doi:10.1063/1.1991989`.
URL `https://pubs.aip.org/aip/apl/article/330557`

[255] M. F. Chisholm, S. J. Pennycook, Direct imaging of dislocation core structures by Z-contrast STEM, Philosophical Magazine 86 (29-31) (2006) 4699–4725. `doi:10.1080/14786430600778757`.

[256] F. Li, H. Nian, K. Du, J. Wang, J. Wang, Y. Zhou, Direct observation of a screw dislocation normal to the beam by Z-contrast STEM, Journal of the American Ceramic Society 95 (2) (2012) 466–468. `doi:10.1111/j.1551-2916.2011.05016.x`.

[257] S. Kim, Y. Jung, S. S. S. Lee, J. J. Kim, G. Byun, S. S. S. Lee, H. H. H. Lee, J. Jung Kim, G. Byun, S. S. S. Lee, H. H. H. Lee, 3D strain measurement in electronic devices using through-focal annular dark-field imaging, Ultramicroscopy 146 (0) (2014) 1–5. `doi:http://dx.doi.org/10.1016/j.ultramic.2014.04.010`.
URL `http://www.sciencedirect.com/science/article/pii/S0304399114000898http://dx.doi.org/10.1016/j.ultramic.2014.04.010`

[258] H. L. Xin, D. A. Muller, Aberration-corrected ADF-STEM depth sectioning and prospects for reliable 3D imaging in STEM, Journal of Electron Microscopy 58 (3) (2009) 157–165. `doi:10.1093/jmicro/dfn029`.

[259] G. Behan, E. C. Cosgriff, A. I. Kirkland, P. D. Nellist, Three-dimensional imaging by optical sectioning in the aberration-corrected scanning transmission electron microscope, Philosophical Transactions of the Royal Society A: Mathematical, Physical and Engineering Sciences 367 (1903) (2009) 3825–3844. `doi:10.1098/rsta.2009.0074`.

[260] M. Alania, T. Altantzis, A. De Backer, I. Lobato, S. Bals, S. Van Aert, Depth sectioning combined with atom-counting in HAADF STEM to retrieve the 3D atomic structure, Ultramicroscopy 177 (2017) 36–42. `doi:10.1016/j.ultramic.2016.11.002`.

[261] E. G. Bosch, I. Lazić, Analysis of depth-sectioning STEM for thick samples and 3D imaging, Ultramicroscopy 207 (April) (2019). `doi:10.1016/j.ultramic.2019.112831`.

[262] F. F. Krause, M. Schowalter, T. Grieb, K. Müller-Caspary, T. Mehrtens, A. Rosenauer, Effects of instrument imperfections on quantitative scanning transmission electron

microscopy, Ultramicroscopy 161 (2016) 146–160. `doi:10.1016/j.ultramic.2015.10.026`.
URL `http://www.sciencedirect.com/science/article/pii/S0304399115300620`

[263] C. Mahr, K. Müller-Caspary, R. Ritz, M. Simson, T. Grieb, M. Schowalter, F. F. Krause, A. Lackmann, H. Soltau, A. Wittstock, A. Rosenauer, H. Soltau, Influence of distortions of recorded diffraction patterns on strain analysis by nano-beam electron diffraction, Ultramicroscopy 196 (2018) 74–82. `doi:10.1016/j.ultramic.2018.09.010`.

[264] G. C. Capitani, P. Oleynikov, S. Hovmöller, M. Mellini, A practical method to detect and correct for lens distortion in the TEM, Ultramicroscopy 106 (2) (2006) 66–74. `doi:10.1016/j.ultramic.2005.06.003`.

[265] J. C. Lagarias, J. A. Reeds, M. H. Wright, P. E. Wright, Convergence properties of the Nelder-Mead simplex method in low dimensions, SIAM Journal on Optimization 9 (1) (1998) 112–147. `doi:10.1137/S1052623496303470`.

[266] J. Zweck, F. Schwarzhuber, S. Pöllath, K. Müller-Caspary, Advanced processing of differential phase contrast data: Distinction between different causes of electron phase shifts, Ultramicroscopy 250 (November 2022) (2023) 113752. `doi:10.1016/j.ultramic.2023.113752`.
URL `https://doi.org/10.1016/j.ultramic.2023.113752`

[267] D. Chruściński, A. Jamiołkowski, Geometric Phases in Classical and Quantum Mechanics, Birkhäuser Boston, Boston, MA, 2004. `doi:10.1007/978-0-8176-8176-0`.
URL `http://link.springer.com/10.1007/978-0-8176-8176-0`

[268] A. Paszke, S. Gross, F. Massa, A. Lerer, J. Bradbury, G. Chanan, T. Killeen, Z. Lin, N. Gimelshein, L. Antiga, A. Desmaison, A. Kopf, E. Yang, Z. DeVito, M. Raison, A. Tejani, S. Chilamkurthy, B. Steiner, L. Fang, J. Bai, S. Chintala, PyTorch: An Imperative Style, High-Performance Deep Learning Library, in: Advances in Neural Information Processing Systems 32, Curran Associates, Inc., 2019, pp. 8024–8035.
URL `http://papers.neurips.cc/paper/9015-pytorch-an-imperative-style-high-per`
`pdf`

[269] K. Müller, M. Schowalter, J. Jansen, K. Tsuda, J. Titantah, D. Lamoen, A. Rosenauer, Refinement of the 200 structure factor for GaAs using parallel and convergent beam electron nanodiffraction data, Ultramicroscopy 109 (2009) 802–814. `doi:10.1016/j.ultramic.2009.03.029`.

[270] H. L. Robert, B. Diederichs, K. Müller-Caspary, Contribution of multiple plasmon scattering in low-angle electron diffraction investigated by energy-filtered atomically resolved 4D-STEM, Applied Physics Letters 121 (21) (2022) 213502. `doi:10.1063/5.0129692`.
URL `https://aip.scitation.org/doi/10.1063/5.0129692`

[271] M. Tanaka, K. Tsuda, M. Terauchi, K. Tsuno, T. Kaneyama, T. Honda, M. Ishida, A new 200 kV Ω-filter electron microscope, Journal of Microscopy 194 (1) (1999) 219–227. `doi:10.1046/j.1365-2818.1999.00446.x`.

[272] B. G. Mendis, An inelastic multislice simulation method incorporating plasmon energy losses, Ultramicroscopy 206 (June) (2019) 112816. `doi:10.1016/j.ultramic.2019.112816`.
URL `https://doi.org/10.1016/j.ultramic.2019.112816`

[273] J. Barthel, M. Cattaneo, B. G. Mendis, S. D. Findlay, L. J. Allen, Angular dependence of fast-electron scattering from materials, Physical Review B 101 (18) (2020) 1–9. `doi:10.1103/PhysRevB.101.184109`.

[274] K. Tsuno, E. Munro, Design of an omega filter for a 200 kV electron microscope, Review of Scientific Instruments 68 (1) (1997) 109–115. `doi:10.1063/1.1147797`.

[275] R. D. Leapman, C. E. Fiori, C. R. Swyt, Mass thickness determination by electron energy loss for quantitative X-ray microanalysis in biology, Journal of Microscopy 133 (3) (1984) 239–253. `doi:10.1111/j.1365-2818.1984.tb00489.x`.

[276] T. Malis, S. C. Cheng, R. F. Egerton, EELS log-ratio technique for specimen-thickness measurement in the TEM, Journal of Electron Microscopy Technique 8 (2) (1988) 193–200. `doi:10.1002/jemt.1060080206`.

[277] K. Iakoubovskii, K. Mitsuishi, Y. Nakayama, K. Furuya, Mean free path of inelastic electron scattering in elemental solids and oxides using transmission electron microscopy: Atomic number dependent oscillatory behavior, Physical Review B - Condensed Matter and Materials Physics 77 (10) (2008) 1–7. `doi:10.1103/PhysRevB.77.104102`.

[278] A. Rosenauer, M. Schowalter, STEMSIM—a New Software Tool for Simulation of STEM HAADF Z-Contrast Imaging, in: A. G. Cullis, P. A. Midgley (Eds.), Microscopy of Semiconducting Materials 2007, Vol. 120, Springer Netherlands, Dordrecht, 2007, pp. 170–172. `doi:10.1007/978-1-4020-8615-1_36`.
URL `http://link.springer.com/10.1007/978-1-4020-8615-1_36`

[279] K. Matsushima, H. Schimmel, F. Wyrowski, Fast calculation method for optical diffraction on tilted planes by use of the angular spectrum of plane waves, Journal of the Optical Society of America A 20 (9) (2003) 1755. `doi:10.1364/josaa.20.001755`.

[280] T. Grieb, F. F. Krause, C. Mahr, D. Zillmann, K. Müller-Caspary, M. Schowalter, A. Rosenauer, Optimization of {NBED} simulations for disc-detection measurements, Ultramicroscopy 181 (2017) 50–60. `doi:10.1016/j.ultramic.2017.04.015`.
URL `http://www.sciencedirect.com/science/article/pii/S0304399116302911`

[281] R. Ballabriga, M. Campbell, X. Llopart, Asic developments for radiation imaging applications: The medipix and timepix family, Nuclear Instruments and Methods in Physics Research, Section A: Accelerators, Spectrometers, Detectors and Associated Equipment 878 (May 2017) (2018) 10–23. `doi:10.1016/j.nima.2017.07.029`.
URL `http://dx.doi.org/10.1016/j.nima.2017.07.029`

[282] F. Kahl, V. Gerheim, M. Linck, H. Müller, R. Schillinger, S. Uhlemann, Test and characterization of a new post-column imaging energy filter, in: Advances in Imaging and Electron Physics, Vol. 212, Elsevier Inc., 2019, pp. 35–70. `doi:10.1016/bs.aiep.2019.08.005`.
URL `https://doi.org/10.1016/bs.aiep.2019.08.005https://linkinghub.elsevier.com/retrieve/pii/S1076567019300576`

[283] Z. Yu, D. A. Muller, J. Silcox, Study of strain fields at a-Si/c-Si interface, Journal of Applied Physics 95 (7) (2004) 3362–3371. `doi:10.1063/1.1649463`.

[284] V. Grillo, The effect of surface strain relaxation on HAADF imaging, Ultramicroscopy 109 (12) (2009) 1453–1464. `doi:DOI:10.1016/j.ultramic.2009.07.010`.
URL `http://www.sciencedirect.com/science/article/B6TW1-4WV781V-3/2/dc9ab8ae256680351c9fc81e027ebf56http://dx.doi.org/10.1016/j.ultramic.2009.07.010`

[285] K. Huang, X-ray reflexions from dilute solid solutions, Proceedings of the Royal Society of London. Series A. Mathematical and Physical Sciences 190 (1020) (1947) 102–117. `doi:10.1098/rspa.1947.0064`.
URL `https://royalsocietypublishing.org/doi/10.1098/rspa.1947.0064`

[286] S. D. Findlay, N. Shibata, H. Sawada, E. Okunishi, Y. Kondo, Y. Ikuhara, Dynamics of annular bright field imaging in scanning transmission electron microscopy, Ultramicroscopy 110 (7) (2010) 903–923. `doi:http://dx.doi.org/10.1016/j.ultramic.2010.04.004`.
URL `http://dx.doi.org/10.1016/j.ultramic.2010.04.004http://www.sciencedirect.com/science/article/pii/S0304399110001129`

[287] R. Hovden, D. A. Muller, Efficient elastic imaging of single atoms on ultrathin supports in a scanning transmission electron microscope, Ultramicroscopy 123 (2012) 59–65. `doi:10.1016/j.ultramic.2012.04.014`.
URL `http://dx.doi.org/10.1016/j.ultramic.2012.04.014`

[288] P. J. Phillips, M. De Graef, L. Kovarik, A. Agrawal, W. Windl, M. J. Mills, Atomic-resolution defect contrast in low angle annular dark-field STEM, Ultramicroscopy 116 (2012) 47–55. `doi:10.1016/j.ultramic.2012.03.013`.
URL `http://dx.doi.org/10.1016/j.ultramic.2012.03.013`

[289] G. Ruben, E. C. Cosgriff, A. J. D'Alfonso, S. D. Findlay, J. M. LeBeau, L. J. Allen, Interface location by depth sectioning using a low-angle annular dark field detector, Ultramicroscopy 113 (2012) 131–138. `doi:10.1016/j.ultramic.2011.11.002`.
URL `http://dx.doi.org/10.1016/j.ultramic.2011.11.002`

[290] G. Ruben, P. Wang, A. J. D'Alfonso, P. D. Nellist, L. J. Allen, Nanohalos: A manifestation of electron channelling in gold nanoparticles, Ultramicroscopy 120 (2012) 10–15. `doi:10.1016/j.ultramic.2012.06.002`.
URL `http://dx.doi.org/10.1016/j.ultramic.2012.06.002`

[291] S. Lee, Y. Oshima, E. Hosono, H. Zhou, K. Takayanagi, Reversible contrast in focus series of annular bright field images of a crystalline LiMn2O4 nanowire, Ultramicroscopy 125 (2013) 43–48. `doi:10.1016/j.ultramic.2012.09.011`.
URL `http://dx.doi.org/10.1016/j.ultramic.2012.09.011`

[292] J. M. Johnson, S. Im, W. Windl, J. Hwang, Three-dimensional imaging of individual point defects using selective detection angles in annular dark field scanning transmission electron microscopy, Ultramicroscopy 172 (June 2016) (2017) 17–29. `doi:10.1016/j.ultramic.2016.10.007`.
URL `http://dx.doi.org/10.1016/j.ultramic.2016.10.007`

[293] D. T. Nguyen, S. D. Findlay, J. Etheridge, A menu of electron probes for optimising information from scanning transmission electron microscopy, Ultramicroscopy 184 (2018) 143–155. `doi:10.1016/j.ultramic.2017.08.020`.

[294] H. Yun, A. Prakash, B. Jalan, J. S. Jeong, K. A. Mkhoyan, STEM beam channeling in BaSnO3/LaAlO3 perovskite bilayers and visualization of 2D misfit dislocation network, Ultramicroscopy 208 (October 2019) (2020). `doi:10.1016/j.ultramic.2019.112863`.

[295] K. Momma, F. Izumi, VESTA 3 for three-dimensional visualization of crystal, volumetric and morphology data, Journal of Applied Crystallography 44 (6) (2011) 1272–1276. `doi:10.1107/S0021889811038970`.

[296] M. Küpers, P. M. Konze, A. Meledin, J. Mayer, U. Englert, M. Wuttig, R. Dronskowski, Controlled Crystal Growth of Indium Selenide, In2Se3, and the Crystal Structures of α-In2Se3, Inorganic Chemistry 57 (18) (2018) 11775–11781. `doi:10.1021/acs.inorgchem.8b01950`.

[297] T. Yamazaki, M. Kawasaki, K. Watanabe, I. Hashimoto, M. Shiojiri, Effect of small crystal tilt on atomic-resolution high-angle annular dark field STEM imaging, Ultramicroscopy 92 (3-4) (2002) 181–189. `doi:10.1016/S0304-3991(02)00131-6`.

[298] D. Zhou, K. Müller-Caspary, W. Sigle, F. F. Krause, A. Rosenauer, P. A. van Aken, Sample tilt effects on atom column position determination in ABF-STEM imaging, Ultramicroscopy 160 (2016) 110–117. `doi:10.1016/j.ultramic.2015.10.008`.
URL `http://www.sciencedirect.com/science/article/pii/S0304399115300462http://dx.doi.org/10.1016/j.ultramic.2015.10.008`

[299] J. Tersoff, New empirical approach for the structure and energy of covalent systems, Phys. Rev. B 37 (12) (1988) 6991–7000. `doi:10.1103/PhysRevB.37.6991`.
URL `http://link.aps.org/doi/10.1103/PhysRevB.37.6991`

[300] S. Plimpton, Fast Parallel Algorithms for Short-Range Molecular Dynamics, Journal of Computational Physics 117 (1) (1995) 1–19. `doi:10.1006/jcph.1995.1039`.
URL `http://www.sciencedirect.com/science/article/pii/S002199918571039Xhttps://linkinghub.elsevier.com/retrieve/pii/S002199918571039X`

[301] A. P. Thompson, H. M. Aktulga, R. Berger, D. S. Bolintineanu, W. M. Brown, P. S. Crozier, P. J. in 't Veld, A. Kohlmeyer, S. G. Moore, T. D. Nguyen, R. Shan, M. J. Stevens, J. Tranchida, C. Trott, S. J. Plimpton, LAMMPS - a flexible simulation tool for particle-based materials modeling at the atomic, meso, and continuum scales, Computer Physics Communications 271 (2022) 108171. `doi:10.1016/j.cpc.2021.108171`.
URL `https://doi.org/10.1016/j.cpc.2021.108171https://linkinghub.elsevier.com/retrieve/pii/S0010465521002836`

[302] Q. Chen, C. Dwyer, G. Sheng, C. Zhu, X. Li, C. Zheng, Y. Zhu, Imaging Beam-Sensitive Materials by Electron Microscopy, Advanced Materials 32 (16) (2020) 1907619. `doi:10.1002/adma.201907619`.
URL `https://onlinelibrary.wiley.com/doi/10.1002/adma.201907619`

[303] K. C. Bustillo, S. E. Zeltmann, M. Chen, J. Donohue, J. Ciston, C. Ophus, A. M. Minor, 4D-STEM of Beam-Sensitive Materials, Accounts of Chemical Research 54 (11) (2021) 2543–2551. `doi:10.1021/acs.accounts.1c00073`.

[304] A. J. D'Alfonso, L. J. Allen, H. Sawada, A. I. Kirkland, Dose-dependent high-resolution electron ptychography, Journal of Applied Physics 119 (5) (2016) 0–5. `doi:10.1063/1.4941269`.
URL `http://dx.doi.org/10.1063/1.4941269`

[305] J. Song, C. S. Allen, S. Gao, C. Huang, H. Sawada, X. Pan, J. Warner, P. Wang, A. I. Kirkland, Atomic Resolution Defocused Electron Ptychography at Low Dose with a Fast, Direct Electron Detector, Scientific Reports 9 (1) (2019) 3919. `doi:10.1038/s41598-019-40413-z`.
URL `http://www.nature.com/articles/s41598-019-40413-z`

[306] C. M. O'Leary, C. S. Allen, C. Huang, J. S. Kim, E. Liberti, P. D. Nellist, A. I. Kirkland, Phase reconstruction using fast binary 4D STEM data, Applied Physics Letters 116 (12) (2020). `doi:10.1063/1.5143213`.

[307] C. M. O'Leary, G. T. Martinez, E. Liberti, M. J. Humphry, A. I. Kirkland, P. D. Nellist, Contrast transfer and noise considerations in focused-probe electron ptychography, Ultramicroscopy 221 (December 2020) (2021) 113189. `doi:10.1016/j.ultramic.2020.113189`.
URL `https://doi.org/10.1016/j.ultramic.2020.113189`

[308] H. Yang, R. N. Rutte, L. Jones, M. Simson, R. Sagawa, H. Ryll, M. Huth, T. J. Pennycook, M. L. H. Green, H. Soltau, Y. Kondo, B. G. Davis, P. D. Nellist, Simultaneous atomic-resolution electron ptychography and Z-contrast imaging of light and heavy elements in complex nanostructures, Nature Communications 7 (2016) 1–8. `doi:10.1038/ncomms12532`.
URL `http://dx.doi.org/10.1038/ncomms12532`

[309] H. Yang, I. MacLaren, L. Jones, G. T. Martinez, M. Simson, M. Huth, H. Ryll, H. Soltau, R. Sagawa, Y. Kondo, C. Ophus, P. Ercius, L. Jin, A. Kovács, P. D. Nellist, Electron ptychographic phase imaging of light elements in crystalline materials using Wigner distribution deconvolution, Ultramicroscopy 180 (2017) 173–179. `doi:10.1016/j.ultramic.2017.02.006`.

[310] L. Zhou, J. Song, J. S. Kim, X. Pei, C. Huang, M. Boyce, L. Mendonça, D. Clare, A. Siebert, C. S. Allen, E. Liberti, D. Stuart, X. Pan, P. D. Nellist, P. Zhang, A. I. Kirkland, P. Wang, Low-dose phase retrieval of biological specimens using cryo-electron ptychography, Nature Communications 11 (1) (2020) 1–9. `doi:10.1038/s41467-020-16391-6`.
URL `http://dx.doi.org/10.1038/s41467-020-16391-6`

[311] F. Schwarzhuber, P. Melzl, S. Pöllath, J. Zweck, Introducing a non-pixelated and fast centre of mass detector for differential phase contrast microscopy, Ultramicroscopy 192 (2018) 21–28. `doi:10.1016/j.ultramic.2018.05.003`.
URL `https://www.sciencedirect.com/science/article/pii/S0304399118300615`

Typeset November 27, 2023

Band / Volume 266
Dissecting iron and heme regulatory networks and adaptation to heme stress in *Corynebacterium glutamicum*
A. Krüger (2023), IV, 274 pp
ISBN: 978-3-95806-686-1

Band / Volume 267
Morphological and functional characterization of layer 5 neurons in rat medial prefrontal cortex, their synaptic microcircuitry and serotonin modulation
R. Rama (2023), 116 pp
ISBN: 978-3-95806-688-5

Band / Volume 268
Magnetic and transport studies of the parent and Fe doped Hexagonal-Mn_3Ge Weyl semimetal
V. Rai (2023), xviii, 156 pp
ISBN: 978-3-95806-695-3

Band / Volume 269
The complex inositol metabolism of *Corynebacterium glutamicum* and its application for the production of rare inositols
P. Ramp (2023), VI, 161 pp
ISBN: 978-3-95806-699-1

Band / Volume 270
Spin- and orbital-dependent band structure of unconventional topological semimetals
K. Hagiwara (2023), v, 115 pp
ISBN: 978-3-95806-701-1

Band / Volume 271
Neutron scattering
Experimental Manuals of the JCNS Laboratory Course held at Forschungszentrum Jülich and at the Heinz-Maier-Leibnitz Zentrum Garching
edited by T. Brückel, S. Förster, K. Friese, M. Kruteva, M. Zobel and R. Zorn (2023), ca 150 pp
ISBN: 978-3-95806-705-9

Band / Volume 272
Ab-initio investigation of the interplay between the hyperfine interaction and complex magnetism at the nanoscale
S. R. S. Shehada (2023), ix, xi, 119 pp
ISBN: 978-3-95806-718-9

Band / Volume 273
Analysis of the signal transduction cascade tuning the 2-oxoglutarate dehydrogenase activity in *Corynebacterium glutamicum*
L. Sundermeyer (2023), VI, 119 pp
ISBN: 978-3-95806-722-6

Band / Volume 274
Multicellular defense against phage infection in *Streptomyces* – impact of secondary metabolites and mycelial development
L. Kever (2023), iv, 246 pp
ISBN: 978-3-95806-724-0

Band / Volume 275
Investigation of the electronic band structure of 2D transition metal dichalcogenides via angle-resolved photoemission spectroscopy
B. Parashar (2023), xvii, 156 pp
ISBN: 978-3-95806-725-7

Band / Volume 276
Strain- and process engineering for polyketides production with *Pseudomonas taiwanensis* VLB120 in two-phase cultivations
T. P. Schwanemann (2023), 230 pp
ISBN: 978-3-95806-726-4

Band / Volume 277
Quantitative atomic-level investigation of solid materials through multidimensional electron diffraction measurements
H. L. Lalandec-Robert (2024), xxi, 152 pp
ISBN: 978-3-95806-735-6

Weitere ***Schriften des Verlags im Forschungszentrum Jülich*** unter
http://wwwzb1.fz-juelich.de/verlagextern1/index.asp

Schlüsseltechnologien / Key Technologies
Band / Volume 277
ISBN 978-3-95806-735-6

Mitglied der Helmholtz-Gemeinschaft

JÜLICH
Forschungszentrum